

A Measurement of Lifetimes of b-hadrons Using a Silicon Microstrip Detector at LEP

Gunnar Mæhlum



Thesis submitted in partial fulfillment of requirements to obtain the degree Doctor
Scientiarum at the University of Oslo, Institute of physics.

July 1993

Abstract

The decays of B-hadrons have been reconstructed using tracks from charged particles recorded in the DELPHI silicon microstrip vertex detector. A detailed technical description of the Microvertex Detector is included.

The reconstruction of the b-hadron decays uses the high spatial resolution of this detector to reconstruct primary and secondary vertices. Single hit precision has been measured to be $8 \mu\text{m}$ and $16 \mu\text{m}$ for 92% and 8% of the hits respectively. The mean error on the radial position of the secondary vertex was measured to be $190 \mu\text{m}$. The b-hadron candidates are selected by imposing invariant mass requirements on the secondary vertices. The sum of the charges of the secondaries determines the charge of the b-hadron parent.

The most popular model for the decay of hadrons containing heavy quarks is the spectator model. According to this model the lifetime of the hadron is determined by the lifetime of the heavy quark, and there should be little difference in the lifetimes of the different species of b-hadrons.

232,114 multihadronic Z^0 decays recorded during the 1991 run of LEP at centre-of-mass energies between 88.2 GeV and 94.2 GeV yield 253 B-hadron candidates. From these the mean lifetime of b-hadron is found to be:

$$\langle \tau_b \rangle = 1.49 \pm 0.11(\text{stat} \pm 0.12(\text{syst}))\text{ps}$$

Using the charge information the mean lifetimes of neutral and charged B-hadrons are found to be:

$$\langle \tau_{\text{neutral}} \rangle = 1.43 \pm 0.21(\text{stat}) \pm 0.14(\text{syst}) \text{ ps}$$

$$\langle \tau_{\text{charged}} \rangle = 1.56 \pm 0.19(\text{stat}) \pm 0.13(\text{syst}) \text{ ps}$$

The ratio of their lifetimes is:

$$\tau_{\text{charged}}/\tau_{\text{neutral}} = 1.09^{+0.28}_{-0.22} \pm 0.09(\text{syst})$$

The mean charged B-hadron lifetime can be attributed to the B^+ meson, as these are expected to be much the most abundant charged species. Using recent measurements for the lifetime of the Λ_b^0 and B_s^0 it is possible to extract the lifetime of the B^0 . Under these assumptions we find the lifetime of the B^0 and B^+ to be:

$$\tau_{B^0} = 1.52 \pm 0.23(\text{stat}) \pm 0.15(\text{syst}) \text{ ps}$$

$$\tau_{B^+} = 1.56 \pm 0.20(\text{stat}) \pm 0.13(\text{stat}) \text{ ps.}$$

The ratio of their lifetimes is,

$$\tau_{B^+}/\tau_{B^0} = 1.03^{+0.27}_{-0.21}(\text{stat}) \pm 0.10(\text{syst})$$

These results confirm the spectator model within experimental uncertainties.

Acknowledgements

I joined the Microvertex Detector Team in May 1987 and started to work on the design of the mechanics of the Microvertex Detector, in particular the detector modules. The Microvertex Detector was installed in DELPHI in September 1989, at the same time as the LEP accelerator was commissioned. This detector was not operational because of a faulty cooling system. An improved version was installed in the early spring of 1990, which worked throughout the 1990 running of LEP. After three years work on the construction and running of the Vertex Detector I left CERN in the autumn of 1990 for the Institute of Physics in Oslo. I returned to CERN in the summer of 1991 and the writing of chapter 3 to 5 was mainly done in 1992. During my absence from CERN a third layer was added to the already existing detector.

After returning to CERN I joined William Murray to work on the b-hadron lifetime analysis described in the last chapters. This work was finished in the winter of 1993.

At CERN and in Oslo I have had a great pleasure to work with and learn from many people. I owe most gratitude to my advisor prof. Torleiv Buran who encouraged me to go to CERN in 1989. As well I thank him for his help and support in the later stages of the work on this thesis. In particular I want to thank for the help I received when applying to the funding agencies, sometimes in vain, to obtain some economic support.

During my first stay at CERN I had the great pleasure to work in the group lead by prof. Peter Weilhammer. I want to thank him for his excellent leadership and guidance. I also want to thank Peter for convincing the CERN management to grant a full year extension of my fellow contract.

When at CERN I was introduced to the topic of silicon microstrip detectors by Roland Horisberger. Many of the bold ideas realized in the Microvertex Detector is due to him and I want to thank him for all the support I received during the first years at CERN.

The work on the mechanics and the module production and design were done in close collaboration with Klaus Rats. Klaus also made all the necessary jigs and tools for the module production. It has been a pleasure to work with Klaus and I thank him for his help with all kinds of mechanical problems.

The several hundred thousands bonds in the detector were all done by Robert Boulter and Jeffrey Bizzell. Bob is as well a wizard with the soldering iron and always prepared to improvise to get a defect module working. Jeff also assembled a great part of the detector modules with meticulous care.

The b-lifetime analysis was initiated by William B. Murray. I want to thank him for all his ideas and for immediately accepting me as a co-worker.

The responsibility for the Microvertex Detector Project was after the initial years taken over by Hans Dijkstra. I want to thank him for his leadership and for many interesting discussions, especially over lunch-time.

To construct a detector demands the hard work of several people, I want to thank a few persons which have been central in the Microvertex Team: Anna Peisert did most of the delicate measurements on the microstrip detectors prior to the installation. Tony Smith designed the repeater electronics. The difficult task of aligning the Microvertex is mainly due to Vincent Chabaud and Ronan Mc. Nulty. Magnus Karlsson did most of the work on the track-hit association software. Massimo Caccia and Agnieszka Zalewska should have credit for their work on the simulation and general software for the Microvertex Detector. Tim Adye provided an excellent software environment for the Microvertex off-line analysis and Mike Tyndel, although leading the work on future projects, was always ready to help, especially during the installation of the Microvertex in DELPHI. In addition numerous people of the DELPHI collaboration

deserves credit for putting all the pieces of hardware and software together to make a working experiment.

I want as well to thank Bjarne Stugu for valuable hints when preparing this thesis.

I spent in total about six years at CERN. I want as well to use this opportunity to thank all my friends, some of who have left CERN, who have contributed to making my life in Geneva and the Pais de Gex a pleasant and interesting experience. So thank you Tom, Helmut, Ralf, Martin, Helen, Steinar, Einar, Trygve, Morten, Jørgen, Ines, Harald and all other which lack of space prohibits me from mentioning.

My parents have always supported me in my decisions, even though it meant that they would see their only son just a few times a year. I thank them for their understanding and help.

Finally I want to thank my office mate Koki Yoshioka for his always good mood and for cheering me up in tough periods.

Contents

1	Introduction	1
1.1	General Remarks	2
1.2	Thesis Outline	2
1.3	The standard model of particle physics	3
1.4	Physics at e^+e^- colliders	6
1.5	b-Hadron Production.	6
1.6	b-Hadron Decay and Mixing between Quark Families.	8
1.7	Analysis Objective	13
2	Experimental Apparatus	15
2.1	LEP	15
2.2	The DELPHI Experiment	16
2.3	The Various Detectors of DELPHI	19
3	The Microvertex Detector	26
3.1	Silicon Microstrip Detectors.	26
3.2	Capacitively Coupled Silicon Microstrip Detectors.	28
3.3	Effect of Radiation on Detector Capacitances	31
3.4	Effect of Radiation on Detector Leakage Current	34
3.5	Acceptance Tests.	34
3.6	The Precision of the Diode Lines	36
3.7	The Preamplifier and Multiplexing Chips.	36
3.8	Detector Modules	40
3.9	Production of Detector Modules.	42
3.10	Overall Detector Mechanics	44
3.11	Readout Segmentation	47
3.12	The Repeater Electronics.	47
3.13	Detector Cooling.	48
3.14	The Extended Detector Installed in 1991	49
3.15	Geometrical Survey	50
3.16	Module Survey	51
3.17	Overall Detector Survey	53
4	Data Acquisition, Trigger and Monitoring	56
4.1	The Readout Processor	56
4.2	The Zero Suppression Algorithm.	59
4.3	The Pulse Generator and Controller	60
4.4	The Data Acquisition System.	61

4.5	The Trigger	62
4.6	Slow Controls	64
4.7	In Situ Stability Monitoring.	65
5	Track and Vertex Reconstruction	68
5.1	Microvertex Detector coordinate reconstruction	68
5.2	The Effect of the Magnetic Field on...	71
5.3	Microvertex Detector Track Association	72
5.4	Alignment Using Particle Tracks	73
5.5	Muon Missed Distance	74
5.6	Track Resolution on the Silicon Planes	77
5.7	Vertex Reconstruction and Fit.	80
5.8	Calibration of Track extrapolation errors	81
6	Event Reconstruction and Simulation	83
6.1	Monte Carlo Simulation	83
6.2	Simulation of the Microvertex Detector	84
6.3	Optimization of the Simulation Program	85
6.4	Hadronic Event Selection	85
6.5	K^0 Identification	86
6.6	Converted Photon Identification	86
6.7	Further Selection Criteria	88
6.8	Secondary Vertex Identification	90
6.9	Kinematic Requirements on the Secondary Vertices.	93
6.10	Missing Charged Particle Search	97
6.11	Selected Sample Composition	97
7	Lifetime Fitting Procedure	100
7.1	Charge Estimation	100
7.2	Proper Time Estimation	101
7.3	Fit 1; Average Acceptance Function.	104
7.4	Fit 2; Individual Acceptances.	107
7.5	Test on D mesons	109
8	B lifetime results and systematic uncertainties	112
8.1	Fit to the Mean b-hadron Lifetime.	112
8.2	Fit to the Charged and Neutral Lifetimes.	115
8.3	Fit to B^0 and B^+ lifetimes.	118
9	Conclusions	123
9.1	Comparison with Other Measurements	124
9.2	Implications for the Model for b-hadron Decay.	126
9.3	Perspectives for Future Measurements	126
A	Derivation of the Likelihood Functions	137
A.1	Uncertainty in Proper Time and Time Dependent Acceptance.	139
A.2	Individual Event Acceptances	139
A.3	References	141

B Reprint of NIM publication	142
C Reprint of NIM publication	149
D Reprint of mounting manual	156
E Reprint of contribution to DPF92.	160
F Reprint of paper published in Physics Letters B.	165

Chapter 1

Introduction

The LEP accelerator was constructed with the purpose of producing Z^0 particles in large amounts. Four experiments are installed around the accelerator to investigate the decay properties of the Z^0 and possibly discover new phenomena. One of these is the DELPHI¹ experiment. DELPHI constitutes a general purpose detector covering most of the solid angle. The detector is located around one of the four points where the electron beams in LEP collide. So far no new particles or phenomena have been observed but an impressive level of precision has been achieved in the measurements of the parameters of the standard model of particle physics, see section 1.3 of this chapter.

All known forms of matter and antimatter are produced in the decay of the Z^0 . In particular, particles containing the heaviest known quark are produced abundantly, see section 1.5. These particles have a lifetime of the order of 10^{-12} seconds, they are produced at high energy and travel a mean distance of about 3 mm before decaying.

The point in space where these unstable particles decay into two or more particles is commonly named a decay vertex. With a detector capable of reconstructing decay vertices with high spatial precision it is possible to isolate from the total sample of Z^0 decay products a sample enriched in the contents of particles containing b-quarks, b-hadrons. With such a sample the production and decay properties, including lifetimes, of b-hadrons can be determined.

Before LEP, little was known about the lifetimes of various species of b-hadrons. With increased knowledge of the lifetimes it is possible to determine which processes dominate in the decay of the b-hadrons, see section 1.6. To improve the capabilities of DELPHI to reconstruct the decay vertices it was decided in 1986 to equip the experiment with a system capable of reconstructing secondary vertices with a precision in the order of $100 \mu\text{m}$, the Vertex Detector. The Microvertex Detector was supposed to be ready at start up of LEP in 1989.

At that time the only known electronic detection method of charged particles with a sufficient spatial resolution was silicon microstrip detectors. Silicon microstrip technology was well established in small systems consisting of 5-20 detectors in fixed target experiments. Large systems of more than 100 silicon microstrip detectors in collider experiments had however not been built. Because of this, many of the components in the detector had to be developed using both new and existing technology.

Achievement in science and fundamental research is to a large extent based upon the development and refinement of technology, even though the technology by itself does not necessarily represent a fundamental development. The lifetime measurements presented in this thesis could not have been done without the adaption and further development of current semiconductor

¹Detector with Lepton Photon and Hadron Identification

technology to the needs of high energy physics. The construction of the Microvertex Detector represents an example of how technology when courageously used opens up new possibilities in fundamental physics research. Due to this, a large part of this thesis is devoted to technical aspects of the Vertex Detector. The other part describes a measurement of lifetimes of b-hadrons as an example of a physics measurement exploiting the capabilities of the Microvertex Detector.

1.1 General Remarks

The success of the Microvertex Detector was not achieved without obstacles. Therefore some personal comments based on the experience gained in this project. The detector is a unique product and it was the first of its kind. We should therefore expect surprises, and be prepared for improvisation. Most of the design work at CERN was carried out by physicists with little engineering experience. We encountered several problems during the installation phase of the project. Some of those problems were caused by insufficient planning and testing of components, especially regarding components which were regarded "simple". Time was lost because of confusion about physical dimensions of the various components. Most of the drawings needed for the work was made as the work carried on, and were often of poor quality. Time was often spent in adjusting pieces, cables etc which did not fit.

We have clearly experienced that a project of the size of DELPHI, and a sub-project such as the Microvertex Detector, needs very careful planning and good organization, as well as experienced technicians. A result of the above mentioned problems was that after installation we were not able to operate the detector because of a malfunctioning cooling system and lost valuable experience in running the detector.

This experience can be summed up:

1. Do everything as simply as possible, avoid "advanced" solutions.
2. If something works, do not "improve" it.
3. Do not believe people who says something is "simple" or "straight forward". They have probably not understood the real problem.
4. Do not believe that any convention of numbering of elements, cables etc. will be followed. Everybody always invents his own numbering convention which is incompatible with any other convention.
5. Do not believe anything which is said to be obvious, it is normally not.

1.2 Thesis Outline

Following this introduction is an outline of the physics motivation for the Microvertex Detector and a discussion of the experimental possibilities provided by this detector.

The second and third chapters are very brief summaries of important aspects of the LEP accelerator and the DELPHI Experiment. Chapters four through six contain a detailed description of the components, the assembly and the survey of the Microvertex Detector. The emphasis is put on the need to ensure a sufficient mechanical precision and stability of the detector. Chapters seven through nine describe the off-line event reconstruction and analysis, the emphasis being on the track and vertex reconstruction precision. Finally chapters ten through

twelve describe the data analysis and the extraction of the lifetimes including a discussion of the various contributions to the errors on the lifetimes.

In addition there are six appendices:

Appendix A shows a derivation of the likelihood functions used for the lifetime fits as described in chapter 7. The author wants to thank W. Murray, R. Sekulin and D. Crenell for help in getting the expressions correct. See also [1] for an introduction to the art of lifetime measurements.

Appendix C is a reprint of an article published in Nuclear Instruments and Methods on the test of a prototype for the Microvertex Detector. The test was performed in a beam of high energy particles at the CERN Super Proton Synchrotron (SPS). The author was responsible for the mechanical layout of the test set-up, and part in the running of the test and in the subsequent data analysis.

Appendix B is a reprint of an article published in Nuclear Instruments and Methods giving a status report on the Vertex Detector project. This was presented by the author at the "3rd Topical Seminar on Perspectives for experimental Apparatus at Future High-Energy Machines and Underground Laboratories, San Miniato, Italy, 1988"

Appendix D is a copy of the manual of the precision mounting of detector modules. The development of the assembly procedures and associated equipment was the responsibility of the author. The work was carried out at CERN in close collaboration with K. Ratz, who produced the necessary apparatus. The manual describes the assembly procedure in a step by step manner and contains all relevant dimensions.

Appendix E is a reprint of a contribution by the author, representing the DELPHI Collaboration, to the American Physical Society, Division of Particles and Fields conference at the Fermi National Laboratory, Batavia, Illinois, USA, November 10th. to 14th. 1992. Here results from this analysis and an alternative analysis on B^+ and B^0 lifetimes were presented. The alternative analysis was performed by other members of the DELPHI Collaboration.

Appendix F is a reprint of an article published in Physics Letters containing the measurement of the average charged and neutral b-hadron lifetimes as described in the last part of this thesis. This work, based on an idea by W. J. Murray, was done by us in cooperation and published under the names of the DELPHI collaboration.

1.3 The standard model of particle physics

A theory with mathematical beauty is more likely to be correct than an ugly one that fits some experimental data. (P. A. M. Dirac, who searched in vain for an alternative formulation of QED), [2]

Elementary particle physics is the study of the basic constituents of matter and their interactions. Several excellent introductions to this field is found in the literature [3,4], here only a brief, none-rigorous outline is given.

Matter is thus considered to be made up of spin 1/2 fermions called quarks and leptons. The particles come in 3 different families and are listed in table 1.1. Ordinary matter is made up of particles from the first family. All the fundamental fermions are considered point-like objects. The model does not predict the number of families. However the study of decays of the Z^0 produced at LEP offered the possibility to determine the number of families, or more precisely, the number of light neutrino species, with unprecedented precision [5]. This was one of the first measurement done by the DELPHI collaboration, and was of fundamental importance. This measurement has been improved later [6], and by using all the data collected in 1989 to 1991

Leptons			charge	T_3
$\begin{pmatrix} \nu_e \\ e \end{pmatrix}_L$	$\begin{pmatrix} \nu_\mu \\ \mu \end{pmatrix}_L$	$\begin{pmatrix} \nu_\tau \\ \tau \end{pmatrix}_L$	0	1/2
			-1	-1/2

Quarks			charge	T_3
$\begin{pmatrix} u \\ d' \end{pmatrix}_L$	$\begin{pmatrix} c \\ s' \end{pmatrix}_L$	$\begin{pmatrix} t \\ b' \end{pmatrix}_L$	2/3	1/2
			-1/3	-1/2

Table 1.1: *The elementary fermions in the Standard Model, T_3 is the third component of the weak isospin. Only the left-handed doublets are shown, the right handed are all singlets under the weak interaction, $T = 0$.*

Interaction	Particle	Range (cm)
Electromagnetic	γ	∞
Weak	$W^- Z^0 W^+$	10^{-16}
Strong	gluon	10^{-13}

Table 1.2: *The gauge bosons of the Standard model*

including, the number of light neutrino species published by DELPHI is 3.07 ± 0.06 [7]. Before LEP an upper limit of 4 families were obtained from astrophysical observations [8].

The u, d, and s quarks are referred to as “light” quarks while the c and b-quarks are referred to as “heavy” quarks. The existence of the t-quark is predicted but it has never been observed. The quarks are fractionally charged but they combine only in such a way to produce particles with integer charge. These composite particles, called hadrons, are composed of quark anti-quark combinations (mesons) or three quark combinations (baryons). The proton, as an example, is composed of two u and one d-quark and thus gets a charge of 1. The quarks are carriers of color and are subject to the strong interaction. Free quarks have never been observed [9]

The heaviest quark so far observed is the b-quark which has a mass approximately 5 times that of a proton. From studies of the decay of the Z^0 it is possible to determine a limit on the mass of the t-quark, m_t , within the model: $43 \text{ GeV}/c^2 < m_t < 215 \text{ GeV}/c^2$ [6]. Under various assumptions, and including results from other experiments, the mass range can be further constrained, $m_t = 132^{+27+18}_{-31-19} \text{ GeV}/c^2$ [10] where the first error is experimental and the second corresponds to a mass of the Higgs particle in the range $50 \text{ GeV}/c^2 < m_H < 1000 \text{ GeV}/c^2$.

The leptons are the electron, e, muon, μ , the tau, τ , and their neutral zero mass partners, the electron, ν_e , muon, ν_μ , and tau, ν_τ neutrinos respectively.

There are four known fundamental forces between the particles. Three of these are listed in table 1.2 along with the spin 1 particles that mediate them. The effect of gravity is negligible in the study of elementary particles.

All charged particles interact via the electromagnetic interaction, which is mediated by the massless photon, γ . The weak interaction is mediated by the heavy vector bosons W^- , Z^0 and

W^+ and affect all particles over a limited distance range. The quarks in the hadrons are held together by the strong interaction mediated by the gluons, which acts over a range larger than the weak force.

An important goal in particle physics is the unification of forces. It is believed that deeper insight will emerge from a unified framework. Maxwell explained the forces of electricity and magnetism in a unified theory which predicted the existence of electromagnetic waves². The electromagnetic theory was later extended to include special relativity and quantum mechanics to form the theory of Quantum Electro Dynamics, QED.

The mathematical structure of the Standard Model is characterized by the gauge group:

$$SU(1) \otimes SU(2) \otimes SU(3)_{\text{color}} \quad (1.1)$$

The weak interaction is not invariant under spatial inversion, parity is thus violated. Under the assumption that the neutrinos are massless only negative helicity neutrinos play a role under the weak interaction. The negative helicity leptons, also called left handed, are therefore arranged in weak doublets and the positive helicity, right handed leptons are arranged in singlets. Similarly the left handed quarks are arranged in doublets while the right handed are singlets under the weak interaction.

The primes on the quarks in table 1.1 indicate that transitions between the quark families are possible. This flavour mixing can be summarized in the elements of the Cabbibo-Kobayashi-Maskawa mixing matrix, see section 1.6

The Standard Model does not predict masses for the fundamental particles, except for the W and Z masses which are given to lowest order:

$$m_W^2 = \frac{\pi\alpha}{\sqrt{2}G_F} \left(\frac{1}{\sin^2 \theta_W} \right) \quad (1.2)$$

$$m_Z^2 = \frac{\pi\alpha}{\sqrt{2}G_F} \left(\frac{1}{\sin^2 \theta_W \cos^2 \theta_W} \right) \quad (1.3)$$

where $\alpha = 1/137.036$ is the fine structure constant, determined from the quantum Hall effect, and $G_F/(\hbar c)^3 = 1.6639 \times 10^{-5} \text{GeV}^{-2}$ is the Fermi coupling constant, determined from the muon lifetime and $\sin^2 \theta_W = 0.2325$ is the weak mixing angle, determined from neutral current processes, and Z-pole observables. α is known to a precision of 0.045 ppm, G_F is known to 17 ppm. Finally the third parameter $\sin^2 \theta_W$ is known to 3441 ppm. The exact value of $\sin^2 \theta_W$ depends however of the renormalization prescription used. The numerical values in the above paragraph are all from [9].

Alternatively the Z^0 mass, $m_Z = 91.179 \pm 0.020 \text{ GeV}/c^2$ as measured by DELPHI [7], can be taken as the third fundamental parameter instead of $\sin^2 \theta_W$, then:

$$\sin^2 \theta_W = \frac{1}{2} \left[1 - \left(1 - \frac{4\pi\alpha}{\sqrt{2}G_F} \frac{1}{m_Z^2} \right)^{1/2} \right] \quad (1.4)$$

is a derived parameter and $m_W = m_Z \cos \theta_W$.

The fermion masses are introduced via symmetry breaking of a scalar field, with its corresponding particle, the Higgs particle, H^0 . The existence of the neutral Higgs particle is of crucial importance for the Standard Model. The H^0 has never been observed, searches done at LEP have however given a lower mass limit. A limit of $38 \text{ GeV}/c^2$ at 95% confidence level has been reported by DELPHI [12], a limit of $48 \text{ GeV}/c^2$ is found in [9]. At the present level of precision the most important unresolved puzzle of the Standard Model is the existence of the H^0 particle.

²The maxwell equations were cast in their present form by O. Heavyside [11]

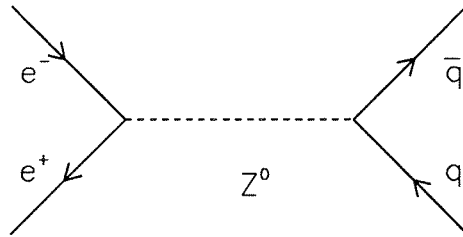


Figure 1.1: *Feynman graph for the process $Z^0 \rightarrow q\bar{q}$*

The electro-weak interactions are thus specified by the model and are determined by e , the electric charge, and the parameter θ_W .

With the exception of the particle masses, the electro-weak sector of the Standard Model is entirely specified by knowing α , G_F , and M_{Z^0} .

1.4 Physics at e^+e^- colliders

e^+e^- colliders provide excellent tools for studying high energy interactions. This is mainly because they offer:

1. Clean production of nature's fundamental building blocks - the quarks and leptons. This is typically in the form of pair production of a fermion and anti-fermion.
2. All the center-of-mass energy is available for the production of these building blocks. This can be contrasted with proton proton or proton anti-proton collisions where hard collisions between two constituents happen at an (unknown) energy, typically around $\leq 1/6$ of the available energy. The 4 quarks not involved in the collision give debris which obscures the study of the hard collision. It is not a "clean" environment.
3. Because of the cleanliness of the e^+e^- environment there is a great potential for discoveries and in-depth study of the phenomena.

1.5 b-Hadron Production.

At the Z^0 pole the quark production proceeds through the Feynman graph in figure 1.1. All the quarks listed in table 1.1, except the t-quark can be produced in the decay of the Z^0 . When the center-of-mass energy of the electron and positron is set to the observed Z^0 mass, the calculated width of the diagram is [13]:

$$\begin{aligned} \Gamma(e^+e^- \rightarrow f\bar{f}) &= \frac{Dm_Z}{24\pi} \left(\frac{gT_3}{\cos\theta_W} - eQ \tan\theta_W \right)^2 \\ &= \frac{G_F}{\sqrt{2}} \frac{Dm_Z^3}{3\pi} (T_3 - Q \sin^2\theta_W)^2 \end{aligned} \quad (1.5)$$

where the contribution from both left and right handed fermions are included. The color factor D is 1 for leptons and 3 for quarks as there are three indistinguishable color states for

c-hadrons			
Symbol	Quark Content	Mass(GeV/c ²)	Lifetime (ps)
D ⁰	cū	1.8645 ± 0.0005	0.420 ± 0.008
D ⁺	cđ	1.8693 ± 0.0005	1.066 ± 0.023
D _s ⁺	cš	1.9688 ± 0.0007	0.450 ^{+0.030} _{-0.026}
D ^{0*} (2010)	cū	2.0007 ± 0.0014	
D ⁺⁺ (2010)	cđ	2.0101 ± 0.0006	
Λ _c ⁺	cud	2.2849 ± 0.0006	263.2 ± 2.0
b-hadrons			
Symbol	Quark Content	Mass(GeV/c ²)	Lifetime (ps)
B ⁰	bd	5.2787 ± 0.0021	1.41±0.14
B ⁺	bu	5.2786 ± 0.0020	1.42±0.14
B _s ⁰	bs	seen [15]	
		[16]	1.02 ^{+0.46} _{-0.31} ±0.10
Λ _b ⁰	bud	seen [17]	0.87 ^{+0.35} _{-0.24} ±0.08
		[18]	1.12 ^{+0.32} _{-0.29} ±0.16

Table 1.3: *The Principal hadrons containing c and b-quarks. For each particle there exists an anti particle with opposite charge and same mass. The D^{0*} and D⁺⁺ are higher angular momentum states of the D⁰ and D⁺ which decay immediately, therefore no lifetime is quoted for them. Data from The Particle Data Group [9] unless referenced. For the B⁰ and B⁺ the values quoted are the averages calculated in section 9.1.*

the quarks, T_3 is the third component of the weak isospin and $e = g \sin \theta_W$ is the electron charge. The dependence of the velocity of the particles in the final state has been neglected. For effectively massless particles with $\beta \sim 1$, the equation 1.5 is correct. For heavy fermions a small correction needs to be added. This correction is -1.4% for the b-quark. The partial width of $Z^0 \rightarrow b\bar{b}$ is measured by DELPHI to be $\Gamma(\bar{b}) = 378 \pm 42$ MeV corresponding to a branching fraction of 0.219 ± 0.024 , [14].

The quarks produced do not appear as free quarks in the final state, but combine with other quarks to form hadrons in a process called fragmentation. This process is only phenomenologically known and can not be calculated by perturbative methods. An outgoing “bare” quark is turned into a hadron by $q\bar{q}$ pair production, and the subsequent “dressing” of the original quark by the anti-quark part of the pair. The quark part is free to continue this process until there is insufficient energy left for $q\bar{q}$ production.

The fragmentation process is often parametrized by a probability function, also called fragmentation function, $f(z)$, where z is defined as the fraction of energy, E and momentum parallel to the quark direction, p_{\parallel} carried away by the hadron:

$$z \equiv \frac{(E + p_{\parallel})_{\text{hadron}}}{(E + p_{\parallel})_{\text{quark}}} \quad (1.6)$$

Note that in this definition the energy and momentum used in the denominator are not equal to the beam energy because of gluon and initial state radiation.

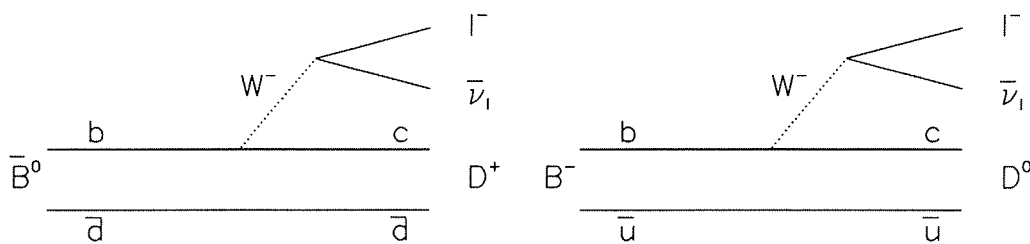
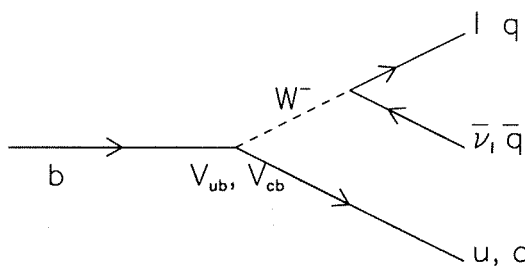


Figure 1.2: The processes $\bar{B}^0 \rightarrow D^+ l^- \bar{\nu}_l$ and $B^- \rightarrow D^0 l^- \bar{\nu}_l$ is shown mediated by the weak charged current, W^- within the spectator model

Figure 1.3: Contributions to b -quark decay. The amplitude for the diagram is proportional to the CKM matrix elements V_{ub} and V_{cb} when the b -quark decays to a u or c -quark respectively. The $q\bar{q}$ pair produced can be any of the quark combinations present in the CKM matrix.



A commonly used parametrization of the fragmentation function was suggested by Peterson et. al. [19]:

$$f(z) = \frac{1}{z(1 - 1/z - \epsilon/(1 - z))^2} \quad (1.7)$$

The principal hadrons containing heavy quarks are found in table 1.3.

1.6 b-Hadron Decay and Mixing between Quark Families.

In the simplest model of the decay of heavy hadrons the constituent heavy quark decays via the weak charged current, as shown in figure 1.2. This approximation is known as the spectator model since the light quark is only a spectator in the process

The heavy quark is considered to be a free particle and its decay properties determine those of the b -hadron. In the context of this model the b -hadron lifetime is just the reciprocal of the b -quark decay width Γ_b , such that all b -hadrons would have similar lifetimes.

This picture already makes sense for the c -quark. The observed lifetimes of the c -hadrons [20], indicate, however, that there must exist corrections to this approximation [21,22]:

$$\tau(D^+) : \tau(D^0) : \tau(D_s^+) : \tau(\Lambda_c) : \tau(\Xi_c) : \tau(\Omega_c) \simeq 2.5 : 1 : 1 : 0.5 : 1.3 : 1.9 \quad (1.8)$$

It is not the purpose of this section to give a comprehensive survey of b -hadron decays, but rather to shed some light on the intricate topic of decays of b -hadrons. The natural starting point for this is therefore the charged current which mediates the weak decay process, such as the semi-leptonic³ \bar{B}^0 and B^- decays shown in figure 1.2, can be written for quarks and leptons as:

³Semi-leptonic denotes decays in which a lepton anti-lepton pair is produced in addition to one or more hadrons, in contrary to non-leptonic decays in which the decay products are hadrons only

$$\begin{aligned}
J_-^\mu = & \frac{g}{2\sqrt{2}}(\bar{u} \bar{c} \bar{t})\gamma^\mu(1 - \gamma_5) \begin{pmatrix} d' \\ s' \\ b' \end{pmatrix} \\
& + \frac{g}{2\sqrt{2}}(\bar{\nu}_e \bar{\nu}_\mu \bar{\nu}_\tau)\gamma^\mu(1 - \gamma_5) \begin{pmatrix} e^- \\ \mu^- \\ \tau^- \end{pmatrix}
\end{aligned} \tag{1.9}$$

where the row vectors are the eigenstates corresponding to the charge 2/3 quarks and the neutrinos. The column vectors are the eigenstates corresponding to the charge -1/3 quarks and the charged leptons, g is the weak coupling constant:

$$\frac{g^2}{8m_W} = \frac{G_F}{\sqrt{2}} \tag{1.10}$$

A similar expression to 1.9 can be written for the charged current associated with the W^+ .

The weak eigenstates corresponding to the charge -1/3 quarks are written with primes to indicate that they are not the same as the mass eigenstates for these quarks. This leads to mixing between the families which is expressed in matrix form as:

$$\begin{pmatrix} d' \\ s' \\ b' \end{pmatrix} = \begin{pmatrix} V_{ud} & V_{us} & V_{ub} \\ V_{cd} & V_{cs} & V_{cb} \\ V_{td} & V_{ts} & V_{tb} \end{pmatrix} \begin{pmatrix} d \\ s \\ b \end{pmatrix} \tag{1.11}$$

The matrix relating these bases was defined for six quarks and given an explicit parametrization by Kobayashi and Maskawa in 1973 [23]. This was a generalization from the four quark case where the matrix is parametrized by a single parameter the Cabibbo angle [24].

By convention the three charge 2/3 quarks, u , c and t is kept unmixed and all the mixing is expressed by the 3×3 unitary matrix operating on the charge -1/3 quarks. The nine elements are complex and it is a principal task of experiment to determine them. Electroweak gauge theory requires the matrix to be unitary, which reduces the eighteen parameters of the matrix to nine. There are five further reductions having to do with the fact that the choice of phase given to the quark fields are arbitrary. This eliminates five more parameters, not six, because a common phase rotation of all six quark fields leave the matrix unaffected.

In principle the values of the elements can be determined from weak decays of the relevant quarks and from deep inelastic neutrino scattering. The 90% confidence limits on the magnitude of the elements are [9]:

$$\begin{pmatrix} 0.9747 & - & 0.9759 & 0.218 & - & 0.224 & 0.002 & - & 0.007 \\ 0.218 & - & 0.224 & 0.9735 & - & 0.9751 & 0.032 & - & 0.054 \\ 0.003 & - & 0.018 & 0.030 & - & 0.054 & 0.9985 & - & 0.9995 \end{pmatrix} \tag{1.12}$$

The ranges are for individual matrix elements. The constraints of unitarity will limit the other elements when a specific matrix element has been chosen.

There exist several parametrizations of this matrix in addition the one proposed by Kobayashi and Maskawa. The differences in these parametrizations do not represent fundamental physical differences. One parametrization proposed by Chau and Keung [25] in which the matrix can be

written as a product of three separate matrices, each one analogous to a rotation between two generations:

$$V = \begin{pmatrix} 1 & 0 & 0 \\ 0 & c_{23} & s_{23} \\ 0 & -s_{23} & c_{23} \end{pmatrix} \begin{pmatrix} c_{13} & 0 & s_{13}e^{-i\delta} \\ 0 & 1 & 0 \\ -s_{13}e^{i\delta} & 0 & c_{13} \end{pmatrix} \begin{pmatrix} c_{12} & s_{12} & 0 \\ -s_{12} & c_{12} & 0 \\ 0 & 0 & 1 \end{pmatrix} \quad (1.13)$$

where $c_{ij} = \cos \theta_{ij}$ and $s_{ij} = \sin \theta_{ij}$. The central matrix of equation 1.13 has the additional term in δ to describe rotations two families apart. Multiplying the matrices gives:

$$V = \begin{pmatrix} c_{12}c_{13} & s_{12}c_{13} & s_{13}e^{-i\delta} \\ -s_{12}c_{23} - c_{12}s_{23}s_{13}e^{i\delta} & c_{12}c_{23} - s_{12}s_{23}s_{13}e^{i\delta} & s_{23}c_{13} \\ s_{12}s_{23} - c_{12}c_{23}s_{13}e^{i\delta} & -c_{12}s_{23} - s_{12}c_{23}s_{13}e^{i\delta} & c_{23}c_{13} \end{pmatrix} \quad (1.14)$$

This parametrization has the advantage that the elements above the diagonal are simple.

It is here appropriate to recall the origin of this matrix, which is in the Higgs sector of the electroweak theory, in particular the part of the action responsible for the quark masses, see [26]. This is supposed to happen via Yukawa couplings of the quarks to a complex Higgs field. The existence of the Higgs field is not experimentally verified. The matrix may therefore be looked upon as a parametrization of experimental results, but that the deeper underlying theory is not yet verified. In this context it is worthwhile to mention that it is not known whether the cause of the observed CP violation⁴ in neutral K meson decay is purely electro-weak or due to the strong interaction. In the CKM context the CP violation is treated as a purely electro-weak effect. CP violation is as well expected in the decay of B^0 . The CP violation is however expected to be strongly suppressed. Because of the relatively small event samples at LEP, CP violation in the B^0 is not expected to be observed. The possible observation of CP violation in B^0 decays is however of great importance.

In the absence of family mixing, (i.e. V diagonal) the quarks would couple only to their doublet partner. This situation would lead to a stable b-quark since it is lighter than its t-quark partner. Within the CKM scheme the b-quark can decay into lighter u and c quarks with amplitudes proportional to the term V_{ub} and V_{cb} respectively. These b-quark decays are illustrated in figure 1.3.

The total b-quark decay rate is the sum of these two contributions:

$$\Gamma_{\text{tot}} = \sum_{q=u,c} \Gamma(b \rightarrow q) \quad (1.15)$$

Each particular transition can be broken up into semi-leptonic, Γ_{sl} and non-leptonic parts, Γ_{nl} :

$$\Gamma(b \rightarrow q) = \Gamma_{\text{sl}}(b \rightarrow q) + \Gamma_{\text{nl}}(b \rightarrow q) \quad (1.16)$$

The amplitudes for the decays can then be written:

$$\mathcal{M}_{\text{sl}} = -\frac{G_F}{\sqrt{2}} V_{qb} \bar{q} \gamma_\mu (1 - \gamma_5) b \bar{l} \gamma_\mu (1 - \gamma_5) \nu_e \quad (1.17)$$

$$\mathcal{M}_{\text{nl}} = -\frac{G_F}{\sqrt{2}} V_{qb} \bar{q} \gamma_\mu (1 - \gamma_5) b \bar{q} \gamma_\mu (1 - \gamma_5) q \quad (1.18)$$

The decay of the b-quark within the spectator model is similar to the decay of muons, with the muon replaced by the b-quark. The model can however be refined by taking into account:

⁴CP = Charge-Parity violation. Until 1964 it was believed that all types of interaction were invariant to the combined operation of CP. It is however observed that this is not true in the decay of the K^0 [4]

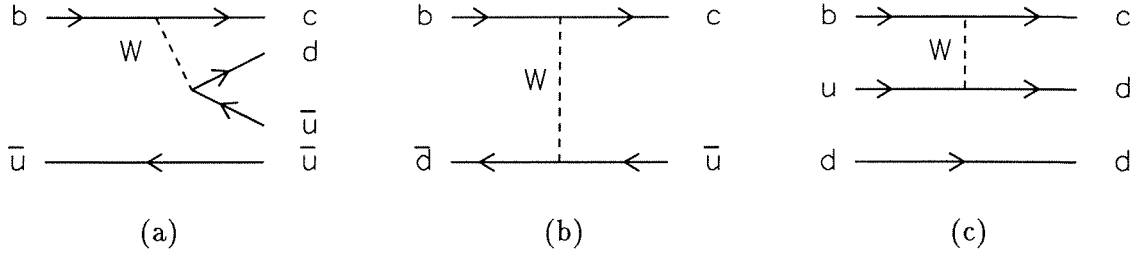


Figure 1.4: Non-spectator model corrections to the b -decay. (a) is a quark interference diagram for the decay of a B^- , (b) is a W exchange diagram of \bar{B}^0 decay and (c) is a W exchange diagram for Λ_b decay.

1. phase space corrections due to finite quark and lepton masses [27],
2. QCD corrections arising from virtual gluon exchange and real gluon emission, [28–34],
3. smearing effects due to the Fermi motion of the constituents inside the decaying bound states, [30].

When taking the corrections 1 and 2 into account, the semi-leptonic and non-leptonic decay rates are:

$$\Gamma_{\text{sl}}(b \rightarrow ql\bar{\nu}_l) = \frac{G_F^2 m_b^5}{192\pi^3} I(r_q, r_l, 0) \eta_{\text{sl}} |V_{qb}|^2 \quad (1.19)$$

$$\Gamma_{\text{nl}}(b \rightarrow q_1 q_2 \bar{q}_3) = 3 \frac{G_F^2 m_b^5}{192\pi^3} I(r_{q_1}, r_{q_2}, r_{q_3}) \eta_{\text{nl}} |V_{q_1 b}|^2 |V_{q_3 q_2}|^2 \quad (1.20)$$

where $I(r_a, r_b, r_c)$ with $r_a = \frac{m_a}{m_b}$ are phase-space factors normalized such that for massless final states $I(0,0,0) = 1$, η_{sl} and η_{nl} are QCD correction factors. The factor 3 in equation 1.20 is because of the additional colour degree of freedom in non-leptonic decays. Note that if these factors are set to 1, and m_b is replaced by the muon mass m_μ , in equation 1.19, then the decay rate becomes that of muons.

The exact values of η_{sl} and η_{nl} is dependent upon the quark masses, the number of excited flavours, f , and the renormalization scale, $\Lambda_{\overline{\text{MS}}}$. With $m_b = 4.8 \text{ GeV}/c^2$, $m_c = 1.35 \text{ GeV}/c^2$, $f = 5$, and $\Lambda_{\overline{\text{MS}}} = 150(300) \text{ MeV}$ one obtains, [35]:

$$\eta_{\text{sl}} = 0.89(0.87) \text{ and } \eta_{\text{nl}} = 1.11(1.18) \quad (1.21)$$

The effect of the Fermi motion, combined with the measured shape of the energy spectrum from semi-leptonic decays can be used to reduce the uncertainty coming from the quark masses by exploiting the constraints on the quark masses provided by the lepton energy spectrum [30].

Using the above expressions, 1.19 and 1.20, for the decay rates, and the values in 1.21 for QCD corrections the following predictions for the b -hadron lifetimes can be calculated:

$$\tau_B \times \frac{|V_{cb}|^2}{10^{-15} \text{ s}} = \begin{cases} 2.9 & (2.8) & \text{(I)} \\ 3.1 & (3.0) & \text{(II)} \end{cases} \quad (1.22)$$

where (I) and (II) refers to two sets of quark masses:

$$(m_b, m_c, m_s, m_{\text{ud}}) = \begin{cases} (4.8, 1.4, 0.15, 0) \text{ GeV}/c^2 & \text{(I)} \\ (5.2, 1.8, 0.5, 0.3) \text{ GeV}/c^2 & \text{(II)} \end{cases} \quad (1.23)$$

and the two numbers given for each mass assumption corresponds to $\Lambda_{\overline{MS}} = 150(300)\text{MeV}$ respectively. The contribution from $b \rightarrow u$ is included assuming a maximum value $|V_{ub}/V_{cb}|^2 = 0.02$

If there are any lifetime differences between the b-hadrons, the origin of these differences must lie outside the spectator model. The following non-spectator effects are expected to have noticeable effects on the lifetimes of the various b-hadrons:

Quark interference which occur dominantly in the channels:

$$B^-(b\bar{u}) \rightarrow c\bar{u}d \quad (1.24)$$

$$\Lambda_b(bud) \rightarrow c\bar{u}d \quad (1.25)$$

The diagram for the process 1.24 is shown in figure 1.4(a). All other B^- or Λ_b decay channels leading to identical (anti)-quark pairs are suppressed either by the Cabibbo angle, the very small $b \rightarrow u$ coupling or by phase space. The interference is destructive and thus leading to a lengthening of the lifetimes of B^- and Λ_b in comparison with the spectator-model prediction.

W exchange is a possible decay mode for hadrons containing a positive quark or anti-quark in addition to the b-quark:

$$\bar{B}_d^0(b\bar{d}) \rightarrow c\bar{u} \quad (1.26)$$

$$\bar{B}_s^0(b\bar{s}) \rightarrow c\bar{c} \quad (1.27)$$

$$\Lambda_b(bud) \rightarrow cdd \quad (1.28)$$

Again all other exchange processes are suppressed by either Cabibbo angle or involve the small $b \rightarrow u$ coupling. The diagrams for the decays 1.26 and 1.28 is shown in figure 1.4(b) and (c). The above reactions tend to shorten the lifetime in respect to the spectator model. For mesons however the effect is suppressed by helicity conservation.

Weak annihilation can only take part in B^- and B_c^- decays. In the B^- decay it is suppressed by the weak $b \rightarrow u$ transition, while for the second case the B_c^- can make transitions to ordinary b-hadrons via the decay of the c-quark.

The above mentioned processes leads to a qualitative hierarchy of lifetimes:

$$\tau(B^-) > \tau(B_s^0) > \tau(B^0) > \tau(\Lambda_b) \quad (1.29)$$

From the above mentioned considerations it can be concluded that the spectator model provides an appropriate framework for the description of inclusive weak decay properties of b-hadrons. Non-spectator corrections, found to be on the level of unity in the c-sector, is expected to drop to a level below 10% in b-decays. The total lifetimes of all weakly decaying b-hadrons should therefore be equal to within a few to ten percent. Exceptions may be expected in the mass eigenstates of the $B_s^0 - \bar{B}_s^0$ system and for hadrons containing a c-quark in addition to the b-quark.

There is however a lack of quantitative understanding of the c lifetime pattern and in the extrapolation from c to b mass range. For this reason the theoretical expectations outlined above have large uncertainties. It is therefore important to measure the lifetimes of the various b hadrons separately to clarify the lifetime issue experimentally.

1.7 Analysis Objective

The primary objective of this analysis is to measure separate lifetimes of neutral and charged hadrons containing a b-quark. No attempt is done in particle identification of the final states. Because of this we are left with a somewhat larger sample than when the final states are fully or partly reconstructed.

As explained above, the introduction of the Microvertex Detector makes this type of measurement possible. The method is based on secondary vertex identification and charge counting. By introducing very strict requirements on the quality of the event reconstruction, the error on the charge due to wrongly assigned or lost particles in the decay vertex of the b-hadron is expected to be minimized. The vertex reconstruction does not include neutral particles. These do not contribute to the charge, and the momentum carried by these particles is parametrized and compensated for in the analysis. Figure 1.5 shows an event with a primary and two reconstructed secondary vertices as reconstructed in the Microvertex Detector.

A high degree of purity of the sample in b-hadrons is obtained by introducing a requirement on the invariant mass of the observed decay products. This leads unfortunately to a very poor efficiency in recognizing the b-hadrons. Because of the method chosen the emphasis in the event sample has to be put on the purity rather than on the efficiency of the selection. There are expected to be no doubly charged B hadrons, as the b-quark charge is only $-1/3$. Hence the number of multiply charged secondary vertices can be used as a measure of the charge confusion probability. The final event sample can be analyzed to find separately the charged and neutral lifetimes as well as the mean lifetime.

With the present size of available event samples this method is justifiable. It is however to be expected that methods combining vertex and final state particle contents reconstruction will be superior in precision as larger event samples become available. In this respect the unique particle identification detectors of DELPHI should be particularly useful.

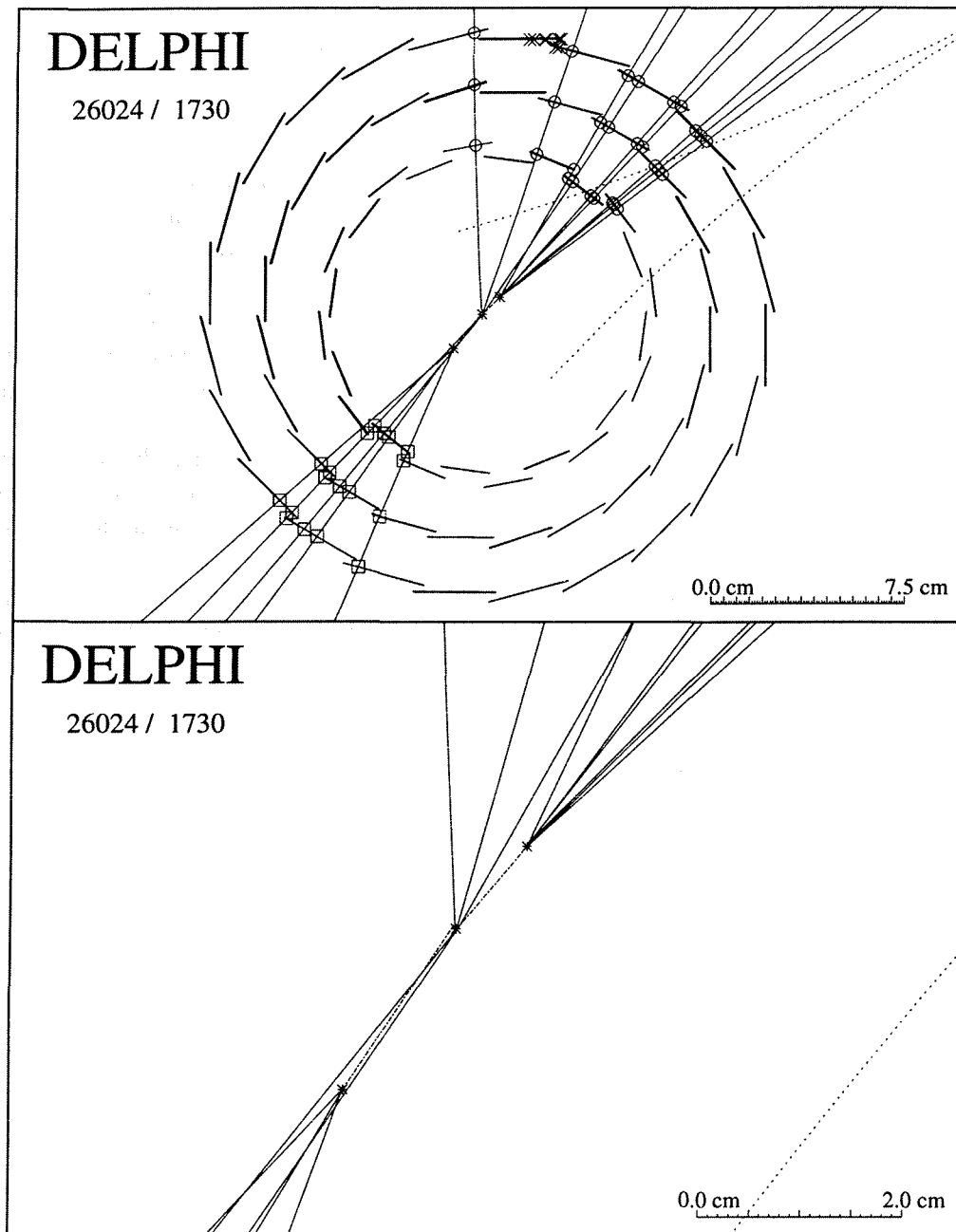


Figure 1.5: *Display of a b-hadron decay candidate from the Microvertex Detector, view along the z axis. The positions of the silicon planes are outlined as tangential lines at fixed radii. The circles and squares indicate the location of the hits on the silicon planes in positive and negative z hemisphere. The vertices are indicated by stars. Some unassigned hits are visible in the upper part of the detector. The two dotted lines are extrapolations of tracks that do not have associated hits in the Microvertex Detector. Having an invariant mass of $0.01 \text{ GeV}/c^2$, they are most probably from a photon that converted outside the Microvertex Detector. The decay distances are indicated by dotted lines joining the vertices. See also figures 2.4 and 2.5 where the same event is shown reconstructed in the whole of DELPHI.*

Chapter 2

Experimental Apparatus

2.1 LEP

The decision for construction of the LEP accelerator and storage ring was taken by the, at that time, 12 member states of CERN in December 1981. The civil engineering work started in 1983. It was the first electron accelerator built on the CERN site. The machine was commissioned in august 1989.

The center of mass energy of the machine is chosen to be close to the Z^0 resonance peak at 91.16 GeV, and the machine is to day the most powerful tool for studying the electro-weak and hadronic properties of the decays of the Z^0 .

Because of the energy loss due to synchrotron radiation the bending radius of the ring was chosen as large as possible given economic and technical limitations. The circumference of the machine is thus about 27 km and that makes it the largest accelerator ever built. W^+W^- pair production at 174 GeV will be studied using LEP after 1994 pending the installation of additional accelerating cavities to boost the center of mass energy to a maximum of 200 GeV.

Maximum beam energy:	60 GeV
Injection energy:	22 GeV
Luminosity:	$1.7 \times 10^{31} \text{cm}^{-2} \text{s}^{-1}$
Circumference:	26.66 km
Interaction Regions:	4
Particles per bunch:	4.16×10^{11}
Mean current per beam:	3 mA
Filling rate:	0.25 mA/min
Energy spread:	0.1%
RF frequency:	352.2 MHz
Acceleration period:	80 s
Revolution time:	88.9 μs
Collision rate	22.2 μs

Table 2.1: *Parameters of LEP*

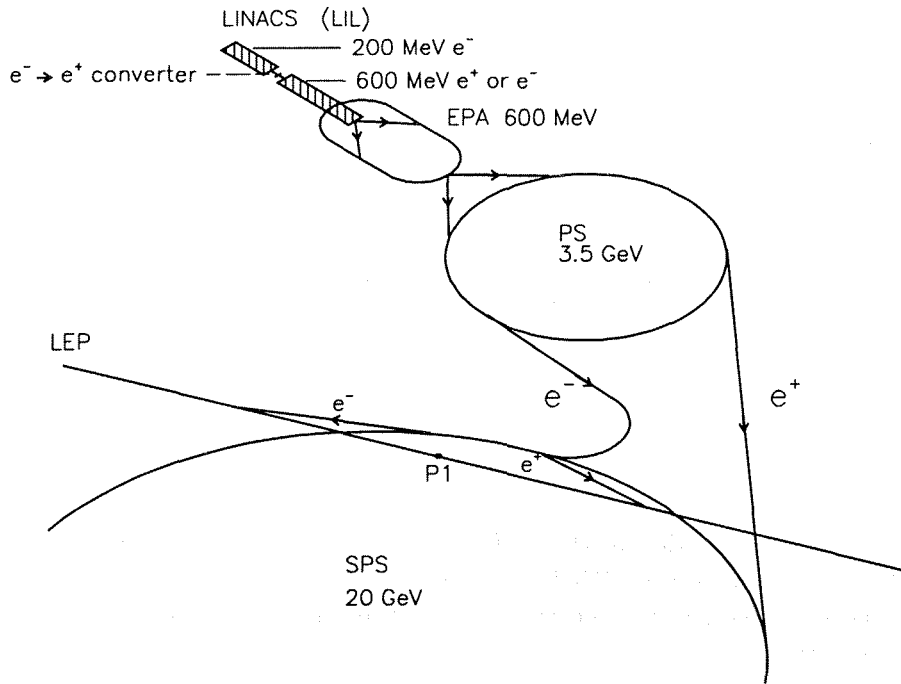


Figure 2.1: *The injection scheme for LEP. High intensity electron beams at an energy of 200 MeV are used to produce positrons in a converter. Both electrons and positrons are accelerated to 600 MeV in a second linac and fed to the EPA. From there beams are injected into PS for acceleration to 3.5 GeV before going to the SPS. The SPS completes their preliminary acceleration to 20 GeV and injects them into the LEP ring. The abbreviations are explained in the text.*

The electron and positron bunches are formed in the Lep Injector Linac¹, LIL where they are accelerated to 600 MeV/c. The bunches are stored in the Electron Positron Accumulator, EPA, before being injected into the Proton Synchrotron, PS, and accelerated to 3.5 GeV/c. From the PS the e^+e^- bunches are injected into the Super Proton Synchrotron, SPS, where they are accelerated another step to 22.2 GeV/c. Finally the beams are injected into LEP accelerated to nominal energy and stored. Figure 2.1 shows the main parts of the accelerator complex used in providing the LEP electron beams. The lifetime of a fill is typically 4 to 8 hours. An excellent review of the design and commissioning of the LEP collider is found in [36].

2.2 The DELPHI Experiment

DELPHI, DEtector with Lepton, Photon, and Hadron Identification, is a general purpose particle detector consisting of a number of tracking, particle identification and calorimetric devices, most of which are mounted in a solenoidal magnetic field parallel to the electron and positron beams in LEP. Figure 2.3 shows a perspective view of the detector. The purpose of the tracking devices is to reconstruct fully the trajectories of the reaction products from the e^+e^- collisions. Given

¹Linac; jargon for linear accelerator

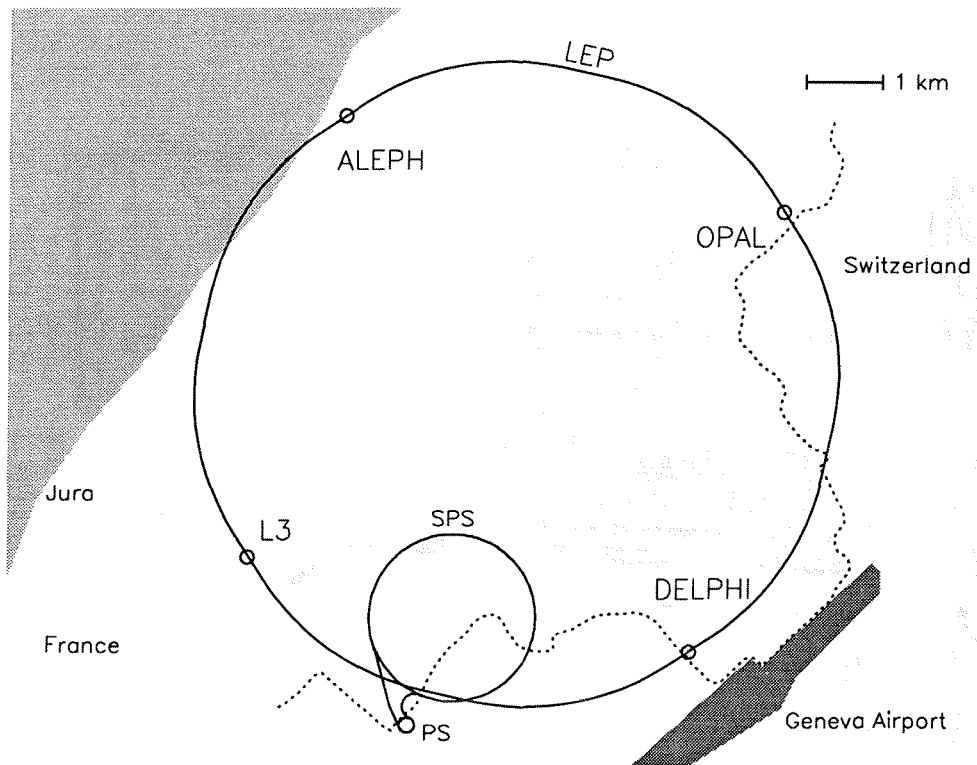


Figure 2.2: The LEP accelerator location in France and Switzerland. The positions of the four experiments, ALEPH, OPAL, DELPHI and L3 are indicated.

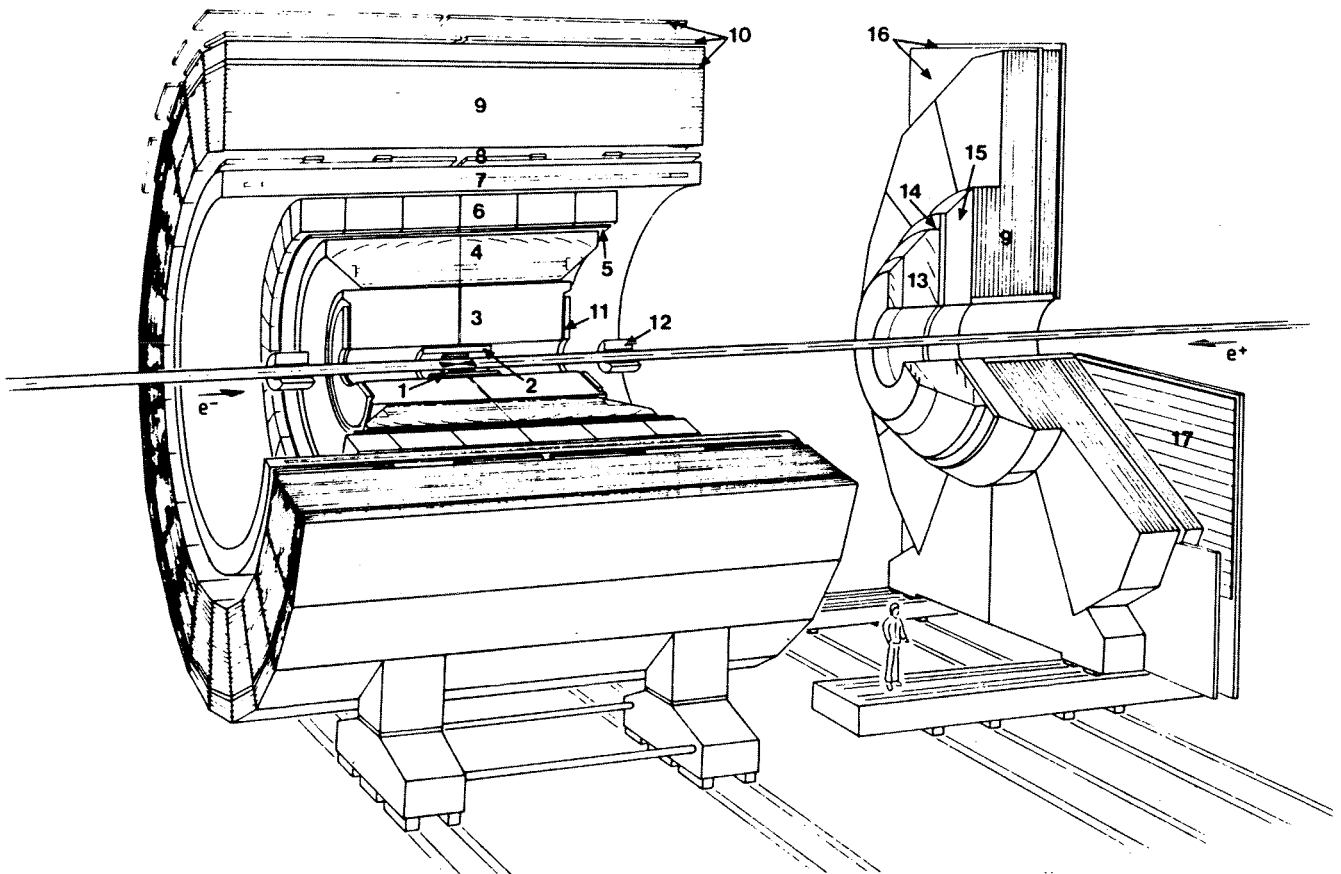


Figure 2.3: *Perspective view of the DELPHI detector, the different parts are: 1: Micro-Vertex Detector, 2: Inner Detector, 3: Time Projection Chamber, 4: Barrel Ring Imaging Cherenkov Counter, 5: Outer Detector, 6: High Density Projection Chamber, 7: Superconducting solenoid, 8: Time of Flight Counters, 9: Hadron Calorimeter, 10: Barrel Muon Chambers, 11: Forward Chamber A, 12: Small angle Tagger, 13: Forward RICH, 14: Forward Chamber B, 15: Forward Electromagnetic Calorimeter, 16: Forward Muon Chambers, 17: Forward Scintillator Hodoscope,*

this information, together with the magnitude of the magnetic field, the particle momentum can be found from the Lorentz formula. The particle identification devices uses the Cherenkov light emitted when fast particles traverse a medium with a refractive index larger than one. The calorimetric devices measures the energy of the particles by sampling the energy deposited when the particles are absorbed in matter.

The DELPHI experiment is described in the technical proposal [37], and in a progress report, [38], finally a description of the detector together with its performance after the first year of running, is published in [39]. References to publications on design and performance of the sub-detectors are also found there.

2.3 The Various Detectors of DELPHI

The DELPHI detector divides in three main parts, the barrel and the two end-caps. The detector has full coverage in the azimuthal angle ϕ . The coverage in polar angle is limited by the beam tube. The barrel covers the region from 43° to 137° in polar angle θ . In the following we refer to the z -axis as the axis along the beams and R as the distance from this axis in the xy plane.

All the detectors in the end-caps lie outside the acceptance of the Vertex Detector and are therefore not used in any of the work presented here. As details on DELPHI are published elsewhere, only a brief description of the experiment is given here. The performance of the barrel track detectors is found in table 2.2 and the calorimeters in table 2.3.

The detectors in the barrel are, starting from inside,

The Vertex Detector, which is described in chapter 3.

The Inner Detector, ID consists of two concentric layers:

1. an inner drift chamber with jet-chamber geometry, giving 24 $R\phi$ points per track and
2. 5 cylindrical Multi-Wire Proportional Chamber, MWPC, layers, each with 192 wires and 192 circular cathode strips. The wires provide fast trigger information and resolve left/right ambiguities from the jet section. The strips give z information, also for the trigger.

The jet chamber has 24 azimuthal sectors. The gas mixture together with field wire grids on both sides of the sense wire planes and operation point were chosen to produce a drift velocity proportional to R . The trigger information is therefore contained in a narrow time-window (~ 100 ns)

The Time Projection Chamber, TPC is the main tracking device in DELPHI. The tracking volume is from $R = 23$ cm to $R = 120$ cm and ± 150 cm in z . Each end cap is divided into six sectors with 192 sense wires and 16 circular pad row, in total 1680 pads.

The TPC provides three dimensional track information and measures the curvature of the track from which the momentum of the particle can be calculated. In addition the energy loss, dE/dx , by the particles traversing can be used for particle identification.

The Barrel Ring Imaging Cherenkov Counter, BRICH will provide hadron identification over most of the momentum range by Cherenkov angle reconstruction from gas and liquid radiators: 4.2σ separation for π/K up to 18 GeV and for K/p up to 30 GeV. The

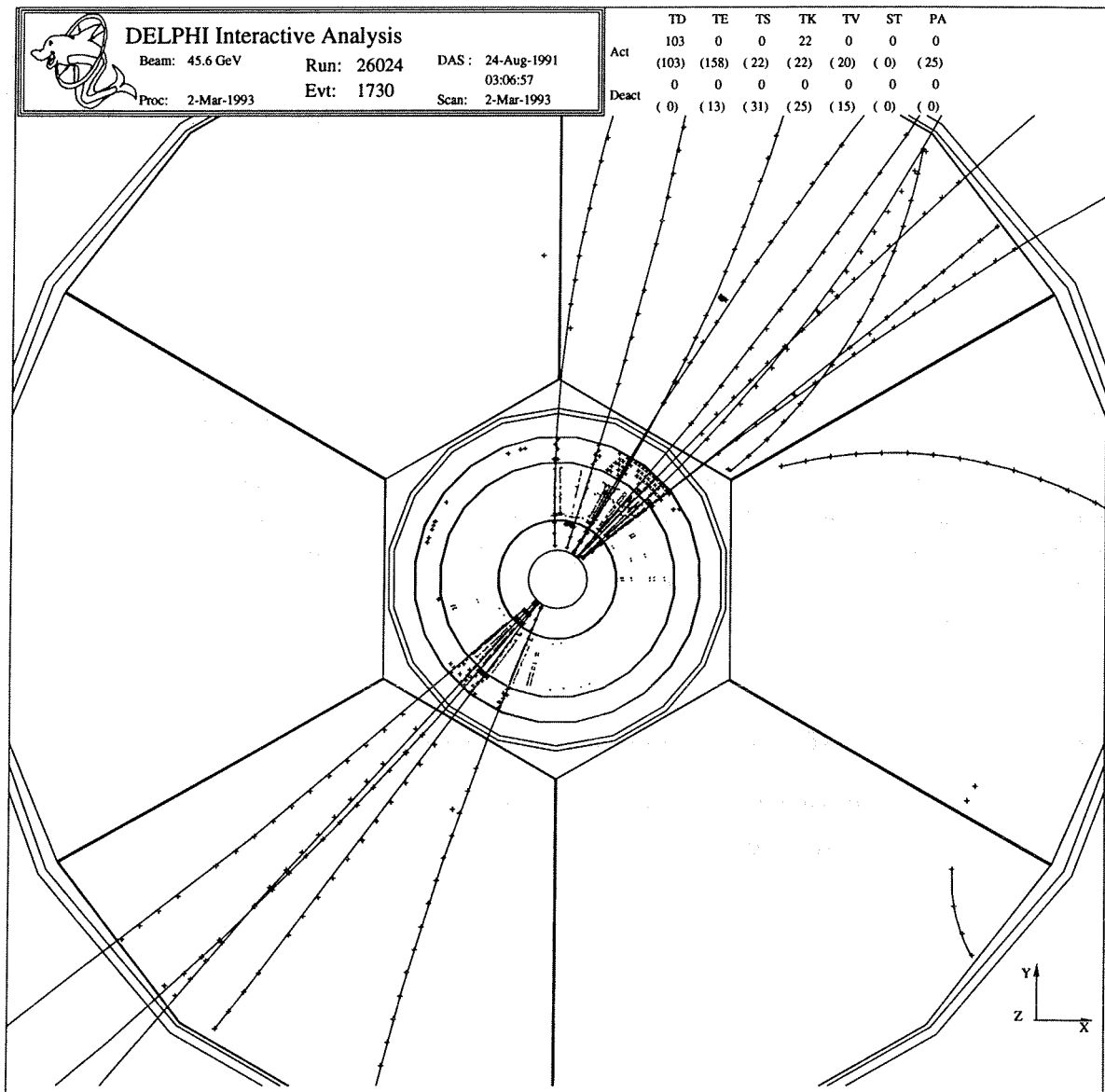


Figure 2.4: Display of a Z^0 decay reconstructed in DELPHI, view along the z axis. This is the same event as is shown in figure 1.5 but here the Inner Detector, between circle 2 and 4 and the TPC, the six outermost large sectors, are included in the view. The Vertex Detector is located between the two innermost concentric circles. The hits in the detectors are indicated as small crosses. The possible photon conversion that was indicated only as extrapolated tracks is here visible in the right side of the TPC.

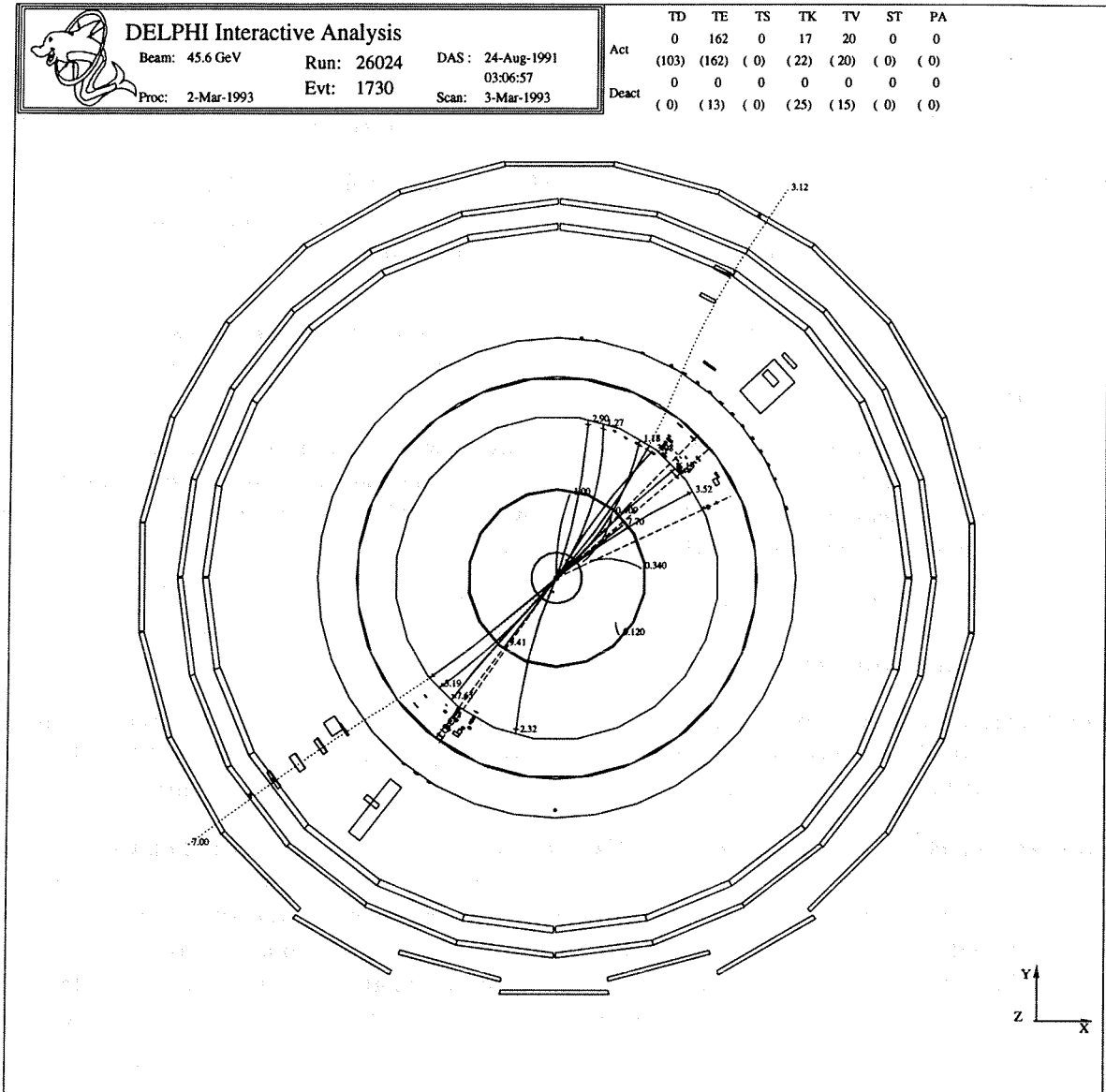


Figure 2.5: This is again the same event as is shown in figure 1.5 but here all the barrel detectors are included in the view. Some activity in the HPC can be seen, with photons extrapolated as dashed lines to the vertex. Hits are as well seen in the Outer Detector. The Hadron Calorimeter shows activity from hadrons and from possible penetrating muons, which has given hits in the muon chambers, upper right and lower left side of the picture.

detector was however only operational during the last months 1991. In 1992 the detector was operational and is expected to improve the particle identification properties of DELPHI considerably.

Outer Detector, OD is essential to provide fast trigger information on both $R\phi$ and z and, because of the small radius of the TPC, to improve the momentum resolution for fast particles.

It is made up of 24 modules, 4.7m long and each containing 145 drift tubes in 5 staggered layers. The modules overlap and provide full azimuthal coverage.

The High Density Projection Chamber, HPC is an application of the time projection principle to calorimetry. It measures the three dimensional charge distribution induced by electromagnetic showers and by penetrating hadrons and muons with good granularity in all three dimensions.

The time-projection principle is realized by using the lead converter as field cage. The ionization charge is then extracted on a single proportional wire plane at one end of each HPC module.

The field cage/converter consists of 41 lead layers with 8 mm spacing giving a depth of 18 radiation lengths. Each layer is formed by trapezoidal lead wires separated by insulator. A voltage gradient between the lead wires provides a field of about 100 V/cm parallel to the beam axis. The maximum drift length is 48 cm.

The HPC covers the barrel area inside the magnetic field from radius 208 cm to 260 cm with 144 separate modules, using a segmentation of 24 in azimuth and 6 along z . The polar angle coverage is 43° to 137° .

The Time of Flight detector, TOF, A single layer of 172 scintillator counters is mounted just outside the solenoid. They cover most of the polar angle from 41° to 139° . The TOF is used for fast triggering of beam events and to reject penetrating cosmic ray particles.

The Barrel Hadronic Calorimeter, HCAL, consists of 24 sectors with 20 layers of limited streamer mode detectors inserted into the 2 cm wide gaps between the 5 cm thick iron plates of the return yoke of the solenoid which functions as absorber. The readout is segmented into pads. The pads are shaped to form towers pointing to the interaction point. Each tower covers $\Delta\phi = 3.75^\circ$ in azimuthal angle and $\Delta\theta = 2.96^\circ$ in polar angle. For triggering purposes logical combinations of groups of 4×4 towers are formed.

The Barrel Muon Chambers, MUB, is made up of two layers of drift chambers. The first layer of 2×24 planks is inserted into the return yoke of the magnet after 90cm of iron and contains 3 staggered drift-chamber planes. The second layer is mounted on the outside of the yoke after additional 20 cm of iron. It consists of overlapping planks with clearance for the passage of cables etc. The drift chambers operate in the proportional mode. The signals are six-fold multiplexed into time digitizers. With 2 ns time digitization a resolution of $\sigma_{R\phi} = 1.5$ mm and $\sigma_z \sim 1$ cm is obtained.

The superconducting solenoid [40] sets up the magnetic field and is located between the HPC and the HCAL. The solenoid has a nominal field of 1.23 T at a current of 5000 A. The iron of the hadronic calorimeter functions as the return yoke of the magnetic field.

The End-Caps consists of:

The Small Angle Tagger, SAT, consists of two identical calorimeters and a silicon track detector. The system detects small angle Bhabha events that are used in the luminosity determination. The calorimeters are mounted close to the vacuum tube on both sides of the detector, covering the polar angle from 2.5° to 7.7° . A lead mask is mounted in front of the calorimeter on one side and the tracking detector in front of the calorimeter on the other side. The mask and the tracker defines the angular acceptance with high precision, which is crucial in the luminosity determination.

The luminosity measurement is of great importance in the determination of the electroweak parameters. However, for the analysis presented here, the luminosity determination is of lesser importance.

The Forward Chambers A, FCA, provides tracking and triggering in the polar angle from 11° to 35° . It is actually mounted on both sides of the TPC and is mechanically a part of the barrel.

The Forward Ring Imaging Cherenkov Counter, FRICH, uses the same principle as the BRICH. The detector was however not fully installed for the data taking period in 1991, and was not operational.

The forward chambers B, FCB, provides tracking and triggering information covering the polar angle from 11° to 35° and greatly improves the momentum resolution in this region.

The Forward Electromagnetic Calorimeter, FEMC, measures electromagnetic energy deposition in the polar angle region from 10° to 36.5° . It consists of two 5 m diameter disks of 9064 lead glass blocks shaped as truncated pyramids pointing towards the interaction region.

The Forward Hadronic Calorimeter, Forward HCAL, measures hadronic energy deposition in the return yokes. The construction and operation is similar to that of the Barrel HCAL.

The forward Hodoscope, HOF, consists of plastic scintillators inserted between the end-cap iron and the second muon chamber plane. It improves the muon detection and trigger efficiencies for beam events and cosmic rays, and provides the only trigger for beam related muons.

The Forward Muon Chambers, MUF, cover the polar angle from 9° to 43° . The detector has two planes, one inside the iron, behind 85 cm of iron, the other outside behind another 20 cm of iron. Each plane, $9 \times 9\text{m}^2$ consists of 4 quadrants, each quadrant consists of 2 orthogonal layers of drift chambers.

detector	Acceptance		no of points along track	point resolution σ (mm)	comments
	R(cm)	$ z $ θ (degrees)			
Vertex Det.	6.5 - 11	12	3	$R\phi$: 0.009	2-track sep: 100 μ m
ID jet	11.8 - 22.3	40	24	$R\phi$: 0.11	
ID trigger	23 - 28	≤ 50	5	z : < 1	
TPC	35 - 111	≤ 134	16	$R\phi$: 0.23 z : 0.9	(a) for ≥ 3 pad rows 192 dE/dx samples $\sigma(dE/dx) = 6.2\%$
OD	198 - 206	≤ 232	5 $R\phi$	$R\phi$: 0.11	fast z information
B-Muon	~ 445 ~ 485	≤ 185	5 z 2 + 2	z : 44 $R\phi$: 1.5 z : 10	two layers separated by 20 cm iron

The data for the muon chambers are from test beam, the other from LEP.

Table 2.2: Track detector performance, from [39].

	Acceptance		Granularity	Depth	Resolution
	R(cm)	z (cm)			
HPC	208-260	≤ 254	$\phi \sim 1^{\circ}$ $z : 4 \text{ mm}$	$18X_0$	$23/\sqrt{E} + 1.1^a$
FEMC	46-240	284-340	$\phi : 1^{\circ}; \theta : 1^{\circ}$	$20X_0$	$[(0.35 + 5/\sqrt{(E)^2 + (6/E)^2}]^{1/2 b}$ 4% at 45.6 GeV
SAT	10-36	233-285	$\phi : 7.5^{\circ} \text{ } 15^{\circ}$ $\theta : 0.7^{\circ}$	$28X_0$	$[1.2^2 + 11.4^2/E]^{1/2} + 2.3$ 5% at 45.6 GeV
VSAT ^(b)	$\sim 6-9$	770	5-7 mrad	$24X_0$	120/ \sqrt{E}
HCAL	320-479 ^c 65-460 ^d	<380 340-489	$\phi : 3.75^{\circ}$ $\theta : 3.0^{\circ c}$ $2.6^{\circ d}$	6λ	

^a In test beam.

^b 12 W/Si layers, $3 \times 5 \times 10 \text{ cm}^2$

^c In the barrel.

^d In the end-caps

Table 2.3: Calorimeter performance, from [39]

Chapter 3

The Microvertex Detector

The philosophy behind the design was to construct the simplest possible detector given the constraints of space, power consumption and useful performance for physics. Fixed target experiments using silicon detectors had ample space for heavy support structures ensuring the stability needed for precise track reconstruction. Requirements of full angular coverage in collider experiments however prohibit any solid mechanical structure close to the interaction region. An important feature was therefore that the silicon detectors were used both as sensing elements and structural components.

In addition new type of silicon micro-strip detector was developed for the Microvertex Detector. A description of these detectors and tests they underwent is presented.

The micro-strip detectors are read using amplifier and multiplexing circuits designed specifically for the detector in CMOS¹ VLSI² technology. The functionality of these circuits is explained.

Because of the importance of precise mechanics for the track reconstruction a detailed description of the mechanical design is given. The production of the components involved breaking new ground in detector construction. A detailed account of the production procedure is therefore given.

The detector was initially designed with two layers of microstrip counters, Outer and Inner layer. The beam tube of smaller radius installed in 1991 allowed for the addition of a third layer closer to the interaction point conveniently named Closer layer.

A thorough survey of the detector was done before commissioning. It proved to be of great importance for the final alignment of the detector, which used particle tracks, to have a good knowledge of the initial position of the detectors.

3.1 Silicon Microstrip Detectors.

The production of silicon micro-strip detectors is similar to the production of semiconductor circuits. Narrow diode strips are made either by ion implantation or by deposition and subsequent diffusion on the polished surface of a high resistivity silicon wafer in a geometry determined by

¹CMOS: Complementary Metal Oxide Semiconductor, a method of making integrated circuits on silicon wafers [41].

²VLSI: Very Large Scale Integration, several tens of thousands transistors are integrated on one single chip. [42]

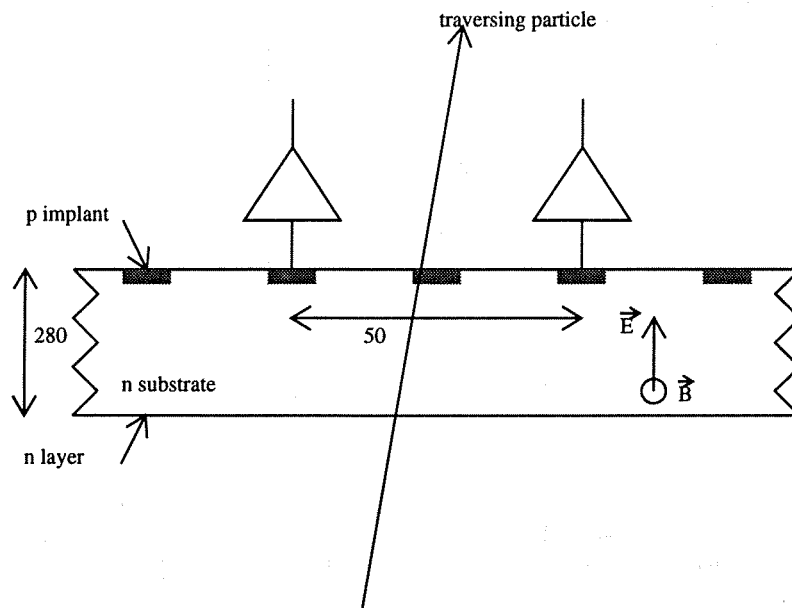


Figure 3.1: Operation of silicon detectors. Holes created by the traversing particle drift in the electric field towards the strips. In our case every second strip is connected to low noise amplifiers. The electric field is directed towards the diode strips, the magnetic field in DELPHI is indicated and normal to the figure plane. (All dimensions in μm).

photo-lithographic technique. On the other side of the wafer a thin layer, strongly doped³ to the same polarity as the bulk silicon, is formed. The high resistivity of the substrate ensures a sufficient low depletion voltage to avoid problems with break down due to excessive electric field in the substrate. This method of making position sensitive radiation detectors was first developed by Kemmer [44].

Some early applications of silicon microstrip detectors are published in [45–49] An historical overview, additional details on the principles of operation of silicon detectors and further references are also found in [50, 51].

The detectors are operated by depleting the substrate of free charge carriers and thus creating an electric field in the bulk silicon. A traversing charged particle ionizes the material creating electron-hole pairs which drift in the electric field. In the case of a weakly n-type substrate and p-type implanted diode strips, the electrons drift to the strongly n-doped side and the holes to the diode strips. The charge on the strips is detected with low noise charge sensitive amplifiers.

³Pure silicon, also called intrinsic, is at room temperature a semiconductor, parts of the conduction band is filled. By adding very small amounts of impurities, doping, with a different number of valence electrons the resistivity of the intrinsic silicon can be reduced. n doping refers to adding an element with more valence electrons thus increasing the conduction band population, p doping refers to adding an element with fewer valence electrons thus inducing vacant orbitals in the valence band. This vacant orbital, or hole, acts in an applied electromagnetic field as if it has charge e^+ and an effective mass m^* [43]

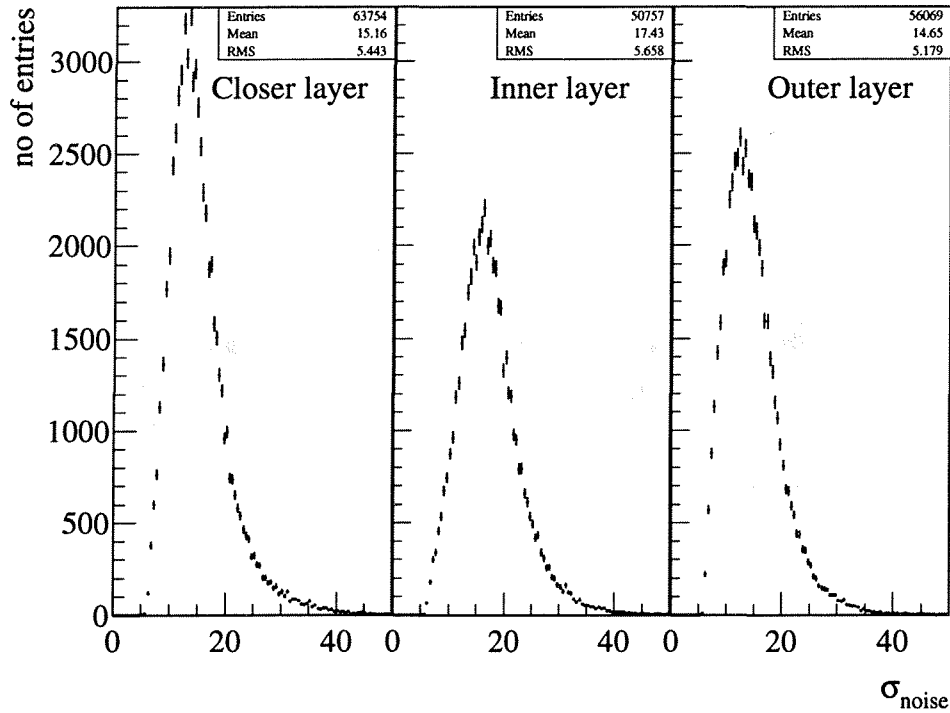
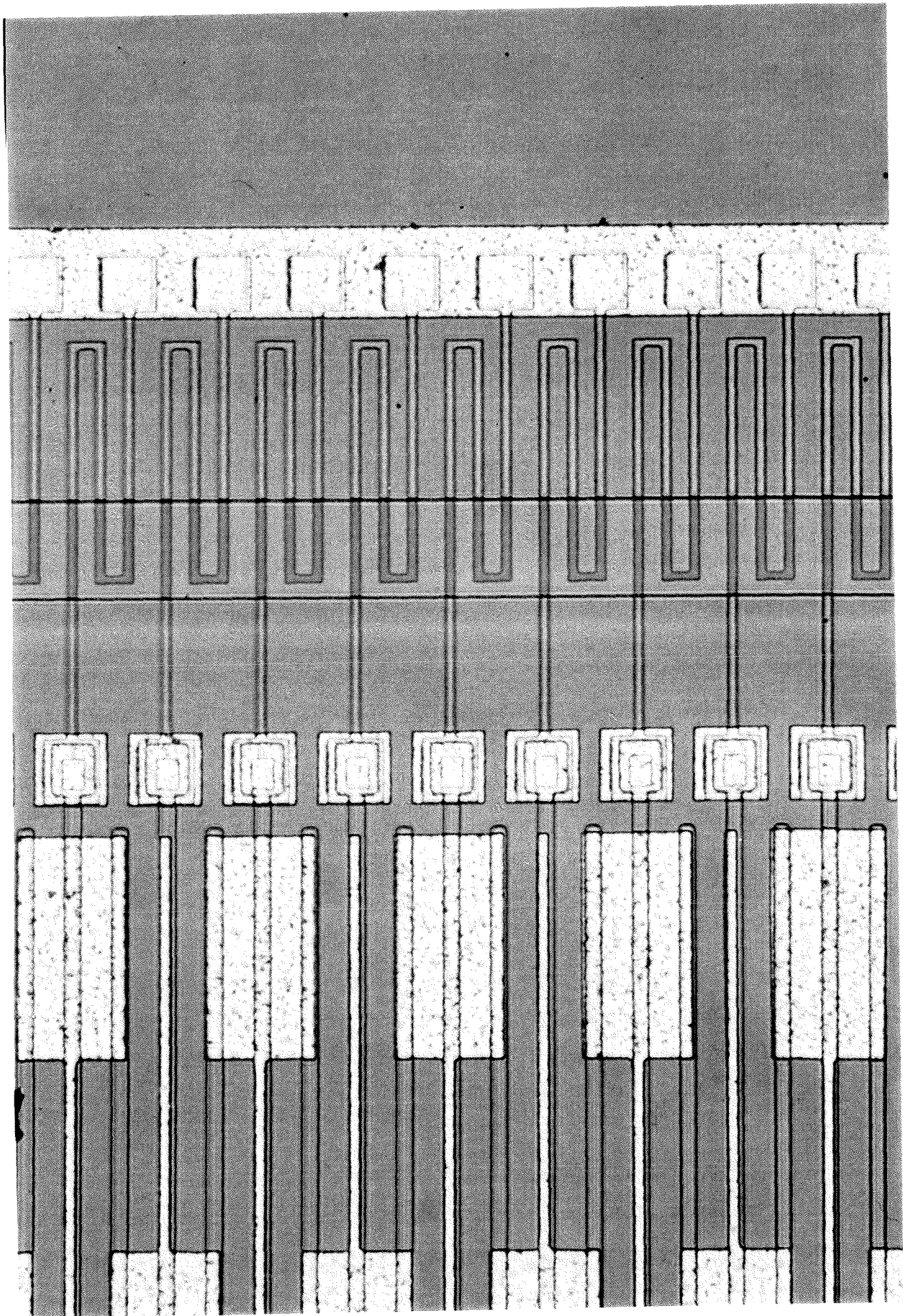


Figure 3.2: Landau spectrum from the detectors from beam events. Horizontal scale energy deposition in units of σ_{noise} . The peak corresponds to the most probable energy deposition, which is 84 KeV for 30 GeV/c pions [54]. The spectra shown includes however particles in the range (1-45) GeV/c. The pulse-heights, PH , have been normalized to the minimum track length in traversing the silicon at different incident angles: $PH = PH / \sin \theta$, where θ is the angle between the silicon plane and the track. The spectra are however broadened because of small gain variations between the detector modules. The peak positions are 13, 15, and 12 for the three detector layers: Closer, Inner and Outer layer respectively (see section 3.10 and 3.14).

The energy spectrum of the ionization charge from high energy particles follows an approximate Landau distribution [52,53]. Figure 3.2 show the pulse height spectrum in units of RMS_{noise} obtained with the microstrip detectors in DELPHI. The pulse heights have been normalized to the minimum track length in traversing the detector at different incident angles. The shown spectra deviates from the true Landau distribution because of ionization effects, amplifier noise and gain variations between channels.

3.2 Capacitively Coupled Silicon Microstrip Detectors.

Using conventional silicon microstrip detectors together with integrated read-out electronics implies that the leakage current of the individual strips are fed directly to the preamplifier input. Because of space limitations and because one needs several tens of picofarad to avoid signal losses by capacitive coupling to the n-side, it is not possible to use discrete coupling capacitors between the diode and the amplifier. The leakage current per strip may vary by a factor up to 1000 across one detector. This does not create problems with the spatial resolution as long as the current stays below about 200 nA/strip, but the leakage current introduces base-



line variations across the detector and requires an ADC with a large dynamic range.

To overcome these problems a microstrip detector with integrated coupling capacitors was designed for the Microvertex Detector⁴. The production method of these detectors and results from a test in a high energy particle beam is published in [55]. These detectors are made on n-type silicon of a resistivity of 3-5 kΩcm leading to a depletion voltage of 60-100 V. The strips are formed by boron deposition and diffusion to a concentration of about 10^{18} atoms/cm³. The diodes are 7 μm wide and are spaced 25 μm apart. The diffusion side of the detector is covered with silicon-dioxide of thickness 200 nm on the diode strips and 1 μm elsewhere. Each diode is connected through an opening in the oxide to a bias-resistor formed of poly-crystalline silicon, from now on simply called poly-silicon, on the oxide surface, with every second strip connected on either end. All the bias-resistors are connected to a common metal line on the supply side. Every second diode is, on top of the thinner oxide, covered by a 5 μm wide aluminium strip. The aluminum strips have 2 bonding pads in both ends for connection to the amplifiers. The thinner oxide is thus the dielectric of a capacitor with the diffusion line and the metal line as plates, see figure 3.4. A guard ring of p-diffusion runs around the active area.

The detectors were produced in three sizes: 26 × 60 mm², 33 × 60 mm² and 53 × 20 mm², having 1281, 1025 and 768 diode strips respectively of 7 μm width and 58000 μm length for the Outer and Inner and length 52000 μm for the Closer layer. Figure 3.3 shows the layout of a corner of a detector. The double set of bonding pads gives the possibility to do a second bonding for repair purposes. Note as well that the sensitive area extends under the bond-pads. This is only possible on capacitively coupled detectors since the bond-pads are insulated from the diode strip.

In the case of capacitively coupled detectors the output signal is given by [55,56]:

$$\frac{V_{so}}{V_{no}} = \frac{\Delta Q}{V_n} \frac{1}{C_p \left[\left(\frac{C_f}{C_c} \right) + 1 \right] + C_f} \quad (3.1)$$

where V_{so} and V_{no} is the output signal and noise voltages respectively, ΔQ is the ionization charge, C_f is the amplifier feedback capacitance, C_c is the coupling capacitance and C_p is the capacitance from the diode strip to the n-side of the detector, C_b , and capacitance to neighboring strips, C_i , lumped together. Only the capacitance to the nearest neighbors is taken into account:

$$\frac{1}{C_p} = \frac{1}{C_b} + \frac{1}{C_i} \quad (3.2)$$

We do not want to loose any charge on the amplifier input by the introduction of the coupling capacitor, compared to a situation with direct coupling of the strips to the amplifiers. The ratio C_f/C_c should therefore be kept small. The physical location of the various capacitances on the detector is shown in figure 3.6.

In order to maximize the signal to noise we observe that:

⁴The detectors were designed, in cooperation with the Microvertex Detector Group, and produced by Center for Industrial Research, SI, Oslo, Norway

Figure 3.3: (Colour inset), Micro-photograph of a capacitively coupled Silicon detector. The white rectangles are the bonding pads, 60 μm × 100 μm for connection to the amplifiers. The darker lines are the 7 μm wide diodes which are spaced 25 μm. Every second diode covered with aluminium which appear as white lines. The bias resistors are the S shaped lines. The common bias line is the outer wide metal line. The guard ring is seen below the bias-resistors.

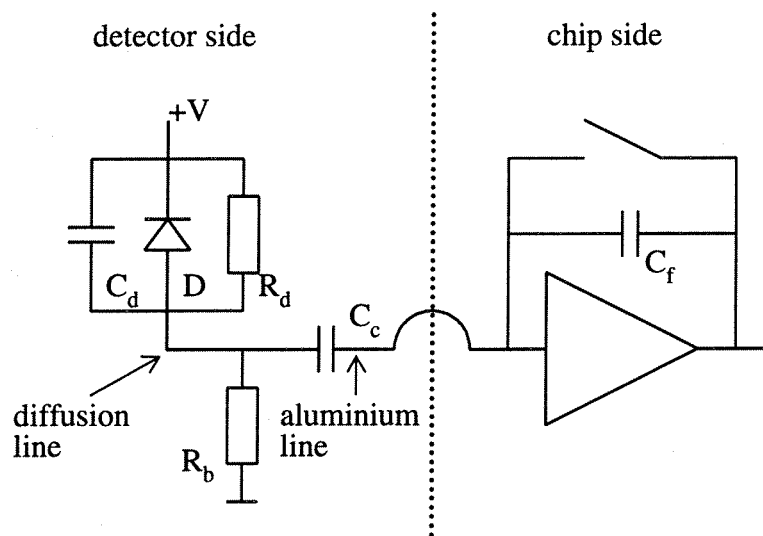


Figure 3.4: Operation of capacitively coupled Si detectors. The preamplifier is not directly coupled to the diode strip, instead a capacitor, $C_c \approx 70\text{pF}$ is formed by the diode and the metal line and a dielectric of $\approx 200\text{ nm}$ thick silicon-dioxide. The diode is here shown with its equivalent circuit of a resistor, $R_d \approx 1\text{ GOhm}$, in parallel with a capacitor $C_d \approx 1\text{ pF}$. The diode is depleted by a positive voltage applied to the n-doped side. The other components are discussed in the text.

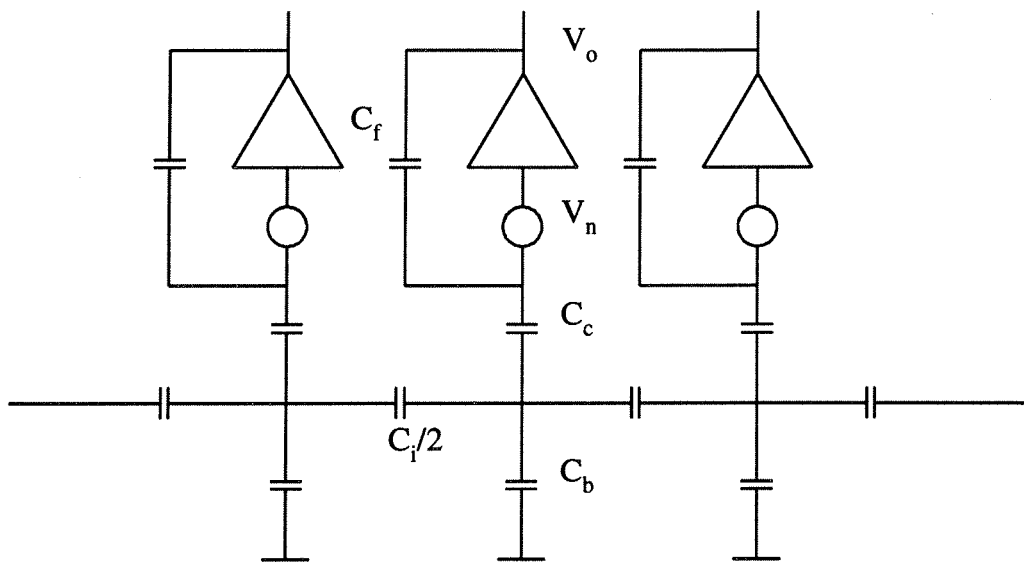


Figure 3.5: Circuit diagram used in the calculation of signal, V_{s_o} , and noise, V_{n_o} output voltages. C_f, C_i, C_c, C_b are the feedback, inter-strip, coupling and capacitance to the n-side respectively. $V_o = V_{s_o} + V_{n_o}$ is the output voltage V_n is the input noise voltage.

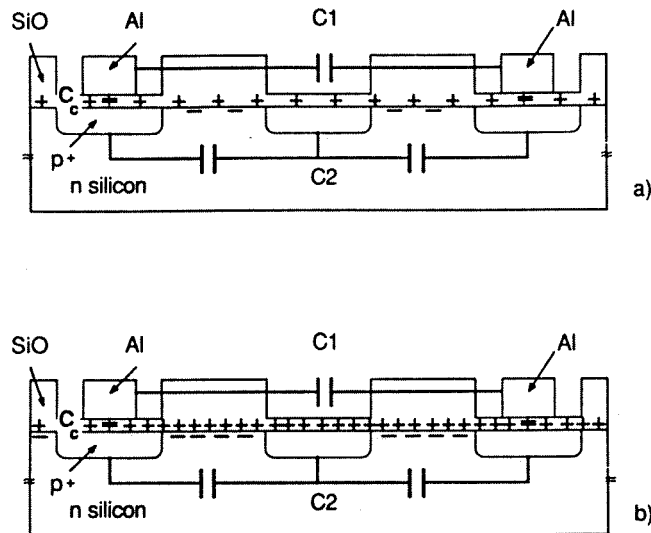


Figure 3.6: *Physical location of the detector capacitances on the detector. C_c is the coupling capacitance between the aluminium and diode lines, C_1 the capacitance between the aluminium lines, and C_2 the capacitance between diode strips. The $+ -$ symbols indicate the polarity of the charge induced by radiation in the material on both sides of the silicon silicon-dioxide interface.*

1. The capacitance C_p should be minimized, since the signal to noise ratio depends almost linearly on $1/C_p$ when C_f/C_c is small.
2. For C_f/C_c small the signal to noise is almost independent of C_c .

We have measured the relevant capacitances on prototype detectors. C_i was measured to be below 5.0 pF, C_b , to be below 1.1 pF and the C_c to be at least 15 pF. The feedback capacitance of the amplifiers is specified from the manufacturer to be 0.4 pF, see table 3.1. From the measurements we are convinced that we do not lose any significant charge on the coupling capacitor. These results are published in [55]. On later production batches the coupling capacitance was increased to about 70 pF through reducing the thickness of the oxide between the metal lines and the diffusion lines, see figure 3.8, [57].

3.3 Effect of Radiation on Detector Capacitances

We have seen that control of the detector capacitances is of great importance when improving the detector performance. We therefore wanted to know if radiation could change any of these parameters, and possibly reduce the performance of the detectors.

The detectors used for the radiation damage studies were smaller versions of the detectors produced for DELPHI. They were made on the left-over space of the same wafers as the detectors used for DELPHI and consisted of 257 diodes each 39 mm long. Except for the smaller size the geometry was exactly as for the detectors used in DELPHI.

The radiation effects were studied using a $^{90}_{38}\text{Sr}$ source of an activity of about 400 MBq emitting electrons with an energy spectrum up to 2.283 MeV. The coupling capacitance, polysilicon line resistance and inter-strip and depletion layer capacitances were measured before

⁵ $^{90}_{38}\text{Sr} \rightarrow ^{90}_{39}\text{Y}$ emitting e^- at 0.546 MeV with a half-life of 28.5 year, the $^{90}_{39}\text{Y}$ emits e^- at 2.283 MeV. Both processes occur with 100% probability

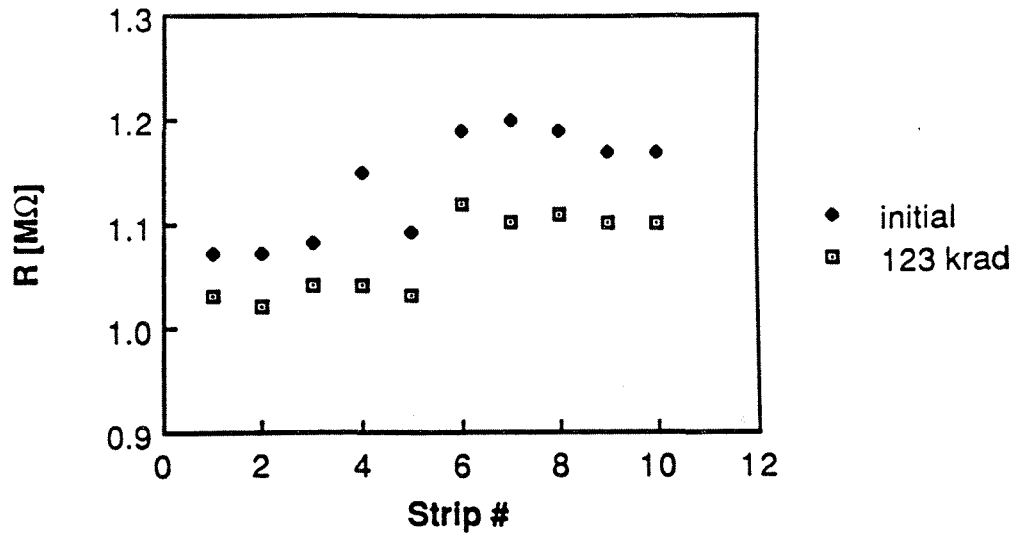


Figure 3.7: *Poly-silicon resistance before and after irradiation, from [57].*

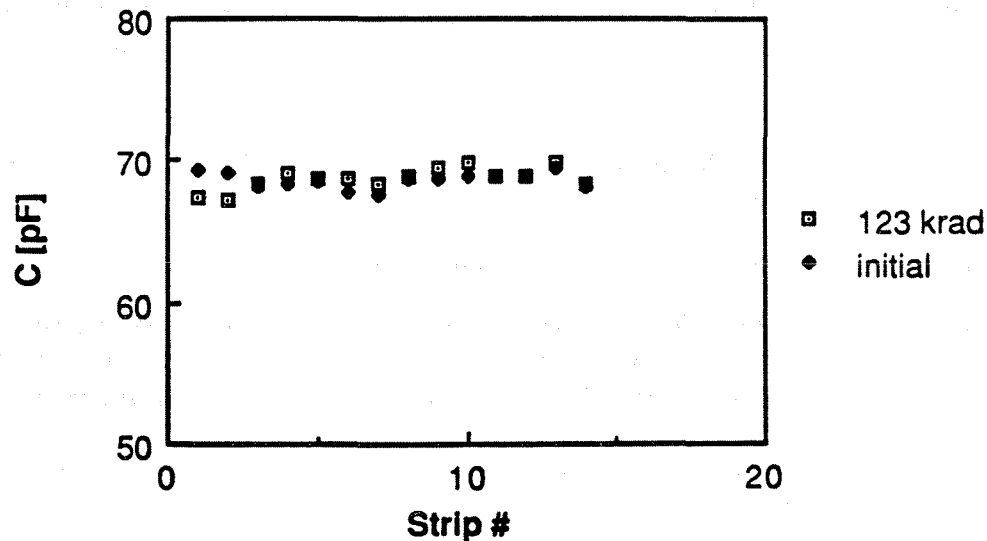


Figure 3.8: *Coupling capacitance before and after irradiation, from [57].*

and after radiation. The results are published in [57], a summary is included because of the importance for the detector performance.

A decrease of about 6% was observed in the poly-silicon line resistance after a dose of 123 krad, see figure 3.7. The lattice damage due to the radiation mimics the addition of an acceptor giving an apparent increase in doping level. This apparent increase in doping level in turn leads to a reduced resistance of the poly-silicon.

The coupling capacitance C_c between the aluminium strip and the diode was measured by injecting a charge to the diode through the contact hole and measuring the decay time. No systematic change was observed before and after irradiation, see figure 3.8.

The depletion layer capacitance was measured using a bridge with a generator frequency of 100 kHz. The capacitance of 39 aluminum strips against the n-doped side was measured as a function of the bias voltage and is shown in figure 3.9. This gives a capacitance of about 1 pF for one strip of 39 mm length with the pitch of 50 μm . After a dose of 190 krad the depletion

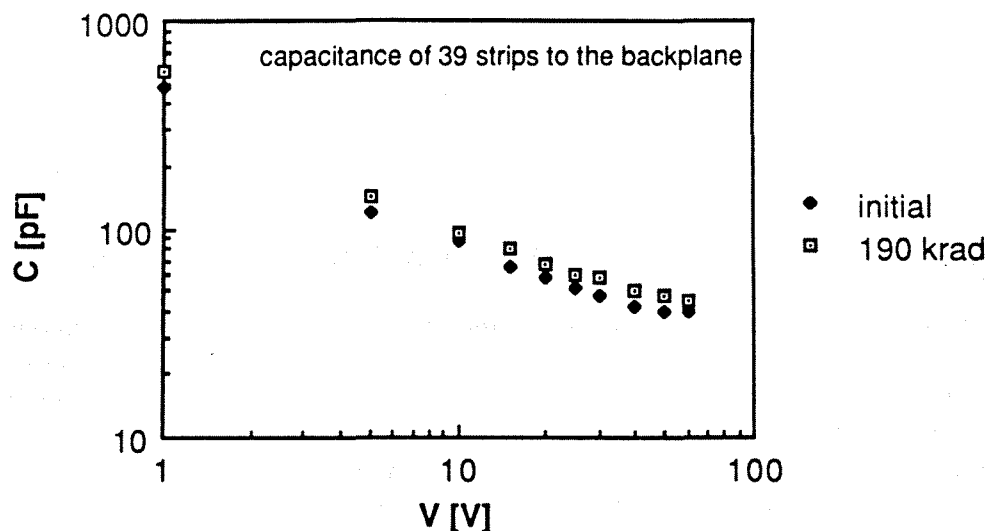


Figure 3.9: Depletion layer capacitance before and after irradiation as a function of bias voltage, from [57].

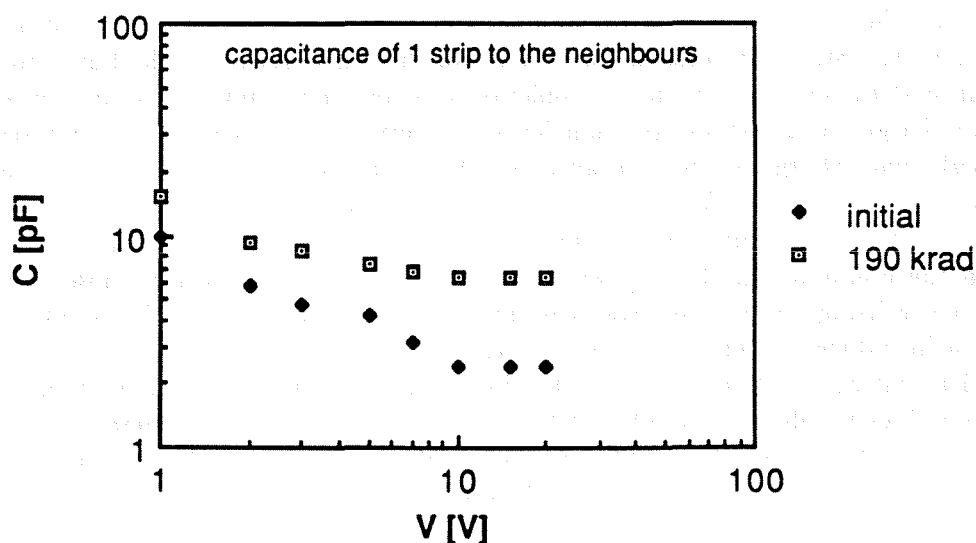


Figure 3.10: Capacitances between aluminium strips before and after irradiation as a function of bias voltage, from [57].

layer capacitance increased by about 10 %.

The capacitance between one aluminum strip and its neighbors, the inter-strip capacitance, C_i , have been measured with the same bridge as well. At full depletion the capacitance was measured to be 2.5 pF before irradiation and 6 pF after 190 krad of irradiation. Figure 3.10 shows the results as a function of bias voltage.

The inter-strip capacitance can be regarded as the sum of two parallel capacitances, see figure 3.6: one with coupling through air and SiO_2 , C_1 , and one through the silicon, C_2 . The main contribution comes from C_2 , composed of two coupling capacitances, C_c , Aluminum to silicon, of about 70 pF in series, and the serial capacitance of the 3 diffusion lines. The presence of an electron accumulation layer generated by positive charges in the Si-SiO₂ interface complicates this picture, and is, as we will see later, of great importance. The contribution from C_1 is

negligible

The radiation creates additional positive charges in the oxide silicon interface, thereby increasing the accumulation layer. The effective distance between the diodes is reduced by the increased accumulation layer, causing the observed reduction in inter-strip capacitance.

3.4 Effect of Radiation on Detector Leakage Current

The capacitively coupled detectors are completely covered with oxide and a different behavior compared to DC coupled detectors in response to radiation damage might be expected. The p⁺ diffusion lines are completely covered with SiO₂, radiation induced charges in the oxide might therefore directly alter the behavior of the lines. [41].

A detector with the low leakage current of 40 nA was chosen for these studies. It was depleted at 40 V and the aluminum strips were left floating during irradiation. After 200 rad an increase of leakage current to 18 μA was observed. A close inspection revealed that most of the leakage current was due to the diffusion lines covered with aluminium strips. We explain this radical behavior as follows: The radiation creates electron-hole pairs in the SiO₂. Charges on the floating surface induce an electric field. Under the influence of this electric field a fraction of the electron-hole pairs will separate and the electrons will drift towards the surface and the holes towards the SiO₂-Si interface, where some of them get trapped. The build up of positive space charge at the interface induces a depletion zone in the p⁺ diffusion zone. As the build up of positive charge continues an inversion layer of electrons is formed at the interface. When a high enough space-charge has formed avalanche break-down occur in the field induced junction and a channel current flows from the electron inversion layer to the back-plane. The electrons created under the aluminium will accumulate on the aluminum surface whereas the electrons created in the non-aluminized oxide will accumulate on the oxide surface close to the Si-SiO₂ interface neutralizing the positive trapped charge. A much higher dose is therefore needed to make the field induced junction on these strips.

After irradiating one detector where the aluminium strips were kept at the same potential as the diffusion lines we observed a different behavior. The leakage current increases from < 50 nA to 1.1 μA after a dose of 850 krad. The conclusion of these tests was that to minimize radiation damage the aluminum and the p⁺ should be kept at the same potential, or with negative potential on the aluminium with respect to the p⁺ lines.

3.5 Acceptance Tests.

We experienced that some detectors had faults coming from the photo-lithographic production method. Typically the faults were interrupted or short circuited diode or metal lines. These faults would reduce the resolution and efficiency off the detectors and should be kept as low as possible. These types of faults were found by visual inspection.

For reasons of stability and noise the leakage current of the detectors must be kept below a few micro ampere per detector. Measuring the electric parameters of all detectors enabled us to select the best ones.

The acceptance tests of the detectors therefore consisted of:

Visual inspection of the detectors. The inspection was done on all detectors received from the producer and consisted of scanning the whole detector surface under microscope. Faults in the lithography like interrupted or short-circuited diodes or aluminium lines were searched for and recorded.

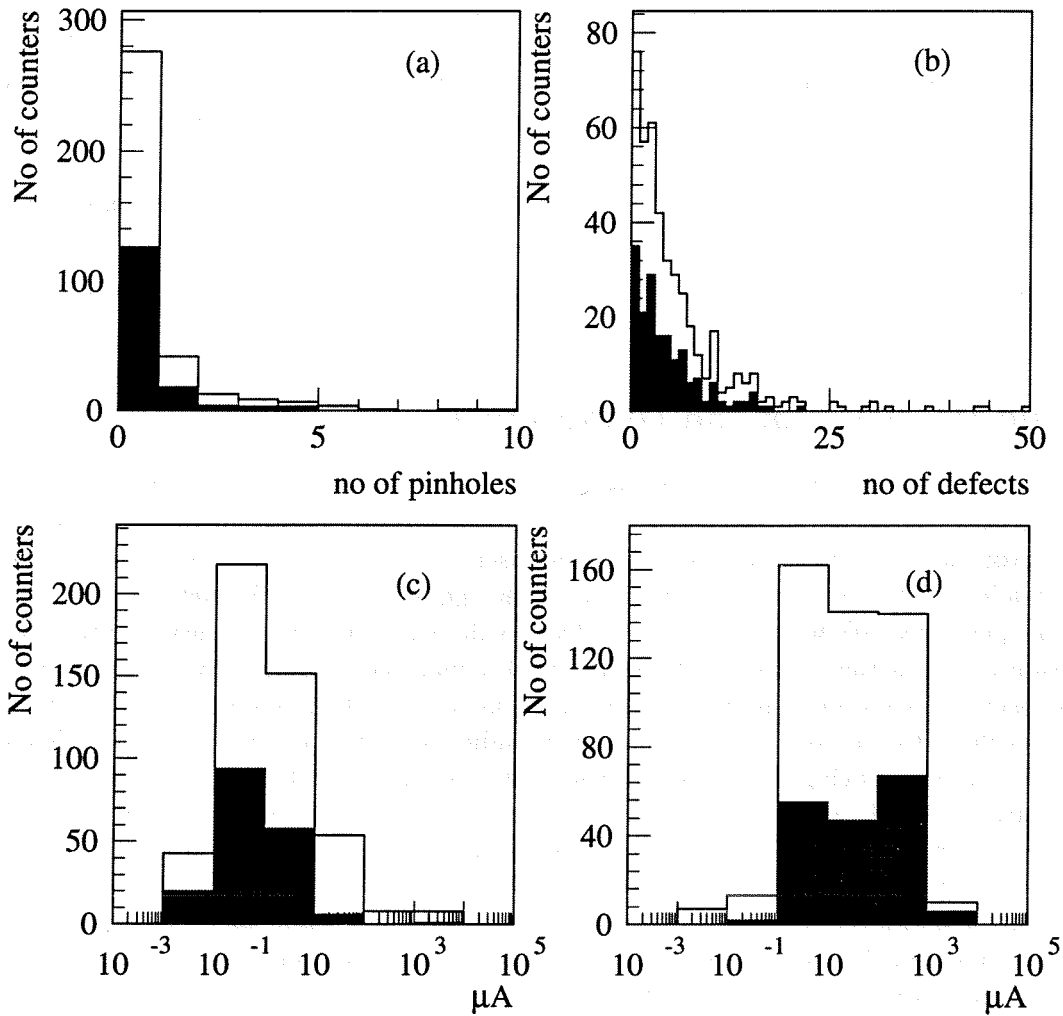


Figure 3.11: Results from acceptance tests, (a): number of pinholes, (b): number of surface defects, (c) leakage current diodes, (d): leakage current guard ring.

Figure 3.11(b) shows results of visual inspection of 499 detectors. The shaded region represents the fraction of the detectors that were used in DELPHI in 1990. In addition the alignment of the diffusion and the aluminium lines was checked and the thickness of the detectors was measured. We had experienced misalignments on earlier detectors. On the production batches this turned out not to be a cause of rejection. The thickness was uniform to within $10\ \mu\text{m}$ and no detectors were rejected because of that.

Electrical tests. The resistance of the poly-silicon resistors was measured on test structures on each wafer and on the detectors themselves. Pinholes in the thin oxide were detected by measuring the resistance between the bias strip and the aluminium strips. The resistance should be greater than $10^{12}\ \text{Ohm}$ indicating no pinholes. The connections to the aluminium strips were made by pressing a piece of conductive rubber⁶ onto the surface of the detector. Knowing the poly-silicon resistance for one strip the number of pinholes can be deduced by adding the resistors.

The coupling capacitance was measured on test-structures in order to give an estimate of the thickness of the thin oxide.

For each detector the leakage current under full bias voltage was measured over a period of a few days.

3.6 The Precision of the Diode Lines

The position of the implant edge was measured on 4 randomly selected detectors and on one photo-mask used in the photo-lithographic processes in the production of the detectors. Two of the detectors were of the same type as the one used in the Microvertex Detector. The other two were made by Micron Semiconductor, United Kingdom and Max Planck Institut Munich, Germany respectively. We wanted to be sure that the diffusion lines were at least straight within the precision of which the impact of charged particles could be measured by the detectors.

The measurements were done with the microscope set up which is described in section 3.9. The x axis is along the strips and the y axis is perpendicular. The xy points were recorded along the strips with 2 mm spacing in 6 passes on each detector. The last 3 passes were done with the detectors turned 180° to remove any systematic shift caused by the translational stages. The measured points were fitted to a straight line for each pass and the fitted line was subtracted from the data to remove any slope caused by the strips not being parallel to x .

Figure 3.12a shows the mean residual in y for each measured point in x . The point error in y direction is $1.1\ \mu\text{m}$. Jumps in y direction of $2\text{-}3\ \mu\text{m}$ is observed indicating that the diffusion line is not straight on the $1\ \mu\text{m}$ level. Our precision in track reconstruction is about 7 micron and this effect has not been taken into account.

Figure 3.12b shows the same measurement done on a photo-lithographic mask that was used in the production of the detectors. There is however no obvious correlation between the two.

3.7 The Preamplifier and Multiplexing Chips.

The only possible way to read out a large number of silicon microstrip detectors in the space available in a collider experiment is to use amplifiers with multiplexed readout of many channels,

⁶The rubber is made conductive by adding a powder of conductive material in production of the rubber. Electrical conduction is achieved by the contact between the conductive grains. The conductivity is very high compared with the silicon oxide, but somewhat lower than that of a metal.

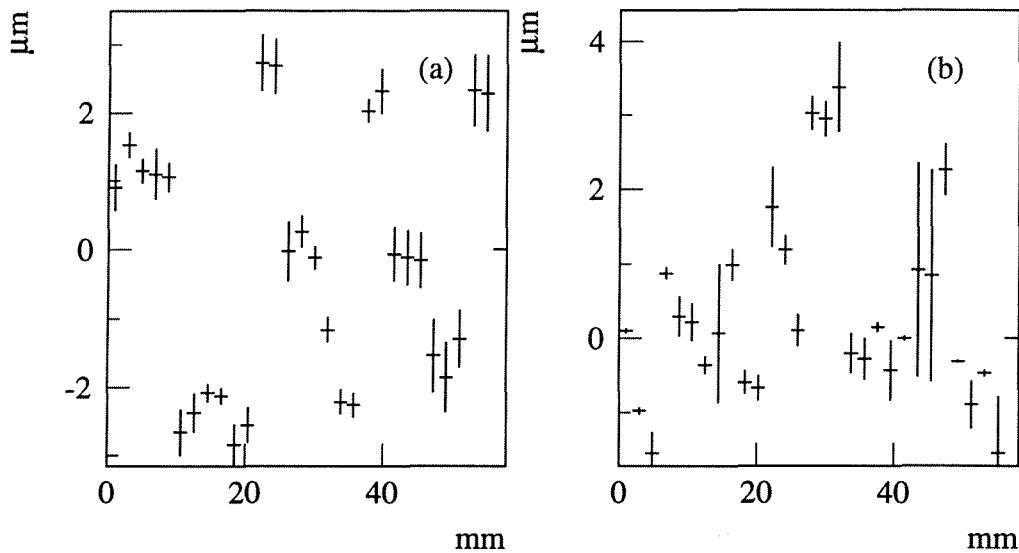


Figure 3.12: (a) The mean y position of the diffusion line along x for three repeated measurements on one detector produced by SI and (b) the same measurement on a photo-lithography mask used in the production of the detector. The error bars in y is the RMS for each x bin.

typically 128 in each circuit, realized as Very Large Scale Integrated circuits. Integrated readout electronics spaced close to the detectors bring other advantages too. The number of cables going to the detector is reduced by a very large factor. Since the electrical connections between the readout lines on the detector and the preamplifiers are short, typically 1 - 2 mm, the capacitance between the readout strip and ground is not increased, preserving the already weak signal from the detectors. For the Microvertex Detector a dedicated circuit, named MX3 was designed by Rutherford Appleton Laboratory, RAL, in the United Kingdom, and produced by MIETEC, Belgium, using a $3\ \mu\text{m}$ radiation resistant CMOS process⁷ [59].

The narrow input pitch realized on the amplifier side in order to match the spacing between the readout lines on the detector necessitated a 2 layer bonding scheme for the detector to amplifier connections. In the present configuration an integration time of $1\ \mu\text{s}$ is desirable for an acceptable signal to noise ratio. Actual integration time used in DELPHI is however $2.5\ \mu\text{s}$ to avoid inducing pick-up of the chip control signals in the Inner Detector sense wires. The Inner Detector has a sensitive window of $2.5\ \mu\text{s}$ to measure the drift of the electrons, in this window it is sensitive to pick up from external sources.

The chips feature double correlated sampling⁸, and requires 6 control signals. The overall sequence consists of a data capture cycle and a readout cycle, see figure 3.13.

Data capture During the data capture cycle the RESET signal goes low and enables the preamplifier. Just before Beam Cross-Over, BCO, the pulse S1 is given to sample the output of the preamplifier onto the capacitor C1. After BCO, S2 is given to sample the output onto C2. The signal is the difference between the charges on C1 and C2. If no readout decision is taken, the cycle repeats itself synchronous with LEP.

⁷The $3\ \mu\text{m}$ refers to the minimum gate length of a single MOS transistor possible in the fabrication process. This value is closely connected to the maximum speed and radiation resistance that can be obtained [58].

⁸The output from the integrating amplifier is sampled before and after an expected input signal on two separate capacitors, the signal is then the difference in charge on the two capacitors.

number of channels:	128
power consumption:	55 mW
band-width:	1 MHz
integration time:	1 μ s
readout frequency:	3 MHz
feedback capacitance:	0.4 pF
gain:	51 dB
Miller Capacitance: ^a	150 pF
gain spread one chip:	3 %
gain spread chip to chip:	10 %
ENC ^b bare chip:	1000 electrons
ENC connected to detector: ^c	2000 electrons
radiation hardness powered: ^d	3 krad
radiation hardness unpowered	10 krad
size	6.4 mm \times 6.4 mm
input bonding pitch	\approx 50 μ m

^aThe Miller Capacitance is defined as the capacitance an external circuit sees at the input of the amplifier.

^bENC: Equivalent Noise Charge, is a measure of the noise of an amplifier in terms of the charge induced by a traversing high energy particle. The most probable signal for a minimum ionizing particle traversing a 300 μ m silicon detector is 24000 e⁻. A noise of 2000 e⁻ therefore gives a signal to noise ratio of 12.

^cThe amplifier was connected to a detector with 6 cm long diodes and 25 μ m spacing between the diodes. Every second diode was connected to an amplifier at either end of the detector.

^dNo significant change of parameters from an operational point of view.

Table 3.1: *Technical Specifications for the MX3 circuit as provided by the manufacturer, from [59].*

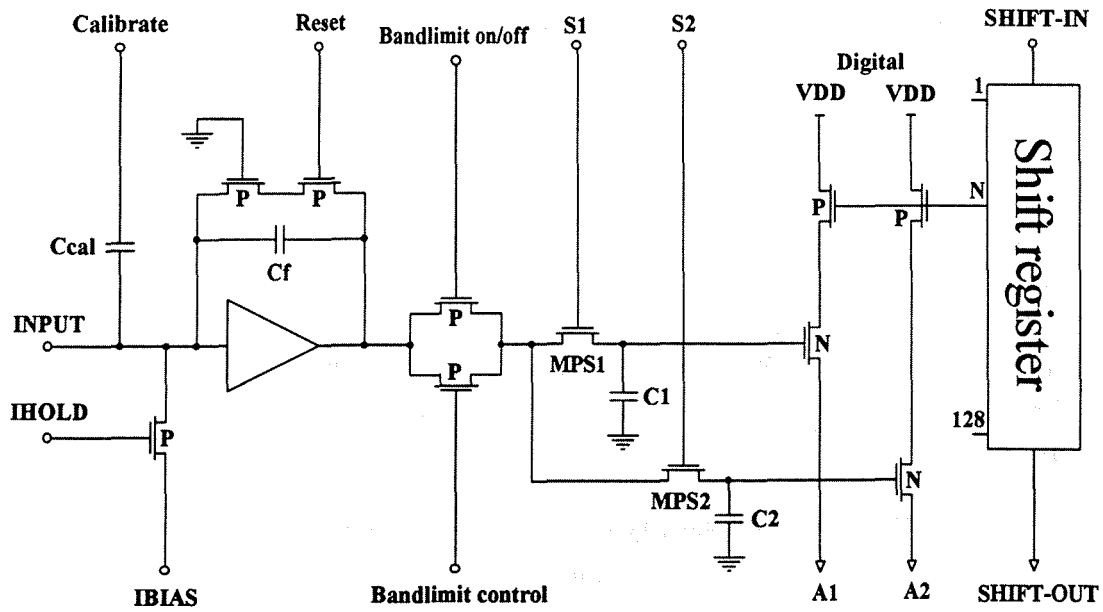


Figure 3.13: Architecture of a single channel of the MX3 amplifier and multiplex circuit.

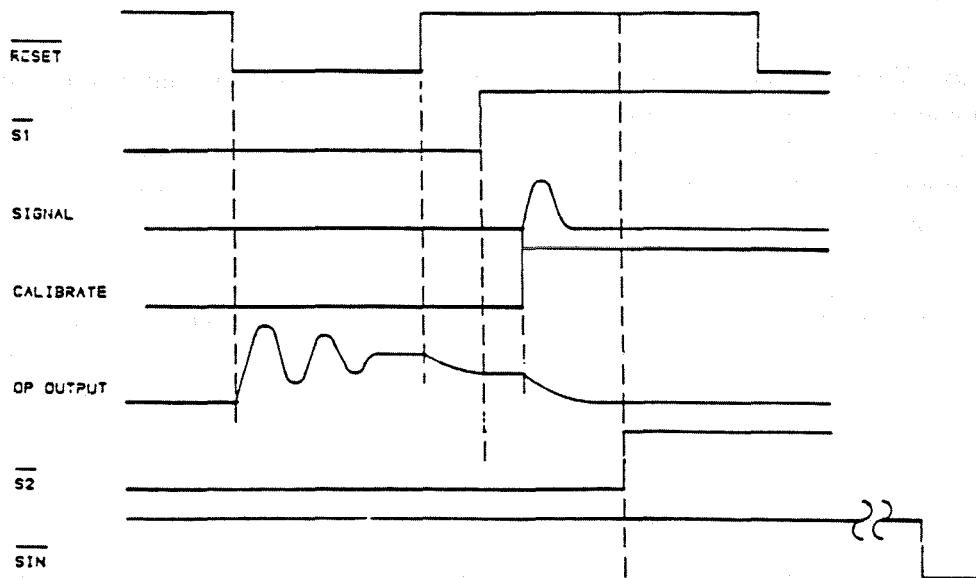


Figure 3.14: Control signals for the MX3 circuit.

Inner layer module. Mass of the components:

item	material	no	mass (g)	sum mass (g)
detector	Si	4	1.04	4.16
hybrid	Al ₂ O ₃	2	1.88	3.76
reference cylinder	58%Cu 39%Zn 3%Pb	2	0.23	0.46
Carbon Fiber	Si C	1	0.41 + 0.96	1.37
Total				9.75

Outer layer module. Mass of the components:

item	material	no	mass (g)	sum mass (g)
detector	Si	4	1.24	4.96
hybrid	Al ₂ O ₃	2	2.33	4.66
reference cylinder	58%Cu 39%Zn 3%Pb	2	0.23	0.46
Carbon Fiber	Si C	1	0.41 + 0.96	1.37
Total				11.45

When weighed each type of module was found to be:

4 chip module: 12.25 g

5 chip module: 14.15 g

Table 3.2: *The various components of the detector modules have been weighed. The discrepancy between the sum of the mass of the components and the measured mass of the modules is attributed to components that were not weighed: the capacitors, the chips, glue and the silicon connecting pieces.*

Readout When a readout decision is taken, the capture sequence is interrupted after S2 and a single pulse is fed to the control input of the shift register RBI, Read Bit In. The clocks PHIE1 and PHIE2 drives the shift register forcing the RBI to ripple through the register and connects the A1, A2 lines to the C1 and C2 of the respective channels. The A1 and A2 lines are fed to external buffering circuits.

The analog signal is found by subtracting A1 from A2. By connecting the RBO (Read Bit Out) of one chip to the RBI of another and connecting together the respective A1 and A2 lines of the chips several chips can be connected together. The digitization of the signal is synchronized with the PHIE1 and the PHIE2 signals. Pulse counting then gives the channel to strip number correspondence.

3.8 Detector Modules

The detector modules consist of 4 silicon detectors attached at each end to hybrid circuits on a ceramic (Al₂O₃) substrate. The hybrid circuits carries the MX3 chips, 4 chips for the Inner and 5 for the Outer layer. The MX3 chips are glued onto the hybrid with conductive epoxy and the connections between the chips and the hybrid are made with wire bonding from the hybrid to the chips. The power supply and driver signals as well as the analog output signals is connected via a Kapton cable, about 7 cm long, soldered to the edge of the hybrid.

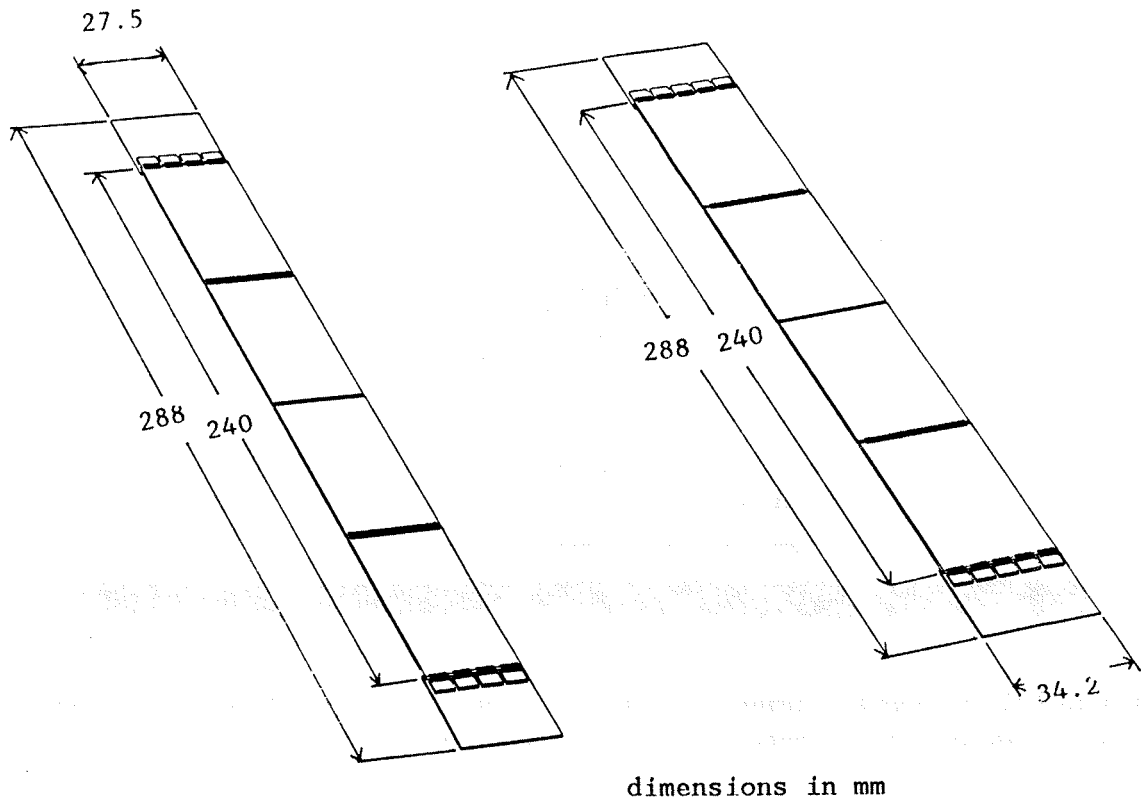
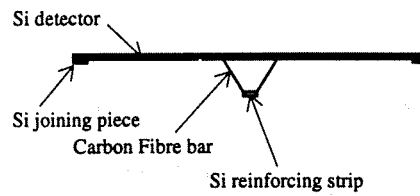


Figure 3.15: Schematic drawing of the detector modules. The readout chips are seen as squares in each end of the modules. The bond wires are indicated. There are 128 bond wires in two layers between each chip and detector.

Figure 3.16: Cross section through the detector modules.



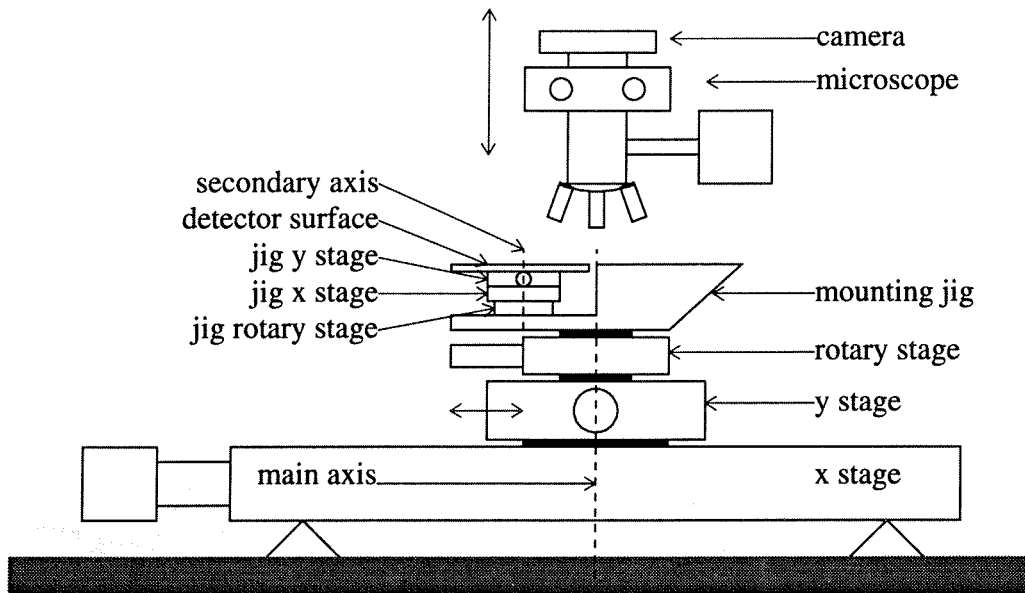


Figure 3.17: Schematic drawing of the microscope and the assembly bench, view along the y axis. The microscope is fixed overhead and can only move in the z direction.

On the backside of the detectors, in the length of the 4 detectors, runs a $200\ \mu\text{m}$ thick carbon fibre reinforcing bar with a trapezoidal cross section. The bar is not attached to the ceramic substrates. $2\ \text{mm}$ wide and $300\ \mu\text{m}$ thick silicon strips are glued to the top of the carbon fibre bar. These strips both increase the rigidity of the module with roughly a factor of 4 and ensures that the module does not get bent due to differences in the thermal expansion coefficient of silicon and carbon fiber.

We wanted to do a thorough survey of the modules and the detector before installation in DELPHI. The survey had to be done using different equipment, the modules would be measured using a microscope, while the detector would be surveyed with a machine touching the detector. To get a connection between the microscopic measurements and the macroscopic measurements a precision cylinder was placed on each hybrid. This cylinder could be measured by both methods and thus provided the microscopic to macroscopic link.

The modules are fastened to the end rings by means of two screws through the hybrids in each end. The modules are the only mechanical connection between the two end-rings. Figure 3.15 shows a schematic drawing of the inner and outer detector modules, a cross section through the modules is found in figure 3.16.

3.9 Production of Detector Modules.

We had to develop new production methods to guarantee the best possible precision of the detector modules. A major difficulty was our decision not to introduce extra material in the detector acceptance in addition to the silicon detectors.

The assembly procedure was set up with the following goals:

1. Achieve an alignment of the sensitive elements in the module plane of the same order as the spatial resolution of the detectors.

	<i>x</i> direction	<i>y</i> direction
table	TCB 200-400	TCB 160-200
step size:	10 μm	1 μm
global precision:	2 μm	2 μm
positioning error:	$(6\mu\text{m} + 10^{-5} \times x)$	not specified

x is travelled distance in micron.

Table 3.3: *Manufacturers specifications of the movable tables used in the assembly*

2. Achieve an highest possible degree of flatness of the modules, preferably the modules should be flat to within 20 μm .
3. Assemble the modules onto the end rings without introducing any stress in the assembly that may distort it.
4. Make it possible to assemble the modules within the strict time limits given. Delays in the production of detectors eventually had the consequence that the production finally had to be done in two shifts.
5. Ensure the highest possible safety for the detectors.

None of the surface features of the microstrip detectors are visible to the naked eye, all the work therefore had to be done under microscope. Precautions had to be taken during handling, the detector surfaces are extremely sensitive to mechanical damage, scratches etc.

The assembly bench, figure 3.17 consists of two precision step-motor translation tables, a metallurgical microscope and two jigs for holding and manipulating the detectors during mounting. The translation tables are mounted perpendicular on top of each other with a step size of 10 μm and 400 mm of travel distance along the strips, *x* direction, for the lower one and step size 1 μm and 160 mm of travel distance perpendicular to the strips for the upper, *y* direction. A precision manual rotary table, ϕ direction, was attached to the upper, *y*, carriage.

Two different jigs carrying the detectors and the hybrids could, one at a time, be mounted on the rotary stage. Each jig consisted of one fixed part attached to the upper rotary table, and one separately movable, in *x*, *y* and ϕ direction. The microscope was fixed overhead of the translational and rotational stages and could only be moved perpendicular to the detectors, *z* direction.

The assembly proceeded in several steps, which were identical for the two types of modules:

Selection of detectors were done on the basis of visual inspection and electrical tests, see 3.5 for details.

First Alignment of two detectors to each other with the strips parallel. using the microscope set-up. After alignment two $2 \times 6 \text{ mm}^2$ aluminized silicon pieces were glued across the gap between the two detectors onto the backside in each adjacent corner of the detectors, using fast setting epoxy (Araldit Rapid) and conductive epoxy (Esolder). The two different epoxies were used because the conductive epoxy needed at least 12 hours for setting, which our production schedule could not tolerate. The aluminated side was facing the detectors to give electrical connection between the backplanes of the two detectors.

Attachment of the hybrid circuit. After that the fast epoxy was hard (3 hours), the two detectors were aligned to a fully tested hybrid circuit. The hybrids had one precision machined edge that functioned as a reference. Connection from the hybrid to the backplane of the detector was done with the same conductive epoxy as above applied on the corner of the hybrid, while Araldit Rapid was used along the adjacent edges of the hybrid and the detector. After the application of epoxy the detector/hybrid assembly was moved to give an overlap between the hybrid and the detector of about 3 mm. The alignment and dimensions were again checked and readjusted if necessary.

Functional test and calibration. We have now what is called an half module. After wire bonding the half module is by itself a complete detecting element and was as such tested and characterized before the assembly could proceed by joining two half-modules into a full module. The tests consisted of a scan across the surface with a pulsed laser beam focused to a spot $\approx 10\mu\text{m}$ in diameter on the detector surface. The gain for every strip were recorded as well as any dead strips were located for eventual use in the analysis of data from beam events.

Second alignment The half modules were assembled into modules in a similar fashion by aligning the two half modules to each other and gluing them together with aluminized silicon pieces as was done initially with the two detectors in a half module.

Carbon fibre bar attachment. The last step in the assembly was to glue the carbon fibre bar to the backside of the module. A difficulty was the bond wires on the top surface which prohibit laying the module upside down. A third jig was used for this operation. The procedure works by sucking the module down onto the carbon fibre bar.

Prior to this the silicon pieces, $2 \times 57 \text{ mm}^2$ were attached to the carbon fiber bar. The carbon fiber bar was immediately placed in a slit in the vacuum and the module carefully lowered by hand onto the jig. The vacuum was turned on and the module was sucked onto the jig making a firm contact with the carbon fiber bar. The module was kept on the jig for at least 3 hours, if possible overnight.

One problem was that the carbon fibre bars were not very straight. Our hope was that the precisely machined surfaces of the vacuum jig would ensure the flatness of the module during and after the epoxy had hardened.

After the carbon fibre step the modules underwent a visual final check out under the microscope and a functional test.

3.10 Overall Detector Mechanics

The original detector was designed to fit in between the inner radius of the Inner Detector (116 mm) and the outer radius of the beam tube (80 mm). The limited space and the installation procedure were the main constraints for the mechanical layout. For the 1991 running period a beam pipe of radius about 55 mm was installed. This gave space for the addition of another layer of microstrip detectors. This additional layer is described in section 3.14.

The overall shape of the detector is two hollow vertically split half cylinders of length 304 mm with inner radius of 82 mm and outer radius of 110.5 mm. The read out of the electronic signals is to one axial side of the detector. which is connected via flat cables, made as copper strips on Kapton substrate, to repeater electronics located about 100 mm axially from the detector, still

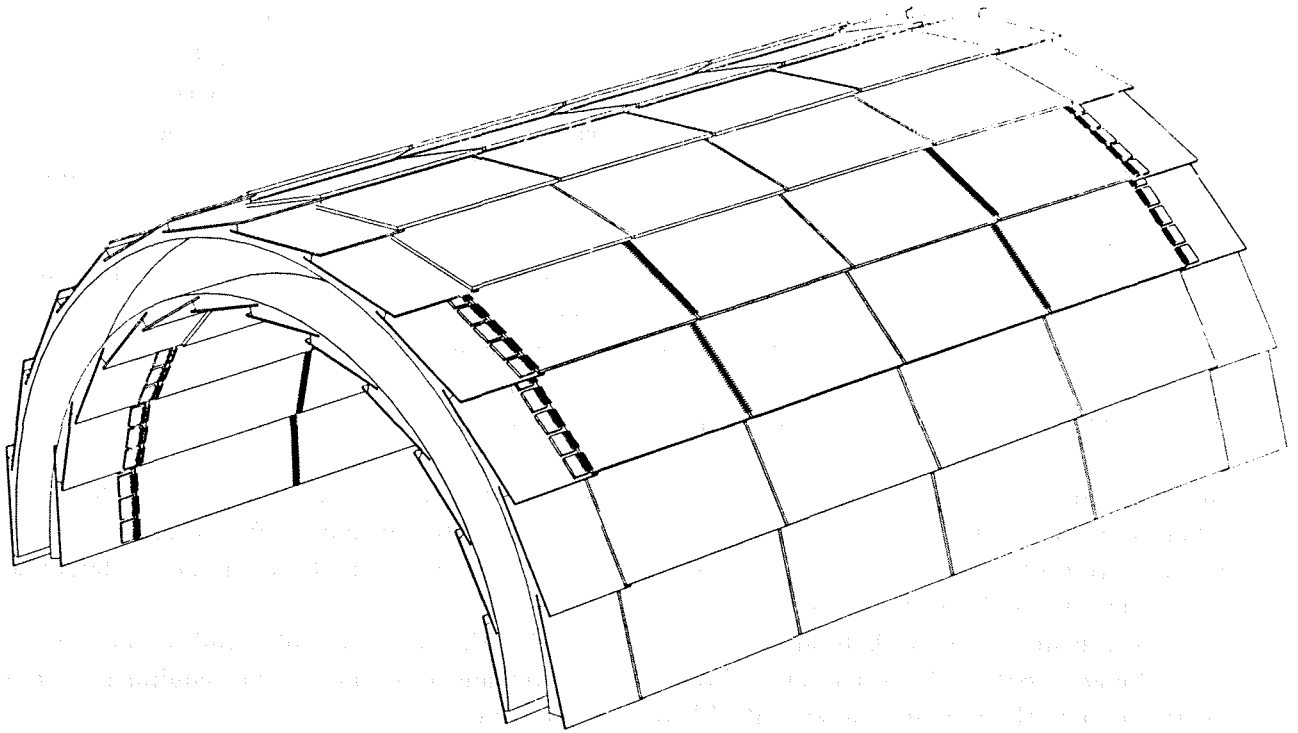


Figure 3.18: Schematic drawing of the Microvertex Detector. When installed in DELPHI the half shell is standing with the split vertical.

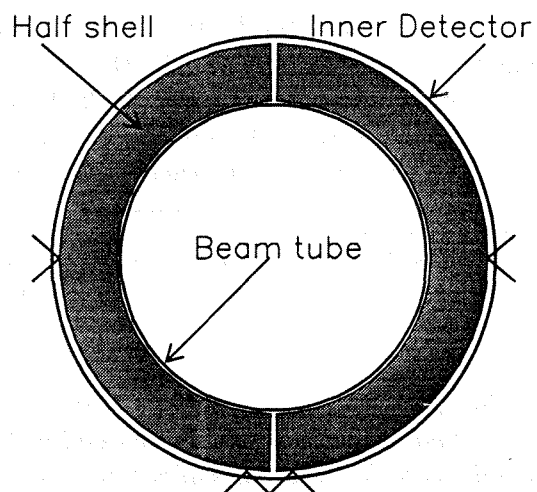


Figure 3.19: Schematic drawing of the support of the 1990 Microvertex Detector. The angular brackets show the positions of the support skates and rails in the Inner Detector. The scale of drawing is 1:4

inside the Inner Detector. The repeater electronics mechanically consist of two half shells each made up of 6 printed circuit boards that fit in between the beam tube and the Inner Detector.

The installation was done with the beam tube in place inside the Inner Detector. During installation the tube was supported by a wire attached to the inside of the TPC support structure and to a ring around the tube at the entrance to the Inner Detector. Because of this arrangement the detector and the repeater had to be divided along the vertical to make the installation possible. The detector and the repeater was put in place by pulling each detector and repeater half shell into the inner detector. The whole assembly rested on skates sliding on carbon fiber bars previously installed in the Inner Detector, see figure 3.10. Because of the circular ribs on the beam tube and since it was not perfectly centered in the Inner Detector it was necessary to move the tube during the installation. This was done by hand when the person pulling the detector and repeater assembly felt increased resistance on the strings. The tube did not have any ribs in the central region and when the detector reached its proper position it would fit snugly in between the ribs⁹ leaving the necessary free space between the beam tube and the detector. There is no solid mechanical connection between the two detector halves after insertion. There is an overlap of the sensitive areas of the two halves which allows us to align them relative to each other using charged particle tracks.

The repeater and the half shell was connected with the Kapton cables and a short string while being inserted. Each half-shell, both the detector and the repeater was equipped with 4 skates, two at the bottom and two at 90° from the bottom.

Each of the detector half-shells consists of 2 end-rings onto which 24 detector modules are mounted in a paddle-wheel like geometry. There are two concentric layers of detector modules, each layer having 12 modules with adjacent modules overlapping each other. The 4 chip wide modules is mounted closest to the beam tube. The two layers will hereafter be called Inner and Outer respectively.

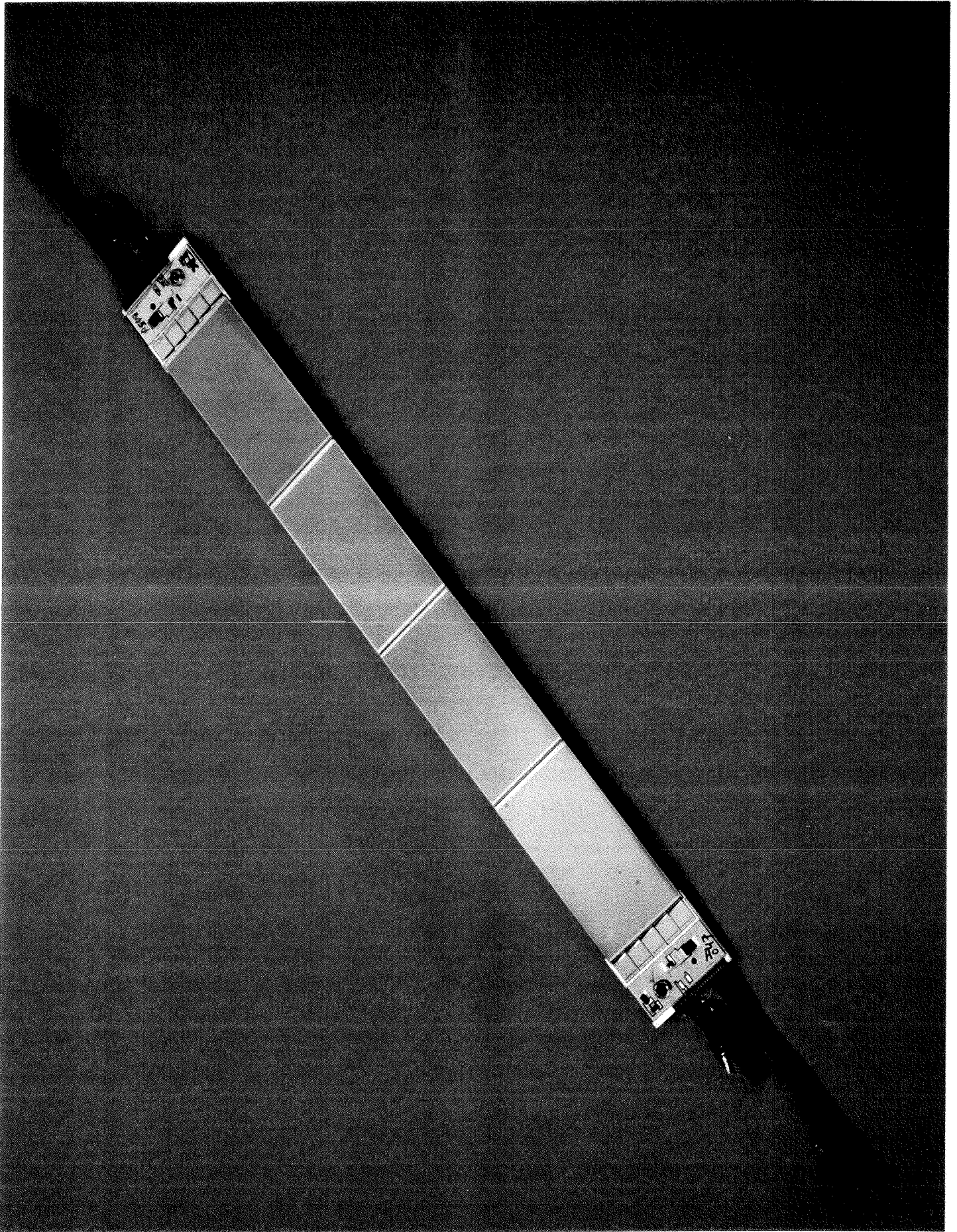
The end-rings are made of high stiffness aluminum alloy machined to high precision by the electro-erosion technique. The end-rings function as well as support for the cooling channels, see section 3.13. An end-plate are fixed to the end rings on the side pointing outwards along the beam-pipe. The end-plates support the 4 skates, the two covers and a flexible circuit-board distributing power supply, clock signals and buffering the analog output signals before the repeater electronics.

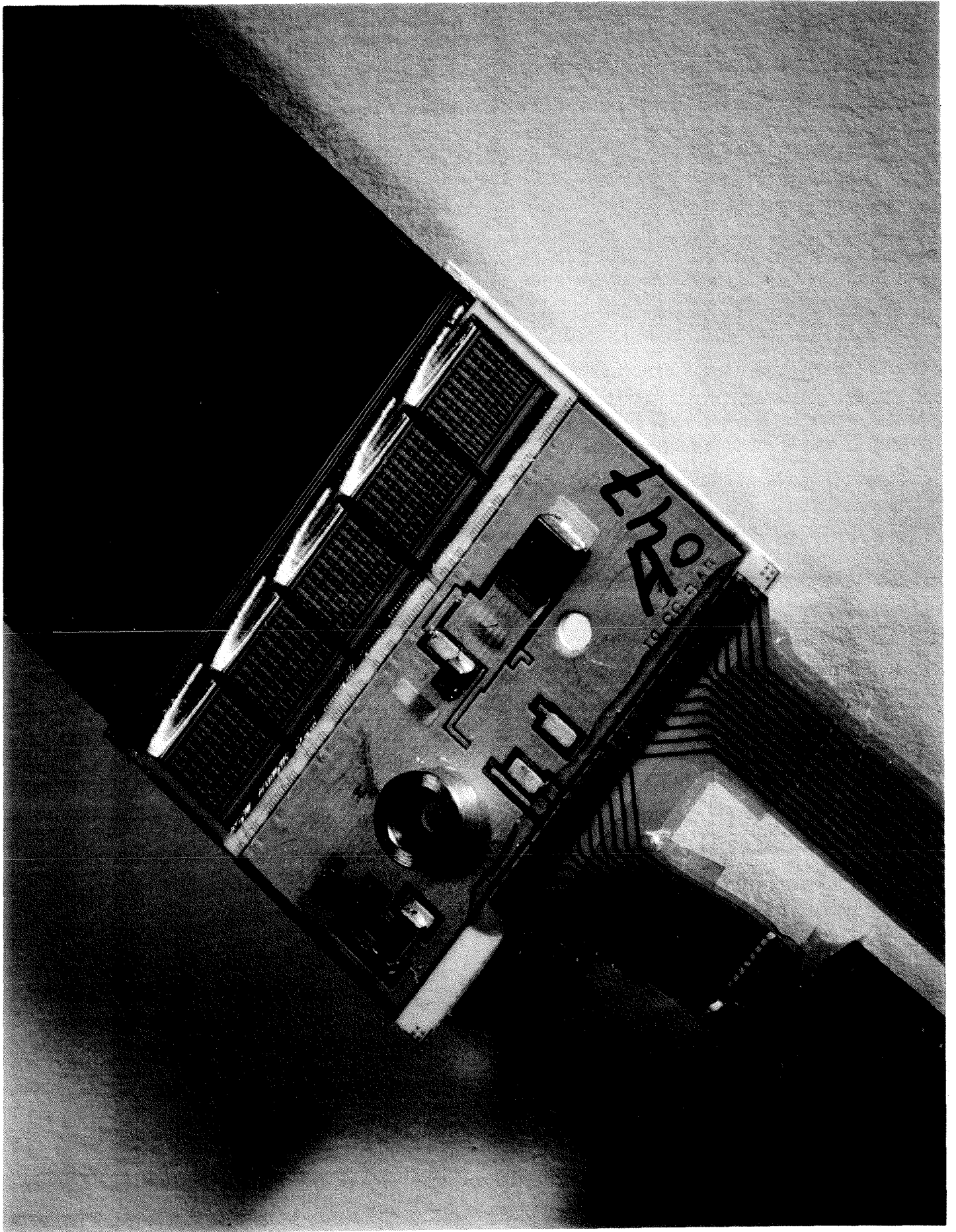
Each half shell is covered by two covers, one at the inner radius and one at the outer radius, consisting of a sandwich of Rohacell (thickness 1 mm for outer cover and 0.8 mm for the inner cover) foam and high stiffness 20 μm thick aluminium foil. Adequate mechanical protection and electrical shielding is thus obtained with a mass of about 20 mg/cm^2 inside the acceptance of the detector. Each cover is attached to the rigid mechanical structure via spokes and held in

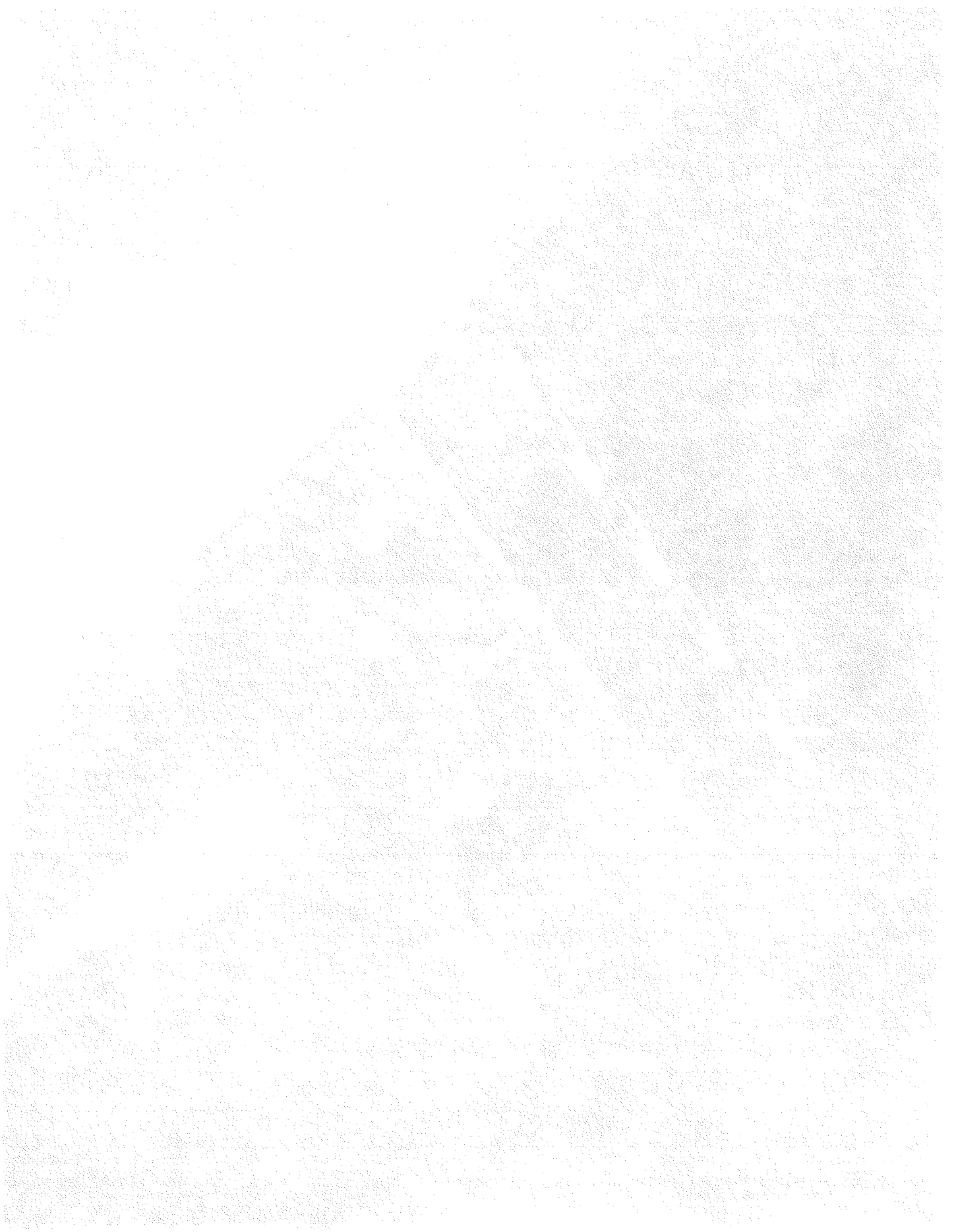
⁹It has to be mentioned that the need for moving the tube initially caused concern for the engineers responsible for the tube. When they soon learned that the detector probably was more fragile than the vacuum tube they let the Vertex Detector Installation Team take care of moving the tube themselves.

Figure 3.20: *(Colour inset) Photograph of a module for the Outer layer. The hybrid circuits with the readout chips are seen in each end of the module consisting of 4 silicon detectors. The Kapton foils with the external signal lines are seen attached to the hybrid circuits.*

Figure 3.21: *(Colour inset) Close up photograph of a module for the Outer layer. The five readout chips are seen together with some external components. The cylinder used for alignment purposes is seen surrounding one of the screw holes of the hybrid circuit.*







Item	material	no	mass (g)	sum mass (g)
4 chip modules		24	12.25	294.0
5 chip modules		24	14.15	339.6
screws M1.6×3	69%Fe 17%Cr 12%Ni	192	0.10	19.2
End Rings	Al	4	137.50	555.0
End plates including spokes and screws	Al	4	59.30	237.2
Inner cover	Al C H	2	16.0	32.0
Outer cover	Al C H	2	26.8	53.6
Bend-Flex		4	34.0	136.0
Short Kapton		24	1.1	26.0
Long Kapton		24	1.8	43.0
cooling tubes	PVC	16m	33g/m	528.0
cooling water	125cm ³ H ₂ O		1g/cm ³	125.0
total				2388.6

Table 3.4: *Mass of the Microvertex Detector. The table shows the contributions to the mass of the detector from the various components.*

place by screws. The outer covers have holes for the optical position monitoring system, see section 4.7. Each of the repeaters are covered at the outer radius with similar covers for electric shielding.

3.11 Readout Segmentation

The read out strips are all wire bonded to separate preamplifiers, which are grouped together 128 at the time on the MX3 chips. The outputs of the 128 channels are on the chips connected to a 128 channels deep analog shift register, which is chained to other MX3 chips. The 4 chips on an inner half module is multiplexed together with 5 chips on an outer half module to form one, half in z , 15° in ϕ sector with a single 1,152 cell shift register. The signals from this read-out sector is then buffered into twisted pair cables, one pair for each sector.

Each sector is connected to one readout unit, positive and negative z side to separate inputs, such that each readout unit reads out one 15° sector for the Inner and Outer layer.

3.12 The Repeater Electronics.

The repeater electronics distribute the power supply to the chips, receives the clock signals from the control room on twisted pairs, converts them to TTL levels and fans the signals out to the MX3 chips. It Receives the analog signals from the readout-chips, buffer and transmits the signals on twisted pairs to the data acquisition system in the control room.

The repeater also has the possibility to generate calibration pulses of various levels onto the back-plane of the detectors.

item	material	no	mass (g)	sum mass (g)
circuit boards		12	30	360
signal cables	Cu C	8	38	304
power cables	Cu C	2	110	220
frame	Al	8	24	192
cooling tubes	PVC	8m	33g/m	264
cooling water	H ₂ O	414cm ³	1g/cm ³	62
Total				1402

Table 3.5: *Mass of the repeater electronics.*

The same constraints on power consumption and space applies to the repeater as to the detector. The repeater was made as light as possible since it is within the acceptance of the central tracking chambers. It was shielded to minimize interference with other detectors and it is water cooled in the same way as the detector.

3.13 Detector Cooling.

The electronics on the detector dissipates about 70 W. Air convection in the confined space between the ID and the vacuum tube is not large enough to lead away the heat generated. Any temperature change of the detector of the order of one or two degrees will lead to considerable movements making precision track reconstruction impossible. It is therefore of the highest importance to keep the temperature of the detector stable to within less than 1°C. The detector is therefore cooled by circulating water from outside DELPHI into channels in the End-rings and in tubes on the circuit boards of the repeater electronics.

Because of the position of the Microvertex Detector inside all the barrel detectors, the cooling system was required to have the highest possible safety against leakage. The system was not allowed to spill any water at all in case of a pipe or hose failure. In the very confined space inside the Inner Detector and inside the acceptance of all the barrel detectors we could not use standard approved fittings for the water connections. Standard stainless steel fittings were too massive and would cause unacceptable multiple Coloumb scattering close to the interaction region, in addition the limited space prohibited their usage.

The design is based on a closed circuit kept below atmospheric pressure at ≈ 0.9 bar. The water is siphoning from an upper reservoir, through the detector to a lower reservoir. A pump replenishes the upper reservoir via a heat exchanger connected to the general cooling water provided in the experimental cavern. Tests done prior to installation have shown that cutting a water pipe close to the detector while the system is running leads to air being sucked into the system and no water is spilled. The reduced cross section of the water lines inside the detector leads to increased flow speed and thus ensures that the water pressure nowhere is above atmospheric pressure.

A hard-wired interlock system will turn off the detector power supplies and the water pump in case of disappearance of the water-flow in any return line from the detector. The temperature of the detector is monitored and the system has kept temperature variations on the detector below 1°C. If the temperature of the detector should get above an upper limit, additional computer controlled monitoring will shut off the power supplies.

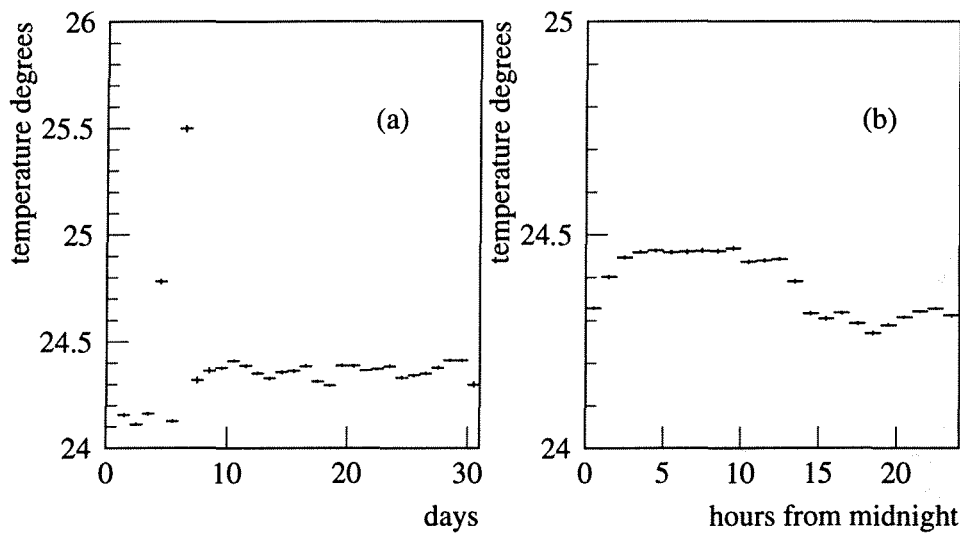


Figure 3.22: *Microvertex Detector temperature.* The graph (a) shows the average temperature measured on 22 different positions on the detector and the repeater averaged over each day in July 1991. (b) Shows the same points averaged over each hour of the days of July 1991. The plots show that the temperature is stable to within 1°C during the time scale of a day and over several weeks. The 4th. and the 6th. of July shows however a jump of about 0.6°C and 1.2°C respectively.

3.14 The Extended Detector Installed in 1991

During the shut down of LEP the winter of 1990 to 91 a new vacuum tube having a central section of beryllium with inner radius 53 mm and thickness 1.45 mm was installed inside DELPHI. The reduced radius allowed for a third layer of microstrip detectors inside the previous two at average radius 6.3 mm.

The sector division from the first two layers were kept for the added layer, with one important change: The modules were not paddle-wheel mounted but rather castellated with every second at different radii. A paddle-wheel like mounting would have given the tracks larger incidence angles on the silicon which could reduce the spatial resolution. The microstrip detectors for this layer have 384 readout strips and are 53.1 mm long and 20.6 mm wide. The hybrid circuits, this time made of beryllium oxide for improved heat conduction, carry 3 readout chips and one additional chip for fanning out clocking signals. The lay-out of the circuit is prepared for double sided detectors and there are printed circuits on both sides of the hybrid. Figure 3.23 shows a view of the upgraded detector.

The reference cylinders used in the survey were replaced by spheres as this were shown to improve the precision of the survey. The procedure for module assembly and alignment was similar to those developed for the two first layers.

The 3 chips on a Closer half module are thus multiplexed together with 3 chips from a neighboring module. This forms one 30° sector in ϕ at either positive or negative z direction. The readout segmentation for the two already existing layers was kept. By this connection scheme we obtain some redundancy. A failure in the readout should only affect either one Closer sector of 30° or one Inner/Outer sector of 15° .

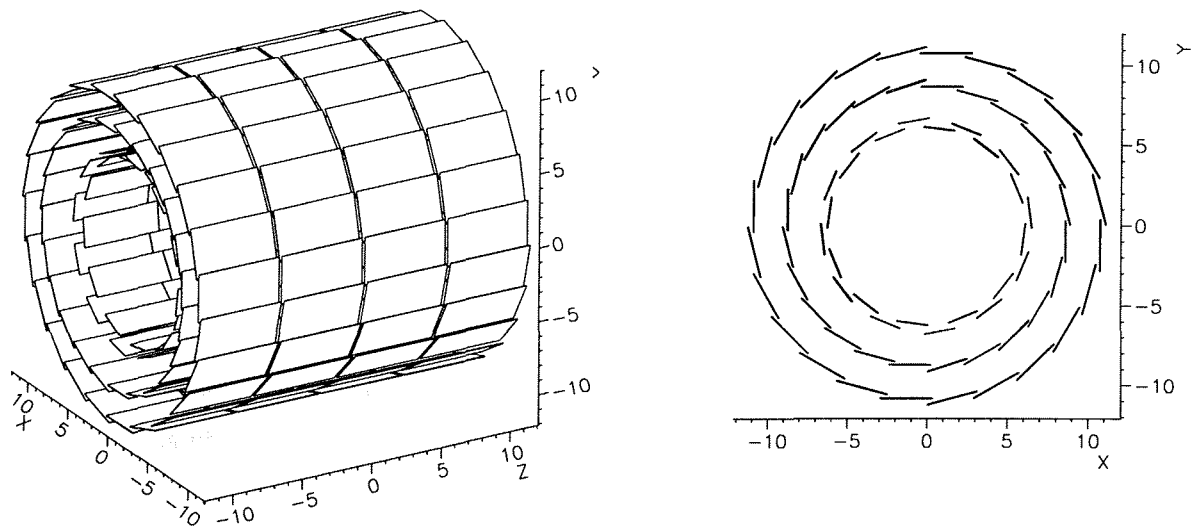


Figure 3.23: Graphical output from the detector description database showing the sensitive areas of the extended detector. Left: view from the side, right: view along the z-axis. The castellated staggering of the Closer layer can be seen.

Because of the reduced radius the modules could be made shorter, keeping the same polar acceptance as before. A shorter strip length should lead to a slightly better signal to noise ratio for this layer since the stray capacitances are smaller. We do however not observe any significant difference. We believe that this is caused by an extra chip on the hybrid inducing larger common mode noise in the signals from the readout chips.

Because of the smaller radius and the absence of ribs, the new vacuum tube greatly facilitated the installation of the detector.

We keep the naming convention, the three layers are thus named Closer, Inner and Outer layer, starting with the layer closest to the interaction region

3.15 Geometrical Survey

The importance of precise mechanics to the track reconstruction in the detector has been mentioned. It is however impossible to maintain an overall assembly precision on the same level that we want to reconstruct the hits from the particle tracks. The detector therefore was surveyed before the installation. The result of this survey was a three dimensional description of the location of the diode strips in a coordinate system local to the Microvertex Detector. This coordinate system was then transformed to the overall DELPHI system using particle tracks for alignment.

The pre-installation survey is a two step procedure. Every module is measured under the microscope to locate the position of the diode strips in the plane defined by the microstrip counters. This is done before the modules are attached to the End-rings. Thereafter the complete detector is surveyed using a three dimensional measuring machine touching the Microvertex Detector. This machine can not locate the individual strips in each detector. Each module is therefore equipped with a reference object which can be measured by both the microscope and

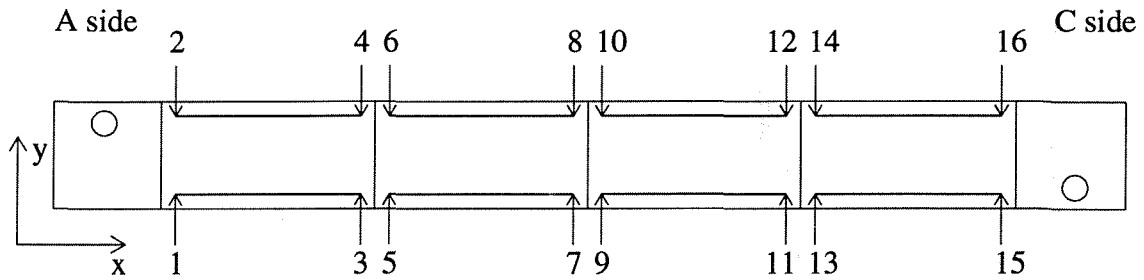


Figure 3.24: Location of points measured with the microscope. The arrows point to the ends of each strip measured. The circles in each end are the reference cylinders that were measured both with the microscope and with the measuring machine.

the machine to provide a link from the microscopic to the macroscopic. This object is for the Outer and Inner layer a hollow cylinder placed around one of the screw holes on each hybrid. For the Closer layer a steel sphere is used.

3.16 Module Survey

After assembly, the modules were measured using the microscope and the translation stages previously used for assembly. 12 points were recorded along the circumference of each reference cylinder and 2 or 3 points on each of the outermost strips on each detector. Figure 3.24 shows the location of the measured points and the relevant coordinate system. For the modules were 3 points were recorded along the strip the second point was halfway along the strip, between point 1 and 2 on figure 3.24 and so on.

Figure 3.25 a) shows the angle between two strips that are connected to the same readout channel. On figure 3.24 this corresponds to the angle between the line 1 to 3 and 5 to 7 and so on. The RMS of the distribution is 1.6×10^{-4} radians, a gaussian fit gives a σ of 1.0×10^{-4} radians. Figure 3.25 b) shows the residuals from a straight line fit of the endpoints of the strips. The RMS is $4.5 \mu\text{m}$, while a gaussian fit has a σ of $3.2 \mu\text{m}$.

An estimate of the precision of measurement can be made under the assumption that the diffusion lines on similar types of detectors all have identical geometry. From the measurements on each detector one can calculate the difference in perpendicular distance between the two outermost diffusion lines. That is the difference in the distances from point 1 to 2, 3 to 4 on figure 3.24 and so on. From counter to counter the distances may vary around $\sim 10 \mu\text{m}$. Within each counter we observe the distribution plotted in figure 3.26 b) with a RMS of $3.6 \mu\text{m}$. The contribution to this spread is the spread in the detector geometry and the error in our measurements.

We explain the spread from detector to detector by the fact that we have not really measured the edge of the diffusion line, which is invisible, but rather the edge of the opening in the thick oxide. We see in the microscope color differences caused by interference in the different oxide thicknesses on and in between the diffusion lines.

The edges of the thinner oxide are not very well defined. This is easily seen in the microscope as a difference in the apparent width of the diffusion lines from detector to detector. The result

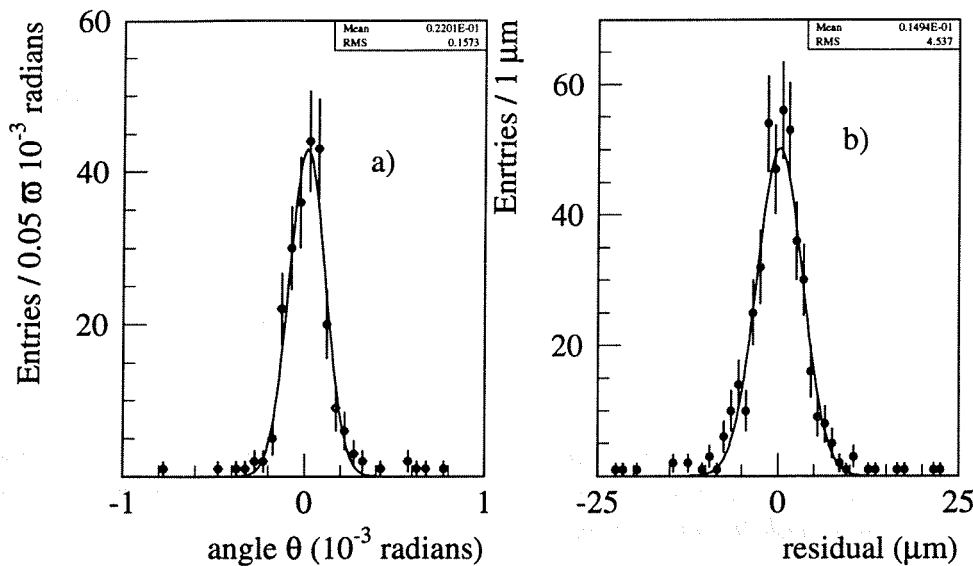


Figure 3.25: a): The angle measured between two strips in two adjacent detectors, connected to the same readout channel. The RMS of the distribution is 1.6×10^{-4} radians, a gaussian fit gives a σ of 1.0×10^{-4} radians. b) Residuals from a straight line fit of the location of the measured position of the endpoints of four strips in the four detectors in each module, the RMS is $4.5 \mu\text{m}$, while the gaussian fit gives $\sigma = 3.2 \mu\text{m}$.

is that the determination of the absolute position of the diffusion line can not be made to much better than about $10 \mu\text{m}$, the relative precision is however better and in the order of the RMS from figure 3.26b, since the oxide openings have constant width within each detector.

A check on the orthogonality of the coordinate system used for these measurements can be obtained by calculating the length of the diagonals in each detector, that is the distance from point 1 to 4 and 2 to 3 on figure 3.24 and so on. For a square system they should be equal. Figure 3.26 a) shows the difference in the diagonals. A shift of $20 \mu\text{m}$ of the mean is seen. Clearly the two axes are not perpendicular. The large width of the distribution is due to the fact that the step size along the x axis was $10 \mu\text{m}$. This has however no effect for the parallelness measurements mentioned above, as long as the module was close to parallel with the x axis during measurement.

This angle was measured by plotting the deviation from 90° in each corner of each counter. In the skew system the rectangular counter looks like a parallelogram. The deviations are plotted in figure 3.27. The absolute value of mean of each these two distributions gives us directly the deviation, which is $(0.6 \pm 0.3) \times 10^{-3}$ radians. The reason for the large error is the step size of $10 \mu\text{m}$ in x direction. Across one counter this leads to a displacement in y from the true value of $60000 \mu\text{m} \times 0.0006 = 36 \mu\text{m}$, in agreement with the measured difference in the diagonals. This value is so large that the module survey data had to be corrected for this before being merged with the survey of the complete detector.

The skew the coordinate system introduces also a systematic shift of the absolute position of the strips relative to the reference cylinders as well as in the distance between the two reference cylinders which was corrected for.

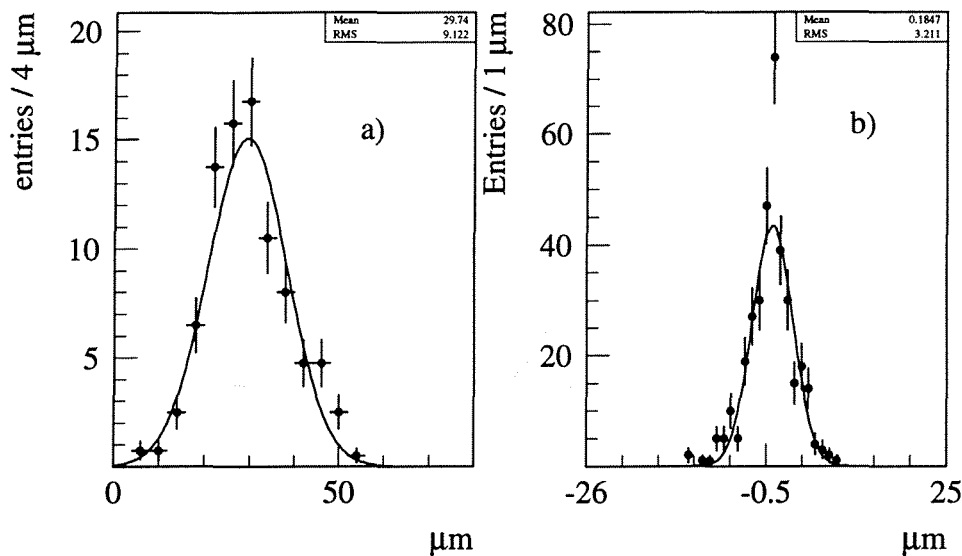


Figure 3.26: *Microscope measurement precision. a): The difference measured in the length of the diagonal for each counter in the modules. b): The difference in perpendicular distance measured between the end-points of outermost strips in each of the counters, the RMS is 3.6 μm.*

3.17 Overall Detector Survey

Before installation in DELPHI the Microvertex Detector was measured using the three dimensional measuring machine acquired for this purpose. The machine is capable of measuring and reconstructing the position and shape in three dimensions of objects such as planes, cylinders and spheres. It works by touching the object and reconstructing the touched point in space. The overall precision of the machine is better than 20 μm in space, [60]. A photograph of the detector undergoing survey on this machine is shown in figure 3.29.

The object to be measured is placed on the granite table of the machine. A granite bridge movable in x , is located above the table. Onto this bridge a second granite bar is attached. This bar is movable in the y and z directions. A measuring head is attached to the lower end of the bar. The head consists of an arm movable in θ and ϕ with respect to the vertical z axis. The end of the arm is fitted with a stylus with a ruby sphere tip. By this arrangement the sphere can be brought into contact with any exposed surface of the object placed on the table. A space point is recorded when the force on the needle exceeds ~ 7 g. Tests have shown that this force does not bend the module within the uncertainty of measurement. The movements of the measuring arm are controlled by the operator and the data are recorded on a computer.

The detector was placed on the granite table using a support similar to the support in DELPHI. For each module more than 20 points were recorded in the silicon plane, and the positions of the reference objects were as well determined. When the Closer layer is mounted the Inner layer is not accessible. The Inner and Outer layer were therefore measured first, then the fully assembled Closer layer was attached to its proper position and the Outer and Closer layer were measured. Each layer were in this way measured at least three times. Any distortions introduced by the mounting of the Closer layer were resolved by comparing the measurements of the Outer Layer before and after the Closer layer was attached.

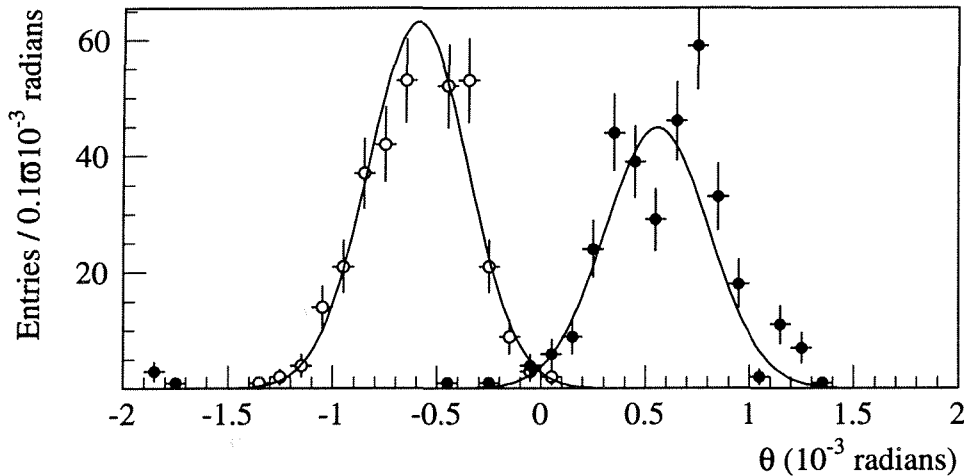
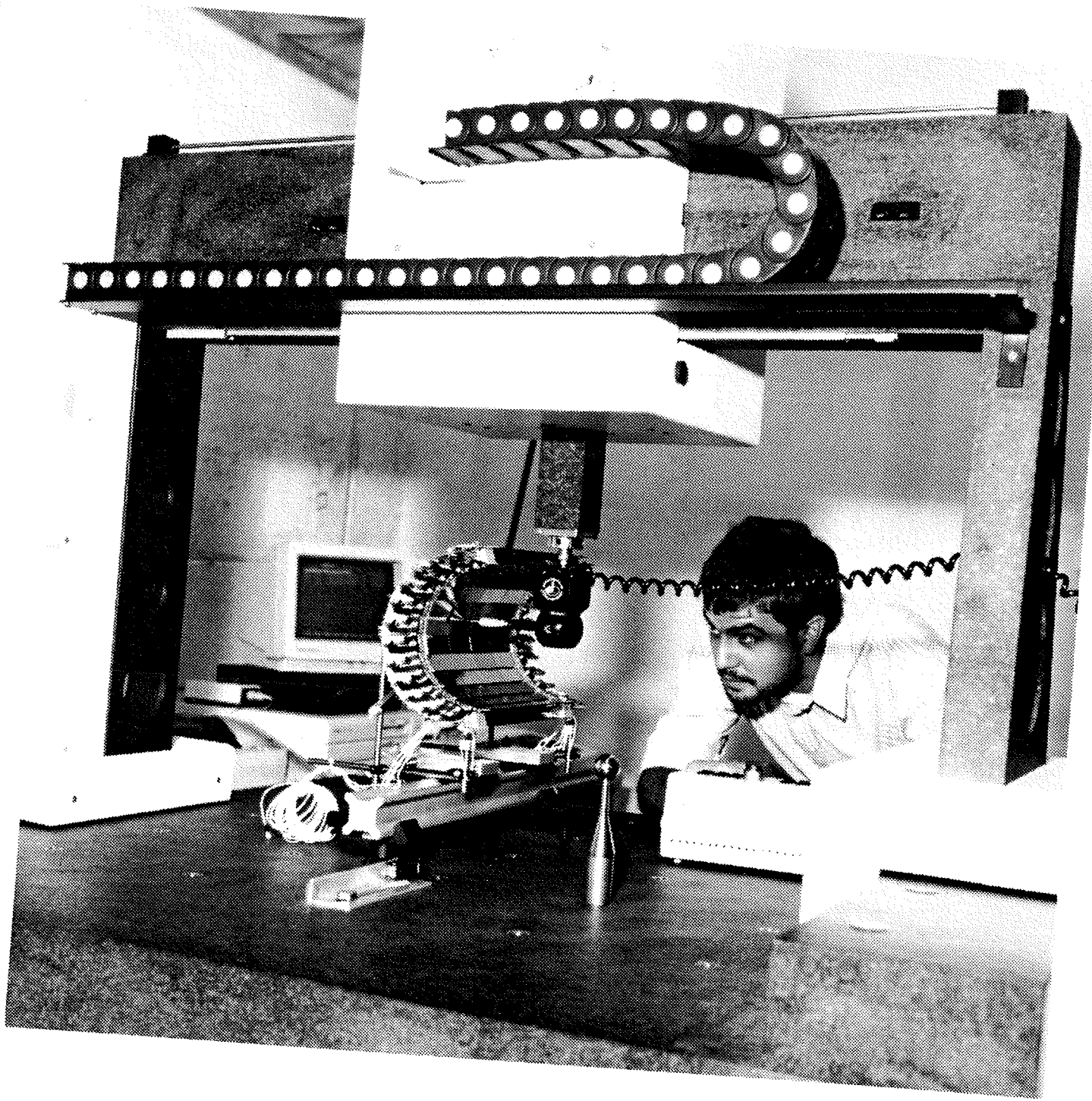
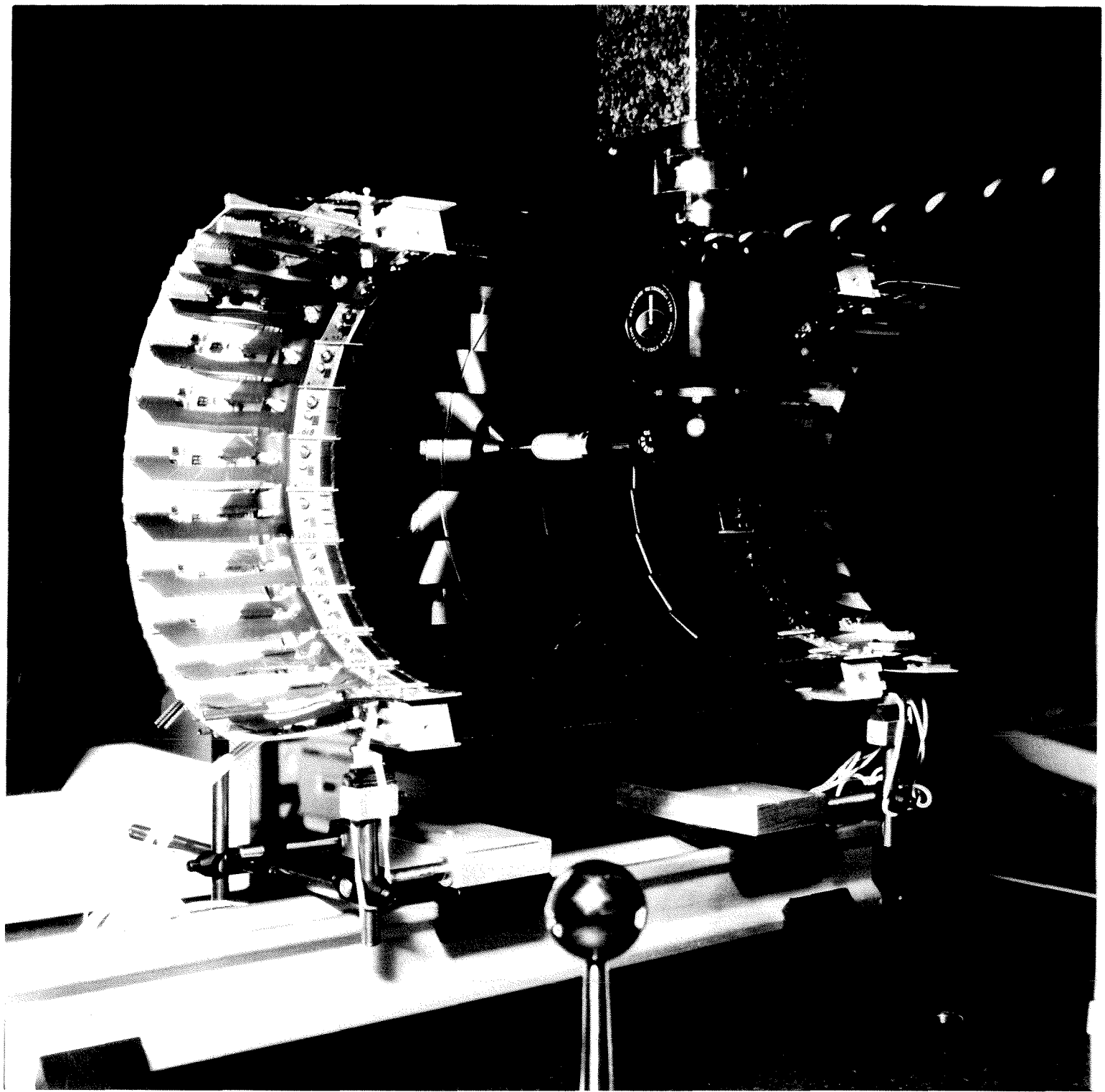


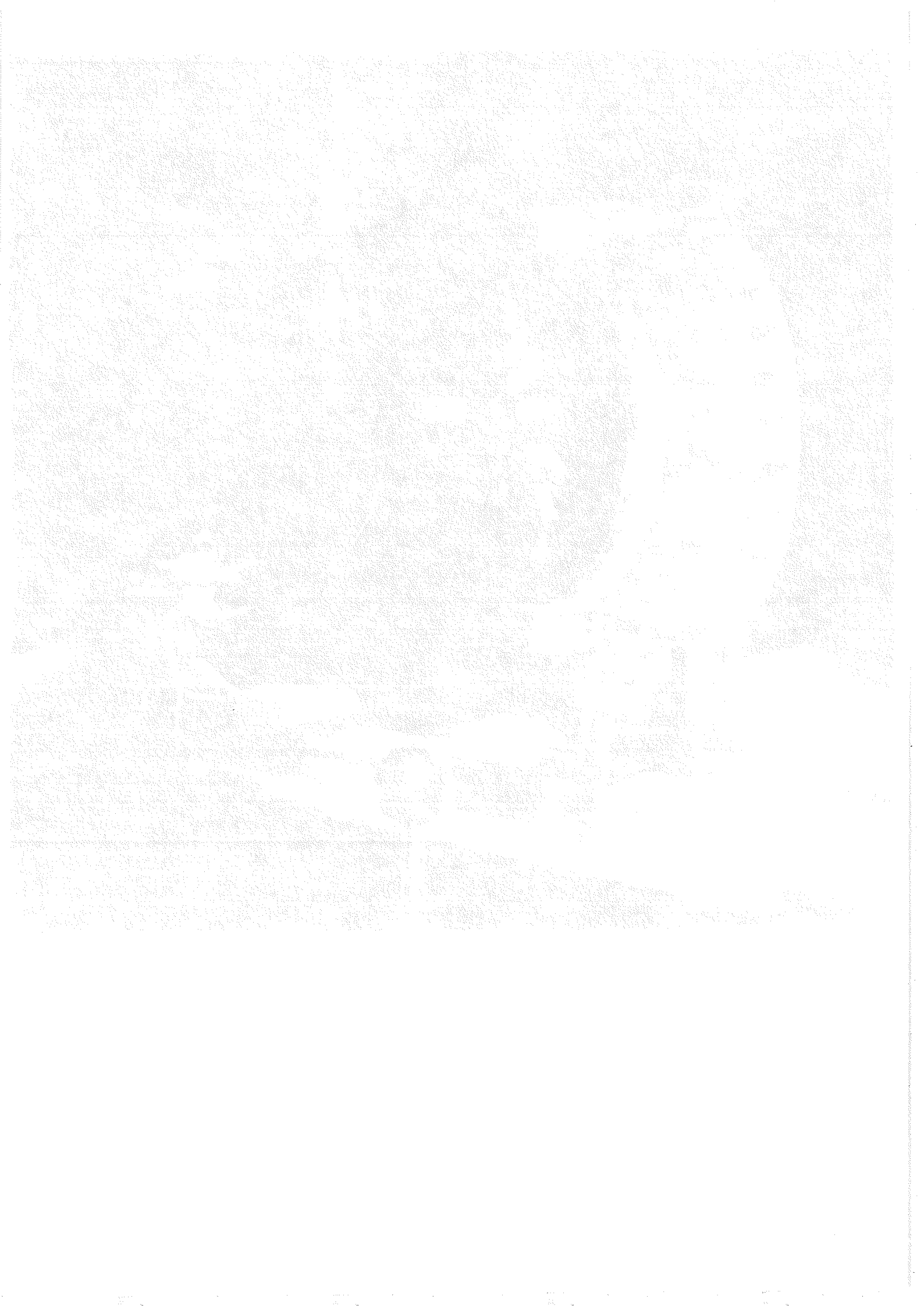
Figure 3.27: Deviation from 90° angle of the corners of the counters. The plot shows the difference from 90° of the angle between the lines connecting the points 1-3-4 and 2-1-3 and so on, as shown in figure 3.24. The mean values for the two distributions are ± 0.6 while the RMS is 0.3 milliradians.

The detector was removed from DELPHI after the 1991 running period. Before the detector was disassembled for repair and replacement of some bad modules, the three dimensional survey was repeated.

After the survey the data was merged with the measurements from the microscope and transformed into the format by the off-line coordinate reconstruction. Figure 3.28 shows track residuals on counters reconstructed using the survey data only. The procedure used to make the plot is explained in section 5.6. The figure should be compared with figure 5.8 which was made using the best possible alignment obtained with tracks, starting from the survey data. We observe that the survey alone gives a resolution of $37 \mu\text{m}$. The alignment with tracks improves this about a factor of four.







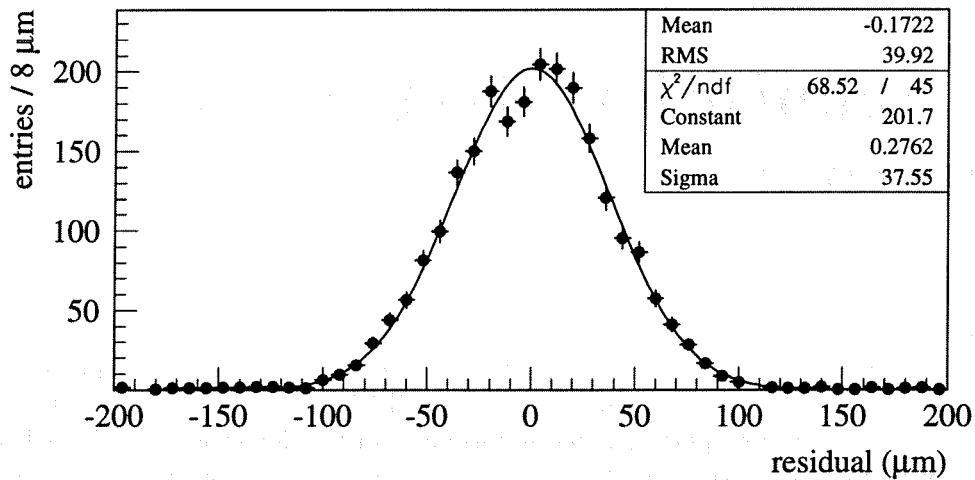


Figure 3.28: Track residuals on Inner layer using alignment from survey data only. The σ of the gaussian fit is $37.1 \mu\text{m}$ corresponding to a resolution of $30 \mu\text{m}$. The track fit procedure and the extraction of the resolution is explained in section 5.6

Figure 3.29: (Next page) The photograph shows the detector placed on the granite table of the three dimensional surveying machine. The bridge holding the measurement head is seen surrounding the detector. The movable measurement head is in the centre with the stylus touching a silicon detector.

Chapter 4

Data Acquisition, Trigger and Monitoring

The DELPHI data acquisition system is based on FASTBUS [61], a modular high speed asynchronous data bus. The trigger is an integral part of the general data acquisition and is sensitive to the topology of the electronic signals in DELPHI induced by the products of the e^+e^- collisions in LEP. During operation the performance of the detector is monitored to check the data quality as well to detect any alarm situation. Various monitoring tasks are therefore built into the data acquisition system. The monitoring is partly done on the main data stream in FASTBUS or, for slowly varying parameters, via a separate data acquisition system specially tailored for this.

The overall important feature of the read-out of the Microvertex Detector is the extensive multiplexing of the signals. The 73,728 strips of the Microvertex Detector are read out on only 60 twisted pair cables, a multiplexing ratio of 1,229 to 1.

The parts of the system relevant for the Microvertex Detector are described, starting with the FASTBUS readout processor.

4.1 The Readout Processor

The read-out processor, SIROCCO IV [62], receives the analog signals from the detector, digitizes them, applies a data reduction algorithm and finally transfer the zero suppressed data to the central data acquisition in DELPHI. The data reduction is necessary due to the large amount of data produced by the Microvertex Detector which would flood the overall data acquisition system of DELPHI. Since the average hit occupancy of the Microvertex Detector is very low, about 1/1000, it would be very inefficient to store the data from all the strips of the detector

The processor, shown in a block diagram in figure 4.2, is a single width Fastbus unit. Each unit consists of two independent channels. Each channel has one differential analog input. The analog signal is digitized in a fast, 20 MHz, 10 bit Flash Analog to Digital Converter, FADC, TRW TDC 1020¹ and stored in a 4 event deep Front End Buffer, FEB. The Front End Logic, FEL, controls the operation and receives control signals from the Local Trigger Supervisor conveniently named PANDORA [63]. Every event is given an account number ACC#, this number and trigger information is stored in the Front End Queue, FEQ.

The pulse-train coming from the detector during the readout cycle is sampled synchronously at with the clocking of the analogue shift-register in the amplifier and multiplexing chips at

¹The ADC was supplied by TRW LSI Products Inc., P.O.Box 2472, La Jolla, CA 92038, USA.

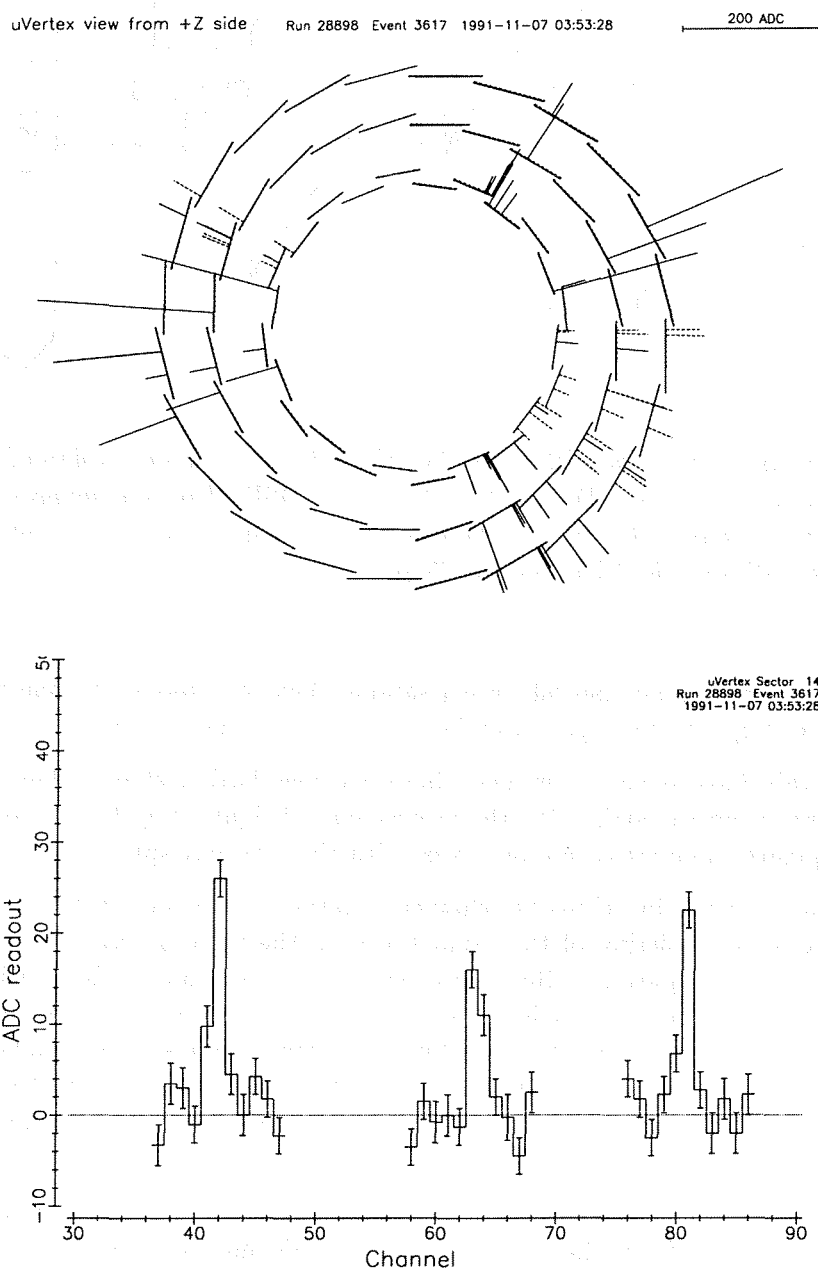


Figure 4.1: On-line event display from a beam event, the upper picture shows the detector viewed along the z axis. The length of the lines on the silicon counters indicates the pulse-height in ADC counts. Notice the very few hits due to noise. The lower picture shows three adjacent charge cluster from the same event. Because of the zero suppression there is of course no signal between the clusters. The error bars show the noise of each channel

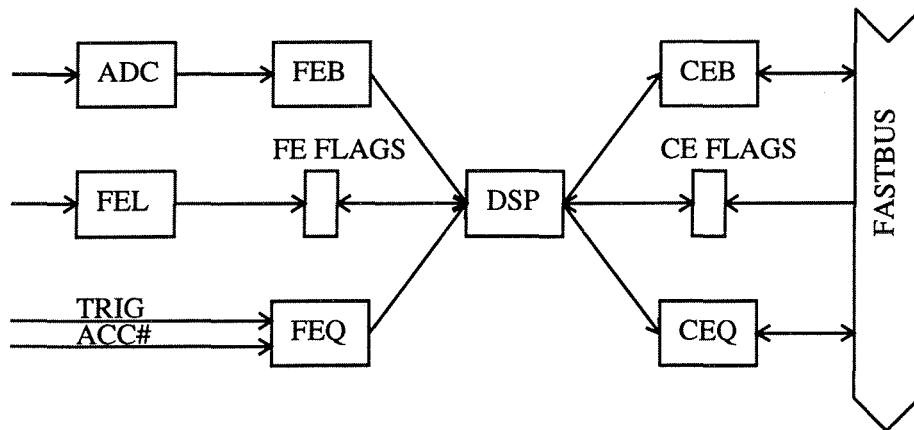


Figure 4.2: Block diagram of the SIROCCO IV, the abbreviations are explained in the text. The main data stream are from the ADC via the FEB to the DSP. The zero suppressed data is stored in the CEB and read out by the central data acquisition via FASTBUS Accounting and trigger information is handled by the FEL and the flags.

2.5 MHz with one sample per period. Each sample thus corresponds to one readout channel, equivalent to one strip. At this speed the digitization takes about 500 μ s.

Some cross talk have been experienced between neighboring strips. This cross-talk is attributed to charge from the strip with the largest pulse-height being transferred to the next in the readout sequence. The cross-talk increases with the read-out speed.

When several multiplexing chips are chained together the output transistor of each channel sees a capacitive load consisting of the capacitance all the input gates of the chained together readout shift registers in parallel. Because of this increased load the band-width of the chips are reduced. They therefore do not have enough time to settle to a stable value between each sample, introducing an offset of the baseline for a strip following a strip with a large pulse-height. This effect might cause a small systematic shift of the cluster centroid in the offline analysis, however since the effect is always in one direction it is removed by the alignment using charged particle tracks.

The data analysis is performed by a Digital Signal Processor, DSP, Motorola DSP 56001 [64]. The DSP reads the data from the FEB, and trigger information from the FEQ. The reduced data is stored in a 4 event deep Crate End Buffer, CEB, the addresses of the data blocks for the different events are stored in the Crate End Queue. The handshake between the DST and FASTBUS is done via the Crate End Flags indicating filled or empty Crate Event Buffers. An event is typically analyzed in about 30 ms. The event size is about 1000 32 bit words for a hadronic Z^0 event and 150 word for an empty event.

The analog signals from the detector might have offset voltages. A Digital to Analog Converter, DAC, connected to the input offsets the analog signals with a suitable amount determined by the DSP. The algorithm is based on offsets measured on previous events. This arrangement cancels any offset on the signals from the detector and ensures a suitable DC level before digitizing.

4.2 The Zero Suppression Algorithm.

To find the channels with the interesting signal it is necessary to evaluate three quantities: the individual channel pedestal, the common noise and the individual channel noise. The evaluation is done using an algorithm based upon previous experience with silicon micro-strip detectors and is programmed in assembly code. A detailed description of the program can be found in [65]:

Channel pedestal subtraction and updating. Each strip has a slowly varying pedestal, P caused by leakage current and variations in gain. The value for the pedestal is stored for each strip and subtracted from the signal, S . The new pedestal value is thereafter calculated as a running average and stored for every strip with a signal to noise ratio less than $3 \times \text{RMS}$ using:

$$P_i = P_{i-1} + \frac{S_i - P_{i-1}}{32} \quad (4.1)$$

where P_i is the pedestal, S_i is signal in ADC counts for event number i . The cut on the signal to noise ratio ensures that strips with charge from particles do not get their pedestals updated. The factor of $1/32$ is found to lead to algorithm that is stable and able to trace the variations in the pedestals but not sensitive to noise fluctuations.

Common noise suppression. Each chip or sector may have a common level, usually called common mode. The common mode is caused by electronic pick-up at the detector. Typically the common mode shift is a few ADC counts. Sometimes, however, the common mode for one chip becomes large. This is normally an indicator that the chip has begun to malfunction. The common mode is defined as the average signal across one chip, 128 channels, excluding strips which are noisy or marked as bad. The common mode is subtracted from the signal.

Figure 4.3 shows a plot of the common noise for the Inner layer. The RMS is 6 ADC counts. There are tails due to chips that are malfunctioning.

Individual strip noise calculation. The single strip noise, N , is defined as the RMS of the digitized signal when there is no ionization charge from a particle on the strip. The DSP calculates and stores the noise values and the signal divided by noise for each strip using the same running average technique as for the pedestals.

$$N_i^2 = N_{i-1}^2 + \frac{S_i^2 - N_{i-1}^2}{1024} \quad (4.2)$$

Cluster search and tagging. A cluster is defined as the 5 strips on either side of a strip with a signal larger than 6 times the noise. For each event the DSP stores a pointer to the strips satisfying this criteria. The clusters may overlap.

Statistics calculations and updating. Noise per chip, defined as the RMS of the common mode, and the number of clusters is calculated and stored for each event.

Zero suppression. Only the cluster data and the statistics block is stored in the FEB.

Output formatting of data. The data is formatted according to convention before being output to Fastbus.

DAC updating. The DC offset on the input is calculated and a number setting the DC offset is output to the DAC.

02/11/91 11.35

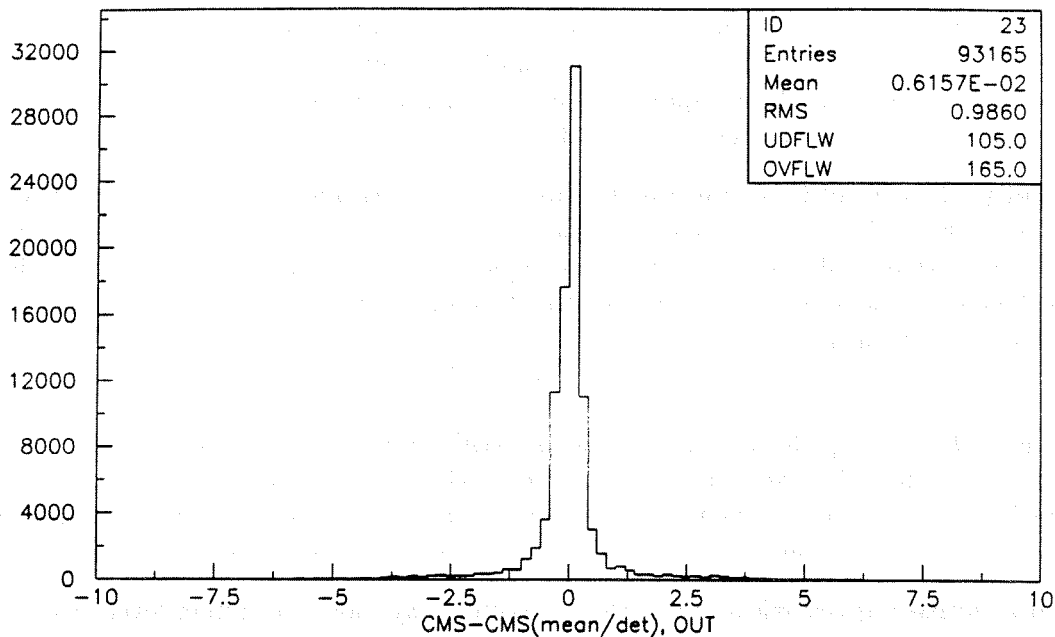


Figure 4.3: *Common noise per chip. The values for the common noises are calculated online by the DSP. Horizontal scale: common noise in ADC counts, vertical scale: no of entries.*

4.3 The Pulse Generator and Controller

We have seen that the MX3 chips needs a certain pulse sequence in order to function properly. A separate FASTBUS unit was made to provide the right pulse sequence [66]. The unit is controlled by PANDORA and the timing of the pulse sequence can be set via FASTBUS. To ensure the correct timing of the multiplexing chips the unit synchronizes the ADCs in the SIROCCOS to a fixed frequency. The synchronization is of great importance since there is a direct correspondence between the timing of the readout and the spatial position of a charge cluster in the silicon.

A displacement in time of 1 period of the detector signal is equivalent to a movement in $R\phi$ of charge cluster equivalent to the readout pitch of $50 \mu\text{m}$. Since only one sample is taken per strip, this sample has to be taken at the same time position for each strip in each event to ensure that no systematic shift of the charge clusters is introduced.

The signal to noise ratio may vary as the pulse-shape from each strip is sampled at different times. There is therefore an optimum time position for the ADC to sample the signal within the cycle for each strip. To find the optimum sample time position the sample time position was scanned across the cycle for one strip while the detector received test pulses from a generator. The sample time position that gave the best signal to noise ratio was chosen and kept for the whole running period.

02/11/91 11.37

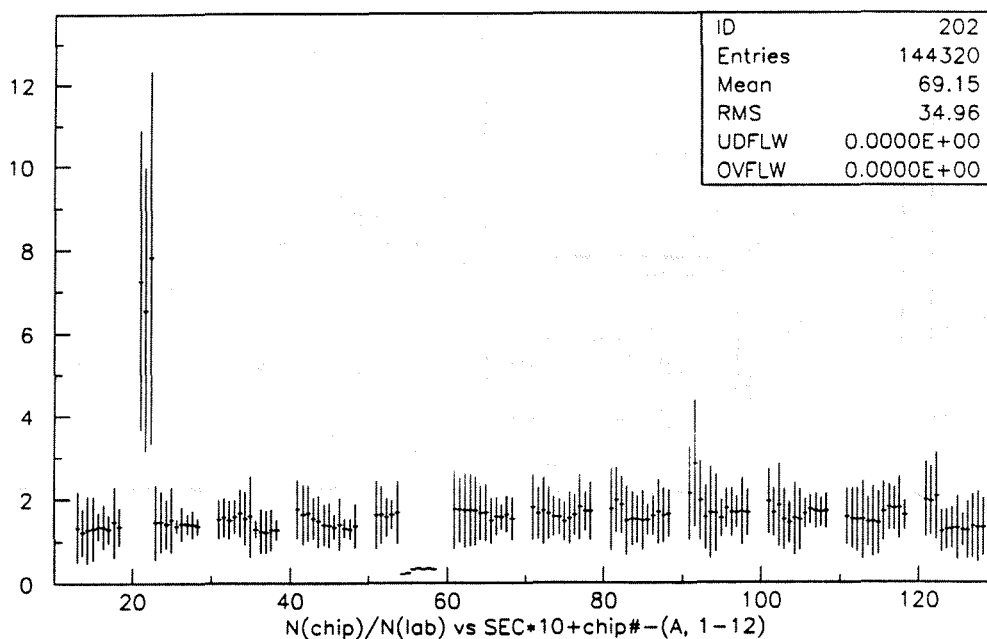


Figure 4.4: Noise per chip calculated by the DSP. horizontal scale: Sector number $\times 10 +$ chip number, A side sector 1 to 12, vertical scale: Noise in ADC counts normalized to the noise measured in the lab prior to installation.

4.4 The Data Acquisition System.

The Data acquisition system gathers data from all the sub-detectors in DELPHI and writes it to magnetic tape in a format readable for the off-line analysis software. The system is very large, consisting of almost 200 fastbus crates, each with up to 24 read-out processors of different types, depending on the requirements of the various sub-detectors. It is controlled by VAX computers², one computer for each sub-detector and one central computer. It is however beyond the scope of this work to give more than a brief description of the data acquisition system, more detailed descriptions are found in [39,67,68].

The system is divided into several partitions, each partition corresponding to one or several sub-detectors. The Central Partition handles the communication with the detector partitions. Each detector partition is equipped with an Equipment Computer Crate which handles communication to and from the Central Partition. Each of these crates are connected to an Equipment Computer, μ VAXII, via a Computer Fastbus Interface, CFI. The Central Partition is accessed from the central computer, OPS, via CERN Host Interface, CHI, and has access to each of the partitions. The equipment computers handles local control tasks and stores the software running in the FASTBUS modules.

The partitions are divided into segments which communicates with the Equipment Computer Crate. The segments consists of the Front-End Crates housing the modules that digitizes the detector signals. These modules are typically, as in our case, ADCs. For the drift chambers

²The computers were delivered by: Digital Equipment Corporation International (Europe), 12 Av. Morgines, 1213 Petit-Lancy, Geneva, Switzerland

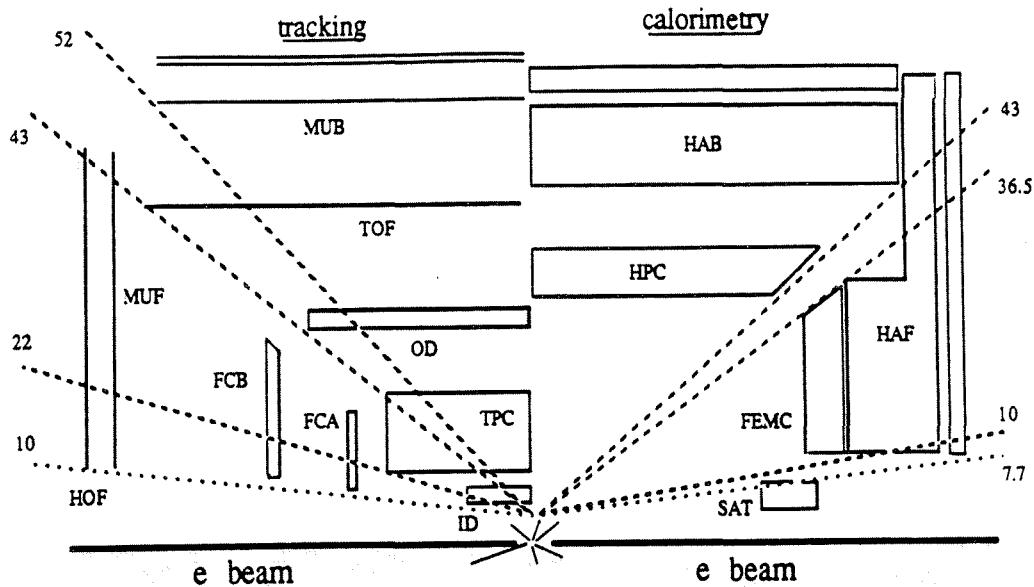


Figure 4.5: *Detectors Participating in the 1st and 2nd level trigger. The polar acceptance is shown in degrees*

digitized time information is provided by Time to Digital Converters, TDCs, and for triggering purposes signals are provided by discriminators.

4.5 The Trigger

The trigger system is sensitive to the topology of the electronic signals recorded in the detector. It recognizes the typical pattern generated by the different decays of the Z^0 and triggers the readout of DELPHI, and should do so with 100 % efficiency to ensure no loss of signal. More details about the trigger are found in [39, 69]

The trigger is divided into three levels. The first level being the fastest and synchronous with the electron bunches in LEP. The first level trigger decision is taken $\sim 4 \mu\text{s}$ after Beam Cross Over, BCO. In the case of a negative signal the data are discarded and the detector is ready for the next BCO. This is situation (a) on figure 4.6. In the case of a positive signal the 2nd level trigger processing is started.

The 2nd level decision is taken $\sim 40 \mu\text{s}$ after the BCO. Consequently the detector is not active during the first beam crossing after a positive first level trigger, leading to a dead time of about 1% at the typical 1st level rate of 400 Hz.

The 2nd level rate is typically a few hertz. A positive 1st level followed by a negative 2nd layer decision is shown in situation (b) on figure 4.6. Finally in the case of a positive second level trigger a $\sim 4 \text{ ms}$ dead-time is introduced to free the Front End Buffers and the data are transferred from the Front End Buffers to the Multi-Event Buffer of each detector partition. This is situation (c) in figure 4.6.

The components of the detector that contribute to the first level trigger are [6]:

A double-arm track trigger was made by coincidences of the ID and OD tracking chambers.

Each detector provided signals for charged particles if there were hits in 3 out of 5 detector

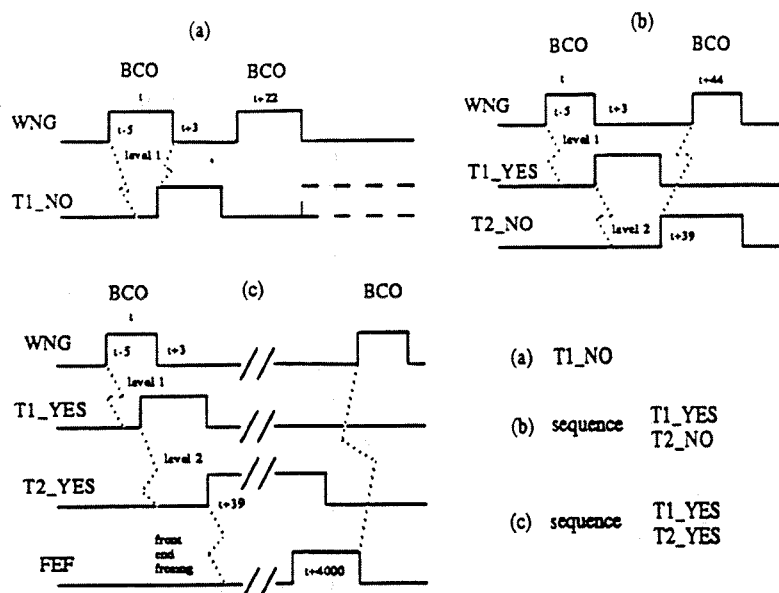


Figure 4.6: Timing diagrams for the 1st and 2nd trigger decision levels: (a) No 1st level trigger, (T1_NO), (b) 1st level trigger but no 2nd level, (T1_YES followed by T2_NO) and (c) 1st and 2nd level trigger, (T1_YES followed by T2_YES).

layers. Then a coincidence between signals in at least two OD quadrants with any signal from the ID was formed.

A single-arm track trigger was made by coincidences of the ID and OD tracking chambers at first level and the TPC at second level. The coincidence was formed between any signal in the ID or OD with a single “track” pointing to the interaction region in the TPC

A Scintillator trigger was made by coincidences of the HPC and the TOF scintillation counters. The TOF counters were sensitive to minimum ionizing particles penetrating the HPC and the solenoid and shower leakage from the calorimeter. The HPC counters were sensitive to electromagnetic showers with an energy larger than 2 GeV. The trigger was the OR of:

1. At least 2 TOF octants.
2. At least 2 HPC octants.
3. Coincidence of any TOF with any HPC octant.

A coincidence trigger between any TOF octant with any OD quadrant.

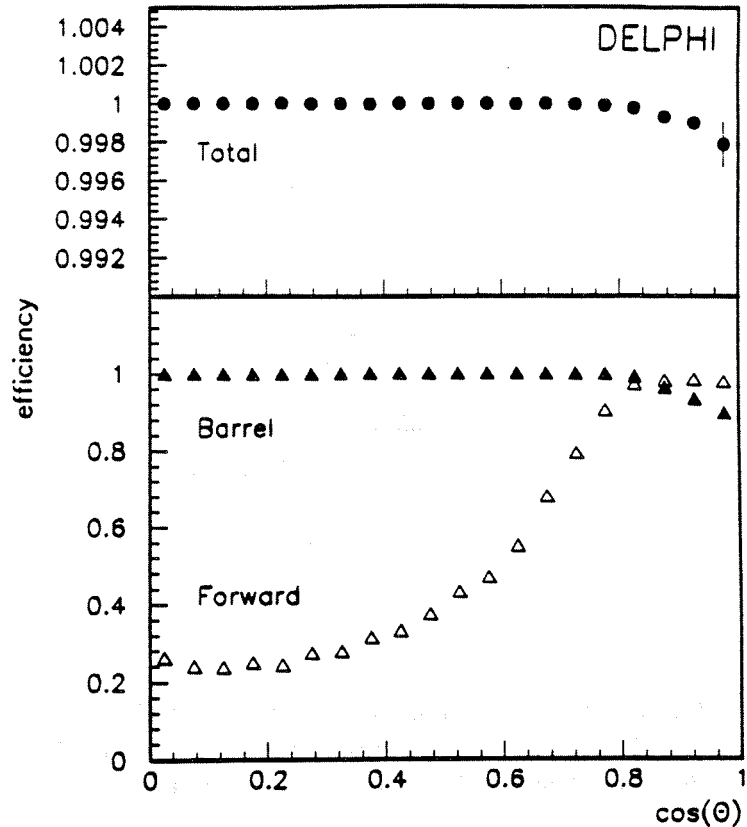
A forward electromagnetic trigger consisted of a single arm component, FEMC energy greater than 4.5 GeV and a back to back component, FEMC energy in both end-caps greater than 3 GeV.

A forward majority trigger was made by coincidence of at least two of the following:

1. A coincidence of back to back quadrants of the HOF

Figure 4.7: *Trigger Efficiency for hadronic events as a function of the polar angle of the sphericity axis, which is defined as the axis which minimizes:*

$$S = 3 \sum_a |P_T^a|^2 / 2 \sum_a |P^a|^2$$
where P is the momentum of the a^{th} hadron and P_T^a the transverse momentum relative to this axis.



2. At least one track detected by coincidences in the forward chambers FCA and FCB.
3. An energy of at least 3 GeV in one FEMC end-cap.
4. A coincidence of one OD quadrant with any ID signal.

A **forward muon back-to-back trigger** was formed by requiring a signal from either HOF end-cap to coincide with signals in back-to-back quadrants of the MUF end-caps.

The trigger efficiency for the relevant sub-triggers for the hadronic and leptonic Z^0 decays was measured using data samples recorded with independent sub-triggers. For the hadronic events used in this thesis the relevant triggers are (1), (3), (4) and the forward trigger (6). Within the Microvertex Detector Acceptance, $|\cos(\theta_{\text{sph}})| \leq 0.65$, the efficiency is very close to 100%, see figure 4.7.

4.6 Slow Controls

For the control and measurement of slowly varying parameters a separate control and data acquisition system has been installed [70, 71] based on the bus system, G64. Typical tasks for this system in DELPHI is the measurement of gas flows, temperatures, supply voltages and currents.

The slow control tasks for the Microvertex Detector are the monitoring of the supply voltages and currents and the temperature on the repeater cards and the end-rings [72]. The depletion zone in the detectors is induced by separate voltage sources, one channel for each detector module, each individually adjustable via front panel controls. These bias voltages and currents

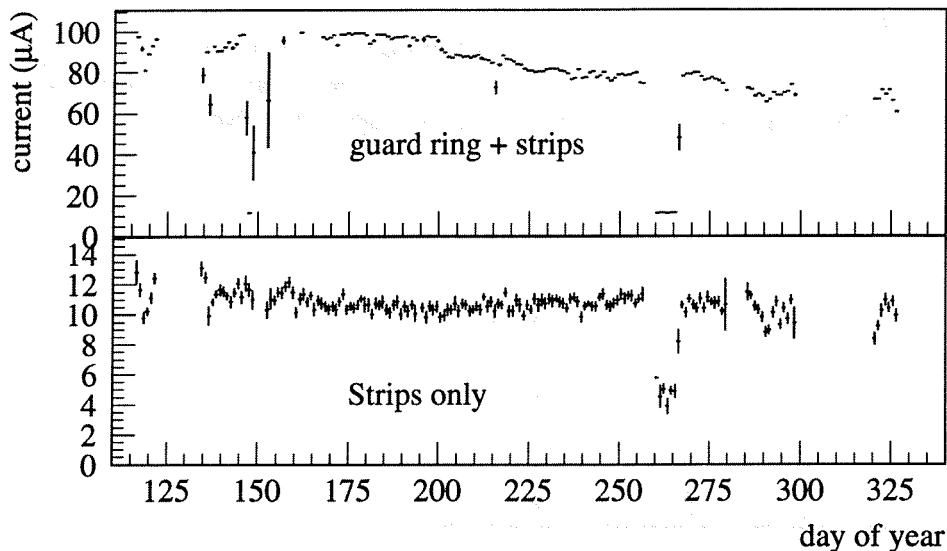


Figure 4.8: Leakage current from sector Closer 18 for the running period

are individually monitored. The system can as well be turned on and off via software running in the slow control system. The depletion voltages is normally on to minimize the risk of radiation damage due to the mechanism outlined in sections 3.3 and 3.4.

The bias current monitored at the supply is for every module the sum of the currents in the strips and in the guard-ring. Since the guard-ring current normally is much higher than the strip current we have for some modules sense wires from the module that enables us to monitor the two currents individually. The bias currents have been very stable during the period of operation.

In addition the slow control system will detect an alarm situation caused by a malfunction in the cooling system leading to an increased temperature of the detector and turn off the power supply.

The data gathered from the G64 system are transferred to the equipment computer and stored. At regular intervals the calibration data for the event reconstruction software is updated. The slow control data is thus available to the off line analysis software.

Programs exist for displaying the slow control variables on a computer terminal, either with numeric output showing the latest values, or using graphical output to show the variation of the measured quantities over the last 24 hours. Figure 4.8 shows the leakage current from one sector as obtained from the stored data. The currents are stable over the year with the strip current about a factor of 10 lower than the total leakage current

4.7 In Situ Stability Monitoring.

The precise alignment achieved for the detector would be of little use if the detector would move in respect to DELPHI or internally deform during operation. In addition to the monitoring which is possible using the particle tracks, an independent system made up of optical fibres and lenses was installed. The system has the advantage of using the detectors as sensing elements and therefore not requiring any additional read-out system.

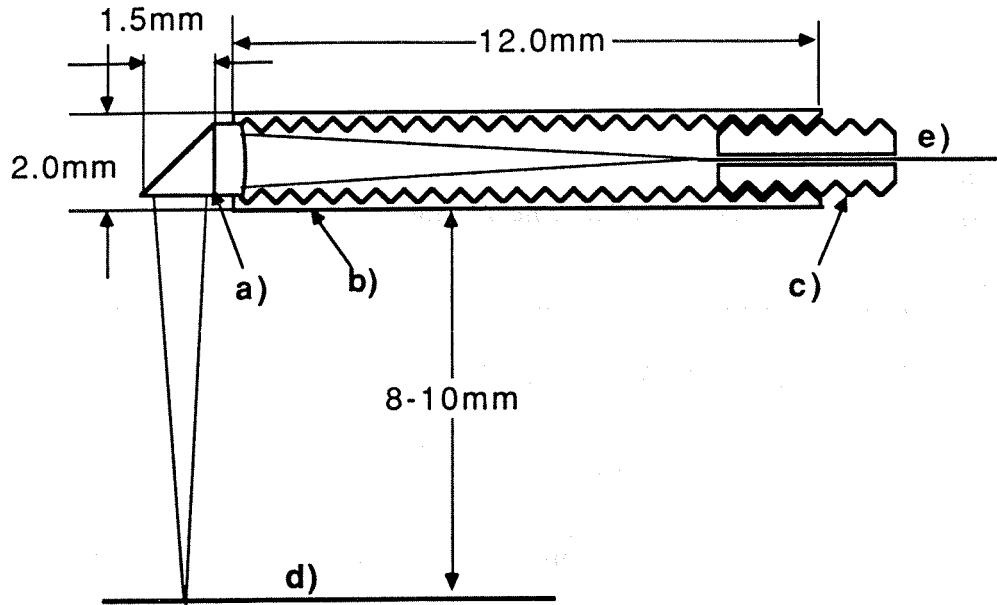


Figure 4.9: *Optical system for stability monitoring. A lens and a prism, a) are mounted in a 2 mm diameter aluminium tube, b). The inside of the tube is threaded in its full length to shut off stray light. The optical fiber, e) is led through a hole in the screw, c), in one end. Focussing is done by rotating the fiber and screw until a spot with a diameter of about $\sim 50 \mu\text{m}$ is obtained on the detector surface d).*

The system consists of 48 lens and prism combinations glued in pairs on the wall of the inner tube of the Inner Detector. Infrared light is fed from outside DELPHI via optical fibres and focused on the detector surface by the lens and the prism through suitably placed holes in the protective covers. One of the lenses focuses light perpendicular to the detector surface and the other under a 30° angle. The fibers are bundled together into two groups, one for the perpendicular lenses and one for the skew. Two independent infrared laser diodes emitting at 1060 nm wavelength is coupled to the two bunches. A trigger is given to the lasers for every 32 beam crossing and the data is collected together with the data from beam events.

The system has shown an excellent stability of the detector. Any movement above a few micrometer has been in correlation with temperature variations of the detector. A forced temperature rise of the detector was made by turning off the cooling circuit. A close correlation between the detector temperature and position is seen in figure 4.10.

The system has a resolution of $1-3 \mu\text{m}$, [73] depending on which particular laser is used. Figure 4.11 shows the position of one of the laser spots as a function of time. The observed movement of the detector over the whole year is in the order of a few micrometer. The jumps are caused by temperature variations when the detector has been switched on and off. Because of the excellent stability no time dependency was introduced in the alignment of the detector.

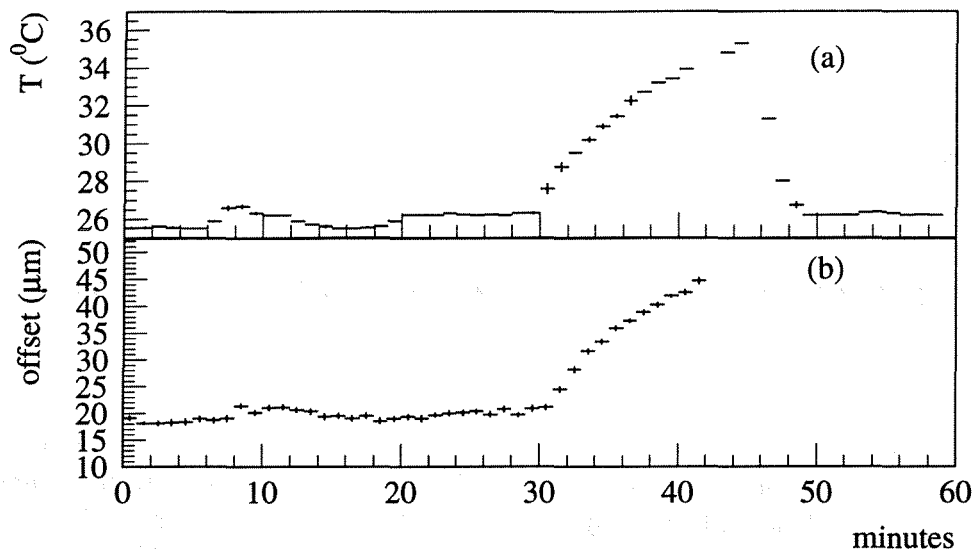


Figure 4.10: Change in position of one of the laser spots during a forced temperature change of the detector. The temperature was raised by turning off the cooling system. The lack of data for the latter part of the scan is due to a failure of the data acquisition system.

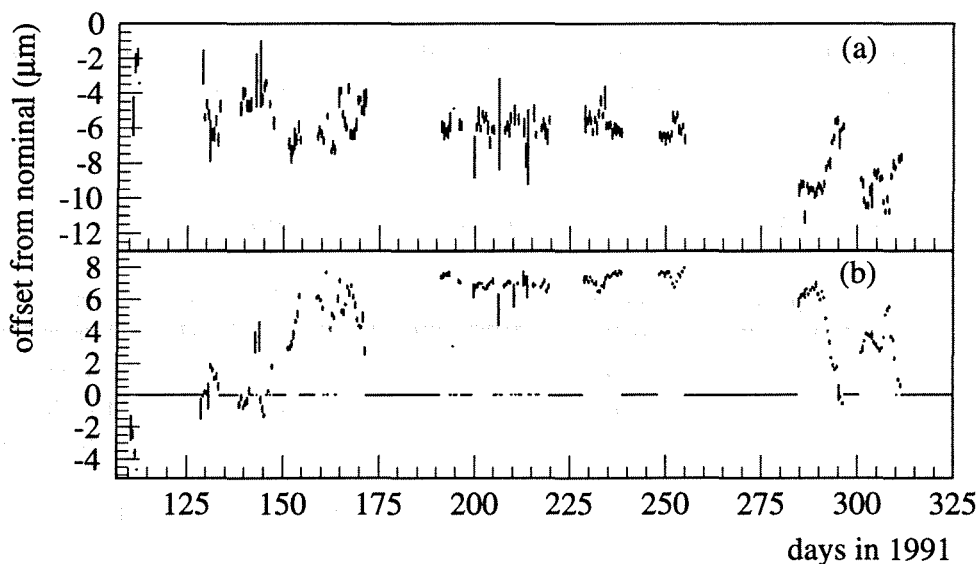


Figure 4.11: Output from the position monitoring system showing the movements of the detector during the 1991 data taking period. (a) is a laser spot on an upper module, (b) one from a lower module. The lower module is more constraint by the detector support and we expect less movements here. The gradual movement of the spots over the year shows an actual movement of the detector.

Chapter 5

Track and Vertex Reconstruction

Before any track reconstruction can be done, the ADC information from the data acquisition system has to be transformed into space points, and the space points have to be combined into particle trajectories. This pattern recognition proceeds by reconstructing track elements in the various track detectors of DELPHI. The track elements are then combined into particle trajectories. The track reconstruction as done on the data from the Microvertex Detector is described here as well as studies using isolated tracks performed to measure the precision of the reconstruction. The global track and event reconstruction is described in chapter 6.

Events with Z^0 decaying into a pair of muons are particularly useful. The muons are produced at one point with the beam momentum and undergo minimal multiple Coulomb scattering in the detector. These events can therefore give us the optimum resolution. The track extrapolation precision for high momentum is found by measuring the distance between the two muon tracks close to their production point.

The intrinsic resolution of the silicon micro-strip detectors themselves was also measured using the tracks from multihadronic events. More details about the evaluation of the hit precision in the Microvertex Detector is found in [74].

5.1 Microvertex Detector coordinate reconstruction

The overall pattern recognition is done by the standard DELPHI offline analysis, DELANA, producing an a set of Data Summary Tapes, DST. The DST contain the parameters of the reconstructed particle trajectories and detector specific information for further track reconstruction and particle identification. The information stored on the DST for the Microvertex Detector contains all the zero suppressed hit information from the readout processor in addition to the reconstructed space points.

Given a cluster of strips with ionization charge, the position in space where the particle traversed a silicon detector is found by first calculating the coordinate locally on the silicon, x_0 . This number varies from zero to the width of the silicon detectors. Using this number and the position in space of the silicon detector, the location of the point where the particle traversed the silicon is found. A possibility for fake hits caused by noise exists. Those hits are removed at a later stage by demanding that there is a track found in DELPHI corresponding to the hits found in the Microvertex Detector, see section 5.3

The calculation of x_0 of each counter is done starting from the online zero-suppressed data, see section 4.2, using an algorithm first published in [75]. The data consists of clusters of strips which have at least two neighbouring channels with a sum of signal S to noise N ratios larger

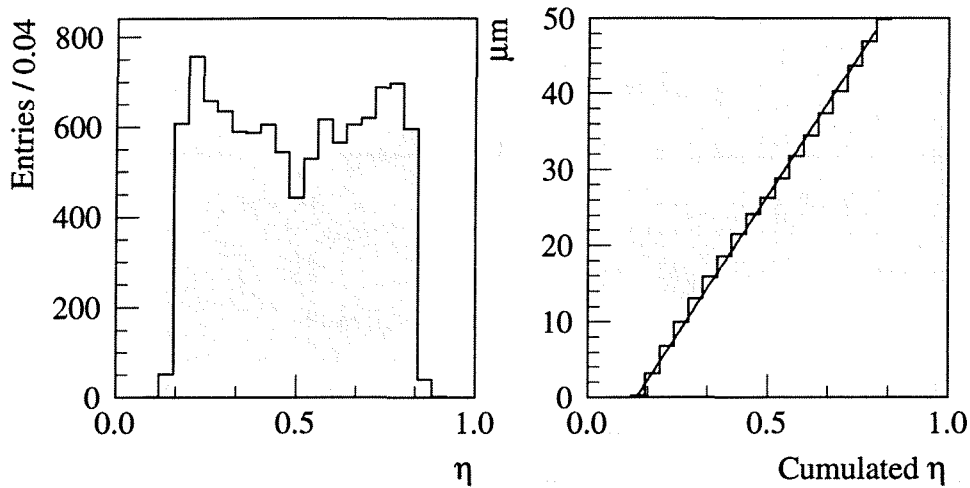


Figure 5.1: Charge division. The graph (a) shows the quantity η defined in equation 5.1. Because of the requirement on the minimum pulse-height the values of η is restricted to $0.17 < \eta < 0.83$. The depletion of values around $\eta = 0.5$ is because the histogram includes particle tracks with large incidence angles, see also figure 5.2. The graph (b) shows the integrated η normalized to the distance between two readout strip. The straight line is a linear fit to the distribution. A linear approximation to this graph is used in the calculation of the impact point of the traversing particle from the charge distribution the neighboring readout-strips.

than 6. Using this data, the algorithm proceeds as follows:

1. A strip belongs to a cluster if its pulse height, S , divided by its noise, N , is larger than a fraction $f \times S/N$ of the channel with the highest S of the cluster. A value for f of 0.2 was found to give the best precision. The cluster size is defined as the number of strips belonging to a cluster.
2. A cluster is accepted if the sum of the S/N individual channels is larger than 6 and there is at least one channel with a $S/N > 3$.
3. The strip with the highest signal to noise is selected.
4. The neighboring strip with the larger signal to noise is selected.
5. The sum of signal to noise of the two strips must be greater than $6 \times \sigma_N$.

Using these two strips the following quantity is calculated:

$$\eta = \frac{PH_i}{PH_i + PH_{i+1}} \quad (5.1)$$

where PH_i and PH_{i+1} are the pulse-heights of strip i and $i + 1$ respectively. The choice of $f = 0.2$ above limits η to the interval $0.17 < \eta < 0.83$.

The impact point, x_0 , for a given η is then

$$x_0 = ip + p \int_0^\eta \frac{dN}{d\eta} \eta \approx ip + p\eta \quad (5.2)$$

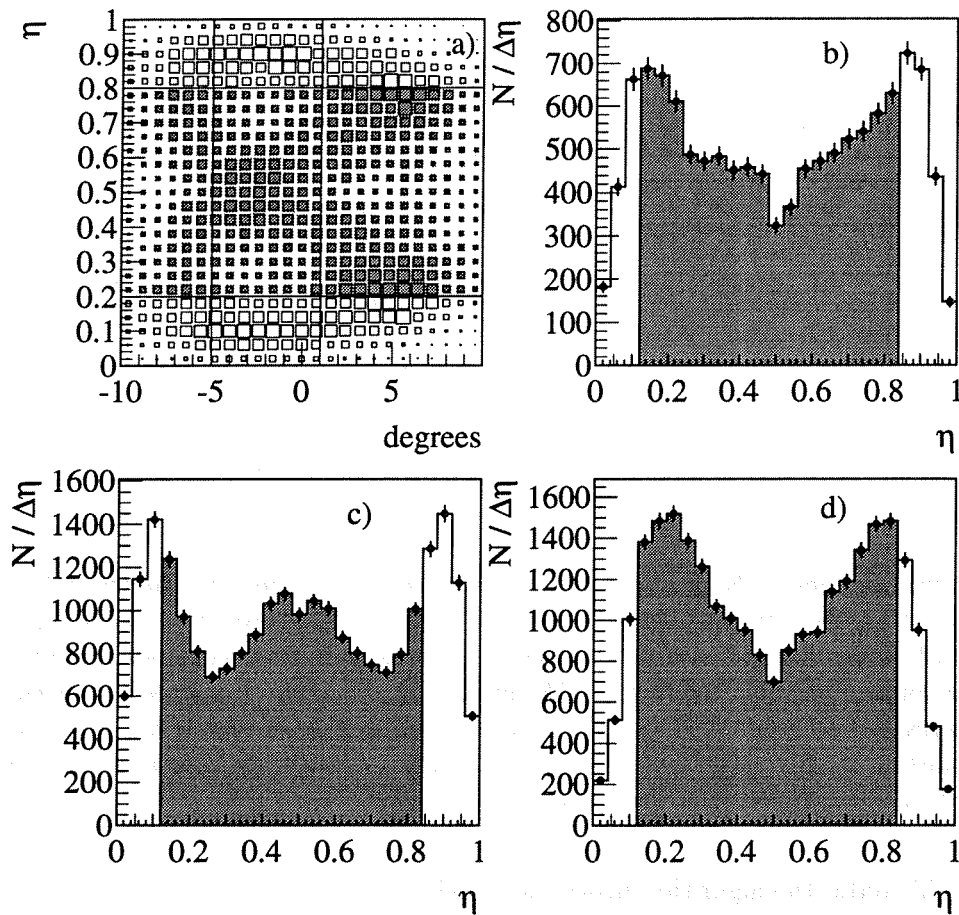


Figure 5.2: The η distribution for as a function of incident angle, α_i of the track on the counter (a), together with a projections, (b), (c) and (d) onto the y axis in the intervals -10° to -6° -6° to 0° and 0° to 10° respectively. The vertical lines on (a) indicate the projection boundaries, while the horizontal lines and the shaded regions on (b), (c) and (d) indicates the allowed value of η .

where i is the strip number of the first strip, P the strip pitch¹, $50\mu\text{m}$.

The approximation is equivalent to the assumption of a linear dependence between the position and the charge division between the two highest pulses.

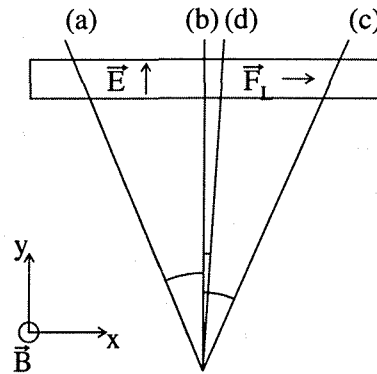
6. For the clusters which contain only one strip, the reconstructed coordinate is the position of that strip.

Figure 5.1 (a) shows the distribution of η and the integrated distribution of η (b) shows the relation between η and the impact point. As seen from the histograms the assumption of a linear dependence is on the average valid. The integrated distribution is therefore approximated by a straight line and the impact point, x_0 is found from equation 5.2.

In figure 5.2 The η distribution is shown as a function of incidence angle. For close to perpendicular incidence angle the η distribution shows a accumulation for values close to $1/2$.

¹The distance between the center of the readout strips.

Figure 5.3: Definition of incidence track angles, (a) track with a positive (b) zero and (c) negative incidence angle. The Lorentz angle is 0.48 mrad on the negative side (d). (drawing not to scale). The magnetic field direction is perpendicular to the x, y plane. The electric field is parallel to the line (b), and directed in the track direction for the Outer an Closer layer and opposite for the Inner layer.



For large incidence angles there is a depletion in this region. The *eta* distribution therefore shows a non-uniformity in the coordinate reconstruction for varying incidence angle. The hit position should therefore be corected as a function of η and incidence angle. This was not done in the standard DELPHI coordinate reconstruction.

Since the strips on the microstrip detectors are nominally parallel to the beam direction no z information is available from the Vertex Detector. Even though the strips nominally are all parallel to the z axis small deviation in the order of 10-20 μm in $R\phi$ positions over the length of one microstrip counter due to misalignments exists. Knowledge about the z coordinate of an extrapolated track is therefore crucial to reconstruct the $R\phi$ coordinate with the best precision. The uncertainty on an individual Microvertex Detector point is therefore larger when the z information is missing. This leads to an extrapolation uncertainty based on the on the Microvertex Detector alone of around 400 μm , see also sections 5.5 and 6.10.

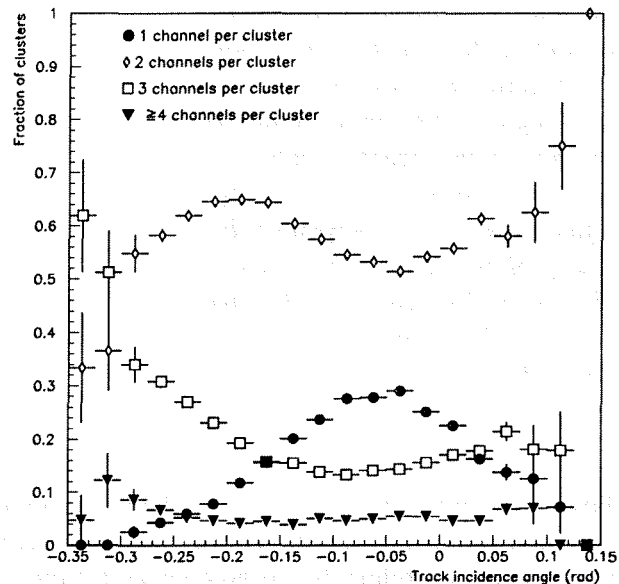
5.2 The Effect of the Magnetic Field on the Ionization Charge Clusters

The magnetic field of DELPHI will cause a drift of the charges perpendicular to the electric and magnetic fields in the silicon.

This drift can be accounted for by an overall shift of the silicon counters along the direction perpendicular to the magnetic field. The modules of the inner and outer layer is mounted in such a way as to minimize this effect. The drift direction is such that for the largest angled tracks the drift direction is in the same direction as the track angle, see figure 5.3 for definitions of the angles, thereby reducing the effect. The Closer layer is however mounted such that the Lorentz force leads to a widening of the charge distribution for tracks passing at positive angles to the counter.

The magnitude of the drift is found by measuring the incident angle that gives the smallest charge spread, also called the Lorentz angle. The Lorentz angle can be found by making histograms of the number of clusters with 1, 2, 3 or more channels as a function of angle, α_i , in the x, y plane between the track and the silicon counter, se figure 5.4. The cluster size should widen for tracks with a large angle. The minimum angle should be displaced from zero towards negative values. The displacement of the centroid, Δx of the charge collected on the diode strips is then simply given by: $\Delta x = \sin(\alpha_i)d_{\text{Si}}$ where d_{Si} is the detector thickness. In figure 5.4 the minimum number of two-channel cluster and the maximum number of one-channel clusters

Figure 5.4: *Relative number of clusters for various cluster-sizes as a function of incident angle of the track onto the silicon counter. Because of the magnetic field, the incidence angle giving the largest fraction of clusters with only one strip is offset from zero, from [74]*



occur at an incidence angle of 0.048 rad

5.3 Microvertex Detector Track Association

The track finding in the DELPHI standard analysis is first done without the Microvertex Detector. Only at the second stage are the tracks extrapolated to the Microvertex Detector and associated with the right cluster and the included in the track fit.

The task of assigning clusters to tracks would be straight forward had the extrapolation precision been accurate enough. This is not the case and residuals from the track extrapolation have a spread of several hundred micrometer with tails extending to the millimeter region.

High track density in jets from hadronic decays and 3 particle decays of τ leptons also makes the task difficult. It is common to find tracks separated by less than one millimeter at the Microvertex Detector for this type of event.

The track association procedure starts by defining a window around a track extrapolated to the Microvertex Detector. The size of this window is determined from the errors on the track, has typically a full width of two millimeters. For each cluster found within the window the track is extrapolated to the next (Inner) layer of the Microvertex Detector. The window size here is determined from the precision of the angle of the track on the outer surface, and for low momentum tracks on the expected amount of multiple scattering, typical window full width is half a millimeter. If a cluster is found, the track is forced through the two clusters and extrapolated to the inner-most layer. At this stage the errors from the external tracks are almost eliminated. The third cluster can thus be required to lie within a very narrow window with a full width of one to two hundred micrometer. The algorithm is improved by first considering the tracks with the smallest errors from the track fit. The not so good tracks are then considered when most of the clusters already have been associated. A second stage recovers tracks that are off by more than one millimeter by redoing the procedure with much looser cuts in the first and second layers.

This procedure with tighter and tighter cuts removes most of the ambiguities in the track to cluster association

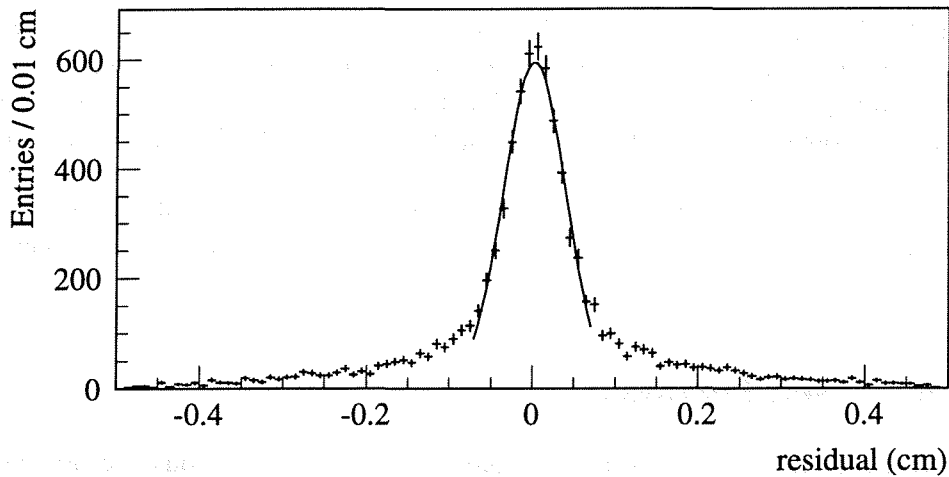


Figure 5.5: *Residuals between hits in the Microvertex Detector and reconstructed tracks. The tracks are extrapolated to the surface of the vertex detector and the distance to the reconstructed charge cluster is measured. The tracks have been associated to hits as described in the text. The Microvertex Detector hits have not been included in the track fit. We observe very long tails in the distribution, the curve is a gaussian fit to the central peak to further visualize the tails. The cut for a track to be associated corresponds to the histogram boundaries.*

5.4 Alignment Using Particle Tracks

The precise three dimensional survey of the detector, combined with the microscope measurements proved to be an excellent starting point for the further alignment of the detector using particle tracks.

This is done in a two step procedure. First the two half shells are aligned relative to each other and to the rest of DELPHI to a precision of $10 \mu\text{m}$. Thereafter the positions of the counters are improved using a minimization procedure essentially internal to the micro Microvertex Detector.

For the external alignment 2000 muon pairs with hits in both the Microvertex Detector and the Outer Detector were used, with the Outer detector defining the DELPHI coordinate system. The muons are produced each with the beam momentum, in one point and directed back to back; viewed in the $R\phi$ plane the muons describe an arc of a circle, ignoring initial and final state radiative effects. This circle is fitted through the hits in the outer detector using the curvature calculated from the beam energy and the polar angle of the tracks. The residuals between the Vertex Detector hits and circle are minimized by considering translations in the x and y planes and 3 rotations. The orientation can be further improved by using the directional information of the tracks from the Outer Detector which determines the direction of the muon at the Microvertex Detector to an accuracy of about 0.1 mrad. After this first step the position of each shell is known to $10 \mu\text{m}$ and each counter to $20 \mu\text{m}$ in the Microvertex Detector coordinate system.

Thereafter the individual counters were aligned using the same muon tracks. A least squares fit was done for each muon pair, with the error on the outer detector point set at $300 \mu\text{m}$ and of the Microvertex Detector points set at $8 \mu\text{m}$. The residuals of the hits to the track were minimized by considering a translation in the plane of each counter normal to the z axis, approximating a $R\phi$ shift, a translation normal to the plane, approximating an R shift, and a

rotation of each counter around the normal to its plane.

A second method used tracks from multi-hadronic events. In each event all tracks with hits in each layer of the Microvertex Detector with a momentum component transverse to the beam direction greater than 4 GeV/c were considered. The tracks were extrapolated to the interaction region and a common vertex was found with a chi-squared probability, $P(\chi^2)$. A requirement on $P(\chi^2)$ was made at 1% eliminating events with badly measured tracks and secondary vertices. Each track in each event passing this requirements are re-fitted using the Microvertex Detector hits and the vertex constraint. The same shifts and rotations as described above is then used in the minimization of the residuals.

5.5 Muon Missed Distance

For this study tracks from Z^0 decaying to two muons were used. By reconstructing each track and finding the shortest distance in x, y plane between the two tracks at some reference point close to the production point we can obtain a measure of the impact parameter resolution of the detector for the particles with the highest momentum. The reference point was taken to be the position of the beam as determined using hadronic tracks. This is a very powerful method, but we are limited by the small number of tracks.

The muons were identified by demanding at transverse momentum of the candidate particle above 15 GeV/c, at least one hit in at least one muon chamber layer and that the deposited energy in the electromagnetic calorimeter was below 1.5 GeV/c² or below 15 GeV/c² in the hadron calorimeter. The impact parameters of the muon tracks had to be below 0.4 cm in the x, y plane and 4 cm along the z axis and the angle between the tracks had to be $180 \pm 10^\circ$ in space and be off different charge. The measured momentum of the muon tracks were required to be 45 ± 5 GeV/c.

In addition the muon track had to have at least 3 hits of which 2 were in different layers of the detector. If there were two and only two tracks satisfying these criteria, an event of the type $Z^0 \rightarrow \mu^+ \mu^-$ was considered to be found.

The distance in the x, y plane between those two tracks, is then defined as the difference in impact parameter of the two tracks with respect to the beam position. The impact parameter is defined as the distance of closest approach of the track circle to the beam position in the x, y plane, with positive sign when the beam position lies outside the track circle, negative sign otherwise.

The impact parameters were found by a fit of each track to a circle determined by the three or more measured points in the Vertex Detector and a fixed, for each track, radius as measured by the rest of the DELPHI tracking system. The fit was rejected if $P(\chi^2)$ was larger than 1%.

Figure 5.5 shows a histogram of the muon missed distance. The distribution has an RMS of 32 μm , a fit of a gaussian to the histogram gives a σ of 30 μm . The measurements of the two muon tracks are independent of each other. The impact parameter error for each track is thus $(30/\sqrt{2} = 21)\mu\text{m}$.

From this measurement we can calculate the error on the reconstructed point on each silicon plane. The radius of curvature R_{xy} of a muon track traversing the Microvertex Detector is

$$\begin{aligned} R_{xy} &= \frac{p_{\text{beam}} \sin(\theta)}{10^{-13} c B} \\ &= 271.2 \text{ cm GeV}^{-1} c p_t \geq 8500 \text{ cm} \end{aligned} \quad (5.3)$$

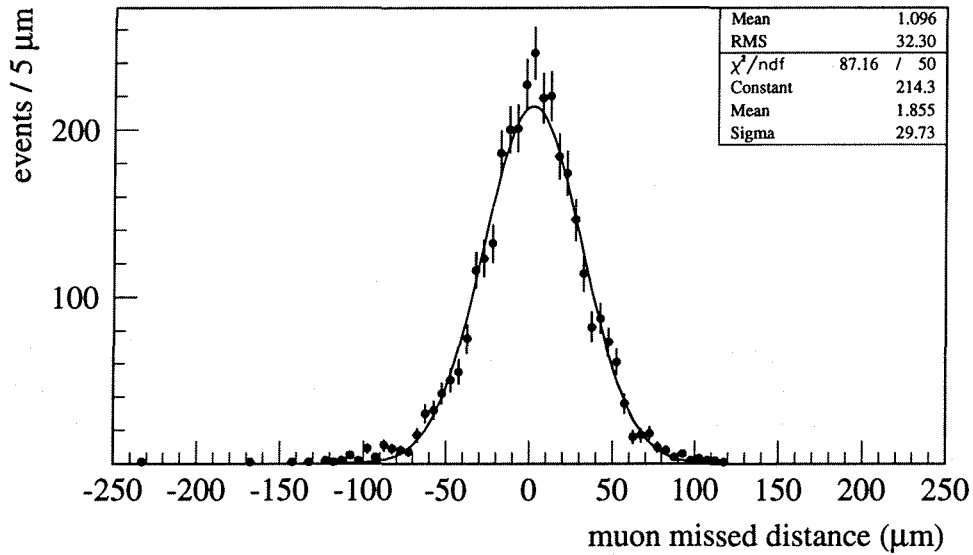


Figure 5.6: Muon missed distance. The σ of the gaussian fit is $30 \mu\text{m}$. The muon missed distance is defined in the text

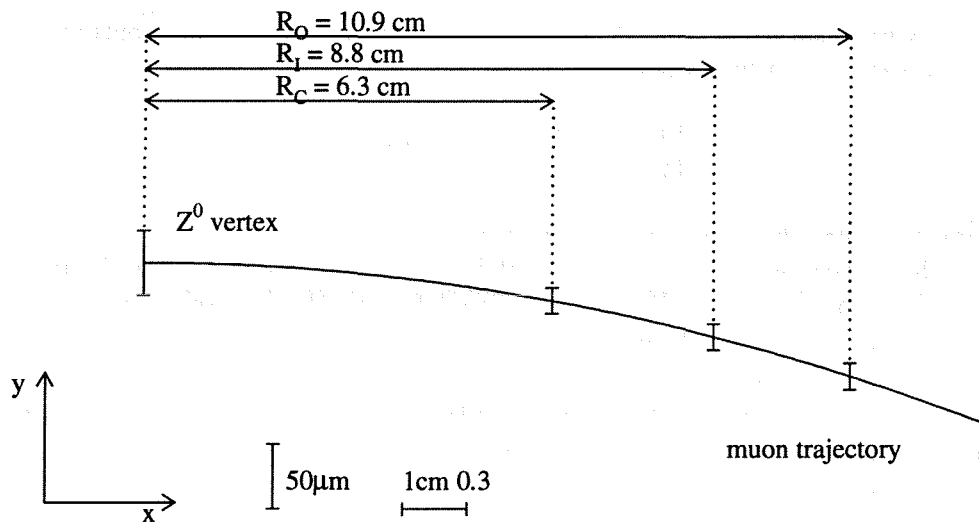


Figure 5.7: Coordinate system used in evaluation of muon missed distance. The drawing shows the location of the three silicon planes and a muon track. The muon missed distance is shown as an error bar at $x = 0$ and $y = R_{xy} \pm 1\sigma_\mu$. Points where the track crosses the silicon layers are shown as crosses with error bars at $\pm 1\sigma_{S_i}$. Notice that the scale is enlarged by a factor of about 250 in the y direction both for the error bars and the curvature.

where $c = 2.998 \times 10^{10}$ cm/s, $B = 1.23$ T is the magnetic field in DELPHI and $p_t = p_{\text{beam}} \sin(\theta)$ is the momentum component transverse to the beam direction. Inside the acceptance of the Microvertex Detector the maximum change of direction of a muon track from the production point to the Microvertex Detector is

$$\Delta\phi \leq R_{\text{VD}}/R_{\text{track}} \simeq 9/8500 \simeq 1 \text{ mrad} \quad (5.4)$$

The trajectory of the particle is given by:

$$y' = R_{xy} - (R_{xy}^2 - x^2)^{1/2} \simeq \frac{1}{2R_{xy}}x^2 \quad (5.5)$$

where the last term is a second order taylor expansion around $x = 0$. For $x = 10$ cm and $R_{xy} = 8500$ cm this approximation is correct to better than 10^{-11} . Using this approximation the contribution to the muon missed distance, σ_μ from the extrapolation uncertainty, σ_{ext} and the uncertainty on the momentum measurement, $\sigma_{\frac{1}{R_{xy}}}$ is:

$$\sigma_\mu^2 = \sigma_{\text{ext}}^2 + \left[\frac{1}{2}x^2\sigma_{\frac{1}{R_{xy}}} \right]^2 + cov \quad (5.6)$$

where cov is the covariance terms and

$$\sigma_{\frac{1}{R_{xy}}} = \frac{1}{Kp_t^2}\sigma_{p_t} = \frac{1}{Kp_t} \frac{\sigma_{p_t}}{p_t} \quad (5.7)$$

is the contribution from the momentum measurement, where $K = 271.2$ cm GeV ^{-1}c and $\sigma_{p_t}/p_t = 0.035$ is measured for muons. Inserting the numbers we get, $\sigma_{\frac{1}{R_{xy}}} \leq 4.2 \times 10^{-6}$ cm $^{-1}$, when $p_t \geq 45$ GeV/c $\sin 45^\circ = 31$ GeV/c. The contribution from the momentum measurement to the muon missed distance is then:

$$\left[\frac{1}{2}x^2\sigma_{\frac{1}{R_{xy}}} \right]^2 = (2.0 \times 10^{-4} \text{ cm})^2 \quad (5.8)$$

The covariance terms are as well in the same order and can be ignored.

It is therefore reasonable to assume no contribution to the muon missed distance from error in the momentum measurement. We are therefore left with the first term only: $\sigma_{\text{ext}} = \sigma_\mu$. as a contribution to the muon missed distance.

To find the contribution to the muon missed distance from the error in the location of the reconstructed charge clusters we therefore calculate as if the trajectories of the muons were straight lines: $y(x) = A_1 + A_2x$ When A_1 and A_2 are uncorrelated the variance, σ_y^2 , on the extrapolated track is given by

$$\sigma_y^2 = \left(\frac{\partial y}{\partial A_1} \right)^2 \sigma_{A_1}^2 + \left(\frac{\partial y}{\partial A_2} \right)^2 \sigma_{A_2}^2 = \sigma_{A_1}^2 + x^2 \sigma_{A_2}^2 = \sigma_\mu \quad (5.9)$$

Under this assumption $\sigma_{A_1}^2$ and $\sigma_{A_2}^2$ are given by the diagonal elements of the covariance matrix of a linear fit to a straight line. We assume equal variance, σ_{S_i} for all the measured points, the covariance matrix is then

$$\begin{pmatrix} V_{11} & V_{12} \\ V_{21} & V_{22} \end{pmatrix} = \frac{\sigma_{S_i}^2}{D} \begin{pmatrix} S_{xx} & -S_x \\ -S_x & S_1 \end{pmatrix} \quad (5.10)$$

$$\begin{aligned}
D &= N \sum_{i=1}^N x_i^2 - (\sum_{i=1}^N x_i)^2 \\
S_x &= \sum_{i=1}^N x_i \\
S_{xx} &= \sum_{i=1}^N x_i^2 \\
S_1 &= \sum_{i=1}^N i = N
\end{aligned} \tag{5.11}$$

where the x_i is the first coordinate of each measurement. In our case $N = 3$, $x_1 = R_C = 6.3\text{cm}$, $x_2 = R_I = 8.8\text{cm}$ and $x_3 = R_O = 10.9\text{cm}$. We want the A_1 and A_2 to be uncorrelated with a diagonal covariance matrix. We therefore translate the coordinate system along the x-axis such that $\bar{x} = \frac{1}{N} \sum x_i = 0$ The covariance matrix is then:

$$\begin{pmatrix} V_{11} & V_{12} \\ V_{21} & V_{22} \end{pmatrix} = \sigma_{S_i}^2 \begin{pmatrix} 0.33 & 0 \\ 0 & 0.09 \end{pmatrix} \tag{5.12}$$

The variance at x is:

$$\sigma_y^2 = \sigma_{S_i}^2 (V_{11} - 2xV_{12} + x^2V_{22}) = \sigma_{A_1}^2 + x^2\sigma_{A_2}^2 = \sigma_\mu^2 \tag{5.13}$$

After the coordinate transformation nominal muon production point is at $x = -8.7\text{cm}$ with measured variance σ_μ^2 . The variance of the measured points in the silicon planes is thus

$$\sigma_{S_i}^2 = \frac{\sigma_\mu^2}{(V_{11} + x^2V_{22})} \tag{5.14}$$

Substituting the numbers we get a resolution of the detector counters of $7.9 \mu\text{m}$. Multiple Coloumb scattering has not explicitly been taken into account in this calculation. This figure includes therefore the contribution from multiple Coulomb scattering in the beam tube and the silicon planes.

5.6 Track Resolution on the Silicon Planes

In this study tracks from multihadronic events with a transverse momentum, p_t , with respect to the beam direction larger than 4 GeV were used. The momentum cut were chosen to reduce the effect of multiple Coloumb scattering and at the same time retain a reasonable large number of tracks.

The RMS projected scattering angle, θ_0 , from multiple Coulomb scattering is given by [9]:

$$\theta_0 = \frac{0.013\text{GeV}}{\beta c p} Z \sqrt{x/X_0} [(1 + 0.038 \ln(x/X_0))] \tag{5.15}$$

where β , p , and Z are the velocity, the momentum and the charge number of the particle respectively, c the speed of light and x/X_0 length of material traversed by the particle divided by the radiation length of the material. For silicon $X_0 = 9.36 \text{ cm}$.

Substituting $p = p_t/\sin(\theta)$, θ is the polar angle of the track, and $x = d_{s,i} \sin(\theta)$, $d_{s,i} = 285 \mu\text{m}$ is the thickness of the silicon, we get

$$\begin{aligned}
\theta_0 &= \frac{0.013\text{GeV}}{\beta c p_t} z \sqrt{\sin(\theta)} \sqrt{x/X_0} [1 + 0.038 \ln(x/X_0)] \\
&\simeq 0.034 \sqrt{\sin(\theta)} \times 0.055
\end{aligned} \tag{5.16}$$

The *maximum* RMS angular deflection due to multiple Coloumb scattering is thus $\sim 0.2 \text{ mrad}$ with this momentum cut and is ignored.

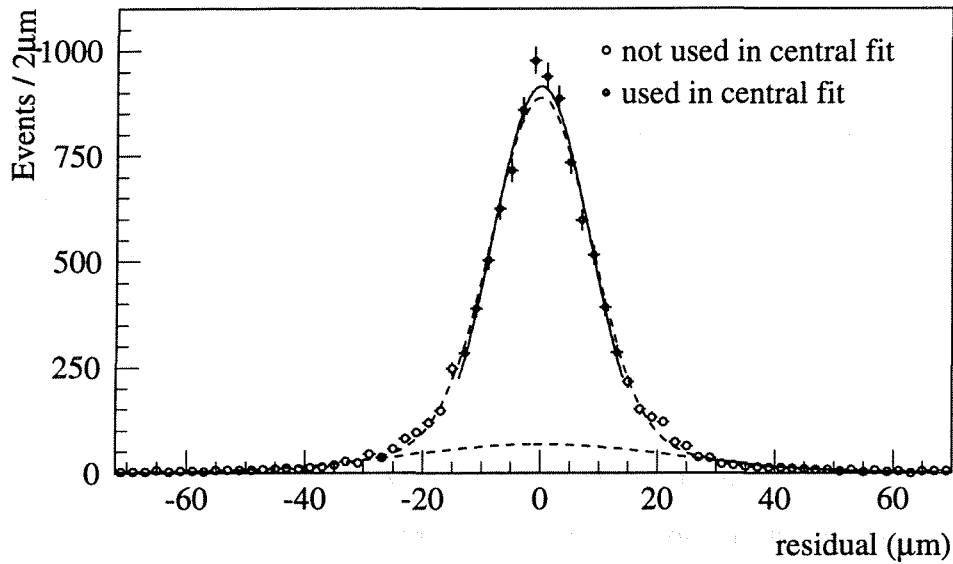


Figure 5.8: *Distribution of track residuals in the Inner Layer, The RMS of the distribution is $14.0 \mu\text{m}$. The continuous line is a fit to a gaussian with $\sigma = 8.4 \pm 0.13 \mu\text{m}$ of the central peak, while the punctuated lines are a fits to two gaussian distributions with widths of $(8.4 \pm 0.4) \mu\text{m}$, and $(22.9 \pm 4) \mu\text{m}$, containing respectively 92% and 8% of the full distribution.*

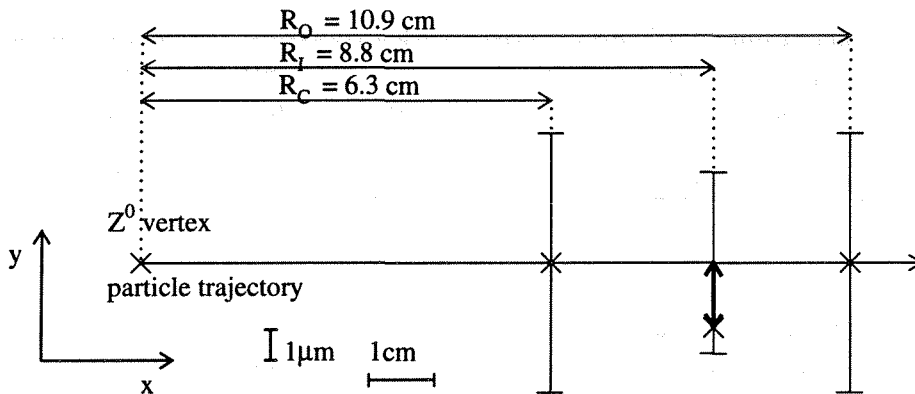


Figure 5.9: *Coordinate system used in the evaluation of detector resolution. The mean radii of the Closer, R_C , Inner, R_C , and Outer, R_C , layers are shown. The reconstructed position of the ionization charge are indicated as crosses. The error bars shows the error on these positions in the silicon plane. For the Inner layer the error bar corresponds to the error on the extrapolation from the Outer and Closer layer. Note that the scale in y direction is about 2000 times the scale in x direction.*

The tracks were reconstructed as the muon tracks, but excluding any hits in the Inner layer. The distance of closest approach from the track circle to the reconstructed hit in the silicon was measured, with the sign as defined above. Figure 5.8 shows the distance of closest approach for all the sectors of the Inner Layer.

When we ignore multiple Coloumb scattering there are three contributions to the observed distribution σ_{obs}

$$\sigma_{obs}^2 = \sigma_{ext}^2 + \sigma_i^2 + \sigma_a^2 = \sigma_{ext}^2 + \sigma_{si}^2 \quad (5.17)$$

Where σ_{exp} is the error on the extrapolation, σ_a is the error from misalignment and σ_i is the intrinsic precision of the silicon detector, Since we can not distinguish between the intrinsic precision and misalignment we combine those into an error from the silicon detector: σ_{si} .

The transverse momentum of the tracks are in this case distributed in the range from 4 GeV to beam momentum. As is explained above the contribution to error on the extrapolation from the momentum measurement is negligible. We therefore use a linear approximation to the track. In the absence of multiple Coloumb scattering there is no reason to expect the resolution of the three layers to be different. The error on the extrapolation error is thus given by:

$$\sigma_{ext}^2 = \left(\frac{R_I}{R_C}\right)^2 \sigma_{si}^2 + \left[1 - \left(\frac{R_I}{R_C}\right) + \left(\frac{R_I}{R_C}\right)^2\right] \sigma_{si}^2 \quad (5.18)$$

Where $R_C = 6.3$ cm, $R_I = 8.8$ cm, $R_O = 10.9$ cm is the average radius of the Closer, Inner and Outer layer respectively. From this we get the error on the extrapolation: $\sigma_{ext} = 0.5\sigma_{si}$

From equation 5.17 the precision of the silicon is then :

$$\sigma_{obs}^2 = \sigma_{si}^2 + 0.5\sigma_{si}^2 = 1.5\sigma_{si}^2 \quad (5.19)$$

The RMS of the observed distribution is $14.0\mu\text{m}$. The distribution has however large tails, it has become custom to fit a gaussian to the central peak of the distribution and quote the σ of the fitted gaussian as the resolution of the counters. Because of the track extrapolation procedure explained above, the variance of the gaussian is divided by $\sqrt{1.5}$ to get the resolution of the silicon detector: $8.4\mu\text{m}/\sqrt{1.5} = 6.9\mu\text{m}$. An alternative is to fit the sum of two gaussian distributions to the histogram, indicated as dashed lines in figure 5.8. For the central peak, $\sigma_1 = (8.4 \pm 0.4)\mu\text{m}$, for 92% of the events and for the tails $\sigma_2 = (22.9 \pm 4)\mu\text{m}$, for 8% respectively. The tails in the distribution are mainly due to ionization charge clusters with unusual shapes and from misalignment which have not been resolved. It is therefore reasonable to quote a resolution of the Microvertex Detector as 92% of the charge clusters have a resolution better or equal to $7\mu\text{m}$, with the remaining 8% having a resolution of $16\mu\text{m}$. These numbers are consistent with the numbers found using the muon missed distance.

When compared with the resolution given by the analysis of the muon missed distance, this smallest number is considerably lower. This is because the contribution from the tails was excluded. In the muon missed analysis. The last analysis tells us the best possible resolution, while the muon missed distance measures the resolution to expect from the detector in measurement of impact parameters of high momentum particles.

These numbers are somewhat larger but consistent with the numbers published in [74]. This can be explained by small differences in track selection when making the distributions. In This analysis no requirements were put on the hit precision in the Closer and Outer layer in contrast to the procedure used in [74].

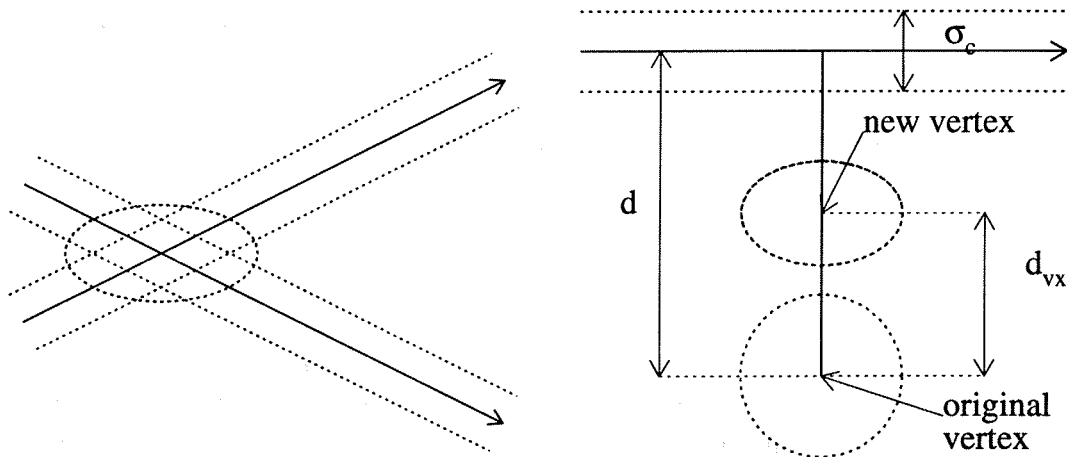


Figure 5.10: *Left: vertex error definition, the punctuated lines show the transverse track error, σ_c , the ellipsis indicate how the vertex error might look like. Right: Situation after the transformation of the coordinate system. The error of the original vertex is a unit circle, while the new vertex is found as a weighted mean on the line joining the point of closest approach to the track and the vertex. The new vertex gets its error scaled only transverse to the track and is drawn as an ellipsis.*

5.7 Vertex Reconstruction and Fit.

The approach in the selection of the b-hadron candidates described later was to find jets where every track has a large impact parameter and then look for a unique secondary vertex in those jets such that the tracks can be unambiguously assigned to either the primary or the secondary vertex. If there is only one such arrangement possible the event is accepted. Then the invariant mass of the charged decay products from the vertex is calculated. If the mass is sufficiently large, the vertex must be from a b-hadron decay. The method that were used both for primary and secondary vertex reconstruction is outlined in this section.

First a seed vertex is formed by finding the intersection between the track circles in the x, y plane of the two highest momentum tracks in the set of selected tracks. The error on this point is calculated using a linear approximation to the tracks in the vicinity of the intersection

$$y_1 = q_1 x + c_1 \quad (5.20)$$

$$y_2 = q_2 x + c_2$$

The intersection is in the linear approximation:

$$x = \frac{y - c_1}{q_1} = \frac{y - c_2}{q_2} \quad (5.21)$$

$$y = \frac{c_2 q_1 - c_1 q_2}{q_1 - q_2}$$

Only the transverse track error, $\sigma_c = \sigma_{\text{extrap}}$, as given by equation 5.33 of the tracks are considered. The error matrix, E , is then:

$$\begin{pmatrix} \sigma_{xx} & \sigma_{xy} \\ \sigma_{yx} & \sigma_{yy} \end{pmatrix} = \frac{1}{(q_1 - q_2)^2} \begin{pmatrix} \sigma_{c_1}^2 + \sigma_{c_2}^2 & (q_2 \sigma_{c_1})^2 + (q_1 \sigma_{c_2})^2 \\ (q_2 \sigma_{c_1})^2 + (q_1 \sigma_{c_2})^2 & (q_2 \sigma_{c_1})^2 + (q_1 \sigma_{c_2})^2 \end{pmatrix} \quad (5.22)$$

If the two circles do not intersect, the middle point of the shortest line joining the circles is used.

Thereafter the remaining tracks are added one by one to this vertex by using a linear approximation to the track in the vicinity of the vertex. A new reference frame is defined each time before the track is added where the error ellipsis of the vertex is a unit circle around origo:

$$\mathbf{M}^t \mathbf{E} \mathbf{M} = \mathbf{1} \quad (5.23)$$

where \mathbf{M}^t is the transpose of the transformation matrix, \mathbf{M} between the two coordinate systems:

$$\mathbf{M} = \begin{pmatrix} \cos \theta & \sin \theta \\ -\sin \theta & \cos \theta \end{pmatrix} \begin{pmatrix} 1/u \\ 1/v \end{pmatrix} - \begin{pmatrix} x_0 \\ y_0 \end{pmatrix} \quad (5.24)$$

where x_0, y_0 is the coordinates of the original vertex, θ is the angle of the ellipsis major axis and u, v is the length of the major and minor axes.

The linear track parameters and errors are transformed accordingly:

$$q' = \frac{m_{21} + qm_{22}}{m_{11} + qm_{12}} \quad (5.25)$$

$$c' = c(m_{22} - m_{12}q') \quad (5.26)$$

$$\sigma_{c'} = \sigma_c(m_{22} - m_{12}) \quad (5.27)$$

The distance, d' , between the track and the vertex, and the error on the distance, $\sigma_{d'}$ are:

$$d' = \frac{c'}{\sqrt{q'^2 + 1}} \quad (5.28)$$

$$\sigma_{d'}^2 = \frac{\sigma_{c'}^2}{1 + q'^2} \quad (5.29)$$

The new vertex and its error, σ_{vx} , is found at the distance d' as a weighted mean on the line joining the closest approach of the track to the vertex:

$$d'_{vx} = \frac{d'}{1 + \sigma_{d'}^2} \quad (5.30)$$

$$\sigma_{vx}^2 = \frac{1}{1 + 1/\sigma_{d'}^2} \quad (5.31)$$

A χ^2 is then formed in the new coordinate system:

$$\chi^2 = \frac{d'^2}{1 + \sigma_{d'}^2} \quad (5.32)$$

Where d' , 5.28, is the distance of closest approach, and $\sigma_{d'}$ is the error on the distance, 5.29, in the new coordinate system respectively.

Before the next track is added the new vertex and its errors are transformed back into the DELPHI reference frame and the procedure is repeated.

5.8 Calibration of Track extrapolation errors

The $R\phi$ component of the track extrapolations is used to decide which tracks belong to the primary vertex and which are coming from the decay of a B hadron. An accurate knowledge of the uncertainty on this extrapolation is therefore essential. In the sections 5.5 and 5.6 the resolution of the Microvertex Detector in the limit of no multiple Coulomb scattering were found.

In this section the extrapolation precision for particles of in the whole momentum range is found. The z coordinates are much less precise than $R\phi$, therefore the vertex reconstruction used only the $R\phi$ projection of the tracks.

There are two contributions to the extrapolation error, which are the intrinsic measurement resolution, σ_{asym} , and the multiple scattering, σ_{scatter} . The track extrapolation error, σ_{extrap} , was parameterized by:

$$\sigma_{\text{extrap}} = \left[\sigma_{\text{asym}}^2 + \left(\frac{\sigma_{\text{scatter}}}{p \sin^{3/2} \theta} \right)^2 \right]^{\frac{1}{2}} \quad (5.33)$$

To reduce systematic uncertainties σ_{extrap} was measured without reference to an external point and using the same tracks as are used in the analysis. In all jets with at least four tracks, the highest momentum three tracks and the lowest momentum three tracks were each used to form a vertex, and the χ^2 probability $P(\chi^2)$ that all three come from a common point was plotted in figure 5.11. This $P(\chi^2)$ depends upon the amount by which the tracks are not completely coincident and σ_{extrap} .

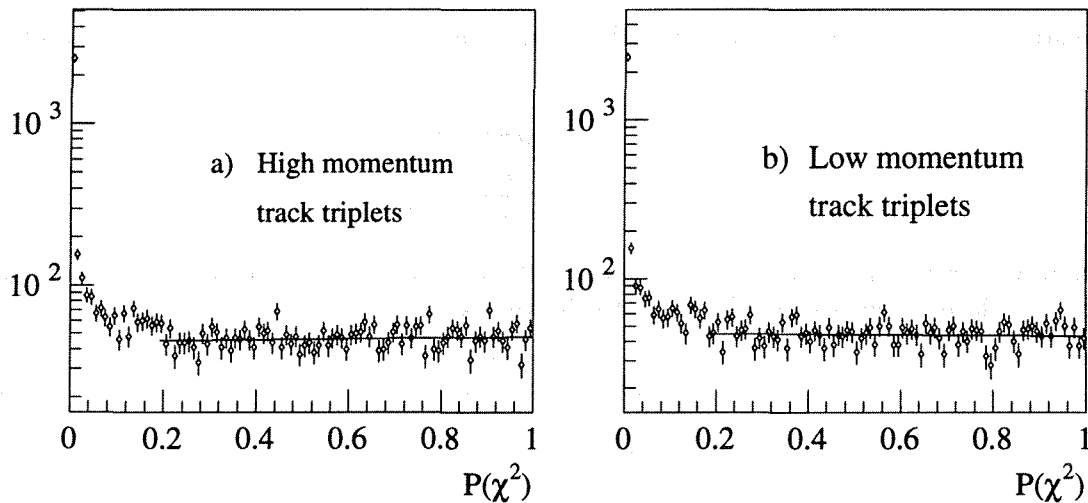


Figure 5.11: The $P(\chi^2)$ distributions for triplets of tracks making vertices, for both the highest momentum triplet, (a), and the lowest (b).

The spike at low probability in figure 5.11 corresponds to particles which do not come from a common vertex and the flat distribution for $P(\chi^2) > 0.2$ to well identified vertices. The two contributions to the uncertainty were varied iteratively until the required flat distribution was obtained for both the highest momentum triplet in the jet and the lowest. The high momentum distribution is more sensitive to the asymptotic uncertainty, and the low momentum distribution to the multiple scattering.

The contributions to the track extrapolation error were found to be:

$$\begin{aligned} \sigma_{\text{asym}} &= 30 \pm 3 \mu\text{m} \\ \sigma_{\text{scatter}} &= 70 \pm 4 \mu\text{m} \end{aligned} \quad (5.34)$$

which is compatible with the muon missed distance found in section 5.5.

Chapter 6

Event Reconstruction and Simulation

The recorded electronic signals from the detector have to be processed and turned into a more understandable form before any physics analysis can be performed. This generally involves tracking the charged particles through the detector, particle identification and calorimetry. The method implemented to track particles is described in [76,77], here a brief summary relevant for this analysis is given. No particle identification nor calorimetry have been used in the subsequent analysis and these subjects are therefore not covered. The track reconstruction in the Microvertex Detector is explained in chapter 5.

In the event reconstruction the DELPHI detector is split logically in polar angle into a barrel, two forward and very forward parts. Only the barrel track reconstruction is considered here.

The track reconstruction proceeds in a several steps:

Track Data, TD, reconstruction. Space points are reconstructed from the electronic signals using information from the geometric and calibration data bases.

Track Element, TE, reconstruction Track elements are reconstructed from the space points assuming an helix motion of the particles in the magnetic field of the detector.

Track building. The track elements are combined into tracks starting with a space point in the TPC as a 'pivot'. At this level ambiguities are allowed to occur, such that one track element can be a part of several tracks.

Track fit. In this final step the ambiguities are resolved by a χ^2 fit where the best track is selected.

For final physics analysis the track parameters at the point of closest approach to the origin, perigee, the unambiguous track elements and a minimum detector specific information are stored on magnetic tape. Because of the very low noise and the online zero suppression it is possible to store the complete event ADC data on these tapes.

6.1 Monte Carlo Simulation

The programs used to simulate events in DELPHI can be divided in two classes: The event generators and the programs used to trace the particles through the detector. The latter programs simulates as well the particle reactions with the material of the detector and the response of the

electronics, including noise. The output of the simulation is in the same format as the data. Ideally the simulation should be indistinguishable from data, but there will always be some residual differences.

To generate the hadronic decays, the LUND parton shower model [78, 79] implemented in the program package JETSET 7.2 [80] has been used. In this model the decay of the Z^0 and the subsequent production of hadrons proceed through three phases:

1. The hard scattering phase, which is treated perturbatively, during which parton showers develop in QCD processes such as quark bremsstrahlung, gluon bremsstrahlung and quark pair production.
2. Treats the soft non-perturbative processes according to the LUND string fragmentation model which transforms the multi-parton state created by the first phase into hadrons.
3. Resonances and short lived particles are allowed to decay into the final state particles, which corresponds to those available for observation.

For b and c-quarks the fragmentation is described by the Peterson probability density function [19]:

$$f(z) = A(\epsilon) \frac{z(1-z)^2}{[(z-1)^2 + \epsilon z]^2} \quad (6.1)$$

$$A^{-1} = \int_0^1 \frac{z(1-z)^2}{[(z-1)^2 + \epsilon z]^2} dz \quad (6.2)$$

Where z is the fraction of the quark momentum carried away by the hadron. The parameter ϵ determines the fraction of the available energy to be carried by the b-hadron, this is often referred to as the hardness of the fragmentation. At LEP the mean scaled energy, $\langle x_E \rangle^1$, for b-hadrons is measured by DELPHI to be 0.704 ± 0.011 [81]. This can be translated to $\epsilon = 0.008^{+0.005}_{-0.004}$. The value used in generating the events was $\epsilon = 0.003$.

Each particle that is produced, and that is long lived enough, is propagated through the material of the detector and allowed to decay according to its lifetime and branching ratios. The effects of multiple Coulomb scattering and energy loss via radiation are taken into account as well as photon conversions and nuclear interactions, [82, 83].

Charged particles leave hits in the various detectors. Drift times and pulse-heights are derived from known detector characteristics and are smeared with detector resolution functions. Random hits due to noise are added. The simulation takes into account known detector inefficiencies.

6.2 Simulation of the Microvertex Detector

When the charged particles are tracked through the Microvertex Detector charge is deposited with fluctuations according to a Landau distribution. In addition random hits due to noise are added and the cluster search and tagging software running in the readout processors are simulated [84].

Inefficiencies due to dead and intermittent readout chips were for the Microvertex Detector not included in the original simulation. These were therefore included later by removing hits in a random way with probabilities found from studies of the efficiency of the detector. The result of these studies exists as tables with efficiencies for each single chip. There are 16 tables

¹ $\langle x_E \rangle = \frac{\langle E_{\text{hadron}} \rangle}{E_{\text{beam}}}$ where E_{hadron} and E_{beam} is the energy of the b-hadron and the beam energy respectively

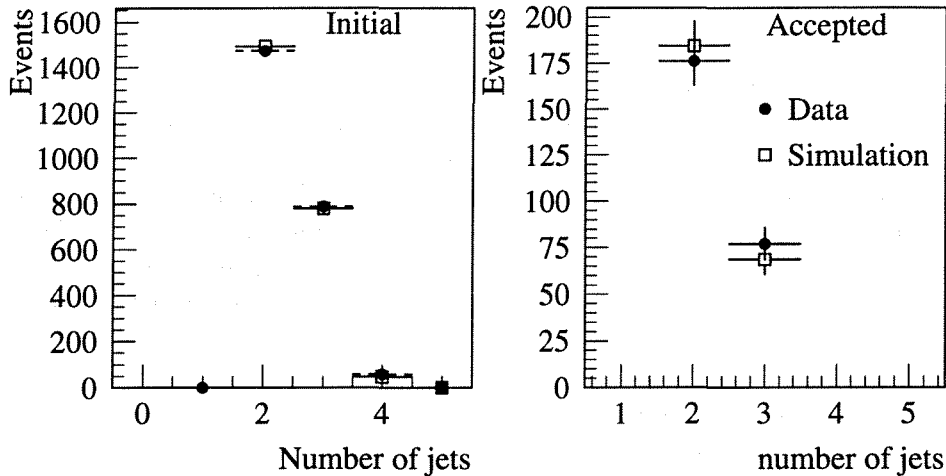


Figure 6.1: *Left: Distribution of jets found in the initial event sample. Right: Distribution of jets in the final event sample.*

corresponding to 16 periods of the 1991 running period. For the simulation all 16 tables are used, each in proportion to the number of tracks that were used to generate each table. This is believed to represent a reasonable approximation to the observed efficiency in the data.

6.3 Optimization of the Simulation Program

To ensure that the simulation is reasonably correct it is important to compare results from the simulation with measurements. Several variables based on event topologies exist for this purpose. Extensive studies have been performed to compare simulation and data. Distributions of several event shape variables from simulation and data are compared in [85]. An excellent agreement between the LUND Parton Shower model and the data is found. The parameters of the Monte Carlo generator were set to values such that the difference between the simulation and the data were minimized.

For the third phase, known branching fractions and lifetimes of the particles are used to control the decay of the particles. For particles with unknown or poorly known characteristics, estimates based on theoretical calculations are used.

Of special importance for this work is the lifetimes of the various b-hadrons. In the simulation the lifetimes were all set to 1.2 ps except for the Λ_b which got a lifetime of 1.3 ps. The values for the lifetimes of the B^0 and the B^+ are thus smaller in the simulation than what was found in the data.

6.4 Hadronic Event Selection

A standard event selection was used that ensured negligible contamination from events with tracks from collisions of the e^+e^- beams with residual gas in the vacuum chamber, 'beam gas events', and $\tau^+\tau^-$ events. Only charged particles measured in the tracking chambers with:

1. momentum above 0.1 GeV/c,
2. measured track length above 50 cm,

3. angle with the beam axis of more than 25° ,

were therefore used in this analysis.

The sum of the energies of these charged particles in each of the forward and backward hemispheres (with respect to the beam) was required to exceed 3 GeV, and the total energy had to be more than 15 GeV, assuming the pion mass for each particle. Furthermore it was required that there were 6 or more charged particles with momenta above 0.2 GeV/c in the event. Events passing these requirements were assumed to be multihadronic events. Only a negligible contamination of from beam-gas scattering and $\tau^+\tau^-$ events are left after this [86].

After the hadronic event selection, the JADE jet clustering algorithm [87] was applied to the charged particle tracks with a scaled invariant mass cut of 0.04. With this value 68% of the events were seen as di-jet events. Only events with three or less jets were used in the analysis, which reduced the chance of assigning the tracks from a b-hadron decay to more than one jet.

6.5 K^0 Identification

The charged particles from a K^0 decay would confuse an attempt to find a secondary vertex close to the interaction point. Therefore all pairs of charged particles were examined to see if they were consistent with coming from the decay of a K^0 .

For each pair of tracks to be considered the following requirements were applied:

1. The track curvature should be of opposite sign.
2. The tracks should have a minimum impact parameter of 0.20 cm for tracks from vertices at radius larger than 7 cm, (outside the Closer Layer), or 0.05 cm for vertices at radius less than 7 cm, but larger than 1 cm. This requirement ensures that the tracks do not originate from the primary vertex.
3. The two tracks should miss each other in z by less than 1 cm.
4. The invariant mass of the two tracks should be in the range 0.485 to 0.505 GeV assuming both tracks to be pions.
5. The tracks should cross each other in the $R\phi$ plane.

About 0.1 K^0 's per event was identified. The pions from the K^0 's were tagged and not considered in the rest of the analysis.

The low value of the K^0 mass reveals a systematic error in the track reconstruction. The deviation is however so small that it is not expected to have any impact on later requirements applied on the invariant mass of decay products from b-hadrons.

6.6 Converted Photon Identification

The electrons from converted photons would confuse the secondary vertex identification in a similar way as the decayed K^0 . An attempt to identify those and exclude the tracks from the subsequent analysis was therefore done.

The tracks from a converted photon emerge with no transverse momentum in respect to the photon direction. The tracks were therefore not required to cross each other in the $R\phi$ plane, instead a minimum distance requirement of 2 mm were used.

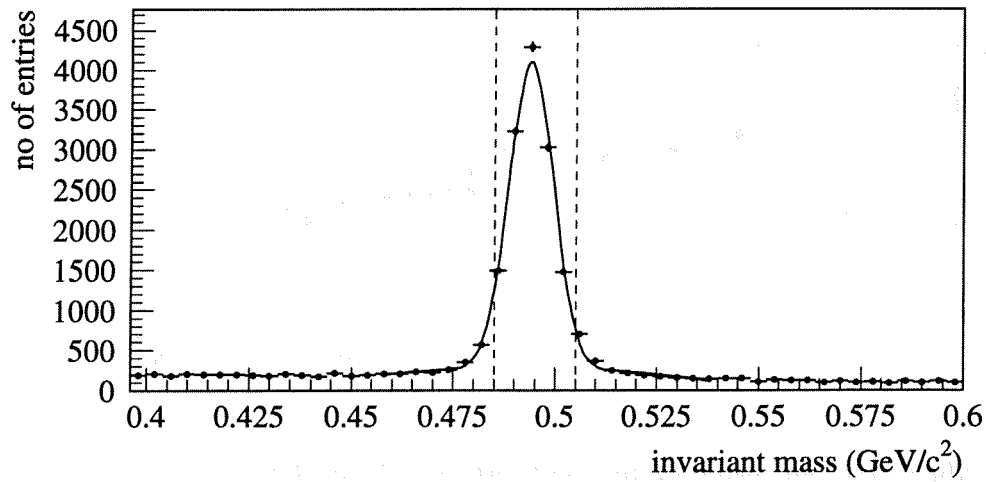


Figure 6.2: Mass distribution for tagged K^0 decays. The central value is: 494 ± 5 MeV. The value is about $3/4$ of a standard deviation lower than 497.7 MeV, the value given in [9]

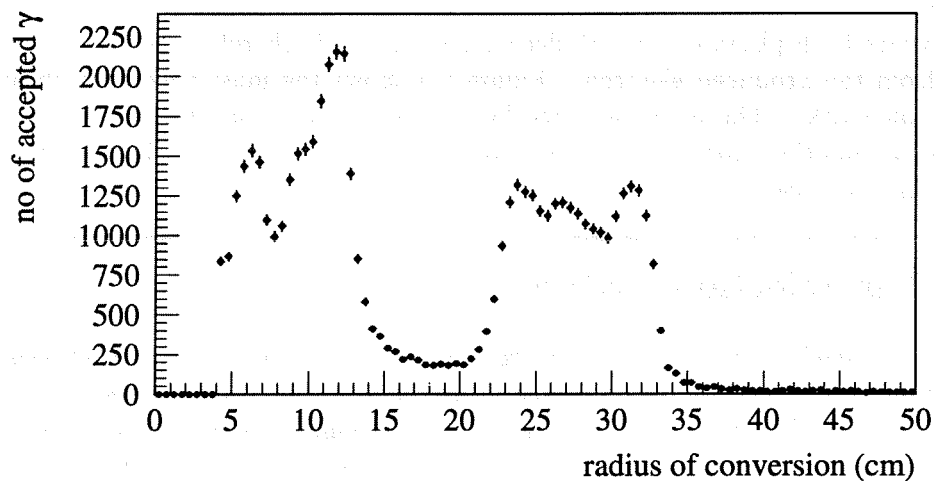


Figure 6.3: Photon conversions versus radius. The graph shows the radial positions of the vertices of converted photons. The number of vertices clearly reflects the distribution of material in the detector.

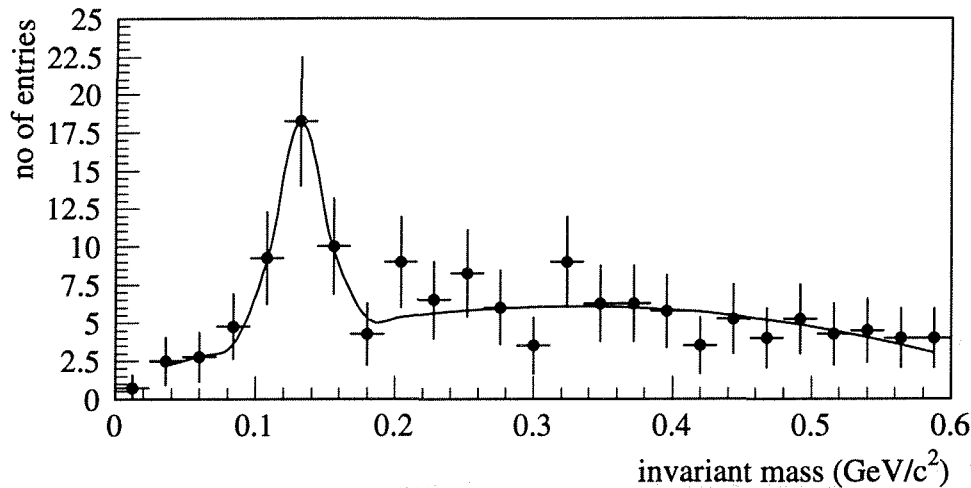


Figure 6.4: Mass spectrum obtained in events where both photons from π^0 decays convert into electron positron pairs. The peak is at 0.132 ± 0.004 GeV/c^2 close to the π^0 mass at 0.135 GeV/c^2 . The line is a fit to a gaussian plus a second order polynomial.

The probability for a photon to convert increases with the amount of material it has to traverse. The radial positions of the photon conversion vertices should therefore reflect the radial distribution of material. In figure 6.3 the number of conversions is histogrammed as a function of radial distance. The vacuum tube, $r = 5.5$ cm, the Microvertex Detector layers, at average radius $\langle r \rangle = 6.3, 8.8,$ and 10.9 cm, the trigger layers of the Inner Detector $r = 22$ to 30 cm and finally the wall of the Time Projection Chamber, $r \simeq 31$ cm are observed as sources of conversions.

In some events both photons from π^0 decays convert. It is therefore possible to reconstruct the π^0 mass from the produced electrons. Figure 6.4 shows the mass spectrum obtained using the four electron tracks. The peak close to the π^0 mass is taken as further evidence that the converted photon identification works as expected. A similar systematic shift of the peak value is found as in the K^0 case.

6.7 Further Selection Criteria

Each jet was examined in turn, and the charged particles within 40° of the jet axis and with momenta larger than 0.5 GeV/c were selected. There had to be at least three charged particles passing these cuts. Studies were done using Monte Carlo generated events to examine the effect of the charge reconstruction precision from these requirements. These studies were performed at the generator level, and served therefore only as an indicator of the intrinsic precision given a perfect detector.

From table 6.1 it is evident that a lower momentum requirement of 0.1 GeV/c reduces the charge reconstruction error. However, the track reconstruction efficiency and precision of DELPHI for those tracks are poor, and will dominate over this intrinsic contribution. The angular requirement was as well investigated, but the momentum requirement was seen as the dominant contributor to the charge reconstruction error.

All selected particles in the jet were required to have hits in at least two of the three layers

Requirement	b-hadron	Probability		
		Correct	± 1	± 2
$p > 0.1 \text{ GeV}/c$	B^0	0.98	0.02	–
	B^+	0.98	0.02	–
	B_s^0	0.98	0.02	–
	Λ_b	0.99	0.01	–
$p > 0.3 \text{ GeV}/c$	B^0	0.85	0.13	0.02
	B^+	0.85	0.14	0.01
	B_s^0	0.91	0.09	–
	Λ_b	0.86	0.12	0.02
$p > 0.5 \text{ GeV}/c$	B^0	0.70	0.27	0.03
	B^+	0.73	0.25	0.03
	B_s^0	0.72	0.24	0.04
	Λ_b	0.64	0.33	0.03
$\theta_{\text{jet}} < 45^\circ$	B^0	0.89	0.10	0.01
	B^+	0.93	0.07	–
	B_s^0	0.90	0.10	–
	Λ_b	0.88	0.11	0.01
$\theta_{\text{jet}} < 40^\circ$	B^0	0.86	0.12	0.02
	B^+	0.91	0.08	0.01
	B_s^0	0.86	0.13	0.01
	Λ_b	0.85	0.09	0.06

Table 6.1: For the different generated species the probabilities of reconstructing the charge correct, wrong by one or two units are tabulated for three values of the momentum requirement and two values of the angular requirement.

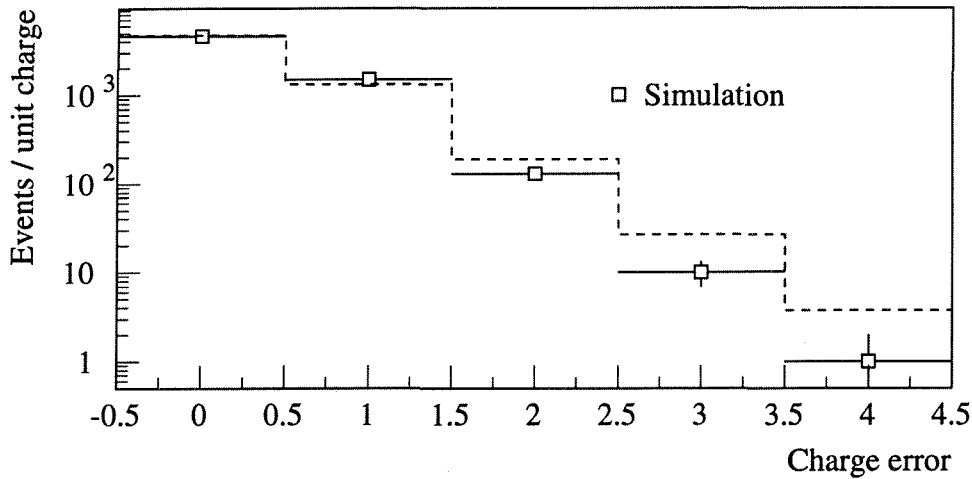


Figure 6.5: *The distribution shows the intrinsic charge reconstruction error after the angular and momentum requirements. This figure should be compared with figure 7.1 where detector effects are taken into account. The step function is a fit to equation 7.1*

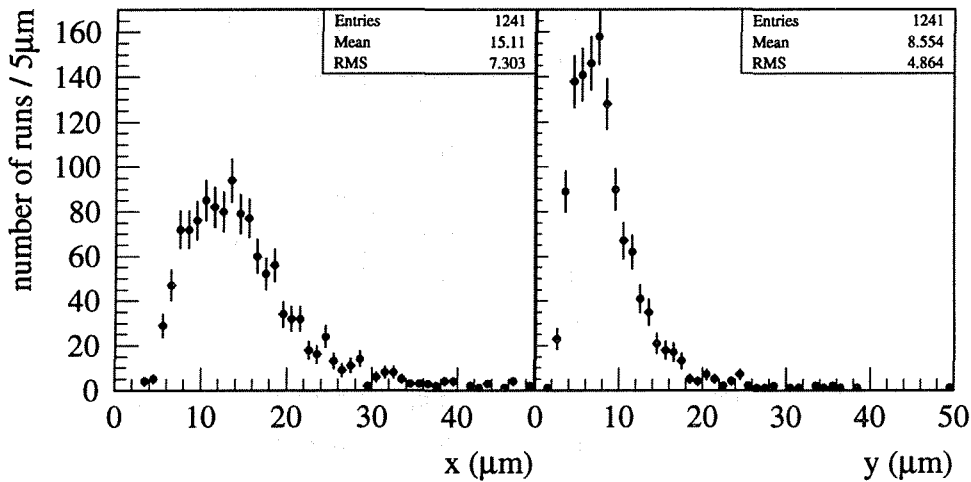


Figure 6.6: *Uncertainty of average interaction point found by a single vertex fit histogrammed for each run used in the analysis. Left: x direction, right: y direction.*

of the Microvertex Detector, in order to be considered to be reliably measured.

This requirement rejected about 80% of the jets, for a variety of reasons. Some particles were outside the angular acceptance of the Microvertex Detector, others came from decays or material interactions at larger radii, sometimes the track fitting was not performed correctly, and sometimes the Microvertex Detector was inefficient.

6.8 Secondary Vertex Identification

In order to determine the charge of the b-hadron the particles has to be assigned to the correct

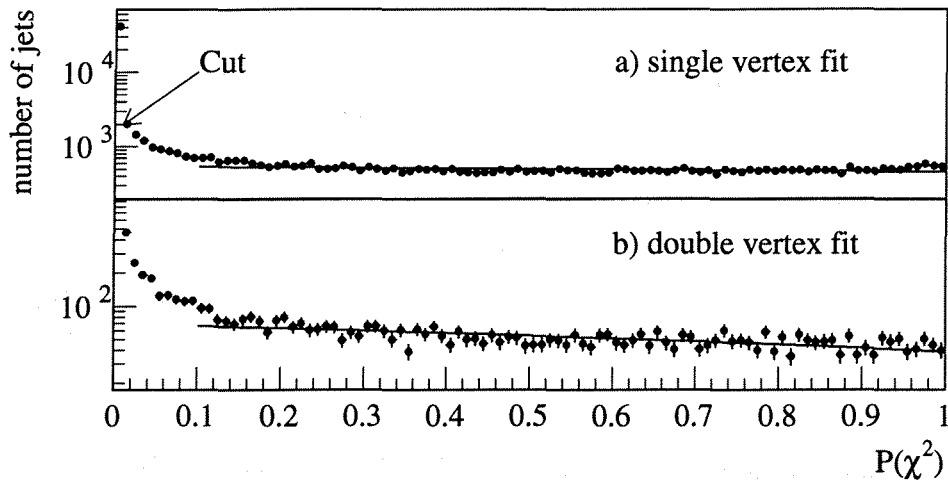


Figure 6.7: a): $P(\chi^2)$ distribution for the primary vertex fit. The flat region of the distribution is jets with a good primary vertex. The cut at $P(\chi^2) = 0.01$ is indicated. b): $P(\chi^2)$ distribution for the primary and secondary vertex fit. Jets were selected if there were only one vertex with a $P(\chi^2)$ greater than 0.01

vertex. A jet produced by a b-quark can contain several vertices: the primary interaction, b-quark decay, c-quark decay and perhaps a s-quark decay. To simplify the analysis the a was assumed to contain only the primary vertex and a single decay vertex. A consequence of this assumption is that a produced c-quark has to decay a short distance from the b decay point for the secondary vertex to be accepted. D mesons are a common decay product of b-hadrons. Small biases in the vertex positions might therefore be expected due to the different lifetimes of the D^0 and D^+ produced in the b-hadron decays. These effects are considered in chapters 7 and 8.

The consistency of the track extrapolations with the interaction point was used to distinguish the particles from a b-hadron decay from primary particles. A typical b-hadron decay includes some particles which can be clearly assigned to either the primary or the secondary vertex. Particles passing close to the b-hadron direction might however be ambiguous. The secondary vertex identification procedure was designed not to allow any such ambiguous particles.

The vertex identification was performed in the xy plane transverse to the beams only. The impact parameter² resolution in z direction along the beams is much poorer than the resolution in the xy plane. It would therefore not improve the vertex reconstruction precision to include the z coordinate.

The impact parameter of a track from a b-hadron decay does not depend on the momentum of the b-hadron for sufficiently large momenta. The track extrapolation precision is however better for high momentum tracks. There is therefore some bias towards high momentum b-hadrons. This bias is however existent in all b-hadron selection procedures which relies on the geometry of the tracks from the decaying b-hadron.

The secondary vertex identification proceeds in three steps:

Average interaction point determination. The average interaction point, also called beam-

²The impact parameter is defined as the distance from the primary interaction point to the point of closest approach of the extrapolated particle track.

Cut applied	Number of Jets		
	Data	Monte Carlo	Ratio
Initial Jet sample	554484	878285	0.63
More than two tracks	499178	793053	0.63
Each has two VD Hits	96659	187199	0.52
Not all from primary	41941	72147	0.58
Clear vertex structure	6528	11502	0.57

Table 6.2: *Effect of each cut in turn on the 232 103 data and 369 609 simulated selected hadronic events. The requirement of 2 VD hits on each track was not well modelled in the Monte Carlo, at least partly because the known inactive silicon modules were not allowed for.*

spot, is determined as a part of the standard DELPHI data analysis. Because of the relatively small sizes of the electron and positron bunches in LEP, typically $10 \mu\text{m}$ and $150 \mu\text{m}$ in vertical and horizontal direction respectively it makes sense to include this point in the vertex fit. In figure 6.6 the error on the average interaction point is histogrammed for the runs used in the analysis. Note that this error is not the beam size. The interaction point is thus defined as the average vertex position in a data taking run. The vertex positions for the individual events in the run were found by a single vertex fit to selected tracks of each run [88].

Primary vertex fit. All selected particles in a selected jet were first used to form a single vertex. Starting with the average interaction point the tracks were added one by one to form a vertex, as described in section 5.7, until all tracks were included. For each track added, the change in χ^2 was calculated.

If the jet contained a resolvable secondary vertex the χ^2 probability, $P(\chi^2)$, of the single vertex would be very small. Particles from the secondary vertex would have been wrongly included. The jet were therefore discarded if it had a $P(\chi^2)$ greater than 1%. Jets with possible secondary vertex is thus in the bin at small values in the histogram of figure 6.7 a).

Primary and secondary vertex fit Next the particles of the jet that contained a secondary vertex were divided into two groups. One group was used to form a primary vertex constrained by the average interaction point, the other to form a secondary vertex. All permutations of the tracks between the two groups were tried. Each permutation assigned all the particle tracks either to the primary or the secondary vertex, with at least two particles assigned to the secondary vertex. The combined $P(\chi^2)$ of the two vertices was required to exceed 1%. The number of degrees of freedom were two less than the number of tracks. If there was one and only one combination of tracks which satisfied this requirement, a satisfactory secondary vertex was considered to be found. Jets with more possible combinations were ambiguous and were rejected. Because no ambiguous tracks were allowed, all particles coming from the b-hadron decay were considered to have been identified. The $P(\chi^2)$ distribution is shown in figure 6.7 b). The distribution is not flat because of the finite decay lengths of the b-hadron decay products.

The effect of each of the requirements on the data sample is listed in table 6.2. Also shown are the results of a Monte Carlo simulation as described in section 6.1.

It can be seen that the requirement of 2 Microvertex Detector hits on each track is not well reproduced by the simulation. This probably reflects the difficulty of reproducing particle

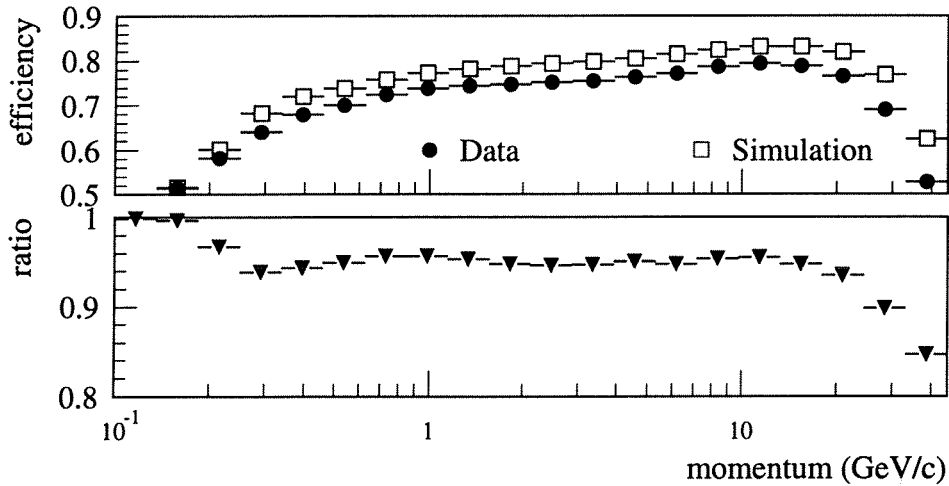


Figure 6.8: *Upper: The probability of having two or more hits on any track for data and simulation as a function of momentum. Lower The ratio between the data and the simulation. The momentum range is from 0.1 to 45 GeV/c. This graph has not been corrected for the Microvertex Detector acceptance and is therefore not showing the Microvertex Detector efficiency.*

re-interactions and track association. The probability of having two hits on any track is in the data 96-99% of that in the simulation for momentum below 20 GeV/c. For higher momentum tracks this probability was lower. Figure 6.8 shows the probability of having two hits on a track for data and for simulation. The simulation clearly overestimates the efficiency of the detector. The ratio plot shows that the discrepancy between the simulation and the data increases for higher momentum tracks.

6.9 Kinematic Requirements on the Secondary Vertices.

Assuming that all charged particles were pions, the invariant mass at the secondary vertex, M_{obs}^π , was calculated. Figure 6.9 shows the invariant mass distribution of the secondary vertices for the data and the simulated events. In this plot all further requirements, to be explained below, have been applied. The simulated events have been subdivided in different primary quark flavours. Because of the unobserved neutral particles and missing charged particles the observed mass is less than the true b-hadron mass. B-hadron decays were selected by requiring M_{obs}^π to be greater than 2.2 GeV. This criterium was based on the observed distribution of the different quark flavours in the simulated sample. There is no entries above the B^0 mass, 5.3 GeV/c², this is taken as evidence for the correct assignment of particles to vertices.

Because the lifetime of the b-hadrons in the simulation were defined considerably shorter than the observed lifetimes in the data, a lower efficiency was to be expected in the simulated sample. To compensate for this the simulated events were weighted to get an apparent lifetime of $\tau_r = 1.5$ ps. The weight is given by:

$$W = \frac{\tau_g}{\tau_r} \exp(t/\tau_g - t/\tau_r) \quad (6.3)$$

where τ_g is the generated lifetime, and t is the proper time of the decay. This procedure demonstrates the consistency of the selections if the mean B lifetimes is around 1.5 ps. The weighting is

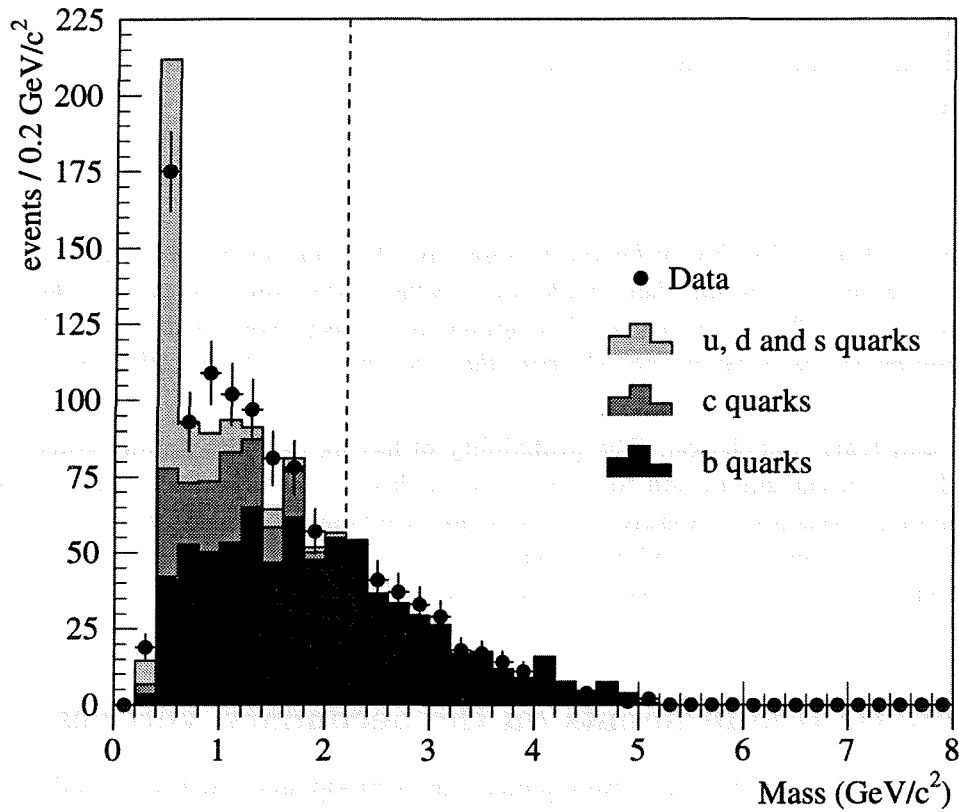


Figure 6.9: The reconstructed mass, M_{obs}^{π} , for Data and simulation. The simulation has been normalized to the same number of selected vertices as the Data and the simulated b-hadron events have been weighted as described in the text. The peak at about $0.5 \text{ GeV}/c^2$ is residual K^0 's that were not removed by the tagging procedure. All cuts have been applied except the mass cut, indicated by the dashed line.

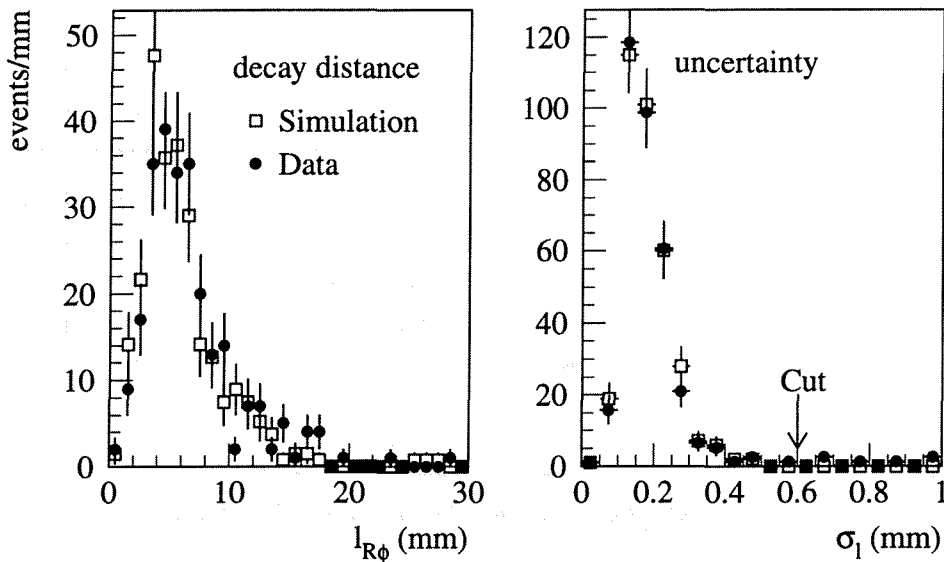


Figure 6.10: *Left: The b-hadron decay distance, $l_{R\phi}$, in the $R\phi$ plane of the accepted events. Right: Geometrical uncertainty on the decay distance σ_1 , the mean of the distribution is $190 \mu\text{m}$.*

however not used for the lifetime fits to the simulated sample as the statistical uncertainties from those fits become unreliable³. The two columns in table 6.3 labelled unweighted and weighted shows the number of events with and without this weighting in effect.

For the sample of jets with two vertices the distance $l_{R\phi}$ between the vertices was calculated. The uncertainty, σ_1 was derived from the vertex uncertainties with no kinematical constraints. The vertices were accepted if σ_1 was less than $600 \mu\text{m}$. This requirement removes configurations with nearly parallel tracks. The typical value of σ_1 was $190 \mu\text{m}$. Note that this criterion not the same as the one used to recognize the secondary vertex, which depends upon all the particles being assigned to either the primary or the secondary vertex. The requirement of no ambiguous tracks had as well the consequence that σ_1 in this analysis was less than the average error found in b-hadron decays.

The decay length distribution for the 253 events finally selected can be seen in figure 6.10.

Next the vector sum of the momenta of all the particles assigned to the secondary vertex was found, and the azimuthal angle, ϕ_{mom} , of the sum of the momenta obtained. Taking the azimuthal angle, ϕ_{geom} , of the vector joining the primary and secondary vertices, the difference $\delta\phi = \phi_{\text{mom}} - \phi_{\text{geom}}$ was computed. The momentum sum points close to the direction of the line of flight of the b-hadron. The distribution of $\delta\phi$ is therefore expected to be peaked at zero. Any difference between ϕ_{mom} and ϕ_{geom} is mainly due to the momentum carried away by unobserved neutral particles.

Furthermore the measurement of the primary and the secondary vertices gives an uncertainty, $\sigma_{\delta\phi}$, on $\delta\phi$ which decreases with increasing decay length. This uncertainty was parameterized from the Monte Carlo simulation as:

$$\sigma_{\delta\phi} = \sqrt{0.033^2 + (140\mu\text{m}/l_{R\phi})^2} \quad (6.4)$$

³If τ_r is fitted so that data and Monte Carlo match we extract $\tau_r = 1.56 \pm 0.06$

Selection	Number of Vertices				
	Data	Unweighted		weighted	
		Simulation	Ratio	Simulation	Ratio
Initial vertex sample	6528	11502	0.57	11881	0.55
Mass > 2.2 GeV/c ²	544	744	0.73	935	0.58
$\sigma_l < 600 \mu\text{m}$	514	706	0.73	898	0.57
$\delta\phi/\sigma_{\delta\phi} < 3$	455	612	0.74	804	0.57
Number of jets ≤ 3	451	601	0.75	791	0.57
$l_{R\phi} < 4 \text{ cm}$	436	568	0.77	758	0.58
$l_{R\phi}^{\text{min}} > 5\sigma_l$	428	566	0.76	756	0.57
$P(\chi^2) > 0.10$	265	360	0.74	496	0.53
No missing charged particles	253	341	0.74	473	0.53

Table 6.3: Cumulated effect of each selection applied to the vertices.

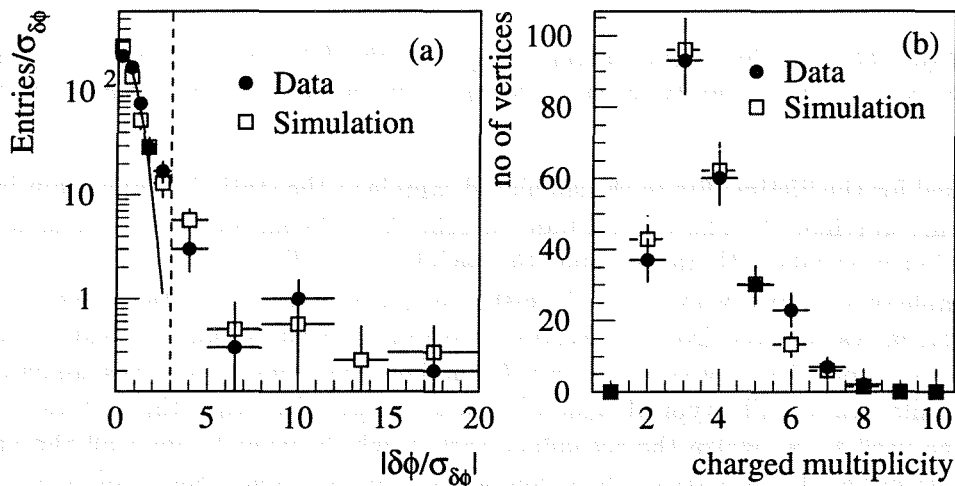


Figure 6.11: (a): Acollinearity distributions for the data and simulation. All selections have been applied except for that on $\delta\phi$ which is indicated by the dashed line. The line is a fit to a one-sided gaussian with mean 0 and $\sigma = 0.8$ (b): The multiplicity distribution of the accepted decay vertices for data and simulation.

where $l_{R\phi}$ is the distance between the primary and the secondary vertex in the $R\phi$ plane. Figure 6.11(a) shows $\delta\phi/\sigma_{\delta\phi}$. Only events with $\delta\phi/\sigma_{\delta\phi}$ less than three were accepted.

In addition the following criteria were applied:

1. The number of jets in the event was required to be three or less.
2. The decay length, $l_{R\phi}$ of the b-hadron vertex was required to be less than 4 cm, well inside the beam pipe. This rejected 3% of the events. It was also required that the minimum acceptable decay length, l^{excess} , (see section 7.4) was more than $5\sigma_l$.
3. the χ^2 probability of the accepted vertex combination was required to be greater than 10%,

while preserving the previous criterion that no other combination should have a probability above 1%.

Table 6.3 shows the effect the mass requirement and the other selections on the sample sizes.

The multiplicity of the accepted secondary vertices is shown in figure 6.11(b). The observed multiplicity is biased by the acceptance and the visible mass requirement and is not the true B meson multiplicity. The mean multiplicity found was 3.75 ± 0.08 for the data and 3.60 ± 0.10 for the Monte Carlo simulation.

6.10 Missing Charged Particle Search

The analysis needs the correct measurement of the charge of the decaying b-hadron. Frequently isolated, unassociated charge clusters were observed in the Microvertex Detector. When such hits are seen in both three layers and they line up pointing towards the interaction region, the probability is very small that these hits are due to noise. These hits are therefore most likely due to charge deposited by a particle coming from either the b-hadron decay or the primary vertex, but not associated to any particle track reconstructed by the main tracking chambers. In figure 6.12 at least three and possibly four such triplets of hits can be seen among several properly reconstructed tracks.

This phenomena is an indication of inefficiencies in the tracking system or interactions between the charged particles and material in the detector before the TPC. Jets which contained such hits were not considered to avoid introducing a possible error in the measured charge.

The Microvertex Detector was therefore searched for unassociated hits in all 3 layers forming a circle consistent with coming from the b-hadron decay point. Because no z information is available for this tracks their extrapolation precision is considerable poorer, about $400 \mu\text{m}$, see section 5.1. It was therefore not possible to use this information to recover the missing tracks.

A track was regarded as compatible with the b-hadron decay point if its distance of closest approach to that point was less than 1.0 mm. This candidate track had as well to be within 40° of the jet direction and have a p_T of more than $0.5 \text{ GeV}/c$. This procedure rejects 5% of the jets, as can be seen table 6.3.

6.11 Selected Sample Composition

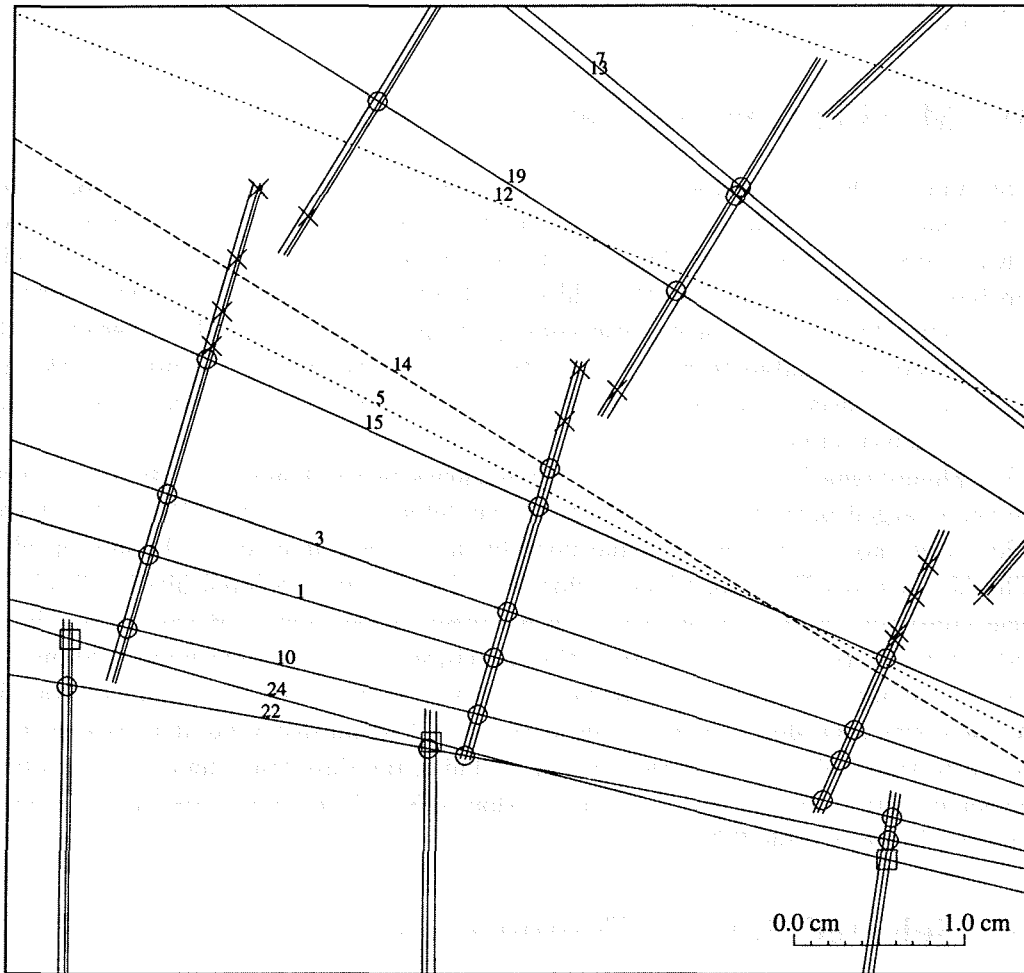
The composition of the simulated events passing all these cuts is listed in table 6.4. There is evidence of an enhancement of B^+ with respect to the other neutral b-hadron species. This could be due to a variety of different effects, notably the longer D^+ lifetime and the variation of efficiency with charged multiplicity, which peaks at three, and therefore favours charged b-hadrons.

Delphi Vertex Detector

Run 23465 event 2951

3/May/93 15:35

B



Itk	R	RPhi	Z	The	phiP	D0	P	Code	Itk	R	RPhi	Z	The	phiP	D0	P	Code
1	11.0	31.2	2.5	1.24	2.84	286	6.7	41	12	11.0	28.4	2.5	1.22	2.75	20155	-2.4	6
2	11.0	64.2	-6.5	1.94	5.94	10619	5.8	6	13	11.0	27.1	2.1	1.28	2.43	-1286	-2.3	6
3	11.0	30.8	2.6	1.25	2.80	171	-4.7	6	14	11.0	29.5	-2.3	1.23	2.57	-11402	2.1	41
4	11.0	66.4	-4.8	1.98	5.91	-13690	-4.1	41	15	11.0	30.0	2.5	1.26	2.71	-135	-2.0	41
5	11.0	29.8	3.0	1.20	2.65	-5093	3.9	41	16	11.0	66.1	-8.1	2.02	5.89	-14750	2.0	41
6	11.0	65.2	-8.7	2.16	5.93	-29	-3.6	41	17	11.0	61.8	-0.2	1.49	5.62	16	-1.6	41
7	11.0	27.1	2.7	1.22	2.43	-1214	-2.8	41	18	11.0	26.8	2.2	1.26	2.78	39264	-1.4	41
8	11.0	66.5	-2.5	1.67	6.05	149	2.8	41	19	11.0	28.1	3.8	1.14	2.56	-176	0.9	41
9	11.0	65.2	-7.1	2.14	6.04	13455	-2.8	41	20	11.0	59.2	8.4	0.87	5.36	-8397	0.8	41
10	11.0	31.7	2.0	1.29	2.89	324	2.5	6	21	11.0	50.8	11.3	0.73	4.70	211	0.5	41
11	11.0	65.6	-1.6	1.61	5.98	7	2.5	6	22	11.0	32.1	3.8	1.16	2.96	233	0.5	41

Figure 6.12: The crosses on the silicon planes between track 15 and 12 show unassociated charge clusters probably due to missing or badly reconstructed tracks. One of the possible tracks passes through the overlaps leaving 6 charge clusters. It is as well likely that the single hit in the Inner layer is associated to track 14 wrongly. Under this assumption there are 4 possible missing tracks in this jet. Because of the possible wrongly measurement of the vertex charge this jet was discarded. The dotted lines correspond to extrapolated unassociated tracks. The circles and squares indicates associated charge clusters in the two z hemispheres.

Type	Fraction of vertices selected	Initial fraction of b-hadrons
B ⁺	53±4%	40.1%
B ⁰	30±3%	40.1%
B _s ⁰	9±2%	11.9%
Λ _b	6±2%	7.9%
Background	2%	—

Table 6.4: *The composition of the selected event sample in the Monte Carlo simulation where all the b-hadron lifetimes are 1.2 ps except the Λ_b which is 1.3 ps. The small enhancement in Λ_b selection efficiency arising from its longer lifetime has been neglected throughout.*

Chapter 7

Lifetime Fitting Procedure

Two separate fit methods are presented. They differ in their treatment of the inefficiency in reconstructing secondary vertices for b-hadrons that decay at low proper times. The first method derives the probability of accepting a vertex as a function of the proper time, the acceptance, from the simulated event sample. The second method finds the acceptance for each event from the data. In each case an unbinned maximum likelihood fit is performed, with the charge and the proper time as input. The proper time is calculated from the measured decay distances and the momentum estimated for the b-hadron. The likelihood function includes an estimation of the probability of getting the charge wrong. This is derived from the number of doubly and triply charged secondary vertices observed.

7.1 Charge Estimation

In order to extract the charged and neutral b-hadron lifetimes, it is important to estimate the charge at each detected secondary vertex as precise as possible. All the charged particles from every b-hadron decay is not always found. The numbers and charges of the observed multiply

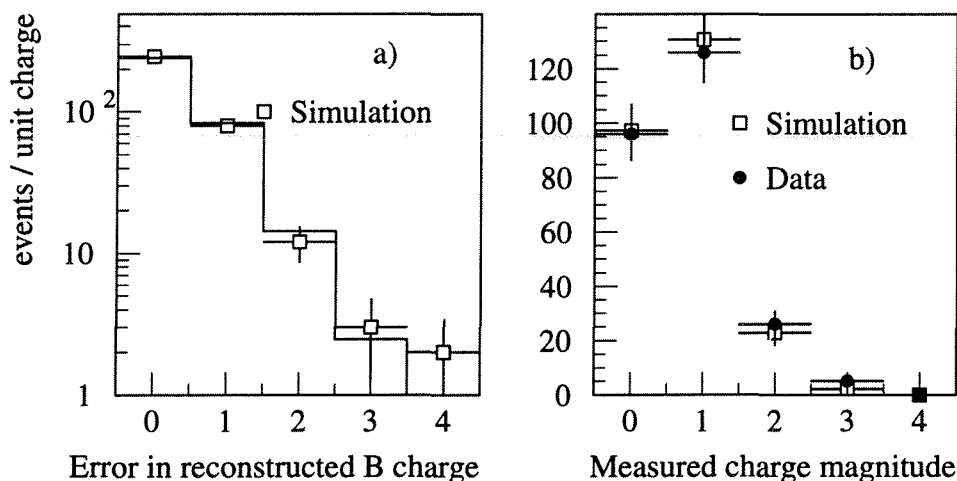


Figure 7.1: a): Magnitude of the difference between the true charge and the reconstructed charge in Monte Carlo simulation. The step function is a fit to equation 7.1. b): Shows the measured charge magnitude distribution for both the data and the simulated events..

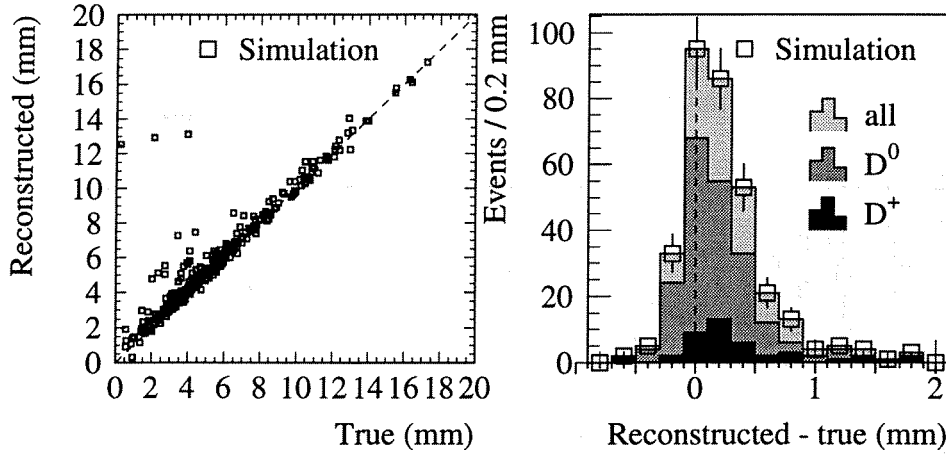


Figure 7.2: *Left: The reconstructed radial projection of the b-hadron decay length versus the true one in mm. Right: The difference between the reconstructed and the true decay length for different decay products of the b-hadron. The dashed line corresponds to a reconstructed decay length equal to the true.*

charged vertices were therefore used to make a correction for undetected charged particles from the b-hadron decays. This procedure assumes the quark model prediction that there are no genuine multiply charged b-hadrons.

The probability of getting the charge of the decaying particle wrong, $P(q \rightarrow Q)$, was modelled as:

$$P(q \rightarrow Q) = \frac{\mathcal{P}^{|Q-q|}}{\sum_{j=-\infty}^{\infty} \mathcal{P}^{|j|}} = \mathcal{P}^{|Q-q|} \frac{1 - \mathcal{P}}{1 + \mathcal{P}} \quad (7.1)$$

where q is the true charge, Q is the observed charge and \mathcal{P} is a free parameter. This can be seen to be a reasonable description of the charge error rate, as shown in Figure 7.1 a).

The charge was measured correctly in $71 \pm 3\%$ of the simulated events, and the overall agreement between Monte Carlo simulation and data, shown in Figure 7.1 b), suggests that the charge error rate will be the same for the data.

7.2 Proper Time Estimation

The proper time, t , was found from the decay length, l , and the b-hadron velocity, $\beta_{rmB} = v_B/c$:

$$t = \frac{1}{v_B \gamma} l = \frac{M_B}{P_B} l \quad (7.2)$$

where M_B is the mass and P_B is the momentum of the b-hadron respectively, $\gamma = 1/\sqrt{1 - \beta_B}$.

The measured decay length, $l_{R\phi}$, is a combination of the decay length of the b-hadron and the subsequent decays of the b-hadron decay products, particularly D mesons. The D meson decays tend to pull the secondary vertex positions towards larger radius. Figure 7.2 compares reconstructed and generated decay lengths for the simulated events. A small excess above the diagonal is seen.

One of the selection criteria was that all particles assigned to the b-hadron should come from a single vertex. This criterium suppresses long lived D mesons from the b-hadron because they

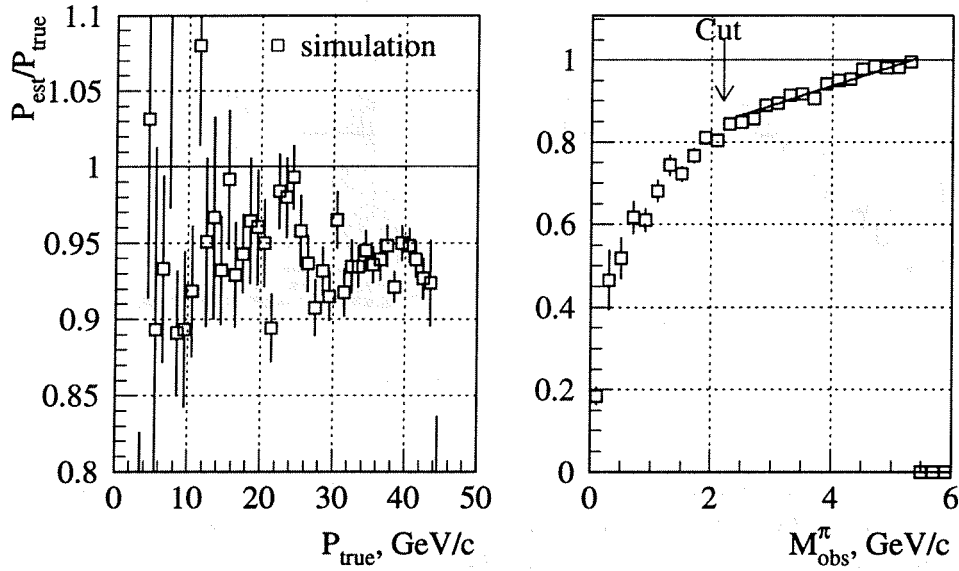


Figure 7.3: *Left: The ratio of the estimated momentum to the true value with $\alpha = 1$, averaged over all b -hadron species from simulation. The simulation did not include any detector effects the angular and momentum requirements were applied. Right: The same ratio as a function of the observed mass of the particles assigned to the secondary vertex. There is an approximate linear dependence in the range $2.2 \text{ GeV}/c^2 < M_{obs}^{\pi} < M_B$. The particles assigned to the secondary vertex were assumed to have the pion mass.*

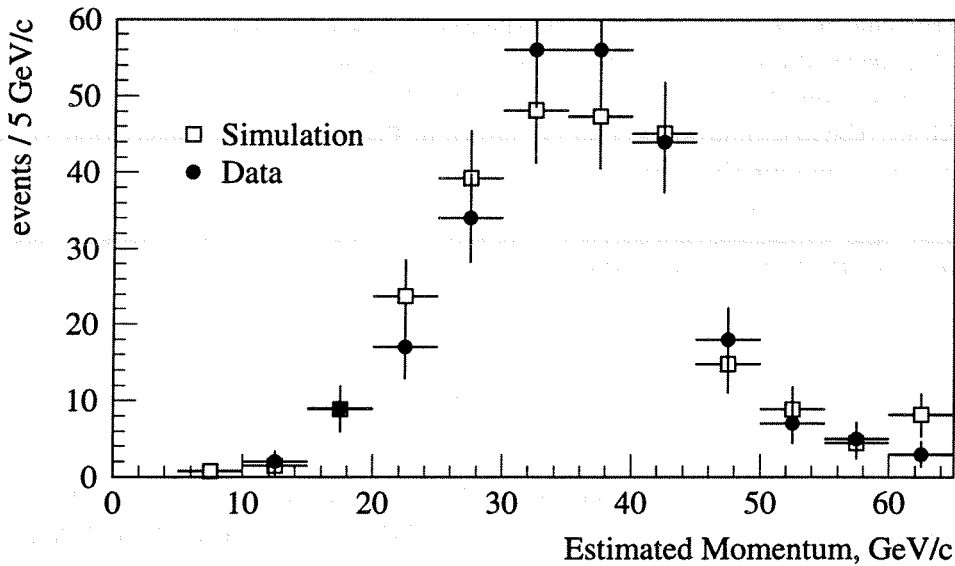


Figure 7.4: *The estimated momentum spectrum, assuming that the true mass of each of the hadrons is $5.27 \text{ GeV}/c^2$. The mean estimated momenta are $33.4 \pm 1.5 \text{ GeV}/c$ for the data and $32.6 \pm 0.5 \text{ GeV}/c$ for the simulation.*

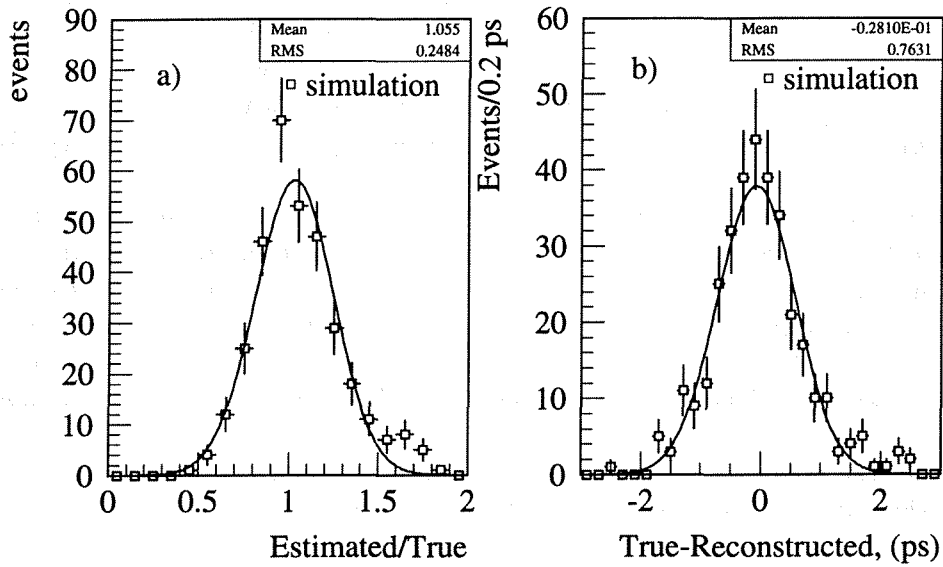


Figure 7.5: a): The ratio of the estimated boost to the true boost for simulated events.
 b) The difference between the true and measured proper time of individual simulated events, after the radius shifts and α factor have been included.

in comparison to the shorter lived D^0 , as seen in figure 7.2. The vertex criteria therefore reduces the shift of the reconstructed vertex away from the real b-hadron decay point.

The shifts seen in the simulation were $220 \pm 30 \mu\text{m}$ and $320 \pm 60 \mu\text{m}$ for D^0 and D^+ mesons respectively. These shifts are 10-15% of the typical b-hadron decay length, (c.f. figure 6.10), and should be contrasted with the more than factor two difference in lifetime for D mesons.

The three dimensional decay length, l , was therefore found from the directly measured length, $l_{R\phi}$, in the $R\phi$ plane using:

$$l = \frac{l_{R\phi} - 220 \mu\text{m}}{\sin \theta} \quad (7.3)$$

where θ is the polar angle of the vector sum of the momenta of the charged particles assigned to the decay vertex and $220 \mu\text{m}$ is a correction taken as the mean of the distribution of figure 7.2 b) for all the b-hadron decay products. Whether the correction has to be explicitly allowed for depends upon the particular fit, see section 7.4.

For sufficiently large velocities the momentum, P_B , of the b-hadron can be estimated using [89]:

$$\left(\frac{1}{P_B}\right)^{\text{est}} = \alpha \frac{M_{\text{obs}}^\pi}{M_B} \frac{1}{P_{\text{obs}}} \quad (7.4)$$

where M_{obs}^π is the observed mass of the b-hadron assuming that all the particles are pions, P_{obs} is the sum of the momenta of the particles assigned to the secondary vertex and α is a correction factor close to 1.

Substituting 7.4 into equation 7.2 gives:

$$t^{\text{est}} = M_B l \left(\frac{1}{P_B}\right)^{\text{est}} = \alpha \frac{M_{\text{obs}}^\pi l}{P_{\text{obs}}} \quad (7.5)$$

where α is a parameter, $\alpha = 1.25 - 0.061M_{\text{obs}}^\pi \text{GeV}^{-1}c^2$ for both charged and neutral b-hadrons. The parameters of α were derived from simulation and depends thus on the b-hadron decay scheme implemented there. The dependence is however rather weak. α deviates from one because of the exclusion of particles with momenta less than $0.5 \text{ GeV}/c$, and the fact that M_{obs}^π was calculated on the assumption that all the particles were pions. In fact it is very likely that at least one was a kaon.

The estimation of α has a statistical uncertainty of 25% in the simulation. The ratio of the estimated to the generated relativistic boost, $\beta\gamma$, is shown in figure 7.5 a). If the lifetime determination has mean τ , and is normal distributed, the contribution from α can be added in quadrature. The introduction of the parameter α therefore increases the uncertainty on the lifetime by a factor of $\sqrt{1 + 0.25^2} = 1.03$. The value of α has some dependence on the species as can be seen in table 7.1. This was not corrected for. The dependence upon true momentum and M_{obs}^π can be seen in figure 7.3.

Note that the true b-hadron mass, M_B , cancels out in equation 7.5. Unfortunately this does not mean that the relation is equally valid for all particles, as α depends upon the masses of the decay products.

Hadron Type	α
B^+	1.084
B^0	1.087
B_s^0	1.063
b Baryon	1.108

Table 7.1: *The average of the parameter α evaluated using the JETSET Monte Carlo without detector effects being considered for four different b-hadrons. The average is made within the allowed mass range for the observed mass. The difference between them is small.*

The momentum estimated for each of the accepted events using equation 7.4 is shown in figure 7.4. The agreement with simulation justifies the use of α derived for simulated events. It is found from figure 7.3 that if the average momentum was different by 30% then α would change by only 2%.

Figure 7.5 b) compares the generated and measured proper time for simulated decays when the decay length and momentum estimations are combined, including the corrections discussed above. The mean was $-0.08 \pm 0.02 \text{ ps}$, and the width $0.65 \pm 0.03 \text{ ps}$. The 0.65 ps resolution on the proper time is significantly less than the mean b-hadron decay time.

7.3 Fit 1; Average Acceptance Function.

The extrapolated tracks of the b-hadron decay products miss the primary vertex by an amount proportional to the decay length and inversely proportional to the b-hadron momentum. It is therefore equivalent to parametrize the acceptance in proper time or in decay distance. The acceptance $\zeta(t)$ was therefore defined as the probability that a b-hadron decay will be found as a function of its proper time.

The function $\zeta(t)$ was derived from Monte Carlo simulation using the proper time distribution of all accepted simulated events regardless of charge as shown in figure 7.6. The simulated lifetime distribution was fitted with the four functions of equations 7.6, 7.7, 7.8 and 7.9 multiplied by e^{-t/τ_g} where $\tau_g = 1.21 \text{ ps}$ was the lifetime of the simulated b-hadrons. Other functions were as well tried but did not give a satisfactory result.

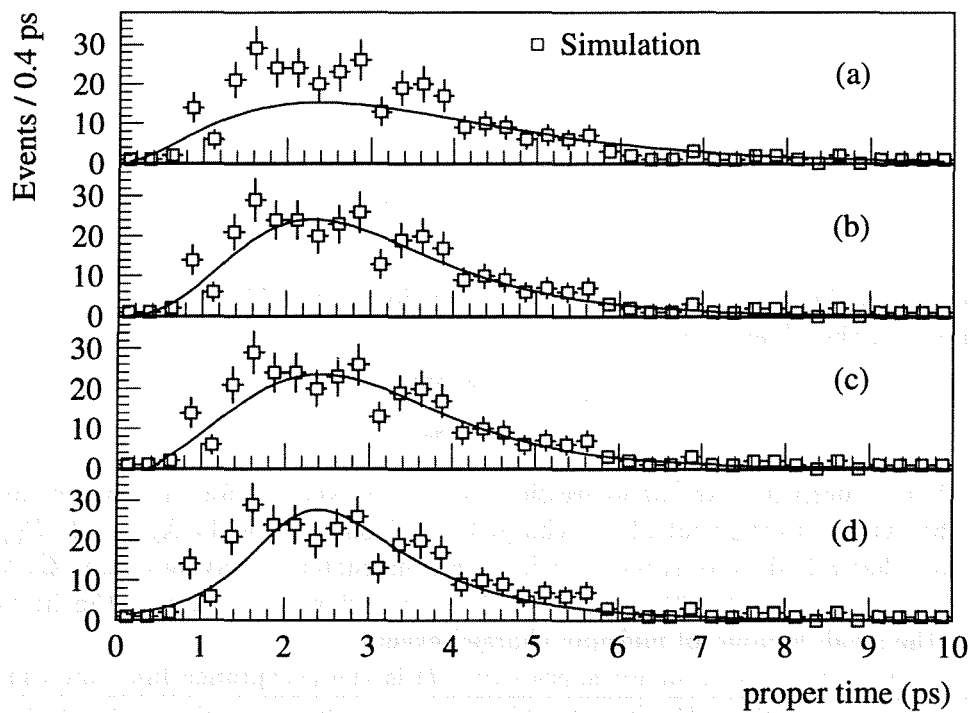


Figure 7.6: The distributions show accepted simulated events with a fit to the acceptance functions times an exponential with fixed lifetime of 1.2 ps superimposed. (a) is a fit to equation 7.6, (b) to 7.7 (c) to 7.8 and (d) to 7.9 respectively.

function	a	b	χ^2/n
7.6	5.8 ± 3.0	18.8 ± 1.7	1.5
7.7	2.5 ± 0.3	16.5 ± 4.2	0.8
7.8	2.1 ± 0.3	13.4 ± 3.2	0.8
7.9	2.3 ± 0.2	0.77 ± 0.07	1.3

Table 7.2: Parameters used in the various average acceptance functions.

$$\zeta(t) = at + bt^2 \quad (7.6)$$

$$\zeta(t) = \frac{t^a}{b + t^a} \quad (7.7)$$

$$\zeta(t) = 1 - e^{t^b/a} \quad (7.8)$$

$$\zeta(t) = 1 + \tanh\left(\frac{1+a}{b}\right) \quad (7.9)$$

The parameters of the functions found from the fits are found in table 7.2.

The likelihood of the i^{th} event is:

$$\mathcal{L}_i = \sum_{\nu} P(q_{\nu} \rightarrow Q_i) \mathcal{N}_{\nu} \omega(t_i) \int_{t_i - 3\sigma_t}^{t_i + 3\sigma_t} e^{-t/\tau_{\nu}} e^{-(t-t_i)^2/2\sigma_t^2} dt \quad (7.10)$$

See appendix A for a derivation of the expression. The sum over ν is for the three components allowed in the fit, which are the neutral and charged b-hadrons and the background. $P(q_{\nu} \rightarrow Q_j)$ is the probability that a hadron of species ν will be reconstructed as having charge Q_j as given by equation 7.1. The parameter \mathcal{P} in equation 7.1, was allowed to vary in the fit and was constrained by the small number of multiply charged events

\mathcal{N}_{ν} is the normalization constant for species ν ; $\zeta(t)$ is the acceptance function which rises with t , and τ_{ν} is the mean life of the hadrons of species ν . The convolution integral allows for the error on the reconstructed time, σ_t , which is taken to be the same for all events. It does not run over unphysical negative values for the true b-hadron lifetime. Note that the acceptance function is outside the integral as it depends upon the measured proper time, not the true proper time.

The normalization constants \mathcal{N} were given by:

$$\mathcal{N}_{\nu} = \frac{f_{\nu}}{\tau_{\nu} \int_0^{t_{\max}} \omega(t) \sum_{\mu} F_{\mu} \frac{1}{t_{\mu}} \int_{t-3\sigma_t}^{t+3\sigma_t} e^{-t_1/\tau_{\mu}} e^{-(t_1-t)^2/2\sigma_t^2} dt_1 dt} \quad (7.11)$$

where the F_{ν} are the relative fractions of the various b-hadron species and the background, $\sum_{\nu} F_{\nu} = 1$, and $t_{\max} = 10$ ps is the maximum proper time allowed in the fit. The f_{ν} 's differ from the production rates because the lifetimes of secondaries can act as a bias in the selection.

The background fraction was set to 2% which was the amount found in the simulated event sample. The charge distribution of the background fraction, $P(q_{\nu} \rightarrow Q_i)$, was defined to be similar to what was expected when combining four or five tracks of random charge. Note that the evaluation of systematic effects which are done later allow the fraction of background to be zero. The exact description of the background is therefore not of crucial importance.

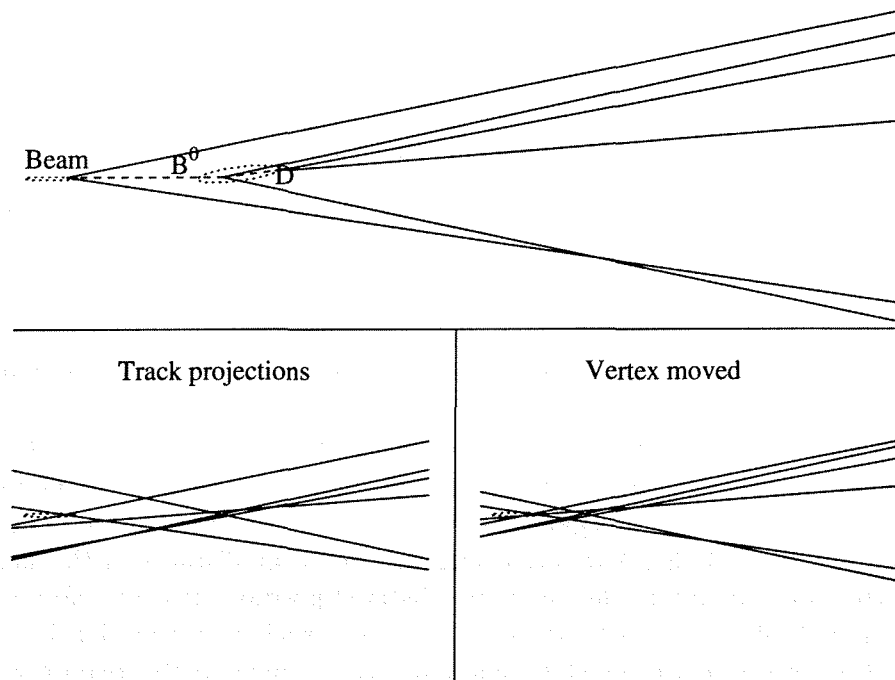


Figure 7.7: The upper figure shows a typical vertex configuration in a b -hadron decay. There are a few tracks from the primary vertex, then a flight distance, the b -hadron decay and a subsequent D decay. The secondary vertex found with the described method is somewhere between the b -hadron and the D decay as indicated by the error ellipsis.

The lower left figure shows the tracks as they appear when the extrapolations are not stopped at the relevant vertices. The picture surely contains ambiguous vertices. The lower right shows the situation when the resolved secondary vertex is moved until a non-ambiguous secondary vertex is not to be found any more. This position, $l_{R\phi}^{\min}$ is then the minimum observable distance for this vertex.

Notice that the range of lifetimes can be varied in the fit. Results are quoted requiring all events to have proper times between 0 and 10 ps. This requirement rejects six long lived events. The systematic uncertainty due to this requirement was estimated.

7.4 Fit 2; Individual Acceptances.

With this method the acceptance is calculated on an event by event basis. The tracks assigned to the b -hadron decay are moved towards the primary interaction without changing the relative positions of the particles from the decay. The distance at which ambiguities start to occur, such that the jet no longer passes the combined χ^2 requirement, is defined as the minimum distance this event could be observed, $l_{R\phi}^{\min}$.

A binary search for $l_{R\phi}^{\min}$ is performed along the line joining the primary and secondary vertex. The secondary vertex is first moved to the point halfway between the original secondary and the primary and a new vertex fit is performed. If the new vertex passes the χ^2 requirement it is moved again halfway towards the primary vertex. If it does not pass it is moved outwards

halfway towards the original secondary vertex. This procedure is repeated until the second best vertex configuration has a probability just above 1% .

The *excess* decay distance is thus given by:

$$l_{R\phi}^{\text{excess}} = l_{R\phi} - l_{R\phi}^{\text{min}} \quad (7.12)$$

The three dimensional decay length, l , is found from the excess decay length in the $R\phi$ plane as:

$$l = \frac{l^{\text{excess}}}{\sin \theta} \quad (7.13)$$

where θ is the polar angle of the vector sum of the momenta of the charged particles assigned to the decay vertex.

The proper time distribution of the decaying particles beyond $l_{R\phi}^{\text{min}}$ is given by their lifetimes. The change in the calculated proper time for individual events due to the finite decay time of the b-hadron decay products is significantly reduced by this method since the actual vertex configuration is kept and therefore any change in the decay distance is the same both at the observed vertex position and at the minimum observed position. It is therefore not necessary to correct for the pull of the vertex by the decay products such as in equation 7.3.

The effect is however not completely removed because some events are observed only because of the shift due to the long lived b-hadron decay products. These events appear with short proper time. The requirement on the visible mass ensures that these events are good b-hadron candidates. Equally important is that the *distribution* of decay distances remains an exponential with decay constant given by the b-hadron lifetime and momentum.

Another result of this procedure is that the uncertainty in the proper time cancels out under the assumption that the proper time uncertainty has a finite distribution, $f(t)$. Put mathematically the process convolutes an infinite exponential with an unknown, finite distribution. The resulting distribution is still an exponential with the same decay constant as the original.

This can be seen by considering the number of decays as a function of proper time, $N(t)$, which is given as:

$$N(t) = N(t_0)e^{-t/\tau} \rightarrow N(t_0) \int_{-\infty}^{\infty} e^{-t_1/\tau} f(t - t_1) dt_1 \quad (7.14)$$

where t is the measured proper time for the decay, $N(t_0)$ is the initial number of particles and $f(t - t_1)$ is a finite function. By substituting $t_1 = t - T$, where T is the minimum time an event could be observed, the convolution integral becomes:

$$\int_{-\infty}^{\infty} e^{-(t-T)/\tau} f(T) dT = e^{t/\tau} \int_{\infty}^{\infty} e^{T/\tau} f(T) dT \quad (7.15)$$

If $f(T)$ decreases faster than $e^{T/\tau}$ increases, which is the case if $f(T)$ is a gaussian, then the convolution integral is a constant, C . The expression for the number of decays reduces to:

$$N(t) = N(t_0)C e^{-t/\tau} \quad (7.16)$$

An effectively infinite exponential is obtained by requiring that the minimum acceptable decay length must be $5 \sigma_l$, where σ_l is the geometrical uncertainty on the secondary vertex position.

The advantage of this method is that it removes the need for the acceptance function obtained from the Monte Carlo simulation which was used in the previous fit as well as the convolution

integral over the proper time error. The likelihood function is therefore in this case somewhat simpler:

$$\mathcal{L}_i = \sum_{\nu} P(q_{\nu} \rightarrow Q_i) \mathcal{N}_{\nu} e^{-t_i^{\text{excess}}/\tau_{\nu}} \quad (7.17)$$

where the sum runs over the charged or neutral b-hadron species considered and over the background. $P(q \rightarrow Q_i)$ is the probability that a hadron of charge q will be reconstructed as having charge Q . $P(q \rightarrow Q_i)$ is modelled as in equation 7.1 and is constrained by the number of multiply charged events. \mathcal{N}_{ν} is the normalization constant for species ν and τ_{ν} is the mean lifetime of b-hadrons of species ν . To simplify the notation t refers to the excess lifetime in the rest of this section.

The normalization constants \mathcal{N}_{ν} are now given as :

$$\mathcal{N}_{\nu} = \frac{F_{\nu}}{\tau_{\nu} [1 - e^{-t^{\text{max}}/\tau_{\nu}}]} \quad (7.18)$$

where the F_{ν} are the relative fractions of the various B species and the background in the selected sample, and $t^{\text{max}} = 8$ ps is the maximum allowed proper time of the events used in the fit. The fractions of the selected sample, F_{ν} , are related to the fractions f_{ν} which would have been observed if the lifetimes had been equal:

$$F_{\nu} = \frac{1}{N} \times \sum_i \frac{f_{\nu} e^{-t_i^{\text{min}}/\tau_{\nu}}}{\sum_{\mu} f_{\mu} e^{-t_i^{\text{min}}/\tau_{\mu}}} \quad (7.19)$$

where N is the number of selected events, and t_i^{min} is the proper time of the minimum decay distance at which event i would have been observed. The fractions f_{ν} , as given in table 6.4. are not the same as the production rates of the various b-hadrons because of the different selection efficiencies for the different decay topologies.

The time range for the fit was now in the excess lifetime, and could still be altered at will. The 2% background fraction, Table 6.4, was modelled to have the charge distribution of four or five charged particles of random charge.

7.5 Test on D mesons

A check on the reliability of the method was performed by measuring the lifetimes of the D hadrons. This is more difficult because is not possible to obtain a pure sample of D mesons by a requirement on the invariant mass of the decay vertex as were done for the b-hadrons. There is no mass range in which a pure D sample can be obtained without contamination from partially reconstructed b-hadron states.

However, in the JETSET model, reasonable D purity was obtained using decays with masses between 1 and 2.0 GeV/c² and an observed ‘‘Lorentz factor γ ’’ of more than 14. b-hadrons cannot have a true ‘‘ γ ’’ of more than around 9. ‘‘ γ_{obs} ’’ was calculated as $E_{\text{obs}}^{\pi}/M_{\text{obs}}^{\pi}$, and it is shown for different quark types in figure 7.8. These requirements together with the previous, as described in chapter 6, yields 33 neutral, 34 charged and 4 doubly charged vertices. The proper times of the selected vertices with the fit results superimposed is shown in figure 7.9.

The γ requirement produces biases in the estimated proper time because of the error on the estimated momentum, which could be investigated with Monte Carlo simulation. The sample also includes significant background, and the proper time resolution, is very similar to the D⁰ lifetime. However, simply running the lifetime fitting program on this sample, using fit 1 with the acceptance function found for b-hadron decays, and neglecting these systematic effects gives

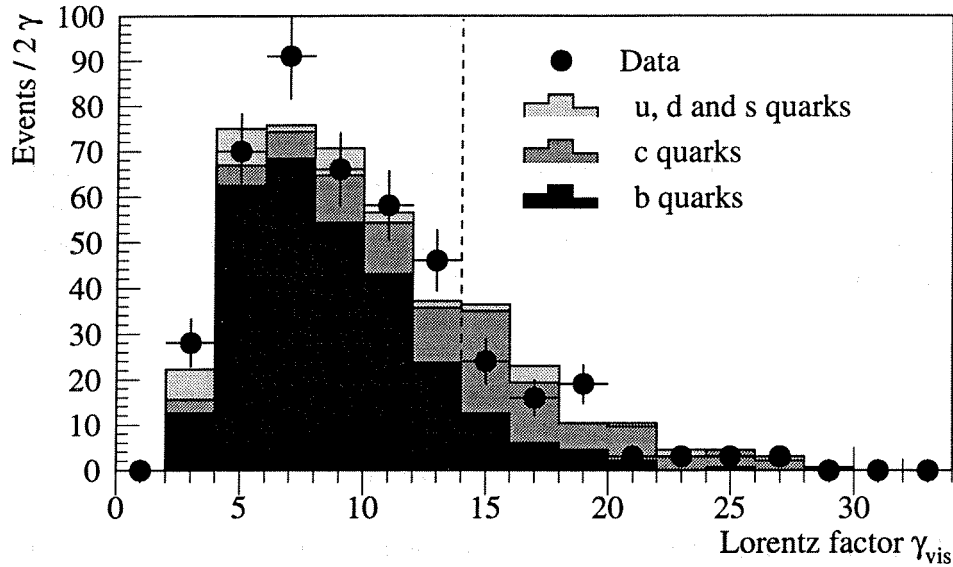


Figure 7.8: The Lorentz factor “ γ_{obs} ” for vertices with measured mass in the range 1.0 to 2.0 GeV/c². The dashed line shows the selection for D meson decays.

the results in table 7.3. For technical reasons the requirement of no tracks found only in the Microvertex Detector was not used.

Parameter	Data value	M.C. value
\mathcal{P}	0.09 ± 0.04	0.15 ± 0.04
f^{charged}	0.50 ± 0.07	0.43 ± 0.07
$\tau^{\text{charged}}, (D^+), (\text{ps})$	1.09 ± 0.16	1.27 ± 0.21
$\tau^{\text{neutral}}, (D^0), (\text{ps})$	0.44 ± 0.06	0.55 ± 0.06

Table 7.3: Results of fitting the D lifetime. See text for details.

In addition to the various approximations above there is some residual b-hadron contamination. The charged lifetime is a combination of the D^+ with lifetime of 1.066 ± 0.023 ps and the short lived D_s^+ and Λ_c^+ . The D^0 has a lifetime of 0.420 ± 0.008 ps.

This test is not meant to be a determination of the D lifetimes, but the agreement of the result with the known D lifetimes shows that the fit method works. The difference in the lifetimes between the charged and the neutral states also shows that the two charges have been separated.

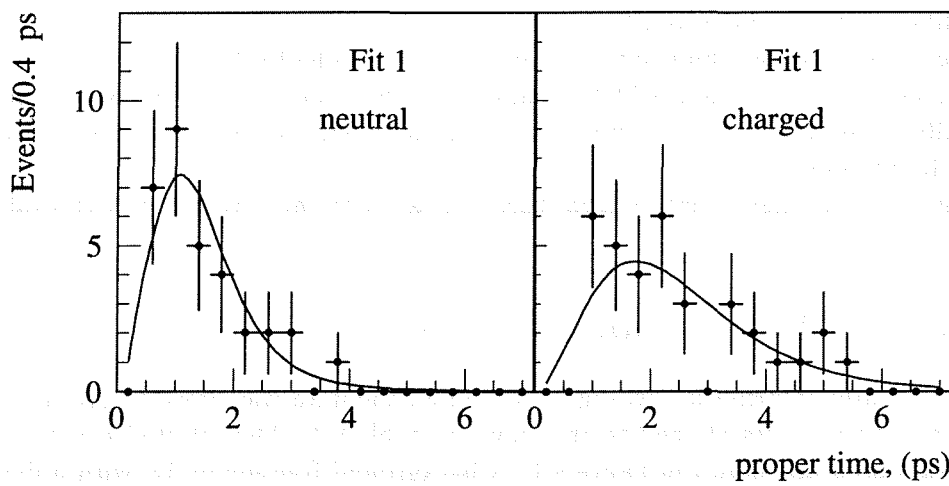


Figure 7.9: Proper times of the D^+ and D^0 candidates with the fit result superimposed.

Chapter 8

B lifetime results and systematic uncertainties

Using both the method of an average acceptance function and the method of individual acceptances, three different fits to b-hadron lifetimes were performed.

By ignoring all the charge information a fit to a mean b-hadron lifetime was performed. Then using the charge information a fit to charged and neutral mean b-hadron lifetimes was obtained. Finally by assuming the fractions of the various b-hadron species, the data was fitted to the B^+ and B^0 lifetimes.

In the subsequent discussion results from these fits are presented together with evaluations of systematic effects.

8.1 Fit to the Mean b-hadron Lifetime.

In this fit the charge information was ignored and all the data was fitted to give an average b-hadron lifetime. The results of the fits are shown in table 8.1. The selected events with the fit results superimposed are shown in figure 8.1. A background fraction of 2% with a lifetime of 3.0 ps was allowed in the fit. This was simply a parametrization of the background found in the simulated event sample.

The fit results for the simulated sample using fit method one for the equations 7.7 and 7.8 deviates about one standard deviation from the generated lifetime of 1.21 ps. The difference between the two results is however negligible. Function 7.7 has been chosen for the subsequent fits to two lifetimes, but function 7.8 could as well have been chosen without significantly altering the results. The fits using equation 7.6 and 7.9 have central values about 3.5 and 2.5 σ from the simulation input respectively. These functions are therefore not considered more as they probably do not represent good models for the actual acceptance.

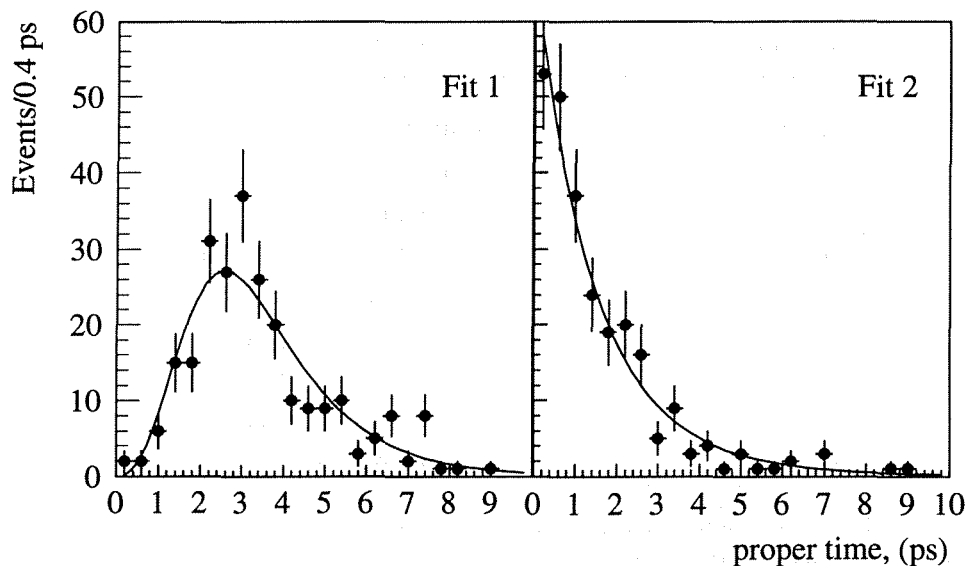


Figure 8.1: The proper times of the accepted events disregarding any charge information. The superimposed lines are the result from the fits. The fit using the acceptance function of equation 7.7 is shown in the left plot, and that using the excess lifetime approach is shown in the right plot.

Fit method	Data (ps)	$-2 \ln \mathcal{L}$	Simulation (ps)	$-2 \ln \mathcal{L}$
1. Acceptance function (7.6)	1.18 ± 0.05	928.7	1.06 ± 0.04	1252.1
1. Acceptance function (7.7)	1.50 ± 0.08	912.3	1.28 ± 0.07	1248.2
1. Acceptance function (7.8)	1.52 ± 0.09	913.5	1.30 ± 0.06	1247.2
1. Acceptance function (7.9)	1.71 ± 0.11	902.4	1.42 ± 0.08	1249.3
2. individual acceptances	1.49 ± 0.11		1.17 ± 0.09	

Table 8.1: Mean lifetime, in picoseconds, measured by the two methods in one parameter fits. The simulated events were generated with a mean lifetime of 1.21 ps. It should be noticed that the parameters of the acceptance functions were derived from the same simulated sample, so the fits should give a value very close to the input value.

Systematic		Lifetime (ps)	
		Fit 1	Fit 2
Acceptance function statistics ^a equation 7.7	$a + 1\sigma$	1.51±0.09	—
	$a - 1\sigma$	1.51±0.08	—
	$b + 1\sigma$	1.43±0.08	—
	$b - 1\sigma$	1.60±0.09	—
Pull from D's ^b	440 μm	1.46±0.08	—
	110 μm	1.55±0.09	—
Momentum estimation ^c	$\alpha \times 0.97$	1.42±0.10	1.44±0.10
	$\alpha \times 1.03$	1.55±0.10	1.54±0.10
Fit time range	0 - 5 ps	1.53±0.15	1.47±0.13
	0 - 20 ps	1.55±0.08	1.51±0.10
Background ^d fraction	0%	1.52±0.08	1.51±0.10
	6%	1.48±0.09	1.47±0.11

^aThe parameters of the acceptance function were varied within $\pm 1\sigma$.

^bThe decay length correction was varied by a factor of two.

^cThe momentum correction factor α was varied within 3% which is the precision with which it was determined from simulation.

^dThe fraction of background allowed in the fit.

Table 8.2: Systematic effects on the mean lifetime in the two fits. Only the acceptance function 7.7 has been used in this evaluation for fit 1.

In table 8.2 the systematic effects found in fit 1 are tabulated. The parameters of the acceptance function were allowed to vary within their statistical uncertainties, see table 7.2. The decay length correction from the subsequent D decays was varied by a factor of two. The parameter α in the momentum estimation was varied within its uncertainty of 3%. The fit was performed for the fit time ranges 0 - 5 ps and 0 - 20 ps. Finally the background fraction was allowed to be zero and 6%.

A large systematic effect arises from the uncertainties in the determination of the parameters of the acceptance function. It is expected that this uncertainty will diminish with a larger event sample. Although with the present size of the event sample it is justified to include it as a systematic uncertainty. The uncertainty on the exact form of the acceptance function is evaluated from the discrepancy of the fit result from the simulation input.

No large effect on the lifetime is observed by excluding the lifetime fit to the proper time range 0-5 ps or extending it to 0-20 ps. Any effect of the time range is however to be regarded as a statistical uncertainty because the time range is included in the normalization of the likelihood function. The fit time range is therefore not included in the summary of systematic uncertainties.

In fit 2 where the acceptances were calculated for each event the effect from the subsequent D decay is expected to be smaller, as discussed in section 7.4. The momentum estimation, fit time range and the background were varied as for fit 1. The possible bias takes into account a possible residual effect of the pull on the vertex position from the subsequent decay of the b-hadron decay products in fit 2, notably the long lived D mesons.

Any difference between the results from fit one and two could be interpreted as an alternative estimate of a systematic uncertainty affecting one of the methods only. The very small difference between the results, 0.01 ps, points in the direction that the major systematic uncertainties is

Systematic	Fit 1 (ps)	Fit 2 (ps)
Acceptance function form ^a	±0.04	—
Acceptance function statistics. ^b	±0.08	—
Pull from D's, factor 2	±0.05	—
Momentum estimation ±3%	±0.05	±0.05
Background	±0.02	±0.02
Possible bias ^c	—	±0.11
Total	±0.12	±0.12

^aThe quoted value is half the difference between the generated lifetime and the fit result for the simulated sample.

^bThe quoted value is half the variation of the fit result obtained when varying the acceptance function parameters $\pm 1\sigma$.

^cThe quoted value is the statistical uncertainty on the fit result on simulated events, scaled to be the same fractional size.

Table 8.3: Summary of systematic uncertainties on the mean lifetime. The quoted values are half the difference between the results in table 8.2 unless otherwise stated.

	Parameter	Data	Simulation	
		Fit Result	Fit result	input
Fit 1 Acceptance	$\langle \tau_{charged} \rangle$ (ps)	1.54±0.14	1.15±0.09	1.20
	$\langle \tau_{neutral} \rangle$ (ps)	1.47±0.16	1.49±0.14	1.21
	f^+	0.55±0.05	0.56±0.04	0.53
	\mathcal{P}	0.18±0.03	0.12±0.02	0.16
	$\langle \tau_{charged} \rangle / \langle \tau_{neutral} \rangle$	1.03±0.17	0.77±0.11	0.99
Fit 2 Excess life time	$\langle \tau_{charged} \rangle$ (ps)	1.56±0.19	1.14±0.11	1.20
	$\langle \tau_{neutral} \rangle$ (ps)	1.44±0.21	1.33±0.16	1.21
	f^+	0.52±0.08	0.66±0.08	0.53
	\mathcal{P}	0.18±0.03	0.13±0.02	0.16
	$\langle \tau_{charged} \rangle / \langle \tau_{neutral} \rangle$	1.09 ^{+0.28} _{-0.22}	0.84 ^{+0.17} _{-0.14}	0.99

Table 8.4: Fit to average charged and neutral lifetimes, with the statistical uncertainties shown. The lifetime ratio is not an independent parameter, but the errors have been calculated in a separate fit. f^+ is the fraction of charged vertices. The value of \mathcal{P} in the data corresponds to a 30% probability of getting the charge wrong. The simulation b-hadron lifetime was 1.2 ps for all states except the Λ_b for which it was 1.3 ps.

common to both fits.

Taken the above considerations into account the systematic uncertainties in the fits to a mean b-hadron lifetime are summarized in table 8.3.

8.2 Fit to the Charged and Neutral Lifetimes.

The proper time distributions of the events split into charged and neutral species is shown

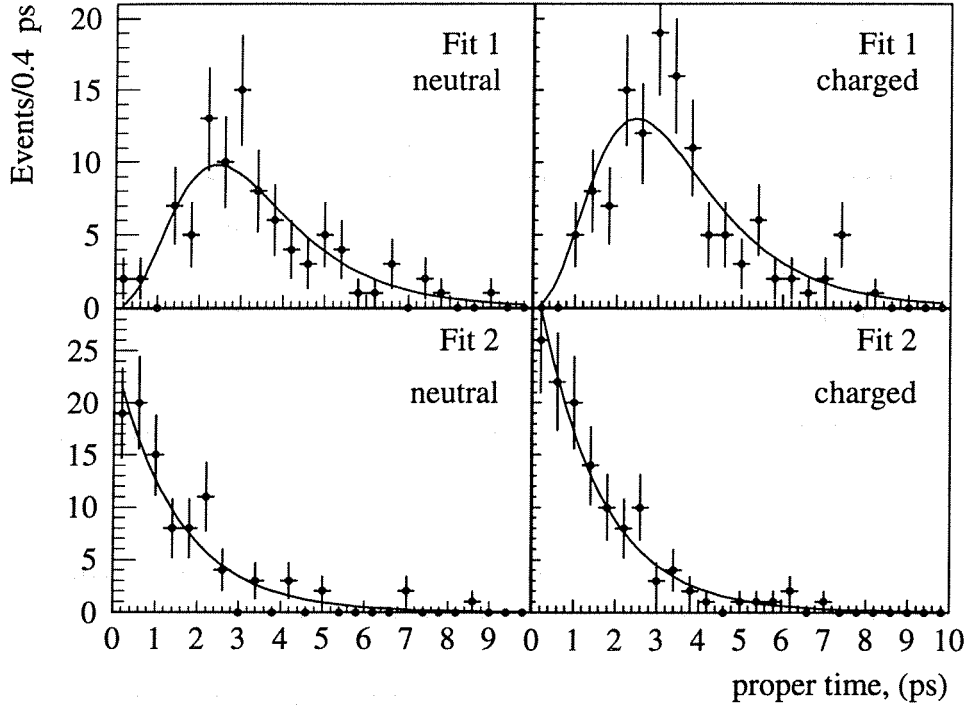


Figure 8.2: *The proper times of the accepted events. The fit using the acceptance function is shown in the top plots, that using the excess lifetime approach in the bottom plots.*

in figure 8.2 with the fit to average charged and neutral lifetimes superimposed.

The results of the fits are shown in table 8.4. It was assumed that all the charged *b*-hadron species have one lifetime and all the neutral ones have another. The relative normalization of the two species has been left free to reduce the dependence upon the simulation.

Tables 8.5 and 8.6 show fit results for similar variations of parameters as were shown for the fit to one lifetime. In addition two other possible systematic effects were investigated.

The first was the treatment the momentum estimation for multiply charged vertices. Normally these events are treated exactly as the neutral and singly charged. The multiply charged vertices are however believed mainly to be due to lost low momentum particles. The fit was therefore tried with the factor α divided by 1.15 for these vertices. This factor was determined from simulation.

The second was the choice of model for the charge measurement uncertainty. An alternative model where the probability of measuring the charge wrong was modelled using a Breit-Wigner like function was tried:

$$P(q \rightarrow Q) = \frac{1}{\mathcal{N}} \left[\frac{|\mathcal{P}|}{(Q - q)^2 + \mathcal{P}} \right]^{3.1} \quad (8.1)$$

$$\mathcal{N} = \sum_{j=-\infty}^{\infty} \left[\frac{|\mathcal{P}|}{(j)^2 + \mathcal{P}} \right]^{3.1} \quad (8.2)$$

where \mathcal{P} is the width of the function, which was a free parameter in the fit, q is the true charge, Q is the measured charge and \mathcal{N} is the normalization of the function. No effect was however seen in any of the two fits.

Systematic		Lifetime (ps)		Ratio
		Charged	Neutral	
Acceptance function statistics	$a + 1\sigma$	1.53 ± 0.15	1.48 ± 0.17	1.03
	$a - 1\sigma$	1.53 ± 0.14	1.48 ± 0.16	1.03
	$b + 1\sigma$	1.46 ± 0.13	1.41 ± 0.15	1.04
	$b - 1\sigma$	1.63 ± 0.16	1.58 ± 0.18	1.03
Pull from D's	110 μm	1.58 ± 0.15	1.53 ± 0.16	1.03
	440 μm	1.43 ± 0.16	1.50 ± 0.18	0.95
Momentum estimation $ Q > 1^a$	$\alpha \times 0.97$	1.46 ± 0.14	1.51 ± 0.18	0.97
	$\alpha \times 1.03$	1.60 ± 0.15	1.56 ± 0.18	1.03
	$\alpha / 1.15$	1.61 ± 0.16	1.47 ± 0.16	1.10
Fit time range	0 - 5 ps	1.67 ± 0.28	1.39 ± 0.24	1.20
	0 - 20 ps	1.50 ± 0.14	1.60 ± 0.17	0.94
Charge error model		1.53 ± 0.15	1.48 ± 0.17	1.03
Background	0%	1.54 ± 0.14	1.49 ± 0.16	1.03
	6%	1.52 ± 0.14	1.47 ± 0.16	1.03

^aThe multiply charged events are mainly due to lost low momentum tracks. To compensate for a possible overestimation of the momentum for these, α was reduced with a factor taken from simulation.

Table 8.5: *Systematic effects in the two lifetime fits using fit method 1.*

The systematic uncertainties associated with these fits are summarized in table 8.7. The same considerations as regards the effect of the fit time range applies here as for the fit to an average b-hadron lifetime and any effect from this is omitted from the summary table. The two standard deviation discrepancy in the fit 1 from the simulation input for charged vertices is interpreted as due to the uncertainty of the exact form of the acceptance function, and is included in the summary table.

The charge unfolding is a similar systematic uncertainty derived from testing the ability of fit 2 to reconstruct the original lifetimes. Using the weighting technique in the simulation analysis the different charge states were given different weights in the fit. This should mimic different lifetimes for the different charge states. The charge unfolding systematic uncertainty then tells how well the fit reproduced the different lifetimes. The row labelled possible bias is included for the same reasons as for the fit to a mean lifetime. The systematic uncertainty on the lifetime ratio is introduced by the assumption that a possible bias only affects one of the charge states.

One possible additional systematic could be a dependence of the charge accuracy on the lifetime. Particularly when vertices can only just be distinguished it is possible that they might have the wrong tracks. This was investigated in simulation, using the known charge, and found to be a negligible effect. In table 8.8 the mean apparent lifetimes of the differently charged events are shown. The mean lifetimes of the multiply charged events are consistent with that of the singly charged events.

A possible effect on the fit result and charge reconstruction precision for increasing mass constraint on the secondary vertex was investigated. Figure 8.3 shows the fit results, while figure 8.4 shows the number of vertices and the relative fractions of different charges for increasing mass requirement. It can be seen that the fraction of doubly charged vertices decreases as the mass requirement is increased. Although, because of the reduced number of events at higher

Systematic		Lifetime (ps)		Ratio
		Charged	Neutral	
Momentum estimation $ Q > 1$	$\alpha \times 0.97$	1.51 ± 0.18	1.39 ± 0.20	1.09
	$\alpha \times 1.03$	1.62 ± 0.20	1.48 ± 0.22	1.09
	$\alpha / 1.15$	1.62 ± 0.19	1.42 ± 0.21	1.09
Fit time range	0 - 5 ps	1.50 ± 0.23	1.48 ± 0.25	1.01
	0 - 20 ps	1.51 ± 0.18	1.48 ± 0.20	1.02
Charge error model		1.56 ± 0.22	1.43 ± 0.23	1.09
Background	0%	1.57 ± 0.19	1.44 ± 0.21	1.09
	6%	1.55 ± 0.19	1.43 ± 0.21	1.08

Table 8.6: *Systematic effects in the two lifetime fit using fit method 2.*

Systematic	Fit 1, Acceptance			Fit 2, Excess life time		
	$\tau_{charged}$	$\tau_{neutral}$	τ_- / τ_0	$\tau_{charged}$	$\tau_{neutral}$	τ_- / τ_0
Acceptance function form	± 0.06	± 0.14	± 0.12	—	—	—
Acceptance function (stat)	± 0.09	± 0.09	—	—	—	—
Pull from D's, factor 2	± 0.08	± 0.03	± 0.03	—	—	—
Possible bias	—	—	—	± 0.11	± 0.11	± 0.07
Charge unfolding	—	—	—	± 0.03	± 0.05	± 0.02
Momentum estimation	± 0.08	± 0.09	± 0.05	± 0.06	± 0.05	± 0.06
Background fraction	± 0.01	± 0.04	± 0.03	± 0.01	± 0.01	± 0.02
Total systematic	± 0.14	± 0.20	± 0.07	± 0.13	± 0.14	± 0.09

Table 8.7: *Summary of systematic uncertainties in the fit to the average charged and neutral *b*-hadron lifetimes.*

Charge	Mean lifetime (ps)
0	1.60 ± 0.16
-1, 1	1.52 ± 0.12
-3, -2, 2, 3	1.60 ± 0.26

Table 8.8: *Mean excess lifetime for different charges.*

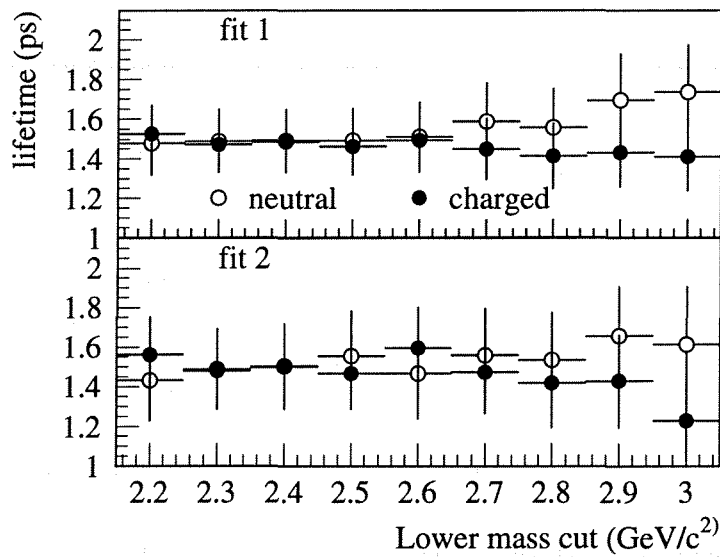


Figure 8.3: Lifetimes for the charged and neutral vertices respectively for lower mass requirement in the range 2.2 to 3 GeV/c².

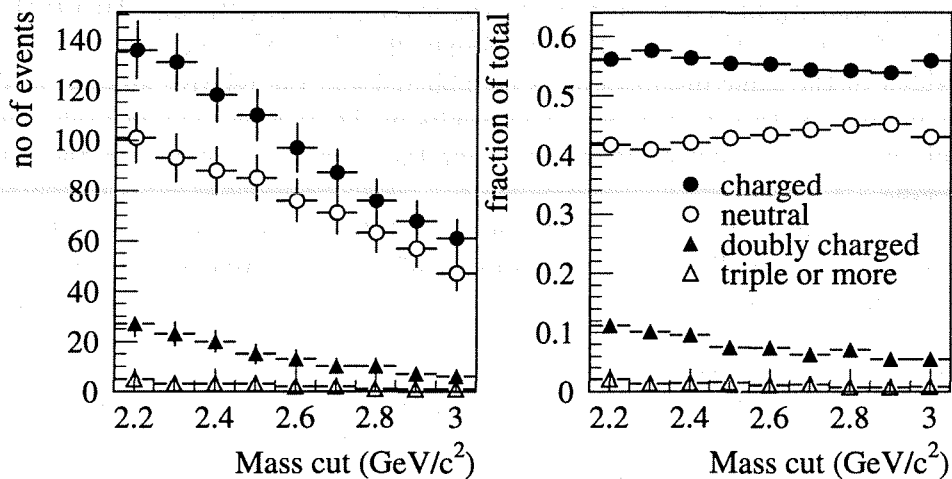


Figure 8.4: Left: Number of vertices of different charges as a function of the mass requirement. Right: Relative fraction of different charged vertices as a function of the mass requirement.

	Parameter	Data value	Simulation
Fit 1 Acceptance function	τ_{B^+} (ps)	1.54 ± 0.14	1.14 ± 0.09
	τ_{B^0} (ps)	1.63 ± 0.26	1.69 ± 0.25
	f_{B^+}	0.55 ± 0.14	0.56 ± 0.04
	\mathcal{P}	0.18 ± 0.03	0.12 ± 0.02
	τ_{B^+}/τ_{B^0}	$0.92^{+0.21}_{-0.17}$	$0.67^{+0.14}_{-0.12}$
Fit 2 Excess lifetime	τ_{B^+} (ps)	1.56 ± 0.19	1.13 ± 0.11
	τ_{B^0} (ps)	1.55 ± 0.25	1.41 ± 0.22
	f_{B^+}	0.51 ± 0.08	0.63 ± 0.06
	\mathcal{P}	0.18 ± 0.03	0.13 ± 0.02
	τ_{B^+}/τ_{B^0}	1.01^{+29}_{-22}	$0.88^{0.22}_{0.15}$

Table 8.9: Results for the B^+ and B^0 lifetimes; only statistical errors are quoted.

mass cuts no improvement in the statistical precision is observed. The lifetimes are consistent with being equal for all mass requirements. The fit has an anti-correlation between the two lifetimes which is clearly seen in the figure.

8.3 Fit to B^0 and B^+ lifetimes.

By assuming a specific composition for the neutral b-hadrons, B^0 , B_s^0 , Λ_b and using previous measurements of the B_s^0 and Λ_b lifetimes, the data can also be interpreted in terms of the lifetimes of the B^0 and B^+ mesons. The B^0 lifetime extracted in such a manner depends critically upon the assumptions, whereas the B^+ lifetime is relatively insensitive to the assumptions.

In the fit the B_s^0 and Λ_b lifetimes were set to the average of ALEPH and DELPHI results as found in table 1.3: 1.05 ± 0.33 ps [15, 16] and 0.98 ± 0.22 ps [17, 18] respectively. The neutral species were divided in the same proportions as in table 6.4 and the relative amount of B^+ was fitted. No other b-hadrons were allowed for. The results of the fit are shown in table 8.9.

The one and two standard deviation contours for the b-hadron lifetimes in these fits are shown in figure 8.5.

The assumptions made about the minority neutral states are very important for the extraction of the lifetime of the B^0 . The variations of lifetimes allowed for are the combined uncertainties from the referenced measurements. The fractions of each of the species were the numbers obtained from the simulated event sample. Those were varied by a conservative factor of two. It should be mentioned that measurements of K^0 , Λ and Ξ^- cross sections at LEP [90] agree with the JETSET predictions to better than this. Note that if the four B fractions and lifetimes from this fit are combined to make an unbiased LEP average, the result is $\langle \tau_B \rangle = 1.44$ ps about 0.05 ps lower than the result in section 8.2.

Fit 1; Average acceptance function

Systematic		Lifetime (ps)		Ratio
		B^+	B^0	
B_s^0 fraction	$\times 0.5$ (4.5%)	1.54 ± 0.14	1.63 ± 0.23	0.94
	$\times 2.0$ (18.0%)	1.54 ± 0.14	1.78 ± 0.32	0.86
$\tau(B_s^0)$	+ 0.33 ps	1.54 ± 0.14	1.59 ± 0.25	0.97
	- 0.33 ps	1.54 ± 0.14	1.76 ± 0.27	0.87
Λ_b fraction	$\times 0.5$ (3.0%)	1.54 ± 0.14	1.64 ± 0.24	0.94
	$\times 2.$ (12.0%)	1.54 ± 0.14	1.76 ± 0.30	0.88
$\tau(\Lambda_b)$	+ 0.22 ps	1.54 ± 0.14	1.64 ± 0.26	0.94
	- 0.22 ps	1.54 ± 0.14	1.71 ± 0.27	0.90
Background fraction	0 %	1.55 ± 0.14	1.70 ± 0.26	0.91
	6%	1.53 ± 0.14	1.67 ± 0.26	0.92

Fit 2; individual acceptances

Systematic		Lifetime (ps)		Ratio
		B^+	B^0	
B_s^0 fraction	$\times 0.5$ (4.5%)	1.56 ± 0.19	1.52 ± 0.24	1.02
	$\times 2.0$ (18.0%)	1.56 ± 0.19	1.61 ± 0.28	1.00
$\tau(B_s^0)$	+ 0.33 ps	1.56 ± 0.19	1.50 ± 0.28	1.05
	- 0.33 ps	1.56 ± 0.19	1.55 ± 0.24	1.03
Λ_b fraction	$\times 0.5$ (3.0%)	1.56 ± 0.19	1.53 ± 0.24	1.00
	$\times 2.$ (12.0%)	1.56 ± 0.19	1.59 ± 0.27	0.97
$\tau(\Lambda_b)$	+ 0.23 ps	1.56 ± 0.19	1.54 ± 0.26	1.02
	- 0.23 ps	1.56 ± 0.19	1.55 ± 0.25	1.02
Background fraction	0 %	1.57 ± 0.19	1.55 ± 0.25	1.02
	6 %	1.54 ± 0.20	1.54 ± 0.26	1.02

Table 8.10: *Systematic effects in the fit to B^+ and B^0 lifetimes*

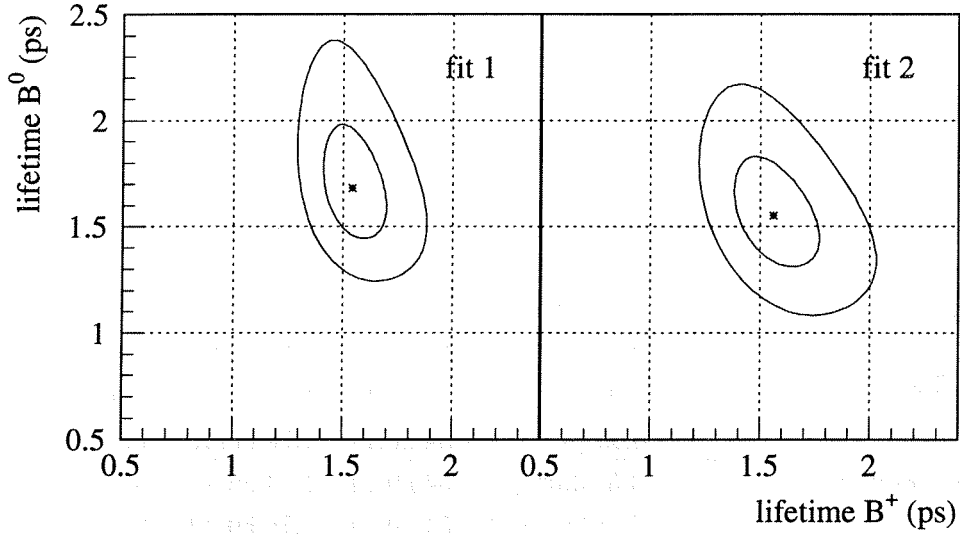


Figure 8.5: The one and two sigma contours for the fits to the B^+ and B^0 lifetimes. Left: fit 1. Right fit 2. Only statistical errors are shown in these plots.

Systematic	fit 1			fit 2		
	τ_{B^+} (ps)	τ_{B^0} (ps)	τ_{B^+}/τ_{B^0}	τ_{B^+} (ps)	τ_{B^0} (ps)	τ_{B^+}/τ_{B^0}
B_s^0 fraction, factor 2	—	+0.04 -0.03	+0.02 -0.02	—	+0.04 -0.02	+0.01 -0.03
$\tau(B_s^0) \pm 0.33$ ps	—	+0.00 -0.03	+0.02 -0.01	—	+0.00 -0.03	+0.02 -0.00
Λ_b fraction, factor 2	—	+0.03 -0.02	+0.01 -0.01	—	+0.03 -0.01	+0.00 -0.02
$\tau(\Lambda_b) \pm 0.23$ ps	—	+0.00 -0.01	+0.01 -0.00	—	—	—
Total assumptions	± 0.00	± 0.05	± 0.03	± 0.00	+0.05 -0.04	+0.02 -0.04
Total Experimental	± 0.14	± 0.20	± 0.07	± 0.13	± 0.14	± 0.09

Table 8.11: Systematic uncertainties in the fit to B^+ and B^0 lifetimes caused by uncertainties in the sample composition. The quoted experimental uncertainties are similar to the fit to mean charged and neutral lifetimes and were taken from table 8.7 and scaled by the increase in statistical uncertainties.

Chapter 9

Conclusions

This thesis presents measurements of b-hadron lifetimes using the DELPHI detector at the LEP accelerator and storage ring. The lifetimes are determined from an unbinned maximum likelihood fit to the proper time measured from secondary vertex reconstruction. A total of 253 events were used. These measurements have shown the excellent track reconstruction precision that is achieved with a central track detector using silicon microstrip detectors combined with integrated front-end electronics. The results of the measurements are as follows:

Hit and extrapolation resolution A single hit precision of $8 \mu\text{m}$ and $16 \mu\text{m}$ for 92% and 8% of the hits is measured. The transverse track extrapolation uncertainty, σ_{ex} , in the plane transverse to the beam direction is measured to be:

$$\sigma_{\text{ex}} = \left[\sigma_{\text{asym}}^2 + \left(\frac{\sigma_{\text{scatter}}}{p \sin^{3/2} \theta} \right)^2 \right]$$

$$\sigma_{\text{asym}}^2 = 30 \pm 3 \mu\text{m}^2$$

$$\sigma_{\text{scatter}}^2 = 70 \pm 4 \mu\text{m}^2$$

where σ_{asym}^2 is the contribution in the limit of infinite momentum and $\sigma_{\text{scatter}}^2$ is the contribution from multiple Coulomb scattering.

The mean radial uncertainty on the secondary vertex reconstruction $\langle \sigma_r \rangle$ was found to be:

$$\langle \sigma_r \rangle = 190 \mu\text{m}$$

b-hadron lifetime results Quoting only the result from the fit with individual acceptances, which was less dependent upon Monte Carlo simulation, the mean b-hadron lifetime is:

$$\langle \tau_b \rangle = (1.49 \pm 0.11(\text{stat}) \pm 0.12(\text{syst})) \text{ps}$$

While this result has somewhat larger errors than the most recent determinations, see section 9.1, it is an independent measurement with quite different systematic errors. This mean, as has been stated before, is weighted towards the lifetime of the longest lived species of b-hadrons.

Results for the mean charged and neutral lifetimes were also found by taking the result with the smaller systematic error. The results are:

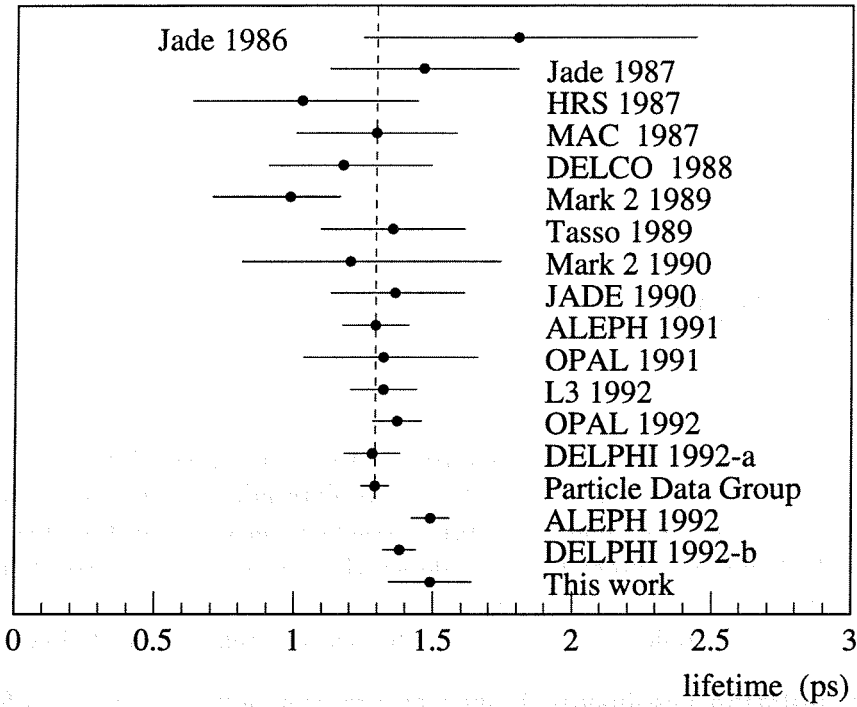


Figure 9.1: Graphical presentation of mean b -hadron lifetimes obtained in various experiments. Data from [9] where as well the references to the works are found. The line indicating the Particle Data Group average covers only those measurements that average is based upon.

$$\begin{aligned}
 \langle \tau_{charged} \rangle &= (1.56 \pm 0.19(\text{stat}) \pm 0.13(\text{sys}) \text{ ps}) \\
 \langle \tau_{neutral} \rangle &= (1.44 \pm 0.21(\text{stat}) \pm 0.14(\text{sys}) \text{ ps}) \\
 \langle \tau_{-}/\tau_{0} \rangle &= 1.09^{+0.28}_{-0.23}(\text{stat}) \pm 0.11(\text{sys})
 \end{aligned}$$

The assumptions stated in the previous section leads to measurements of the B^+ and B^0 lifetimes. The experimental and the uncertainties due to the physics assumptions have been combined into a common systematic uncertainty. The results are as follows:

$$\begin{aligned}
 \tau_{B^+} &= (1.56 \pm 0.19(\text{stat}) \pm 0.13(\text{sys}) \text{ ps}) \\
 \tau_{B^0} &= (1.55 \pm 0.25(\text{stat}) \pm 0.18(\text{sys}) \text{ ps}) \\
 \tau_{B^+}/\tau_{B^0} &= 1.01^{+0.29}_{-0.22}(\text{stat}) \pm 0.12(\text{sys})
 \end{aligned}$$

9.1 Comparison with Other Measurements

Measurements of the mean b -hadron lifetime have existed since some time, it is therefore natural to compare this results with the measurements.

The mean b -hadron lifetime as measured by several experiments is shown in figure 9.1. As expected the uncertainties decrease for the more recent measurements. The dashed line shows

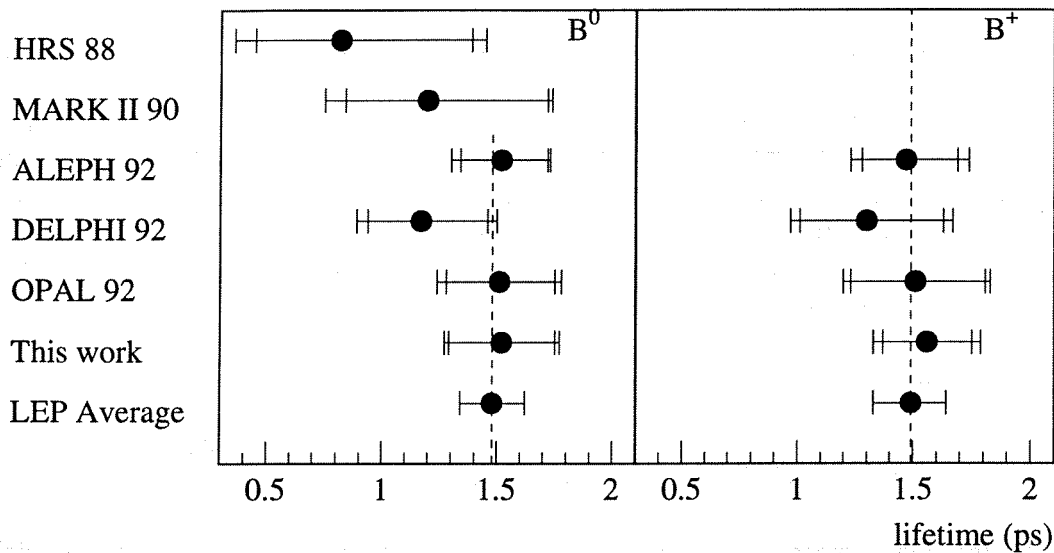


Figure 9.2: Graphical presentation of B^0 and B^+ lifetimes obtained in various experiments. The line indicates the weighted average of the measurements.

the Particle Data Group average [9], often called the world average. This is a weighted average calculated according to the following formula:

$$\bar{\tau} \pm \delta\bar{\tau} = \frac{\sum_i w_i \tau_i}{\sum_i w_i} + \left(\sum_i w_i \right)^{-1/2} \quad (9.1)$$

where $\tau_i \pm \delta\tau_i$ is the lifetime and its uncertainty obtained in each measurement and

$$w_i = (\delta\tau_i)^{-2} \quad (9.2)$$

is the weight assigned to each measurement. The sum, of course, is over the measurements.

The most recent measurements of the mean b-hadron lifetime; ALEPH 1992 [91], DELPHI 1992 [92] and this work are not included in the world average. When considering the measurements published after 1990, an apparent rise in the mean lifetime can be seen. Especially the ALEPH 1992 result is significantly higher than the world average.

Considerable less information is available on the separate lifetimes of B^+ and B^0 mesons. Figure 9.2 shows a graphical presentation of some measurements of the B^+ and the B^0 lifetimes. The ALEPH 92, [93], DELPHI 92, [94] and OPAL 92, [95] use correlations between the decay products of the B-meson to determine the B-meson type, see also appendix E The dashed lines show the weighted averages of the measurements:

$$\bar{\tau}_{B^+} = (1.49 \pm 0.14) \text{ ps}$$

$$\bar{\tau}_{B^0} = (1.48 \pm 0.14) \text{ ps}$$

With the present level of precision all the measurements are compatible.

9.2 Implications for the Model for b-hadron Decay.

A short introduction to the spectator-model for the decay of b-hadrons was given in section 1.6. The prediction of the model is that there should be no difference between the lifetimes of charged and neutral B-mesons. With additional corrections to this model, any lifetime differences should still be within 10%. The results of this measurement does not indicate any significant difference between the lifetimes of charged and neutral b-hadrons. Neither is any difference seen between the lifetimes of B^0 and the B^+ mesons when additional assumptions about the sample composition which the measurement was based upon is included. Within current experimental precision the spectator-model for b-hadron decay is therefore confirmed.

An expression for one of the matrix elements of the CKM matrix were given in equation 1.22. Inserting the result for the mean b-hadron lifetime from this measurement gives:

$$|V_{cb}| = \frac{10^{-15}\text{s}}{1.49 \times 10^{-12}\text{s}} = \begin{cases} 2.9 & (2.8) \\ 3.1 & (3.0) \end{cases} = \begin{cases} 0.044 & (0.043) \\ 0.046 & (0.045) \end{cases} \quad (9.3)$$

for the various quark mass ranges and values of $\Lambda_{\overline{MS}}$. Assuming the spectator model, the theoretical uncertainty, actually the range of the numbers, is 10% of the mean. The experimental uncertainty on the lifetime is 14%.

From this it is reasonable to expect $|V_{cb}|$ to be in the range:

$$0.036 < V_{cb} < 0.052 \quad (9.4)$$

Which is a somewhat narrower range than found in equation 1.12. The large theoretical uncertainties and assumptions must however be emphasized.

9.3 Perspectives for Future Measurements

This measurement was based upon a total of about 250 000 hadronic Z^0 decays. At the moment of writing a total of about 1 000 000 Z^0 decays have been recorded by DELPHI. With this increased event sample the statistical uncertainty on the measurements is expected to drop, in principle by a factor of two. The larger event sample as well should yield larger samples of partially reconstructed b-hadrons. With those samples it should be possible to improve substantially the precision on individual lifetime measurements for the b-hadron species. A larger event sample constitutes as well a better base for estimating systematic uncertainties since many systematic effects now are hidden by statistical fluctuations.

Especially worth mentioning is the RICH detector which was almost fully operational for the 1992 run period. The particle identification properties of this detector combined with the high precision of the Vertex Detector should greatly increase the number of reconstructed decays of b-hadrons leading to increased knowledge of branching ratios and lifetimes of b-hadrons.

Improvements in the detector apparatus is as well expected to boost the precision of this type of measurements. The silicon microstrip technology has shown its usefulness at LEP. Without doubt this type of charged particle detectors will play an important role in all major high energy physics experiments at existing and future accelerators. All LEP experiments have installed silicon microstrip vertex detectors at the time of writing, some with two-dimensional readout. For resolving secondary vertices the additional z information provided by those will especially help in reducing ambiguities in the assignment of tracks to vertices. For future proton colliders very large, a factor of hundred more channels, silicon microstrip detectors systems are under study.

The very interesting question of possible CP symmetry violation in b-hadron decays will probably not get an answer at LEP. For this we have to wait for experiments at proposed "B-meson factories" or high luminosity proton colliders.

List of Figures

1.1	Feynman graph for the process $Z^0 \rightarrow q\bar{q}$	6
1.2	Spectator model decay	8
1.3	b-quark decay.	8
1.4	Non-spectator corrections.	11
1.5	Event display of a b-hadron decay candidate	14
2.1	The injection scheme for LEP.	16
2.2	The LEP Accelerator	17
2.3	Perspective view of the DELPHI detector	18
2.4	Event display of a Z^0 decay	20
2.5	Event display of a Z^0 decay	21
3.1	Operation of silicon detectors	27
3.2	Landau spectrum from the detectors	28
3.3	Micro-photograph of Capacitively Coupled Silicon Detector	29
3.4	Operation of capacitively coupled Si detectors.	30
3.5	Circuit diagram used to calculate signal and noise voltages	30
3.6	Detector Capacitances	31
3.7	Poly-silicon resistance before and after irradiation.	32
3.8	Coupling capacitance before and after irradiation.	32
3.9	Depletion layer capacitance before and after irradiation.	33
3.10	Capacitances between aluminium strips.	33
3.11	Results from acceptance tests.	35
3.12	Straightness of diffusion lines	37
3.13	The MX3 architecture	39
3.14	Control signals for the MX3 chip	39
3.15	Schematic drawing of the detector modules.	41
3.16	Cross section through the detector modules.	41
3.17	Microscope and assembly bench	42
3.18	Schematic drawing of the Microvertex Detector.	45
3.19	Schematic drawing of the support of the Microvertex Detector.	45
3.20	Photograph of a module for the Outer layer	46
3.21	Close up photograph of a module for the Outer layer	46
3.22	Microvertex Detector temperature	49
3.23	Schematic drawing of the 3 layer detector.	50
3.24	Location of points measured with the microscope.	51
3.25	Microscope measurements of modules.	52
3.26	Microscope measurement precision	53
3.27	Deviation from straight angle of the corners of the counters.	54

3.28	Track residual on Inner layer	55
3.29	The three dimensional surveying machine	55
4.1	On-line event display	57
4.2	Block diagram of the SIROCCO IV.	58
4.3	Common noise	60
4.4	Noise per chip	61
4.5	Detectors participating in the trigger	62
4.6	Trigger timing	63
4.7	Trigger Efficiency for Hadronic events	64
4.8	Detector leakage current	65
4.9	Optical system for stability monitoring	66
4.10	Forced temperature change of the detector	67
4.11	Output from the position monitoring system	67
5.1	charge division	69
5.2	Charge division in magnetic field.	70
5.3	Definition of track angles.	71
5.4	Lorentz angle.	72
5.5	Residuals between hits in the Microvertex Detector and reconstructed tracks	73
5.6	Muon missed distance	75
5.7	Coordinate system used in evaluation of muon missed distance	75
5.8	Counter Resolution	78
5.9	Coordinate system used in the evaluation of detector resolution	78
5.10	Vertex error definition	80
5.11	$P(\chi^2)$ distributions for three track vertices	82
6.1	Jet distribution	85
6.2	K^0 invariant mass distribution	87
6.3	Photon conversions versus radius	87
6.4	Mass spectrum from converted photons.	88
6.5	Intrinsic charge precision	90
6.6	Average interaction point	90
6.7	$P(\chi^2)$ distributions for the vertex fits	91
6.8	Probability of two hits on any track	93
6.9	Reconstructed mass	94
6.10	Decay distance of accepted events	95
6.11	Acollinearity and multiplicity distributions	96
6.12	Missing charged particles	98
7.1	Charge measurement precision	100
7.2	Reconstructed versus true decay lengths	101
7.3	Ratio of true to estimated momentum	102
7.4	Estimated momentum spectrum	102
7.5	True and reconstructed boost and proper time	103
7.6	Acceptance of b events	105
7.7	Vertex Configuration	107
7.8	Lorentz factor for selected D mesons	109
7.9	D meson proper times	111

8.1	Mean b-hadron lifetime	113
8.2	The proper times of the accepted events	115
8.3	Lifetimes for different mass requirements	119
8.4	Number of events of specific charge versus mass	119
8.5	one and two sigma contours.	120
9.1	Graphical presentation of mean b-hadron lifetimes	124
9.2	Graphical presentation of B^+ and B^0 lifetimes	125

List of Tables

1.1	Elementary fermions.	4
1.2	Gauge bosons.	4
1.3	c and b-hadrons	7
2.1	Parameters of LEP	15
2.2	Track detector performance	24
2.3	Calorimeter performance	25
3.1	Technical Specifications for the MX3 circuit	38
3.2	Mass of detector modules	40
3.3	Manufacturers specifications of the movable tables.	43
3.4	Mass of the detector	47
3.5	Mass of the repeater electronics	48
6.1	Charge reconstruction precision	89
6.2	Events passing vertex cuts	92
6.3	Number of selected vertices.	96
6.4	Selected sample composition	99
7.1	α parameter for different hadrons.	104
7.2	Parameters of the acceptance functions	106
7.3	D lifetime results	110
8.1	Mean b hadron lifetime	113
8.2	Systematic effects on the mean lifetime fits	114
8.3	Summary of systematic uncertainties on the mean lifetime.	114
8.4	Fit to average charged and neutral lifetimes	116
8.5	Systematic effects in the two lifetime fit, method 1	117
8.6	Systematic effects in the two lifetime fit, method 2	117
8.7	Summary of systematic uncertainties in the two lifetime fit	118
8.8	Mean excess lifetime for different charges.	118
8.9	B^+ and B^0 lifetimes.	120
8.10	Systematic effects in the fit to B^+ and B^0 lifetimes	121
8.11	Systematic uncertainties in the fit to B^+ and B^0 lifetimes.	122

Bibliography

- [1] L. Lyons and D. H. Saxon, Rep. Prog. Phys. **52** (1989) 1015–1081
- [2] R. Corby Howis and H. Kragh, Scientific American **268** (1993) 62–67
- [3] F. Mandl and G. Shaw, Quantum Field Theory, (Wiley, 1984)
- [4] D. H. Perkins, Introduction to High Energy Physics, third edition, (Addison Wesley, 1987)
- [5] DELPHI Collaboration, Phys. Lett. **B 231** (1989) 539
- [6] DELPHI Collaboration, Nucl. Phys. **B 367** (1991) 511–574
- [7] DELPHI Collaboration, Preliminary results from 1991 DELPHI data on the Z^0 Resonance Parameters and its Electroweak Couplings, Contributed to the Rencontre de Moriond 1992, DELPHI 92-29, 1992.
- [8] Denegri et al, Rev. Mod. Phys. **62** (1990) 1
- [9] Particle Data group, Physical Review D **45** (1992)
- [10] The LEP Collaborations: Aleph, Delphi, L3 and Opal, Phys. Lett. **B 276** (1992) 247
- [11] J. Nahim, Scientific American **262 Number 6** (1990) 80–87
- [12] DELPHI Collaboration, Nuclear Physics B **373** (1992) 3–34
- [13] A. D. Martin F. Halzen, Quarks and Leptons: An introductory Course in Modern Particle Physics, (Wiley, 1984)
- [14] DELPHI Collaboration, Phys. Lett. **B 281** (1992) 383
- [15] DELPHI Collaboration, Phys. Lett. **B 289** (1992) 199
- [16] ALEPH Collaboration, A measurement of the B_s^0 lifetime, Presented at the American Physical Society Division of Particles and Fields conference, Fermi National Laboratory, Batavia, Illinois, USA, November 10th. to 14th. 1992
- [17] DELPHI Collaboration, Measurement of Λ_b production and Lifetime in Z^0 decays, DELPHI 92-81, 1992., Presented at the American Physical Society Division of Particles and Fields conference, Fermi National Laboratory, Batavia, Illinois, USA, November 10th. to 14th. 1992
- [18] ALEPH Collaboration, Phys. Lett. **B 297** (1992) 449–458
- [19] C. Peterson et al, Phys. Rev. D **27** (1983) 105–111

- [20] H. Schröder, (Springer-Verlag, Berlin Heidelberg, 1989,)
- [21] M. A. Schifman, (DESY, Hamburg, 1986,)
- [22] M.A. Schifman, (Nucl. Phys. B (proc. suppl.) 3 1988 289,)
- [23] M. Kobayashi and T. Maskawa, Prog. Theor. Phys **49** (1973) 652
- [24] Cabibbo, Phys. Rev. Lett. **10** (1963) 531
- [25] L. L. Chau and W. Y. Keung, Phys. Rev. Lett. **51** (1984) 1802
- [26] J. D. Bjorken, Theoretical Topics in B-Physics, SLAC-PUB-5389, December 1990, Lectures given at the 18th annual SLAC Summer Institute on Particle Physics, Stanford, July 16-27, 1990
- [27] R. Rückl, Proc. Int. Conf. on High Energy Physics, Leipzig, 1984, (Akad der Wissenschaften der DDR, Zeuthen, GDR, (now FRG), 1984,) p. 135
- [28] E. Pietarinen A. Ali, Nucl. Phys. **B 154** (1979) 519
- [29] N. Cabibbo et al., Nucl. Phys. **B 155** (1979) 93
- [30] G. Altarelli et al., Nucl. Phys. **B 208** (1982) 365
- [31] G. Corbo, Phys. Lett. **116 B** (1982) 298
- [32] G. Corbo, Nucl. Phys. **B 212** (1983) 99
- [33] J. Ellis et al., Nucl. Phys. **B 100** (1975) 313
- [34] G. Altarelli et al., Nucl. Phys. **B 187** (1981) 461
- [35] J. Kuhn et al., Heavy Flavours at LEP, MPI-PAE/PTh 49/89 and CERN PRE 89-063, section 2.6
- [36] S. Myers, The Lep Collider, from Design to Approval and Commissioning., CERN 91-08
- [37] DELPHI collaboration, DELPHI Technical Proposal, DELPHI 83-66 1993 and CERN/LEPC/P 2, 17 May 1983
- [38] DELPHI collaboration, DELPHI Progress Report, DELPHI 84-60, 1984 and CERN/LEPC 84 6, LEPC/PR 6, 26 September 1984
- [39] DELPHI Collaboration, Nucl. Instr. and Methods **A303** (1991) 233
- [40] J. P. Grillet, Technical Specification of the Superconducting Solenoid for the DELPHI Collider Experiment, 6 February, 1985, DELPHI 85-14, 1995
- [41] E.H. Nicollian and J.R. Brews, MOS Physics and Technology, (Wiley, 1982)
- [42] S.M. Sze, VLSI Technology, 2nd edition, (McGraw-Hill Book Company, 1988)
- [43] C. Kittel, Introduction to Solid State Physics, Sixth Edition, (Wiley, 1986)
- [44] J. Kemmer, Nucl. Instr. and Methods **A169** (1980) 499

- [45] J. B. England et al., Nucl. Instr. and Methods **185** (1981)
- [46] B. D. Hyams et al., Nucl. Instr. and Methods **A205** (1983) 99
- [47] R. Klanner, Silicon Detectors, Invited talk at Topical Seminar on Perspectives of Exp. Apparatus at Future High Energy Machines, San Miniato 1984.
- [48] P. Weilhammer, Experience with Si Detectors in NA32, Internal Report CERN-EP/86-54, CERN, 1986
- [49] R. Alberganti et al., Nucl. Instr. and Methods **A248** (1986) 337-353, Charm Production Experiment E691, Contribution to the XXII Int. Conf on High Energy Physics, Berkely 1986. NA14 Experiment.
- [50] G. Mæhlum, Silicon strip detectors for minimum ionizing particles, Cand. Scient. thesis, Institute of physics, University of Oslo, 1986.
- [51] F. Sauli, Instrumentation in High Energy Physics, (World Scientific Publishing Co., 1992), Review on silicon Microstrip counters by A. Peisert
- [52] L. Landau, Journal Phys. (USSR) **8** (1944)
- [53] G. Hall, Nucl. Instr. and Methods **A220** (1983) 356-362
- [54] S. Hancock et al., Physical Review A **28** (1983) 615-519
- [55] M. Caccia et al., Nucl. Instr. and Methods **A260** (1987) 124
- [56] T. Tuuva, Silicon Strip Detectors with VLSI Readout, Ph.D. thesis, Department of High Energy Physics, University of Helsinki, 1990.
- [57] H. Dijkstra et al, Radiation tests with Capacitively coupled Silicon Detectors, Contribution to the XXIV International Conference on High Energy Physics, Munich, August 4-10, 1988
- [58] N. Weste and K. Eshraghian, CMOS VLSI Design, A systems Perspective, (Addison Wesley, 1985), Chapter 4.9
- [59] J. Stanton, A Low Power Low Noise Preamplifier for a 128 Channel Read-Out Integrated Circuit, RAL-89-009 1989.
- [60] A. Andreazza et al., Results on the Delphi Microvertex Alignment from a Precise 3-D Mapping, DELPHI 91-37, 1991.
- [61] FASTBUS ANSI/IEEE STD. 960-1986, IEEE, New York, USA
- [62] N. Bingefors and M. Burns, Sirocco IV, Hardware and Software Manual, DELPHI 88-48, 1988
- [63] S. Cairanti et al, PANDORA (The DELPHI Local Trigger Supervisor) User Manual, DELPHI 89-12, 1998.
- [64] DSP56000/DSP56001 Digital Signal Processor User's Manual., Available from: Motorola Ltd., European Literature Center, 88 Tamers Drive, Blakelands, Milton Keynes, MK14 5BP, England

- [65] P. Jalocha, DSP Notes, Internal Vertex Detector Note
- [66] M. Pegoraro G. Barichello, Microvertex Fan Out, DELPHI 90-19
- [67] The DELPHI Fastbus Data Acquisition System, DELPHI 91-92, 1991., Presented at the Computing in High Energy Physics conference, Tsukuba, Japan, March 11-18 1991.
- [68] Architecture and Performance of the DELPHI Fastbus Data Acquisition and Control System, DELPHI 91-93, 1991., Presented at the Computing in High Energy Physics conference, Tsukuba, Japan, March 11-18 1991
- [69] J.A. Fuster et al., The Online Software for the first and Second Level Trigger of DELPHI, DELPHI 91-112, 1991.
- [70] T. Adye et al., Computer physics Communication **57** (1989) 466
- [71] T. Adye et al., The Slow Control of the DELPHI Experiment at LEP, DELPHI 93-12, 1993.
- [72] C. Meroni et al., Microvertex Slow control Manual, DELPHI 90-52, 1990.
- [73] W. Trischuk, Laser Spot Monitoring of the Micro-Vertex Detector, Internal Vertex Detector note.
- [74] N. Bingeors et al., Nucl. Instr. and Methods **A328** (1993) 447-471
- [75] E. Belau et al., Nucl. Inst and Meth. **214** (1983) 253-260
- [76] P. Billoir et al., Report on Global Track and Vertex Fitting in the DELPHI Detector, DELPHI 86-99, 1986.
- [77] Data Analysis Group, Report on Local Pattern Recognition Methods for the Individual Detectors in DELPHI, DELPHI 86-56, 1986.
- [78] T. Sjöstrand, Computer Physics Comm **39** (1986) 347
- [79] M. Bengtsson T. Sjöstrand, Computer Physics Comm **43** (1987) 367
- [80] M. Bengtsson T. Sjöstrand, The Lund Monte Carlo Programs, JETSET version 7.2
- [81] DELPHI Collaboration, Z. Phys. C **56** (1992) 47-61
- [82] DELPHI collaboration, DELSIM, DELPHI Event generation and Detector Simulation Reference manual, DELPHI 89-68, 1989.
- [83] DELPHI collaboration, DELSIM, DELPHI Event generation and Detector Simulation User's Guide, DELPHI 89-68, 1989.
- [84] M. Caccia et al., The DELPHI Vertex Detector Simulation Reference Manual, DELPHI 91-34, 1991.
- [85] DELPHI Collaboration, Z. Phys. C **54** (1992) 55-73
- [86] DELPHI Collaboration, Phys. Lett. **B 281** (1992) 383-393
- [87] JADE collaboration, Z. Phys. C **33** (1986) 23-31

- [88] D. Johnson et al., A Beamspot Database for Lifetime Measurements, 18 March 1992, DELPHI 92-36, 1992.
- [89] B. Franek, Rutherford Appleton Laboratory, RAL-85-026 1985.
- [90] DELPHI Collaboration, Phys. Lett. **B 275** (1992) 231-242.
- [91] ALEPH Collaboration, Phys. Lett. **B 295** (1992) 174-186
- [92] Refined Measurement of the Average Lifetime of B Hadrons using High pt Muons, DELPHI 92-83, 1992.
- [93] ALEPH Collaboration, Measurement of the \bar{B}^0 and B^- Meson Lifetimes, CERN-PPE/93-42, submitted to Phys. Lett. B
- [94] DELPHI Collaboration, Z. Phys. C **57** (1993) 181-195
- [95] OPAL Collaboration, Measurement of the B^0 and B^+ lifetimes, CERN-PPE/93-33, submitted to Phys. Lett. B

Appendix A

Derivation of the Likelihood Functions

If we have a set of independent measured quantities, \mathbf{x} , from a probability density function, $f(\mathbf{x}; \mathbf{A})$, where \mathbf{A} is an unknown set of parameters. The method of maximum likelihood consists of finding the set of values of \mathbf{A} which maximizes the joint probability density for all the data, given by:

$$\mathcal{L} = \prod_i f(\mathbf{x}_i; \mathbf{A}) = \prod_i \mathcal{L}_i \quad (\text{A.1})$$

where \mathcal{L} is called the likelihood. Since both \mathcal{L} and $\ln \mathcal{L}$ is maximized for the same set \mathbf{A} it is sufficient to solve the likelihood equation:

$$\frac{\partial \ln \mathcal{L}}{\partial A_n} = 0 \quad (\text{A.2})$$

Alternatively the minimum of $-\ln \mathcal{L}$ can be found numerically as is the case here.

In our case the measured quantities is the observed proper times, t_i , and the charge, Q_i . The vector of unknown parameters is the lifetimes of the different particles, τ_ν , and the fraction of different species, F_ν , of charge, q_ν , in the sample.

We therefore need to find the probability, $P(t_i, Q_i; \tau_\nu, F_\nu)$, of observing a decay at proper time, t_i , of charge, Q_i , of particle, ν , as a function of the lifetime, τ_ν , and the fraction, F_ν , of this particle in the sample.

The simplest case is when we have only one type of particle and no charge information. In this case the number of decayed particles, $N(t)$, for an initial sample of particles, $N(0)$, with mean life, τ , is given by the exponential decay law:

$$N(t) = N(0)e^{-t/\tau} \quad (\text{A.3})$$

where τ is the lifetime of the particle. The probability, $P(t_i; \tau)$, of observing $N(t_i)$ particles at time t_i is thus given by

$$P(t_i; \tau) = \frac{N(t)}{N(0)} = \frac{e^{-t_i/\tau}}{\int_0^\infty e^{-t/\tau} d\tau} = \frac{e^{-t_i/\tau}}{\tau} = \mathcal{L}_i \quad (\text{A.4})$$

As a check we see that

$$\frac{d}{d\tau} \sum_i^{N_0} \ln \mathcal{L} = 0 \quad \text{for} \quad \tau = \frac{\sum_i t_i}{N_0} \quad (\text{A.5})$$

as expected.

If we have a mixture of particles of type ν with lifetimes, τ_ν , the probability of observing a decay of a specific type of particle, $P(t_i; \tau_\nu)$, is then

$$P(t_i; \tau_\nu) = \frac{N_\nu(0)}{N(0)} N_\nu(t) = F_\nu \frac{e^{-t_i/\tau_\nu}}{\tau_\nu} \quad (\text{A.6})$$

where $F_\nu = N_\nu(0)/N(0)$ is the fraction of particles of type ν at $t = 0$ with $\sum_\nu F_\nu = 1$.

Introducing boundaries on the observable time, $t^{\min} < t_i < t^{\max}$ we get:

$$P(t_i; \tau_\nu) = F_\nu \frac{\frac{1}{\tau_\nu} e^{-t_i/\tau_\nu}}{\int_{t^{\min}}^{t^{\max}} \frac{1}{\tau_\nu} e^{-t/\tau_\nu}} = \frac{F_\nu e^{-t_i/\tau_\nu}}{\tau_\nu [e^{-t^{\min}/\tau_\nu} - e^{-t^{\max}/\tau_\nu}]} \quad (\text{A.7})$$

When introducing the charge we get a mixture of particles ν of charges q_ν with lifetimes τ_ν . Our measured quantities is the proper time t_i and charge Q_i . If we always observe the correct charge, $Q_i = q_\nu$ for particle ν then the probability of observing a particle ν becomes:

$$P(t_i, Q_i; \tau_\nu, F_\nu) = \frac{\sum_\nu \delta_{q_\nu}^{Q_i} \frac{F_\nu}{\tau_\nu} e^{-t_i/\tau_\nu}}{\int_{t^{\min}}^{t^{\max}} \sum_{Q_j} [\sum_\nu \delta_{q_\nu}^{Q_j} \frac{F_\nu}{\tau_\nu} e^{-t/\tau_\nu}] dt} \quad (\text{A.8})$$

where

$$\delta_{q_\nu}^{Q_i} = \begin{cases} 1 & \text{if } Q_i = q_\nu \\ 0 & \text{if } Q_i \neq q_\nu \end{cases} \quad (\text{A.9})$$

The normalization is over the observable region in proper time, $t^{\min} < t_i < t^{\max}$, the observed charges, Q_j and the number of particle species ν .

Summing over the charges and integrating we get:

$$P(t_i, Q_i; \tau_\nu, F_\nu) = \begin{cases} \frac{\sum_\nu F_\nu \frac{1}{\tau_\nu} e^{-t_i/\tau_\nu}}{\sum_\nu F_\nu [e^{-t^{\min}/\tau_\nu} - e^{-t^{\max}/\tau_\nu}]} & \text{for } Q_i = q_\nu \\ 0 & \text{for } Q_i \neq q_\nu \end{cases} \quad (\text{A.10})$$

The summations runs thus only over the particle species with the same charge as observed.

If we assume that there is a certain probability, $P(q_\nu \rightarrow Q_i)$, $\sum_j P(q_\nu \rightarrow Q_j) = 1$, that a particle of species ν with charge q_ν will be observed as having charge Q_i , were Q_i not necessarily is the same as q_ν , the probability of observing a particle ν of charge q_ν becomes:

$$P(t_i, Q_i; \tau_\nu, F_\nu) = \frac{\sum_\nu P(q_\nu \rightarrow Q_i) F_\nu \frac{1}{\tau_\nu} e^{-t_i/\tau_\nu}}{\int_{t^{\min}}^{t^{\max}} \sum_\nu [\sum_{Q_j} P(q_\nu \rightarrow Q_j) F_\nu \frac{1}{\tau_\nu} e^{-t/\tau_\nu}] dt} \quad (\text{A.11})$$

summing over the observed charges Q_j :

$$P(t_i, Q_i; \tau_\nu, F_\nu) = \frac{\sum_\nu P(q_\nu \rightarrow Q_i) F_\nu \frac{1}{\tau_\nu} e^{-t_i/\tau_\nu}}{\sum_\nu \int_{t^{\min}}^{t^{\max}} F_\nu \frac{1}{\tau_\nu} e^{-t/\tau_\nu} dt} \quad (\text{A.12})$$

Since $P(t_i, Q_i; \tau_\nu, F_\nu)$ is normalized we can write:

$$\mathcal{L}_i = P(t_i, Q_i; \tau_\nu, F_\nu) \quad (\text{A.13})$$

The general result is then:

$$\mathcal{L}_i = \sum_{\nu} P(q_{\nu} \rightarrow Q_i) \mathcal{N}_{\nu} e^{-t_i/\tau_{\nu}} \quad (\text{A.14})$$

$$\mathcal{N}_{\nu} = \frac{F_{\nu}}{\tau_{\nu} \int_{t^{\min}}^{t^{\max}} \sum_{\mu} F_{\mu} \frac{1}{\tau_{\mu}} e^{-t/\tau_{\mu}} dt} \quad (\text{A.15})$$

where the summation variable in the denominator has been changed from ν to μ .

Integrating A.15 over the observable proper time we get:

$$\mathcal{N}_{\nu} = \frac{F_{\nu}}{\tau_{\nu} \sum_{\mu} F_{\mu} [e^{-t^{\min}/\tau_{\mu}} - e^{-t^{\max}/\tau_{\mu}}]} \quad (\text{A.16})$$

Letting $t^{\min} = 0$

$$\mathcal{N}_{\nu} = \frac{F_{\nu}}{\tau_{\nu} \sum_{\mu} F_{\mu} [1 - e^{-t^{\max}/\tau_{\mu}}]} \quad (\text{A.17})$$

A.1 Uncertainty in Proper Time and Time Dependent Acceptance.

Uncertainties, σ_i , on the individual data points can be included as a convolution of the probability density function with a gaussian [1]. A time dependent acceptance $\omega(t)$ can be introduced as a simple multiplicative factor:

$$\mathcal{L}_i = \sum_{\nu} P(q_{\nu} \rightarrow Q_i) \mathcal{N}_{\nu} \omega(t) \int_{-\infty}^{\infty} e^{-t/\tau_{\nu}} e^{-(t-t_i)^2/2\sigma_i^2} dt \quad (\text{A.18})$$

$$\mathcal{N}_{\nu} = \frac{F_{\nu}}{\tau_{\nu} \int_{t^{\min}}^{t^{\max}} \sum_{\mu} \omega(t) \int_{-\infty}^{\infty} e^{-t/\tau_{\mu}} e^{-(t-t')^2/2\sigma_i^2} dt dt'} \quad (\text{A.19})$$

For numerical analysis the convolution integral has to be limited:

$$\mathcal{L} = \sum_{\nu} P(q_{\nu} \rightarrow Q_i) \mathcal{N}_{\nu} \omega(t) \int_{t_i - n\sigma_i}^{t_i + n\sigma_i} e^{-t/\tau_{\nu}} e^{-(t-t_i)^2/2\sigma_i^2} dt \quad (\text{A.20})$$

$$\mathcal{N}_{\nu} = \frac{F_{\nu}}{\tau_{\nu} \int_{t^{\min}}^{t^{\max}} \sum_{\mu} \omega(t) \int_{t_i - n\sigma_i}^{t_i + n\sigma_i} e^{-t/\tau_{\mu}} e^{-(t-t')^2/2\sigma_i^2} dt dt'} \quad (\text{A.21})$$

where n has to be chosen sufficiently large.

Which is the expressions used in section 7.10 and 7.11 found in section 7.3 If the integration over the proper time acceptance are from 0 to t^{\max} with t^{\max} large compared to the lifetimes, the integral will be close to unity. In our case $t^{\min} = 0$ and $t^{\max} = 10$ ps.

A.2 Individual Event Acceptances

When the acceptance is calculated on an event by event basis we have seen that there is no need for the global acceptance function, $\omega(t)$. The gaussian convolution reduces as well to a constant

and can be dropped from the likelihood, see section 7.4. The normalization A.15 however gets modified to have event dependent integration boundaries, $t_i^{\min} < t_i < t_i^{\max}$:

$$\mathcal{N}_\nu = \frac{F_\nu}{\tau_\nu \int_{t_i^{\min}}^{t_i^{\max}} \sum_\mu F_\mu \frac{1}{\tau_\mu} e^{-t/\tau_\mu} dt} \quad (\text{A.22})$$

Our measured time is however the *excess*, t_i^{ex} , proper time:

$$t_i^{\text{ex}} = t_i - t_i^{\min} \quad (\text{A.23})$$

which is the proper time in excess of the minimum proper time, t_i^{\min} , that it would be possible to observe the decay.

We also have:

$$t_i^{\max} = t_i^{\min} + T^{\max} \quad (\text{A.24})$$

where T^{\max} is the same for all events. Inserting A.23 and A.24 into A.14 and A.22 we get:

$$\mathcal{L} = \sum_\nu P(q_\nu \rightarrow Q_i) \mathcal{N}_\nu e^{-(t_i^{\text{ex}} + t_i^{\min})/\tau_\nu} \quad (\text{A.25})$$

$$\mathcal{N}_\nu = \frac{F_\nu}{\tau_\nu \int_{t_i^{\min}}^{t_i^{\min} + T^{\max}} \sum_\mu F_\mu \frac{1}{\tau_\mu} e^{-(t + t_i^{\min})/\tau_\mu} dt} \quad (\text{A.26})$$

Integrating and rearranging:

$$\mathcal{N}_\nu = \frac{F_\nu}{\tau_\nu \sum_\mu F_\mu e^{-t_i^{\min}/\tau_\mu} [1 - e^{-(T^{\max})/\tau_\mu}]} \quad (\text{A.27})$$

Which could be used in the fit with individual acceptances. The actual expressions used were however derived along a slightly different line of thought:

We want to derive an acceptance from the observed minimum proper times, t_i^{\min} . The acceptance for a single event is thus defined as the number of particles of type ν that would be observed at minimum time t_i^{\min} divided by the number of particles of all types that could be observed at the same minimum time:

$$\omega_\nu(t_i) = \frac{N_\nu(t_i^{\min})}{\sum_\mu N_\mu(t_i^{\min})} \quad (\text{A.28})$$

Substituting the exponential decay law, but this time in t_i^{\min} :

$$\omega_\nu(t_i) = \frac{f_\nu e^{t_i^{\min}/\tau_\nu}}{\sum_\mu f_\mu e^{t_i^{\min}/\tau_\mu}} \quad (\text{A.29})$$

were f_ν is the fractions of the different species that would have been observed if their lifetimes were equal.

Summing and averaging the single acceptances over all the observed decays gives the observed fraction of species ν of the total sample:

$$F_\nu = \frac{1}{N} \times \sum_i^N \frac{f_\nu e^{-t_i^{\min}/\tau_\nu}}{\sum_\mu f_\mu e^{-t_i^{\min}/\tau_\mu}} \quad (\text{A.30})$$

When constructing the likelihood function we can now assume all dependence of the observed minimum times on the particle type to be contained in the observed fractions, as given by A.30.

We can therefore write down the likelihood function without any explicit dependence on the t_i^{\min} as long as we use A.30 for the observed fractions.

$$\mathcal{L}_i = \sum_{\nu} P(q_{\nu} \rightarrow Q_i) \mathcal{N}_{\nu} e^{-t_i^{\text{ex}}/\tau_{\nu}} \quad (\text{A.31})$$

$$\mathcal{N}_{\nu} = \frac{F_{\nu}}{\tau_{\nu} [1 - e^{-T^{\text{max}}/\tau_{\nu}}]} \quad (\text{A.32})$$

$$F_{\nu} = \frac{1}{N} \times \sum_i^N \frac{f_{\nu} e^{-t_i^{\text{min}}/\tau_{\nu}}}{\sum_{\mu} f_{\mu} e^{-t_i^{\text{min}}/\tau_{\mu}}} \quad (\text{A.33})$$

The above expressions reduce to A.14 and A.15 for only one particle type. For several particle types the expressions are different. Both have been tried on the data. The discrepancy in the fit results between the two likelihood function is negligible. The major reason for this being the choice of the upper time limit, $T^{\text{max}} = 8$ ps which is considerable larger than the lifetimes. The contribution of the acceptance in proper time to the normalization is therefore very small.

A.3 References

- [1] Phys Lett B 302 (1993) 356-368

Appendix B

Reprint of NIM publication

PROGRESS IN THE CONSTRUCTION OF THE DELPHI MICROVERTEX DETECTOR

M. BURNS, H. DIJKSTRA, R. HORISBERGER, L. HUBBELING, B.D. HYAMS, G. MAEHLUM,
A. PEISERT, J.P. VANUXEM, P. WEILHAMMER and A. ZALEWSKA *

CERN, CH-1211 Geneva 23, Switzerland

W. KRUPINSKI, H. PALKA and M. TURALA

Institute of Nuclear Physics, Cracow, Poland

T. PALENIUS and E. SUNDELL

Åbo Akademi, Turku, Finland

T. TUUVA

University of Helsinki, Finland

M. CACCIA, W. KUCEWICZ, C. MERONI, M. PEGORARO, N. REDAELLI, R. TURCHETTA,
A. STOCCHI, C. TRONCON and G. VEGNI

INFN, Milan, Italy

M. MAZZUCATO, F. SIMONETTO and G. ZUMERLE

INFN, Padua, Italy

P. ALLPORT, G. KALMUS, P. SELLER, J. STANTON and M. TYNDEL

Rutherford Appleton Laboratory, Chilton, Didcot, Oxon., OX11 0QX, UK

N. BINGEFORS

University of Uppsala, Sweden

The design and progress in the construction of the DELPHI microvertex detector are presented. The layout is described, together with results on precision mounting of silicon detectors. The development of ac-coupled silicon microstrip detectors was an important contribution to the design. The use of low-power CMOS readout chips facilitates the cooling of the detector. A description of the fourth-generation readout processor for silicon strip detectors, the SIROCCO IV, implemented in FASTBUS, is given. Finally, two complementary systems for in-situ position monitoring of the detectors are described.

1. Introduction

This article presents important progress made in the construction of the DELPHI microvertex detector. The physics aspects of this detector were reported by A. Zalewska at this conference (3rd Topical Seminar on Perspectives for Experimental Apparatus at Future

High-Energy Machines and Underground Laboratories, San Miniato, 1988). A general overview of the detector can be found in refs. [1] and [2].

The detector has to be assembled to high precision. Considerable advances have been made in the assembly and alignment procedures, including features which allow the reconstruction of the position in space of all sensitive elements prior to installation.

Space and power considerations require the use of integrated readout electronics for the microvertex detector. A problem connected to the use of integrated

* On leave of absence from the Institute of Nuclear Physics, Cracow, Poland.

readout electronics with conventional dc-coupled detectors is the flow of leakage current to the amplifier input stages. This causes base-line variations of the readout, and so requires an ADC of large dynamic range. This difficulty initiated the development of detectors with integrated coupling capacitors and bias resistors [7].

Different chips have been manufactured for the readout of silicon microstrip detectors. The NMOS Microplex chips [4,5] have been known for several years. The high power consumption of the Microplex necessitated pulses power running, which has been demonstrated successfully [12]. However, it seemed convenient to build a chip with lower consumption. A chip similar in design to the original Microplex, called MXII, was therefore built [6]. This is the chip we intend to use in the experiment.

This report will present the overall design of the DELPHI microvertex detector together with results on mechanical precision in the assembly of detector modules and measurements on the silicon detectors and the MX II chips, and finally a description of the planned position-monitoring systems to be installed with the detector is given.

2. The mechanical design

Our design is kept simple, with the main objectives to have high rigidity combined with low mass. The design also includes components for 3-dimensional

measurement of the detector to enable us to reconstruct the position in space of the sensitive elements.

The design is shown in fig. 1 and is characterized by two concentric layers of silicon at average radius $r_1 = 90$ mm and $r_2 = 109$ mm around the LEP beampipe. The detector will fit in between the inner detector at radius 118 mm and the beampipe at radius 80 mm. The coverage in θ is $\pm 45^\circ$. Only the $R\Phi$ coordinate is measured.

Each of the two layers is formed by 24 modules, each consisting of 4 detectors (see fig. 2), the sensitive area of each detector being 32×58 mm² and 25.6×58 mm² for the outer and inner layer, respectively. A carbon fibre profile is attached to the backside. The readout chips are placed on a ceramic substrate attached to each end of the module, which also carries the hybrid circuits. The chips read out two daisy-chained detectors at the ends of the modules. Each half-module (two daisy-chained detectors plus a hybrid circuit) is tested for functionality before it is joined with the other half-module. The hybrid circuit also includes components for pulsed power supply of the analog part of the readout chips.

The modules are mounted on aluminium rings, called end rings, and held in place by two screws through each of the ceramic substrates into the aluminium. The end rings contain channels for the cooling medium and support the signal bus carrying control signals to the chips and the buffering circuits of the output signals. Each module is connected at both ends via short Cap-

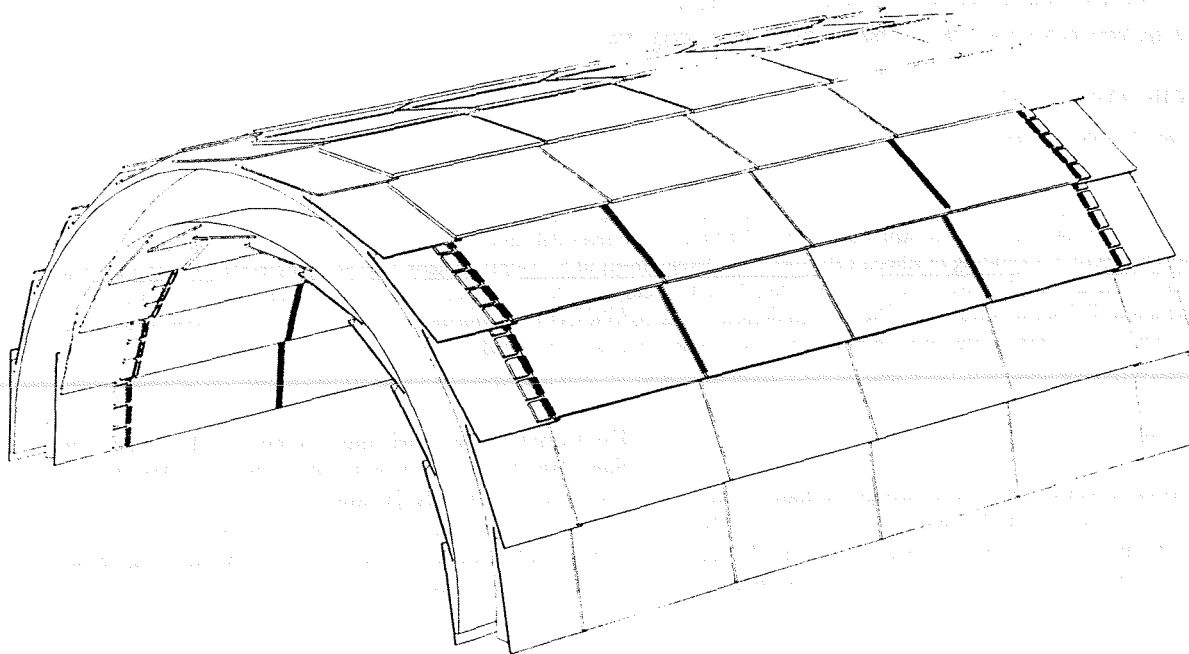


Fig. 1. Schematic drawing of one half-cylinder of the microvertex detector. In DELPHI the cut of the cylinder will be oriented vertically.

III. TRACKING DETECTORS

ton cables from the ceramic substrate to contacts on the signal bus.

The detector is designed to be installed just before closing the end caps of DELPHI, after the beam pipe is installed. Each of the end rings is vertically divided into two half-rings to make the detector able to pass the beam pipe support. The two half-cylinders will slide along the beam pipe on rails mounted on the inner detector and on the support structure of the inner detector. The design is such that it will be possible to take the detector in or out of DELPHI when the end caps are opened. This gives us the possibility to delay the installation in order to avoid excessive exposure of the detector to radiation during the LEP start-up phase. The two half-cylinders will not be mechanically connected after insertion. There will however be an overlap of the sensitive area between the two half-cylinders, which should enable us to find their relative positions using particle tracks.

Each of the half-cylinders will be covered on both the inside and the outside for mechanical protection

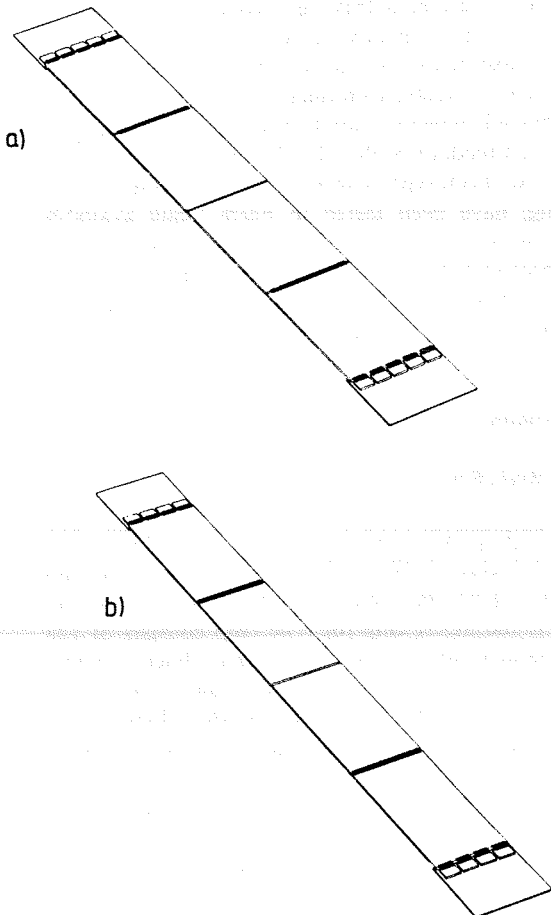


Fig. 2. Layout of the detector modules for the microvertex detector, (a) for the outer layer and (b) for the inner layer.

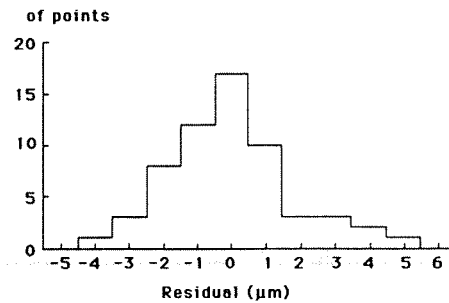


Fig. 3. Obtained mechanical precision in the assembly of half-modules.

and electrical shielding. The covers are made of 1 mm Rohacell foam sandwiched between two layers of 20 μm thick foil of hard aluminium. In this way the cover gets a density of 15 mg/cm^2 .

The modules will be assembled to a high degree of parallelism between the strips of the four detectors in each module. So far, 15 half-modules have been assembled. The position, in the detector plane, of the implant at each end of one strip on the two detectors constituting a half-module is already measured on these 15 half-modules. The four measured points are fitted to a straight line to compensate for an overall tilt of the half-module during measurement. The distribution of the residuals has an rms of 1.7 μm and is shown in fig. 3.

2.1. Survey of the detector

To simplify the off-line alignment task a thorough survey of the detector will be done prior to installation.

After assembly each of the half-cylinders will be measured in 3 dimensions using a high-precision industrial measuring machine [9]. This type of machine operates with a small probe touching the detector at a large number of points. The position in space of all planes belonging to one of the half-cylinders is then reconstructed by software.

However, this machine cannot measure microscopic objects on the detector surface such as the diode strips. The position, in the plane of the detectors, of the diode strips of all four detectors will therefore be measured, using a microscope, prior to mounting with respect to a reference object placed on each of the hybrids. The position of this object is then measured by the measuring machine after the modules are mounted onto the end rings. Using this method, we will be able to reconstruct the position in space of the sensitive elements and prepare a calibration file.

3. The microstrip counters

Silicon strip detectors have been used to give high spatial resolution in several experiments [3]. The use of

readout electronics bonded directly to the detectors in addition to the large number of channels prohibit the use of an external coupling capacitor between the detectors and the charge-sensitive amplifiers. With conventional dc-coupled detector this means that leakage current flowing to the amplifier input stage results in shifts and drift of the output pedestal levels.

To avoid these problems we have, in corporation with SI (Center for Industrial Research, Oslo, Norway), developed detectors with integrated coupling capacitors and independent bias resistors for each strip. The bias resistors consist of polysilicon lines.

This design gives a very flat baseline distribution and greatly reduces baseline drift due to drift in leakage current. A higher leakage current can also be tolerated on a single strip without any danger of driving the preamplifier to saturation. Fig. 4 shows an oscilloscope picture of the signal from the Microplex chip connected to an ac-coupled detector. The very flat baseline distribution is clearly visible.

The capacitors are formed by growing a thin oxide on the diode strip before the metallization stage in the processing. Biasing of the strips is done through separate polysilicon resistors deposited on the surface of the detectors and connected to each of the strips and a common bias line. Fig. 5 shows a photograph of the bond pad area showing the diode strips, the bond pads and the polysilicon resistors. The bond pad is $100 \times 60 \mu\text{m}^2$ and the line width of the polysilicon resistors and the diode strips is $5 \mu\text{m}$. The detectors will be produced with 1281 and 1025 diode strips at $25 \mu\text{m}$ pitch for the outer and inner layer, respectively. The readout will be of every second strip.

Long-term (300 h) measurements on full-scale prototypes, $32 \times 58 \text{ mm}^2$ active area, give a distribution of leakage currents per detector. For 10% of the prototype

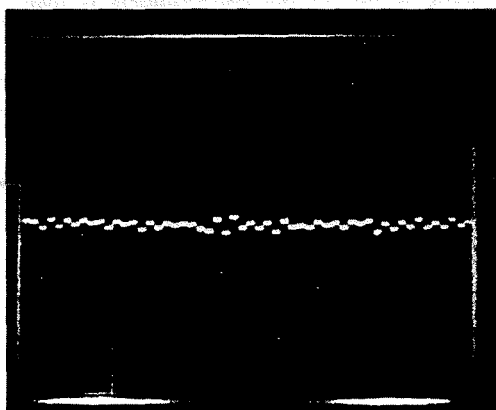


Fig. 4. Oscilloscope picture of the readout of an ac-coupled detector showing the flat pedestal distribution. Horizontal scale $5 \mu\text{s}/\text{div}$, vertical scale $100 \text{ mV}/\text{div}$. One minimum ionizing particle corresponds to 50 mV .

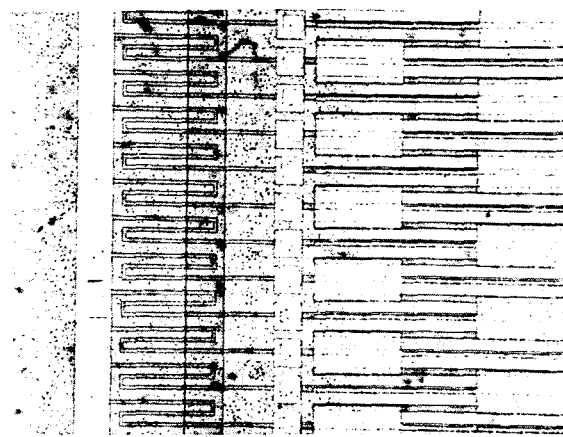


Fig. 5. Photograph of the bond pad area of an ac-coupled detector showing the bond pads, $60 \times 100 \mu\text{m}^2$, the diode strips and the polysilicon resistors with $5 \mu\text{m}$ line width.

detectors $I \leq 1 \mu\text{A}$, for 48% $I \leq 10 \mu\text{A}$, for 65.5% $I < 100 \mu\text{A}$ and for 100% $I < 1000 \mu\text{A}$. For the detectors with a fairly high leakage current we have found that the current is mainly caused by a few bad strips and that most of the detector can be fully used.

We have successfully produced one half-module with daisy-chained detectors, total strip length 12 cm, and multiplexed readout of the 512 channels.

A set of prototype detectors, 18 mm wide and 30 mm long, have been tested in beam using available equipment in the NA32 experiment at the SPS at CERN. The subsequent data analysis gives a spatial resolution with $\sigma = 5.5 \mu\text{m}$ from a detector with $50 \mu\text{m}$ readout pitch and $25 \mu\text{m}$ strip pitch [7].

4. Electronics

4.1. Readout chip

The high power consumption of the NMOS Microcomplex chip (2 W) initiated the design of a chip with similar performance but lower power consumption (65 mW); the MXII chip [6]. The chip consists of 128 input channels at $50 \mu\text{m}$ input pitch. Each channel consists of a folded cascode input stage with source follower output. The chip incorporates double correlated sampling. The signals are read out serially through an analog shift register. The main source of power consumption lies in the input stage. The chip is fabricated using a $3 \mu\text{m}$ radiation-resistant CMOS process (Mietec), with chip size $6.4 \times 6.4 \text{ mm}^2$. Power consumption is 65 mW at 5 V dc, rise $10\text{--}90\% \leq 100 \text{ ns}$ and open loop gain is 1500. Gain and noise have a spread with 4% rms. The measured equivalent noise charge can be expressed as $\text{ENC} = 650\sqrt{c_D + 2.5 \text{ pF}}$ [6]. Table 1

III. TRACKING DETECTORS

Table 1
Equivalent noise charge, ENC, and rise time of the MXII chip as a function of connected diode strip length

	MXII alone	MXII + 1 detector	MXII + 2 detectors
Strip length [nm]	0	60	120
Rise time [ns]	≤ 60	≤ 200	≤ 280
ENC [e]	1100 ± 80	2100 ± 160	2700 ± 200

summarizes the ENC as a function of connected diode strip length. The noise performance is poorer than the NMOS VLSI circuits ($ENC = 1500e$ at 10 pF) and a new circuit allowing noise reduction through bandwidth-limiting the amplifier output is currently in process.

4.2. Front-end electronics

The front-end electronics will be implemented as FASTBUS-cards, Sirocco IV [8], each card containing two identical subchannels. Each subchannel will have its ADC-card, a front-end buffer four events deep, a signal processor (Motorola DSP56001) and an output buffer also four events deep.

The expected conversion rate (= the multiplexing rate of the microplexes) is 4.6 MHz and a subchannel can receive up to 2048 data words per event, which equals 16 readout chips.

The purpose of the signal processor is to perform "intelligent" zero suppression of the data from the silicon strips and reduce the amount of data presented to the data acquisition system. The program controlling the signal processors can be downloaded via FASTBUS, allowing easy software adjustments.

5. The position-monitoring systems

The position-monitoring systems assume half-cylinder alignment outside DELPHI. The insertion procedure should not distort the detector beyond the elastic limit. It is however impossible to know the final position exactly. The thermal conditions to be expected inside DELPHI are not well known. The position-monitoring systems will therefore monitor relative position changes during data taking for software alignment. Two complementary systems will be installed. One system relying on capacitive methods and one using fibre optics.

5.1. The capacitive displacement measuring system

Capacitive probes will be attached to the end rings. The capacitance between these probes and grounded electrodes placed on the inner detector inner wall will

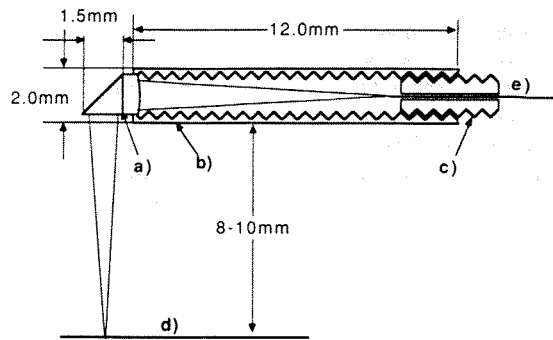


Fig. 6. Schematic drawing of one of the lens/prism combinations to be used in the optical position-monitoring system, showing (a) the lens prism, (b) the threaded aluminium tube, (c) the screw fixing the fibre, (d) the detector and (e) the fibre.

be read out. In this way the displacement of each sensor relative to the grounded electrode can be measured with a resolution better than $1 \mu\text{m}$. A set of several sensors will enable us to reconstruct the displacement of the half-cylinder relative to the inner detector inner wall in every spatial direction [10]. The system will be built starting from commercially available components from Capacitec [11]. The total amount of material corresponds to less than 0.01% of L_{rad} .

The system will be read out through the standard acquisition system. The installation of the grounded electrodes on the ID inner wall is already scheduled.

5.2. The optical displacement measuring system

This system has the advantage of being fast, it can read out every beam crossing through the standard data acquisition system. It is insensitive to electrical interference and uses the detector themselves as probes.

The system will consist of a number of lens prism combinations, as shown in fig. 6, glued onto the inner detector inner wall. The lenses will project light from an optical fibre through holes in the cover onto the detectors. The light spot on the detectors will be $75 \mu\text{m}$ in diameter. An option for adjusting the spot size exists for all the lens/prism combinations. At present all the parts are produced and waiting for installation.

6. Conclusions

The overall design work of the DELPHI microvertex detector is finished. It is shown to be possible to assemble the detector to high precision, and then do a survey to localize in space the position of all the sensing elements. The difficulties encountered in the installation of the detector in DELPHI have been solved in a satisfactory way. Silicon microstrip detectors with in-

tegrated coupling capacitors and bias resistors have been produced and tested successfully in beam. With the induction of the CMOS readout chip MXII the difficulties caused by the high power consumption of the Microplex chip have been removed. The complementary position-monitoring systems ensure that any position changes in the detector during data taking for off-line alignment are monitored.

References

- [1] The DELPHI Microvertex detector, DELPHI 86-86 GEN 52, 6 October 1986.
- [2] G. Anzivino et al., Nucl. Instr. and Meth. A263 (1988) 215.
- [3] S.R. Amendolia et al., Nucl. Instr. and Meth. 176 (1980) 449;
J.B. England et al., Nucl. Instr. and Meth. 1985 (1981) 331;
B.D. Hyams et al., Nucl. Instr. and Meth. 205 (1983) 99;
J.F. Baland et al., Nucl. Phys. B1B (1988) 303.
- [4] B.D. Hyams, Nucl. Instr. and Meth. 225 (1984) 606.
- [5] J.T. Walker, S. Parker, B.D. Hyams and S.L. Shapiro, Nucl. Instr. and Meth. 226 (1984) 606.
- [6] J. Stanton, RAL report, to be published.
- [7] I. Evensen et al., Nucl. Instr. and Meth. A260 (1987) 124.
- [8] N. Bingefors and M. Burns, Sirocco IV - Hardware and Software Manual, DELPHI Note, in preparation.
- [9] Galaxy 3-D measuring machine, Poli S.P.A., Varollo Sesia, Italy;
N. Redaelli and G. Vegni, Measurements of the DELPHI end-ring prototypes, DELPHI microvertex internal communication.
- [10] A. Breakstone, Summary of Capacitive Displacement Monitor Tests, SLAC Memorandum, May 27, 1988;
R. Turchetta, Preliminary Study of a Capacitive Displacement Measuring System for the DELPHI Microvertex Detector, DELPHI 88-6, Track 44, 12 April 1988, DELPHI Collaboration.
- [11] Capacitec, Inc., P.O. Box 819, 87 Fitchburg Road, Ayer, MA 0143, USA.
- [12] T. Tuuva, R. Horisberger and L. Hubbeling, EP Internal Note 86-04, 4 December 1986.

Appendix C

Reprint of NIM publication

BEAM TEST RESULTS FROM A PROTOTYPE FOR THE DELPHI MICROVERTEX DETECTOR

V. CHABAUD, H. DIJKSTRA, M. GRÖNE, M. FLOHR, R. HORISBERGER, L. HUBBELING,
G. MAEHLUM, A. PEISERT, A. SANDVIK and P. WEILHAMMER

CERN, CH-1211 Geneva 23, Switzerland

A. CZERMAK, P. JALOCZA, P. KAPUSTA, M. TURALA and A. ZALEWSKA

Institute of Nuclear Physics, Cracow, Poland

E. SUNDELL

Åbo Akademi, Turku, Finland

T. TUUVA

University of Helsinki, Helsinki, Finland

M. BATTAGLIA, M. CACCIA, W. KUCEWICZ, C. MERONI, N. REDAELLI, R. TURCHETTA,
A. STOCCHI, C. TRONCON and G. VEGNI

INFN, Milan, Italy

G. BARICHELLO, M. MAZZUCATO, M. PEGORARO and F. SIMONETTO

INFN, Padua, Italy

P. ALLPORT and M. TYNDEL

Rutherford Appleton Laboratory, Chilton, Didcot, Oxon., OX11 0QX, UK

H.J. SEEBRUNNER

Fachhochschule Heilbronn, Heilbronn, FRG

Received 23 January 1990

Results are presented from a test in the CERN SPS North Area of a prototype of the DELPHI microvertex detector. Full-sized modules built up from prototype ac-coupled detectors and VLSI readout electronics were used. The spatial resolution of the detectors equipped with prototype VLSI chips was measured to be $6.5 \mu\text{m}$. The system aspects, including the readout, were found to work well. Extrapolating to the final components we expect to achieve a measurement precision of $5 \mu\text{m}$ with the DELPHI microvertex detector.

1. Introduction

The DELPHI microvertex detector will consist of two cylindrical shells of silicon microstrip detectors close to the beam pipe. Silicon detectors, with their very high spatial resolution, have been used successfully in the past in fixed target charm and beauty experiments [1], to extract cleanly the small fraction ($\leq 1\%$) of events containing charm or beauty. At LEP, 42% of all hadronic events are expected to originate from $c\bar{c}$ or $b\bar{b}$

fragmentation and therefore contain at least two particles with lifetimes in the range 10^{-13} to 10^{-12} s. The ability to tag primary quark flavours on an event-by-event basis and to study the spectroscopy of the heavy flavour hadrons will enhance the physics potential of the DELPHI detector [2].

The vertex detector is shown schematically in fig. 1. Details can be found in refs. [3,4]. It has been designed to measure the $R\phi$ coordinate of charged tracks with a precision of $5 \mu\text{m}$, as close to the interaction point as

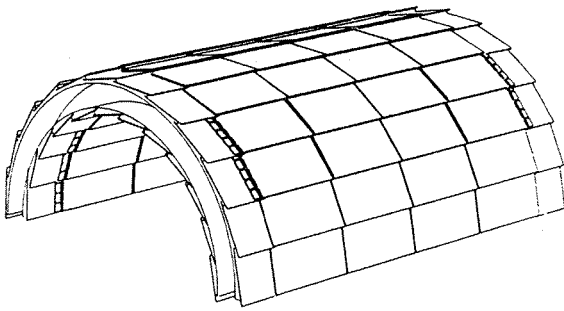


Fig. 1. Schematic view of a half shell of the DELPHI microvertex detector.

possible. In practice this is limited by the relatively large-diameter beam pipe required for the initial safe operation of the LEP machine. There will be two layers of microstrip detectors at radii of 9 and 11 cm with a length of 24 cm. Each layer is built up of 24 overlapping modules. A module consists of four microstrip detectors with strips parallel to the beam axis. The strip pitch of $25\ \mu\text{m}$ was chosen to give the required spatial resolution of $5\ \mu\text{m}$. The basic detector unit, a half module, consists of a pair of capacitively coupled silicon detectors [5] daisy-chained together. The readout pitch is $50\ \mu\text{m}$. Each readout strip is connected to a charge-sensitive amplifier. These amplifiers have been built on a fully custom-designed VLSI circuit, the MX3 [6]. Each chip consists of 128 amplifiers and multiplexing circuitry. The complete vertex detector consists of 192 individual silicon microstrip detectors with a total surface area of $0.33\ \text{m}^2$ and 55 296 readout channels. These are multiplexed at the readout chip so that all the channels are read out on 48 twisted pair cables. The readout rate is 2.5 MHz. Data reduction is achieved on-line by zero suppression and cluster identification using a purpose-built programmable Fastbus unit, the Sirocco 4 [7].

The aim of the beam test was to measure the spatial resolution of the silicon detectors directly and to gain experience in the operation of such a large system. Ideally we would have liked to test all the final components, but many items were still under development. Including a high-precision reference beam telescope, a total of ten silicon detectors was instrumented and read out (10 880 channels). Algorithms were developed off-line for estimating and continuously updating pedestals and rms noise. Cluster-finding algorithms were also developed. A first attempt was made at understanding the problems associated with the alignment and stability of the vertex detector.

2. Beam test hardware

The experimental arrangement used during the beam test is shown schematically in fig. 2. A minimal prototype of the DELPHI microvertex detector was prepared consisting of one inner and two outer modules. Each half module consists of a pair of ac-coupled silicon detectors daisy-chained together giving 12 cm long read-out strips. Only one of the two half modules in each module was equipped with electronics and read out. The detectors were produced by SI (Oslo) and have already been described elsewhere [5]. The mechanical assembly was the same as it will be for the complete detector when mounted in the DELPHI experiment. The modules were mounted on precision end rings which in turn were supported by a replica of the inner wall of the inner detector.

The electronic readout chain was based on that proposed for the DELPHI experiment but several of the key items were only available in prototype form. The CMOS microplex chip used in the test, the MX2, has the same functionality as the final chip, the MX3 which was not yet available for the beam test experiment. The performance of both chips is summarized in fig. 3. The MX3 has lower noise at the expense of a lower bandwidth. The power consumption, $0.5\ \text{mW}/\text{channel}$, and

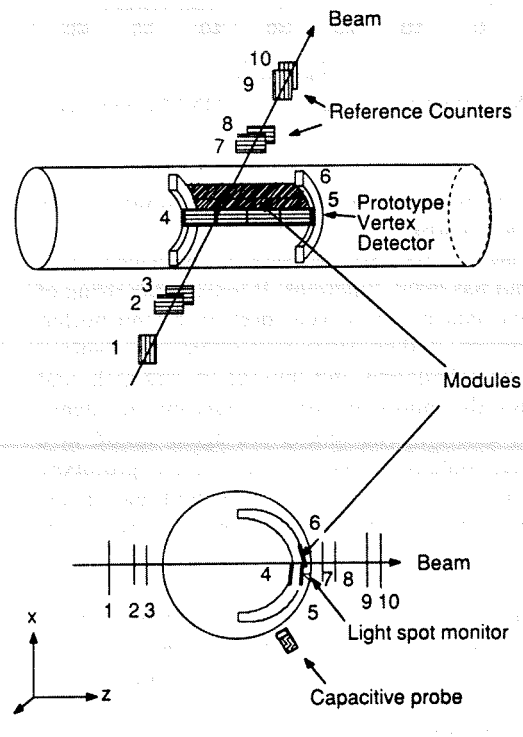


Fig. 2. The detector arrangement for the beam test (not to scale).

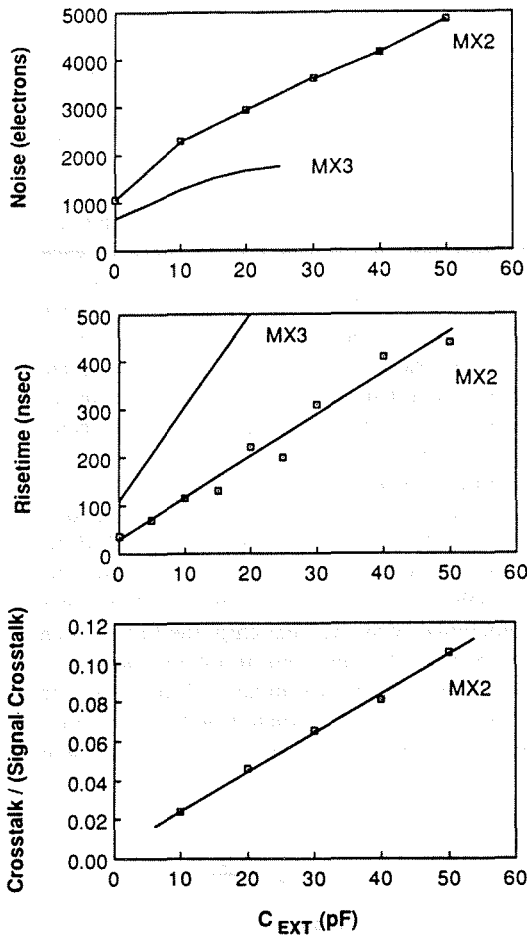


Fig. 3. MX2 performance vs capacitance (MX3 from ref. [6]).

the radiation tolerance (greater than 55 krad) are the same for both chips.

The readout processor foreseen is implemented in Fastbus and has many functions. It accepts the string of multiplexed data into a 4-event deep front-end buffer. A signal processor then controls the data processing – typically the calculation and storage of pedestals and noise values, the subtraction of pedestals and the identification of clusters. The results are again stored in a 4-event deep output buffer. For this test a prototype CAMAC unit, without processor, was used and all the raw data was recorded directly on magnetic tape so that algorithms for the data reduction could be developed off-line.

The trajectory of the beam tracks was defined using crossed pairs of silicon detectors [9] as shown in fig. 2. These had 25 μm readout pitch and were equipped with NMOS microplex chips [8]. These reference detectors were read out through the same data acquisition system.

The two position monitoring systems foreseen for the vertex detector were installed and evaluated. A

capacitive probe monitored movement of the vertex detector assembly with respect to the reference counters. An optical system composed of quartz fibres with a 50 μm diameter core and 1.5 mm diameter focussing lenses and prisms, projects light spots onto the silicon detectors themselves. It was installed in such a way that it could monitor movement between the vertex detector and its support.

3. Analysis chain

For each trigger the raw pulse-height data from all the 10880 channels were written on tape. Neither the pedestal subtraction nor the zero suppression features of the Sirocco were used. The off-line software therefore had the tasks of correctly associating each data element with a physical strip number; of calculating pedestals and noise values, subtracting pedestals and selecting valid signals; of finding clusters, calculating hit coordinates and fitting tracks.

The raw data in each channel consists of three contributions:

- 1) An overall dc level common to all 128 channels of a single microplex chip multiplexed onto one output. This varies from trigger to trigger and can be caused by external noise sources.
- 2) A pedestal or zero level, reflecting fluctuations in channel characteristics across the VLSI circuits. For the reference counters, which are not capacitively coupled, there is also a contribution from the leakage currents of each strip.
- 3) The charge collected as a result of the passage of a minimum ionizing particle through the detector (i.e. the signal).

The first component is calculated on a trigger-by-trigger basis by finding the average pulse-height per chip in ADC counts. The average is calculated for each chip using only “valid” channels (see below) and is then globally subtracted from all the data from that chip. The individual pedestals are calculated by averaging the residual pulse height in each channel over many triggers. Updating of the average pedestal and of pedestal rms is performed:

$$\text{Ped}^{N+1} = \text{Ped}^N + \frac{(\text{Pulse-height} - \text{dc}^{N+1}) - \text{Ped}^N}{W_1} \quad (1)$$

$$(\sigma^{N+1})^2 = (\sigma^N)^2 \left(1 - \frac{1}{W_2}\right) + \frac{((\text{Pulse-height} - \text{dc}^{N+1}) - \text{Ped}^N)^2}{W_2} \quad (2)$$

The choice of W_1 and W_2 depends on the level of fluctuations in the pedestal and noise values. Different

values were tried. Setting both to 50 gives noise values which agree well with those found from calculating the standard deviation of the residual signal per channel taken over many triggers.

After these corrections the data is unpacked into the physical detector strip numbering and the reference counters are scanned for clusters. Strips which are dead, saturated or have noise greater than 10 ADC counts (i.e. 3 times the average) counts are excluded as "not valid". Of the 8960 reference detector channels, about 500 are affected. A cluster is then defined as the sum of all contiguous valid strips satisfying both of the following conditions:

- 1) Signal in each strip greater than $2.58 \times \sigma$, i.e. the probability of a noise fluctuation should be less than 1%.
- 2) Signal in each strip greater than one-eighth of the peak value of the minimum ionizing pulse-height distribution for that detector. The mean value of this peak is 52 with a spread of 5.7 ADC counts.

Only clusters, where the integrated signal exceeds half the peak value are kept. With this definition, the average number of strips per cluster is 2.4 ± 0.2 . For estimating the hit position via charge division, only the neighbouring two strips with the largest signals are used.

After preliminary alignment, the reference counter clusters are used to define tracks through the half modules. These are then used to select the range of strips in the half module through which the particle has passed.

4. Results with reference counters

Performance of the reference counters was found to be well matched to our requirements. After cutting out bad channels, an average noise for the reference counters of 3.3 ADC counts was measured giving an average signal/noise ratio of 15.8. Fig. 4 shows the cluster pulse-height distribution for a reference counter.

After the cluster reconstruction, a straight line fit is performed through the four planes of reference detectors measuring the x-coordinate. Fitted tracks are accepted if: 1) their slope is less than 10 mrad, 2) at least three of the four planes have a reconstructed cluster, 3) the maximum residue between the extrapolated track position and the hit on each of the reference planes is less than 50 μm .

For the runs considered here, high-energy (> 60 GeV) beam particles were used so that multiple scattering effects were negligible. The correction for the true resolution of the reference counters from the measured residues is then straightforward, taking account of the least-squares fit procedure used which employs all counters to define the track parameters. In the absence of

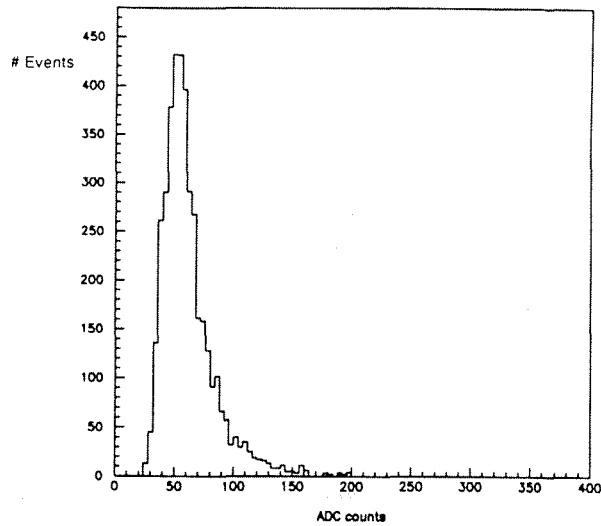


Fig. 4 Pulse-height distribution for reference detectors (all clusters $> \frac{1}{2}$ min I) obtained in beam test.

multiple scattering and assuming all detectors have the same intrinsic resolution:

$$\sigma_x^i = \frac{\text{rms}(\text{Residue}^i)}{\left(1 - \left[\sigma_z^2(z_i - \bar{z})^2 / N\sigma_z^2\right]^{1/2}\right)}, \quad (3)$$

$$\sigma_z^2 = \frac{\sum_{i=1}^N (z_i - \bar{z})^2}{N}.$$

The correction factors that must be applied in our case to the residue distributions to get the true resolution estimates for each detector are 1.481 ($i = 1, 4$) and 1.356 ($i = 2, 3$). Note, as the counters were grouped in pairs, almost measuring at a single z -coordinate when compared with the distance between each pair, the resolution is approximately $\sqrt{2} \times \text{rms}$ of the residue distribution. The resolution of the four horizontal counters was found to be equal to or four better than $\sim 5\%$.

The mechanical alignment of the reference counters was very good, and the detectors were found to be parallel to within 0.25 mrad. These small corrections were applied to the data. The fully corrected residue distribution for one of the reference detectors is shown in fig. 5. It has a full width at half maximum of $9.2 \pm 0.3 \mu\text{m}$. The expected relationship $\text{rms} = \text{FWHM} / 2\sqrt{2 \ln 2}$ did not hold as there were non-Gaussian tails to the residue distribution. This is known to come from the dependence of the detector resolution on the track impact point with respect to the readout strips. This is particularly pronounced if one assumes that the division of the collected charge depends linearly on the relative strip distances. In fact it was found that the FWHM increased by $> 50\%$ between samples of tracks traversing midway between strips and those

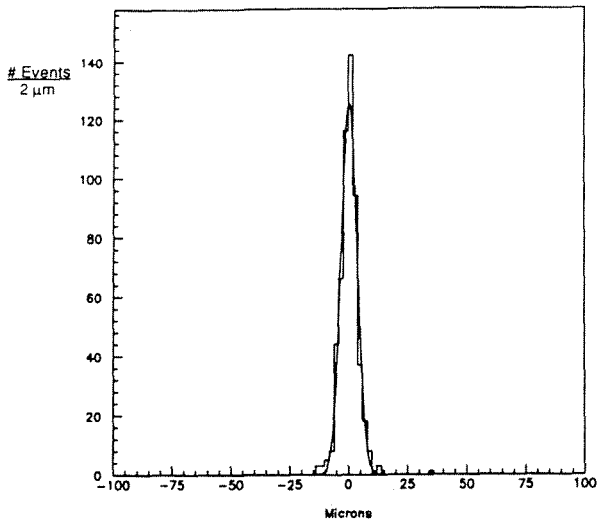


Fig. 5. Residues for a reference detector.

passing through a strip. Crude corrections were applied for the nonlinearity in the relation between charge distribution and position which did reduce the non-Gaussian tails of the residue distribution but did not alter the values of the FWHM. From the FWHM we obtain a resolution of $3.9 \pm 0.1 \mu\text{m}$, compared with the best value of $2.6 \mu\text{m}$ [1] measured using dc-coupled detectors and discrete component electronics.

5. Results with half modules

The capacitively coupled detectors for the DELPHI microvertex detector have been designed with very narrow ($\sim 6 \mu\text{m}$) diodes to achieve low interstrip capacitance – on average 1.3 pF/cm has been measured. This has to be compared with 2.5 to 3 pF/cm measured on other detectors with similar layout [5]. From fig. 3 it can be seen that for a minimum ionizing signal of 24000 electrons, the S/N expected from the MX3 for a 12 cm long detector is 16:1. This has been confirmed directly by exposing a detector assembly to an americium source ($60 \text{ keV } \gamma$). The signal-to-noise ratio measured with Am was 11.5:1 (fig. 6), which extrapolates to a ratio of 16:1 for minimum ionizing particles. The S/N ex-

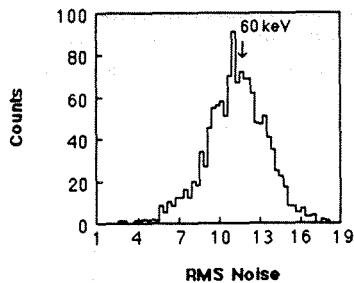


Fig. 6. Americium pulse-height distribution measured in DELPHI equipped with MX3.

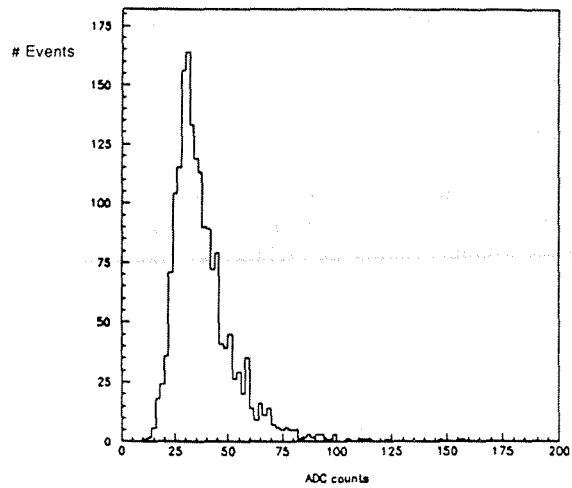


Fig. 7. Pulse-height distribution for half modules (only clusters on tracks) from beam particles.

pected for the beam test assembly, using the then available MX2, is 8:1 (fig. 3).

The measured average noise for these detectors was $4.0 \pm 0.2 \text{ ADC counts}$. The signal, as estimated from the peak of the pulse-height distribution (fig. 7) obtained in the experiment was $28 \pm 2 \text{ ADC counts}$ giving a signal/noise of about 7:1, in good agreement with the measurements using external capacitors.

The spatial resolution achieved in a large system depends on many factors apart from the electronic noise. It is therefore important to independently measure the spatial resolution directly. Also, since no attempt was made to align the half modules with respect to the reference system, our data provided a useful opportunity to explore alignment techniques. We found

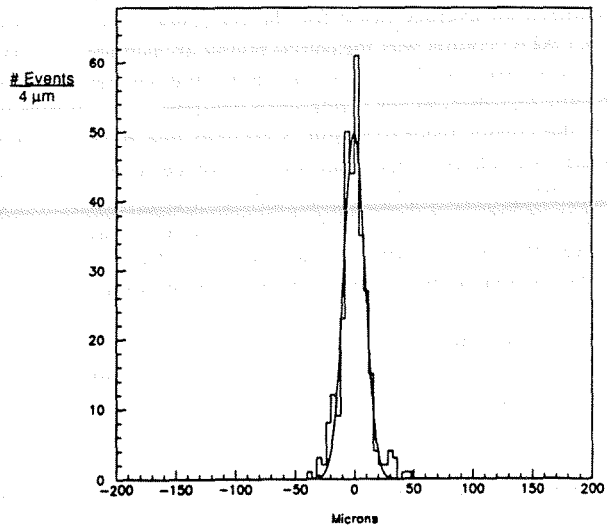


Fig. 8. Residues for the DELPHI half module.

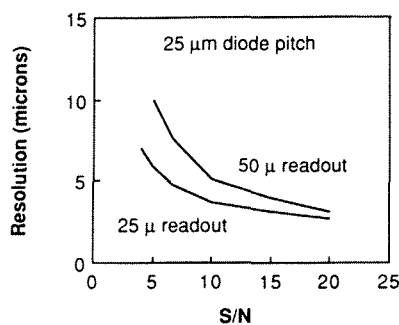


Fig. 9. Calculated resolution for 25 μm diode pitch silicon strip detectors.

that the strips were not parallel to the reference y -direction and corrections of up to 2 mrad were needed. Also we saw evidence of movement of all three half modules between different runs taken at different times. Given the mounting of the half shells within a long tube supported on a metallic moveable stage, this is not surprising. Temperature variations between day and night alone gave rise to relative motions of half-shell and reference system of 10 μm . This was measured by the in situ capacitive probe monitoring system. Possible movements of the half shell with respect to its support tube were investigated using the light spot monitoring system. No displacements were found.

Applying all the cuts and corrections described above (in particular, an event-by-event correction of displacements observed with capacitive probes), and cleaning the data further by requiring a $S/N \geq 5$ for single strip clusters to be accepted, the residue distribution shown in fig. 8 is found for the DELPHI module #4. Calculating the spatial resolution from the FWHM of this distribution we find an rms of 6.5 μm . A Gaussian fit to this distribution yields $\sigma = 8.3 \pm 0.4 \mu\text{m}$, which leads to a resolution of $\sigma = 8 \mu\text{m}$ after subtraction of the error of the predicted impact point. The fraction of events in the tails of the experimental distribution outside the Gaussian fit is 9%. We performed a cross-check on our result by fitting the residues of events whose impact in the DELPHI module #4 is within $\pm 10 \mu\text{m}$ of the centre of a readout strip (sample A) and events with an impact of $\pm 15 \mu\text{m}$ around the middle line between readout strips (sample B). We find from Gaussian fits $\sigma = 10.5 \pm 1 \mu\text{m}$ for sample A and $6.8 \pm 0.6 \mu\text{m}$ for sample B. In fig. 9 the calculated resolution for Si strip detectors as a function of S/N is shown for 50 μm pitch readout and 25 μm pitch readout. Both our results for the reference detectors and the DELPHI module agree well with the calculated resolution. From fig. 9 and fig. 4 we conclude that the DELPHI modules equipped with the MX3 CMOS VLSI will achieve the desired resolution of $\sigma = 5 \mu\text{m}$.

6. Conclusions

Prototypes of many of the components to be used in the DELPHI microvertex detector project have been built and tested together under realistic experimental conditions. The system worked well and we were able to derive the signal/noise and spatial resolution of both NMOS microplex equipped 25 μm direct-coupled detectors and CMOS (MX2) microplex equipped 50 μm daisy-chained capacitively coupled detectors with one intermediate diode. The resolution values extracted from FWHM were 3.9 and 6.5 μm . The latter resolution is limited by the electronics noise of the prototype MX2 chip. The improved signal/noise performance for the final DELPHI modules equipped with the MX3 VLSI circuit, measured to be 16:1, implies that the detector modules will give the 5 μm resolution specified in the DELPHI microvertex detector proposal [3].

Acknowledgements

We wish to acknowledge the valuable assistance we received from many people. The test would not have succeeded without the good beam provided by the SPS (our especial thanks to N. Doble) and the tolerance of our DELPHI colleagues sharing the beam line. We would like to thank J. Lidbury and N. Beadle at RAL and K. Ratz at CERN for the design and construction of the precision mechanics. We are indebted to P. Seller and J. Stanton for the microplex chips MX2 and MX3. R. Boulter provided us with beautifully mounted detector assemblies. Of course we would have had no data without the help of M. Jonker from the DELPHI on-line group. We also wish to thank A. BJORKEBO for the tape management and finally C. Ponting for her hard work on this paper and the figures.

References

- [1] P. Weilhammer, Experience with Si detectors in NA32, Workshop on New Solid-State Devices for HEP, Berkeley, California (1985) p. 83;
- R. Alberganti et al., Nucl. Instr. and Meth. A248 (1986) 337;
- E691 contribution to the XXIIIrd Int. Conf. on HEP, Berkeley (1986).
- [2] H. Dijkstra et al., Nucl. Instr. and Meth. A277 (1989) 160.
- [3] DELPHI microvertex detector, Addendum to the technical proposal, DELPHI 86-86 GEN-2 (Oct. 1986).
- [4] M. Burns et al., Nucl. Instr. and Meth. A277 (1989) 154.
- [5] M. Caccia et al., Nucl. Instr. and Meth. A260 (1987) 124.
- [6] J. Stanton, A low power low noise amplifier for a 128 channel read-out integrated circuit, RAL-89-009 (1989).
- [7] N. BINGEFORS and M. BURNS, Sirocco IV, Hardware and Software Manual, DELPHI 88-48 TRACK-48 (1988).
- [8] J.T. Walker et al., Nucl. Instr. and Meth. 226 (1984) 200.
- [9] These detectors were produced by Micron Semiconductor.

Appendix D

Reprint of mounting manual

1. Introduction

2. Mounting the unit

3. Electrical connections

4. Operation

5. Maintenance

6. Troubleshooting

7. Specifications

8. Appendix

9. Index

10. Glossary

11. Notes

12. Diagrams

13. Tables

14. Figures

15. References

16. Acknowledgments

17. Contact information

18. Revision history

19. Copyright

20. Disclaimer

21. Warranty

22. Terms and conditions

23. Privacy policy

24. Environmental policy

25. Safety information

26. Regulatory compliance

27. Other information

28. Revision 1.0

29. Revision 1.1

30. Revision 1.2

31. Revision 1.3

32. Revision 1.4

33. Revision 1.5

34. Revision 1.6

35. Revision 1.7

36. Revision 1.8

37. Revision 1.9

38. Revision 2.0

39. Revision 2.1

40. Revision 2.2

41. Revision 2.3

42. Revision 2.4

43. Revision 2.5

44. Revision 2.6

45. Revision 2.7

46. Revision 2.8

47. Revision 2.9

48. Revision 3.0

49. Revision 3.1

50. Revision 3.2

51. Revision 3.3

52. Revision 3.4

53. Revision 3.5

54. Revision 3.6

55. Revision 3.7

56. Revision 3.8

57. Revision 3.9

58. Revision 4.0

59. Revision 4.1

60. Revision 4.2

61. Revision 4.3

62. Revision 4.4

63. Revision 4.5

64. Revision 4.6

65. Revision 4.7

66. Revision 4.8

67. Revision 4.9

68. Revision 5.0

69. Revision 5.1

70. Revision 5.2

71. Revision 5.3

72. Revision 5.4

73. Revision 5.5

74. Revision 5.6

THE PRECISION MOUNTING PROCEDURE

GM

A detailed description of the procedures for the precision mounting of single detectors to complete modules is given.

The mounting will be done in 4 main steps, using 3 different assembly jigs.

step 1. Two detectors are aligned relative to each other using jig no.1 and connected to constitute a DETECTOR UNIT. Reference for the alignment is the edge of the implant of the diode strips on the detectors.

step 2. The detector unit is aligned with the reference edge of the hybrid and these two are connected to constitute a HALF-MODULE. After this step the bonding of the readout chips and the detectors will be done.

step 3. The two half modules are aligned on jig no.2. Reference for alignment is the implant edge as in point 1.

step 4. The carbon fibre reinforcement bar is attached to the backside and the silicon reinforcement strips are attached to the carbon fibre bar.

Mounting procedure in detail.

Step 1, alignment of two detectors:

- 1.1 Clean the chucks with alcohol, blow off dust.
- 1.2 Put the two detectors on the vacuum chucks. Apply vacuum.
- 1.3 Align
 - 1.3.1 Use the edge of the implant on corresponding strips as reference, not the aluminium lines. The aluminium strips does not necessarily define the sensitive area of the detector
 - 1.3.2 Align first the detector on the fixed chuck by rotating the hole jig. Use the microscope at low and high magnification for coarse and fine alignment respectively. **Important:** Reposition the jig each time when switching between different objectives of the microscope.
 - 1.3.3 Align the the detector on the movable jig.
 - 1.3.4 Adjust the distance between the detector to be $200 \pm 10 \mu\text{m}$ measured at the top edges.
 - 1.3.5 Realign if necessary, in most cases it is.
- 1.4 Prepare epoxy. Apply epoxy to the sandblasted side of the two silicon pieces used for keeping the unit together. Put the silicon pieces on the support connected to the eccentric screw, raise the support.
- 1.5 Do final alignment/checking. **Important:** This must be done within 5 minutes after the epoxy has been mixed in the case of Araidit Rapid.
- 1.6 Leave the detector unit on the jig for at least 3 hours in the case of the epoxy used being Araidit Rapid.

Step 2: Joining of detector unit to hybrid.

There are two cases.

2.1 The hybrid is a RIGHT version and is resting on the fixed part of the jig.

2.2 The hybrid is LEFT version and is resting on the movable part of the jig.

Depending on 1 or 2, two slightly different procedures is to be followed. However in general always start with aligning the components lying on the fixed part of the jig.

2.1 The hybrid is a RIGHT version

2.1.1 Put the detector unit on the chucks. Apply vacuum to the MOVABLE part only. Put the RIGHT hybrid on the fixed chuck firmly against the pins. Apply vacuum to the hybrid.

2.1.2 Align the reference edge for the hybrid to be parallel to the x movement using the pins as reference.

2.1.3 Position the detector unit such that the distance from the strip closest to the edge and the edge of the hybrids are 1.10 ± 0.01 mm.

2.2 The hybrid is LEFT version

2.2.1 Put the detector unit on the chucks. Apply vacuum to the FIXED part only. Put the LEFT hybrid on the movable chuck firmly against the pins. Apply vacuum to the hybrid.

2.2.2 Align the detector unit rotating the jig using the implant edges as reference.

2.2.4 Position the hybrid such that the distance from the strip closest to the edge of the detector and the edge of the hybrids are $xxxx \pm 5 \mu\text{m}$.

2.2.3 Align the reference edge for the hybrid to be parallel to the x movement using the pins as reference.

2.3 Prepare both conductive epoxy and Araldit. Apply a SMALL amount of conductive epoxy to the hybrid at 3 points, on each side and in the middle, apply Araldit in between. Use EXTREME care not to spill any epoxy on the chips or detectors as this will ruin the bond pads. Keep the amount of glue within the first gold line, excessive glue may short the detector back-plane to the readout chips and make the half module UNUSABLE.

2.4 Move the table to get a 3.00 ± 0.01 mm overlap of hybrid and detector.

2.5 Check overall dimensions and REALIGN within 5 minutes. See fig. 1 for the correct dimensions. Experience shows that realignment is necessary in all cases.

2.6 Leave the half module on the jig for at least 3 hour for the epoxy to harden.

2.7 The half module is now finished mechanically. Next step is bonding, testing and calibration of the half module.

Step 3, joining of half modules

- 3.2 Clean chucks. Put on the two half modules, apply vacuum.
- 3.3 Align the right half module (resting on the fixed part of the jig), using the edges of the implant in each end of each detector as reference, by moving the jig.
- 3.4 Align the right half module in y with reference as above using the tables.
- 3.5 Displace right half in X, until a gap of 0.20 ± 0.01 mm measured on the top edges between the detectors is obtained.
- 3.6 Attach the reinforcing pieces as under point 1.4
- 3.7 Do final alignment/checking. This must be done within 5 minutes after the epoxy have been mixed in the case of Araldit Rapid.
- 3.8 Leave on jig for at least 3 hour for epoxy to harden.

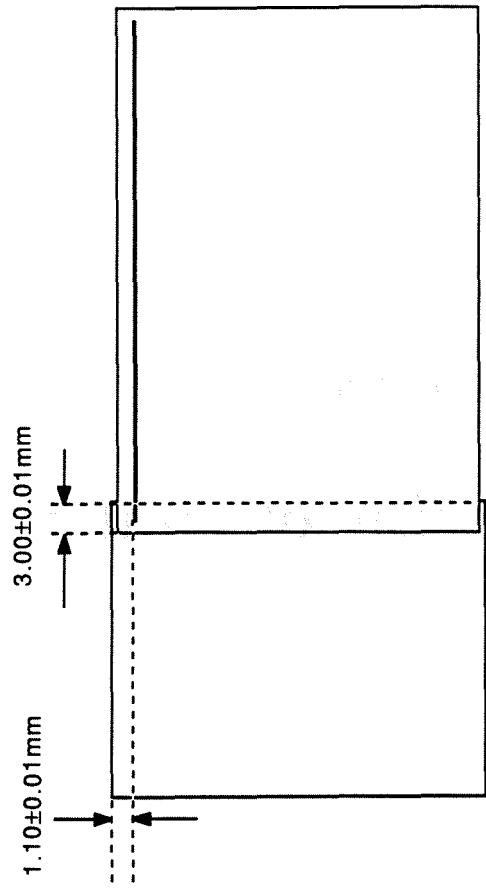
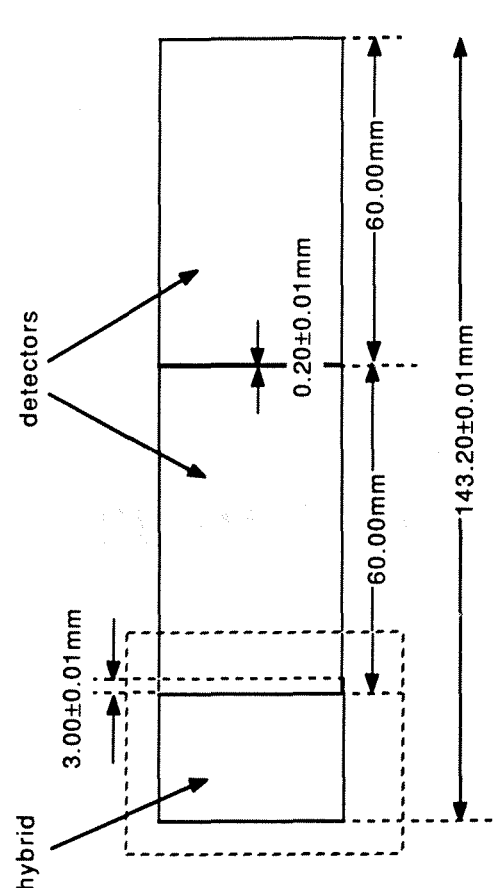
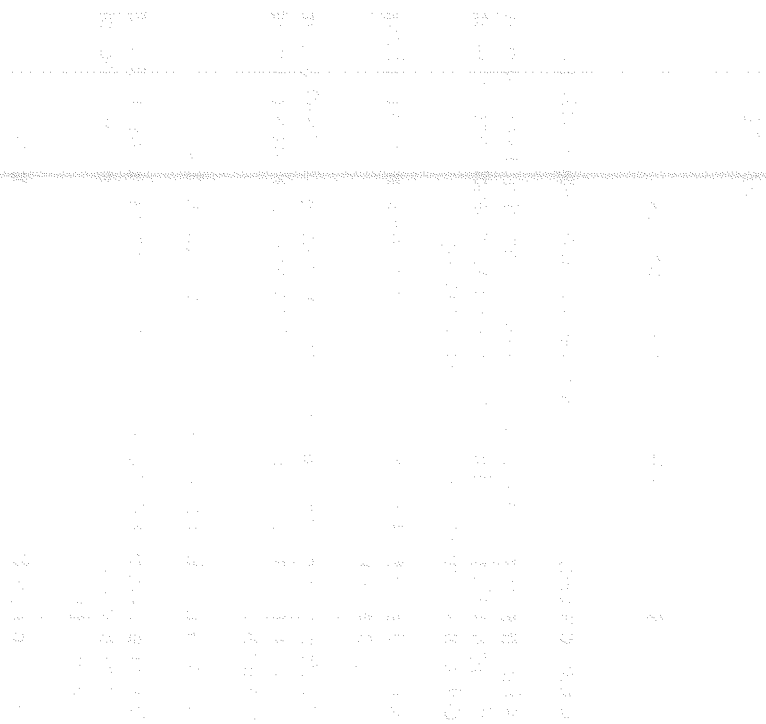


Figure 1 the dimensions of a half module, the lower part showing enlarged the overlapping region between hybrid and detector.

Appendix E

Reprint of contribution to DPF92.



The table is extremely faint and illegible. It appears to have several columns and rows of text, but the content is not readable. It may be a list of items or a data table.

LIFETIMES OF CHARGED AND NEUTRAL B HADRONS PRODUCED IN Z^0 DECAYS

Gunnar Maehlum

Institute of Physics, University of Oslo, pob. 1048 Blindern

N-0316 Oslo, Norway

Representing the DELPHI Collaboration

ABSTRACT

The lifetimes of neutral and charged B hadrons have been measured using the DELPHI detector at LEP. Highly enriched samples of b-hadrons are obtained by identifying the high p_t lepton from the semileptonic b decay in correlation with a reconstructed D meson or by uniquely reconstructing the secondary vertex from the b decay. The proper times are determined using the measured decay length of the b-hadron.

1. Motivation

We have now measurements of the mean lifetimes of b-hadrons with a precision better than 5%. Four different species of b-hadrons have been observed, the \bar{B}^0 , B^- , B_s^0 and Λ_b . If differences in the lifetimes between the various b-hadrons exist the concept of a "mean" b lifetime is not valid since the decay length distribution is not described by a single exponential.

The lifetimes of hadrons in the charmed sector are known to be different: $\tau(D^+)/\tau(D^0) = 2.5 \pm 0.1$. This can be understood qualitatively in terms of interference effects in non-leptonic decay modes. For the decay mode $D \rightarrow K\pi$ there are two diagrams leading to similar final states. In the case of D^+ the two final states are identical, $\bar{K}^0\pi^+$, whereas for D^0 there are the two states $K^+\pi^-$ and $\bar{K}^0\pi^0$. Destructive interference between the two graphs in D^+ decay is the main cause of the lifetime difference. This interference is not possible in the D^0 decay since the final states are distinguishable.

The spectator diagram is believed to dominate in the decays of b-hadrons due to the larger mass of the b quark thus leading to similar lifetimes of the different b-hadrons.

This paper presents direct lifetime measurements on samples enriched in B^0 and B^+ content. The silicon microstrip vertex detector installed in DELPHI allows precise decay vertex determination with a precision in the order of $100\mu\text{m}$ in the plane transverse to the beam direction. The proper time of the decays are determined from the decay distances combined with an estimate of the b-hadron energy.

2. D-lepton Correlations¹

From figure 1 it can be seen that neutral B mesons decay semileptonic to a charged $D^{(*)}$ (where $D^{(*)}$ is either a D^{*+} or a D^+). Similarly charged B mesons decay semileptonic to neutral D mesons. The weak decay of the D meson is such that the charged kaon must have the same charge as the lepton from the $B \rightarrow D\ell\nu$ transition. This correlation is then used to determine the charge of the decaying B meson.

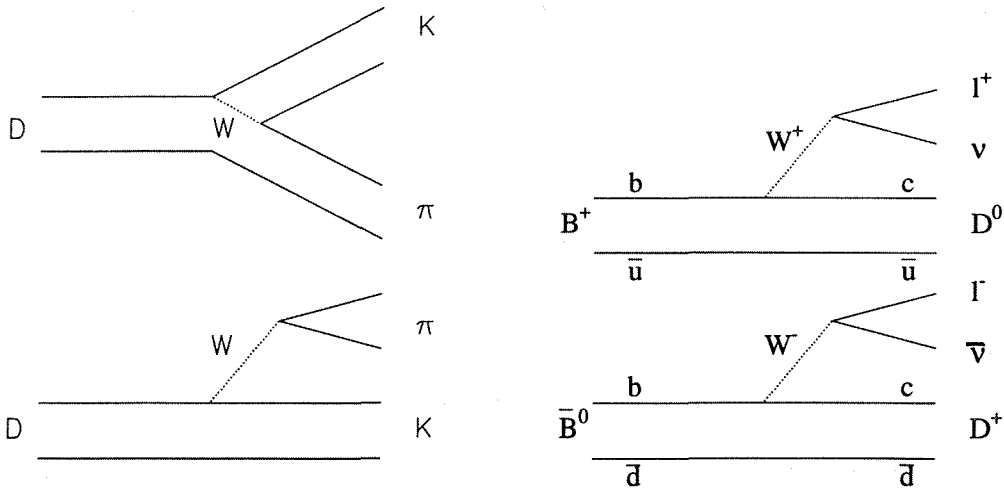


Figure 1: Left: Internal conversion (upper) and spectator (lower) diagrams in nonleptonic D decays. Right: B^- (upper) and B^0 (lower) semileptonic decay diagrams.

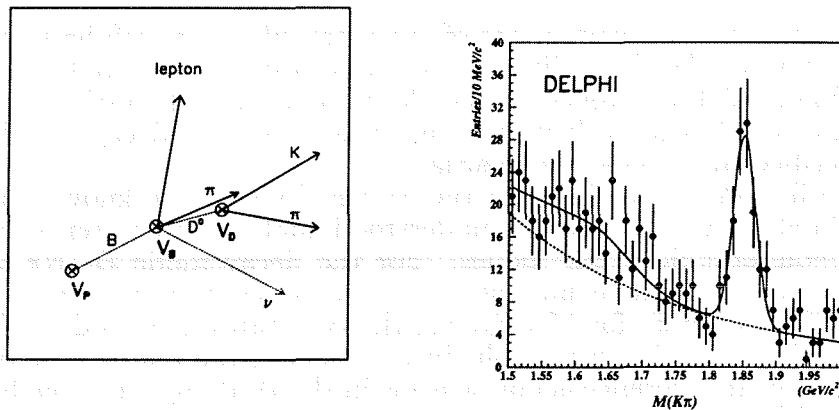


Figure 2: Left: Vertex geometry. Right: D^0 signal in the $K\pi$ channel.

Figure 2 shows the vertex geometry. The D mesons are reconstructed by first identifying an electron or a muon with a momentum of at least 3 GeV/c and a high transverse momentum p_t with respect to the jet axis. $K\pi$ vertices, V_D , are searched for using only tracks in the same hemisphere as the lepton. The D^0 candidates are extrapolated to search for a vertex, V_b , with the identified lepton. The decay length is the distance from the primary vertex V_p to V_b .

Evidence for charmed mesons in multihadronic events with an identified lepton is shown in figure 2. A total of 92 ± 14 $D^0 \rightarrow K^- \pi^+$ candidates, 35 ± 8 $D^+ \rightarrow K^- \pi^+ \pi^+$ candidates, 30 ± 6 $D^{*+} \rightarrow (K^- \pi^+) \pi^+$ candidates and 31 ± 10 $D^{*+} \rightarrow (K^- \pi^+ \pi^+ \pi^-) \pi^+$ candidates were found. The lifetimes were determined using an event by event maximum

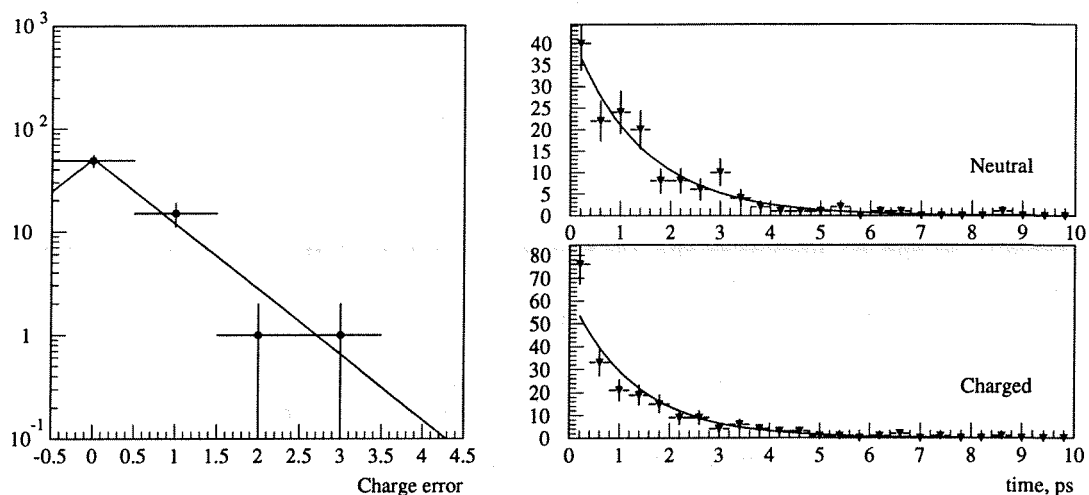


Figure 3: Left: Charge measurement precision. Right: Proper time distributions

likelihood fit.

The results of the fit are, in picoseconds:

$$\bar{B} \rightarrow D^0 l^- X \quad 1.27_{-0.18}^{+0.22}(\text{stat}) \pm 0.15(\text{syst})$$

$$\bar{B} \rightarrow D^+ l^- X \quad 1.18_{-0.27}^{+0.39}(\text{stat}) \pm 0.15(\text{syst})$$

$$\bar{B} \rightarrow D^{*+} l^- X \quad 1.19_{-0.19}^{+0.25}(\text{stat}) \pm 0.15(\text{syst})$$

The simple charge correlation is however complicated by production of higher spin D resonances (D^{**}) or nonresonant $D^{(*)} + n \cdot \pi$. The D^{**} charge is mixed into the $D^{(*)}$ and pion charges reducing the B-D charge correlation. Recent measurements by ARGUS and CLEO indicate that these contributions might be as large as 40% of the semileptonic branching ratios. The lifetimes of B^0 and B^+ thus were extracted after unfolding this effect using a model for D^{**} production and measured branching ratios. The results are in table 1.

3. Vertex Charge²

The idea is to separate all the charged particles in a jet into two unique vertices, one from the primary Z^0 decay and one from the b decay. The finite decay length of the D meson produced in the b decay can be neglected compared to the longer b decay distance. The charge of the decaying b-hadron is reconstructed by simply adding up the charges of the particles assigned to the b vertex.

First a primary vertex is formed constrained by the beam spot. The $P(\chi^2)$ of the vertex fit was required to be less than 1%. Jets which formed a satisfactory single vertex were thus not considered further. Then all the tracks in a jet were divided into two groups and all possible permutations of tracks were tried in a fit to a primary and a secondary vertex. The jet were retained only if the combined $P(\chi^2)$ for the primary and secondary vertex were larger than 10% and there were no other combinations with a $P(\chi^2)$ larger than 1%.

The charge measurement is about 80% correct with misidentification rates of 10% for $\Delta Q = \pm 1$ and 1% for $\Delta Q = \pm 2$, figure 3, determined from the rate of doubly

Hadron	D-lepton (ps)	Vertex charge (ps)
B^+	$1.30_{-0.29}^{+0.33} \pm 0.15 \pm 0.05$	$1.42 \pm 0.10 \pm 0.17 \pm 0.12$
B^0	$1.17_{-0.23}^{+0.29} \pm 0.15 \pm 0.05$	$1.39 \pm 0.16 \pm 0.10_{-0.45}^{+0.23}$
$\tau(B^+)/\tau(B^0)$	$1.11_{-0.39}^{+0.51} \pm 0.05 \pm 0.10$	$1.02 \pm 0.14 \pm 0.11_{-0.16}^{+0.26}$

Table 1: B^0 and B^+ lifetime results, the first error is statistical, the second experimental systematic and the third is the contribution from D^{**} production in the case of DI correlation and contribution from the composition in the case of vertex charge.

charged vertices and cross checked with Monte Carlo.

An event by event maximum likelihood fit gives the results (in ps):

$$\begin{aligned} \tau_{charged} &= 1.32 \pm 0.13(\text{stat}) \pm 0.15(\text{syst}) \\ \tau_{neutral} &= 1.47 \pm 0.17(\text{stat}) \pm 0.15(\text{syst}) \\ \tau_+/\tau_0 &= 0.91 \pm 0.17(\text{stat}) \pm 0.09(\text{syst}) \end{aligned}$$

This result is obtained by measuring the *excess decay length* from the minimum visible decay length obtained from data for each event. This results are consistent with a fit using an average acceptance function obtained from Monte Carlo.

The neutral verices originates from the decay of B^0 , B_s^0 and Λ_b , while the charged vertices mainly stem from B^+ with a possible small contribution from Σ_b^+ baryons. To extract the B^0 and B^+ lifetimes the charge misidentification were unfolded and the production rates of B_s^0 and Λ_b were modeled. The lifetimes of the latter were taken from recent LEP measurements. The results are in table 1.

4. Conclusions

Within errors the lifetimes of B^0 and B^+ are equal and no such effect as seen in the charm sector is observed.

5. Acknowledgemests

I thank D. Bloch, W. Murray for explanations and plots.

6. References

1. DELPHI Collaboration, *A Measurement of B Meson production and Lifetime Using DI Events in Z^0 decays*, CERN-PPE/92-174, contributed paper.
2. DELPHI Collaboration, *A measurement of the mean lifetimes of neutral and charged b-hadrons*, contributed paper.

Appendix F

Reprint of paper published in Physics Letters B.

A Measurement of the Mean Lifetimes of Charged and Neutral B-Hadrons

DELPHI Collaboration

Abstract

The decays of B-hadrons have been reconstructed using the charged particles recorded in the DELPHI silicon microstrip detector. The sum of the charges of the secondaries determines the charge of the B-hadron parent. Some 232 114 multihadronic Z^0 decays recorded during the 1991 run of LEP at centre-of-mass energies between 88.2 GeV and 94.2 GeV yield 253 B-hadron candidates with well-measured charge. From these the mean lifetimes of neutral and charged B-hadrons are found to be 1.44 ± 0.21 (stat) ± 0.14 (sys) ps and 1.56 ± 0.19 (stat) ± 0.13 (sys) ps respectively. The ratio of their lifetimes is $1.09^{+0.28}_{-0.23}$ (stat) ± 0.11 (sys). Under some assumptions on the abundance and lifetime of the Λ_b^0 and B_s^0 states, the B^0 and B^+ lifetimes are inferred.

(To be submitted to Physics Letters B)

P. Abreu²⁰, W. Adam⁷, T. Adye³⁷, E. Agosti³⁰, I. Ajinenko⁴³, R. Aleksan³⁹, G. D. Aleksiev¹⁴, A. Algeri¹³, P. Allen⁴⁹, S. Alinedze²⁵, S. J. Alsvaag¹, U. A. Amaldi¹, A. Andreazza²⁷, P. Antilogus²⁴, W. D. Apel¹⁵, R. J. Arpsimon³⁷, Y. Arnold³⁹, B. Asman⁴⁵, J.-E. Augustin¹⁸, A. Augustinus³⁰, P. Baillon⁷, P. Bambade¹⁸, F. Barao²⁰, R. Barate¹², G. Barbellini⁴⁷, D. Y. Bardhin¹⁴, G. J. Barker³⁰, A. Baronecchi⁴¹, O. Barot²⁵, W. Barter⁵⁰, M. J. Bates³⁷, M. Battaglia¹³, M. Baubiller²², K.-H. Becks⁵², C. J. Beeston³⁴, M. Begalli³⁶, P. Belliere⁶, Yu. Belokopytov⁴³, P. Beltracchi⁸, D. Benedic⁸, A. C. Benvenuti⁵, M. Berggren¹⁶, D. Bertrand¹⁶, F. Bianchi¹⁶, M. S. Bilenky¹⁴, P. Billio²², P. Bjarne²³, D. Bloch⁸, S. Blyth³⁴, V. Bocci³⁸, P. N. Bogolubov¹⁴, T. Bolognese³⁹, M. Bonesini²⁷, W. Bonivento²⁷, P. S. L. Booth²¹, G. Borisov⁴³, H. Borner⁷, C. Bosio⁴¹, B. Bosjancic⁴⁴, S. Bosworth³⁴, O. Botner⁸, B. Bouquet¹⁶, C. Bourdarios¹⁶, T. J. V. Bowcock²¹, M. Bozzo¹¹, S. Bralbant², P. Branchini⁴¹, K. D. Brand³⁵, R. A. Breuner⁷, H. Briand²², C. Bricean², R. C. A. Brown⁷, N. Brummner³⁰, J.-M. Brunet⁶, L. Bugge²³, T. Buran³⁵, H. Burtmeister⁷, J. A. M. A. Buytaert¹, M. Caccia¹, M. Calvi²⁷, A. J. Camacho Rozas⁴², R. Campion²¹, T. Camporesi¹⁷, V. Canale³⁸, F. Cao², F. Carena⁷, L. Carroll²¹, C. Caso¹¹, M. V. Castillo Gimenez⁴⁹, A. Cattai⁷, F. R. Cavallo¹⁶, L. Cerrito³⁸, V. Chabaud²⁹, A. Chan¹, Ph. Charpentier¹, L. Chaussau²², P. Chauvaud²², P. Checchia³⁵, G. A. Chelkov¹⁴, L. Chevallier³⁹, P. Chliapnikov⁴³, V. Chrochovicz²², J. T. M. Chrin⁴⁹, P. Collins³⁴, J. L. Contreras²⁵, R. Contri¹¹, E. Cortina⁴⁹, G. Cosme¹⁸, F. Couchot¹⁸, H. B. Crawley¹, D. Crommelin¹, G. Crosetti¹¹, M. Crozon⁶, J. Cuevas Maestro³³, S. Czellar¹³, E. Dahl-Jensen²⁸, B. Dalmagne¹⁸, M. Dam³², G. D. D'Amico²⁸, E. Daubie², A. Daum¹⁵, P. D. Dauncey¹, M. Davenport⁷, P. David²², J. Davies²¹, W. Da Silva²², C. DeFio⁶, P. Delporte⁶, N. Demaria⁴⁶, A. De Angelis⁴⁷, H. De Boeck², W. De Boer¹⁵, C. De Clercq², M. D. M. De Feo⁴⁹, P. A. M. De Groot³⁰, C. De La Vaissiere²², B. De Lotto⁴⁷, A. De Min²⁷, H. Dijkstra⁷, L. Di Ciaccio³⁶, J. Dolbeur⁶, M. Donszelmann⁷, K. Doroba³¹, M. Dracos¹, M. Drees⁵², M. Driess³¹, Y. Dufour⁷, F. Dupont², D. Edsall¹, L.-O. Eck⁴⁶, P. A. M. Eerola⁴, R. Ehret¹⁵, T. Ekelof⁴⁸, G. Elkspong⁴⁵, A. Elliot Peisert³⁵, J.-P. Engel¹⁸, N. Ershaidat²², V. Falaleev⁴³, D. Fassoulotis³¹, M. Feindt⁷, M. Fernandez Alonso⁴², A. Ferrer⁴⁹, T. A. Filippos³¹, A. Firestone¹, H. Foeth¹⁷, E. Fokitis³¹, F. Fontaneli¹¹, K. A. J. Forbes²¹, J.-L. Foussat²⁶, S. Franconi²⁴, B. Franek³⁷, P. Frenklid⁶, D. C. Fries¹⁵, A. G. Frodesen⁴, R. Fruhwirth⁵⁰, F. Fulda-Queizer¹⁸, K. Furuval³¹, H. Furstenau⁵, J. Fuster¹⁷, D. Gamba⁴⁶, C. Garcia⁴⁹, J. Garcia⁴², C. Gaspar⁷, U. Gasparin³⁵, Ph. Gavillet⁷, E. N. Gaziz³¹, J.-P. Gerber⁸, P. Giacomelli⁷, R. Gokhale⁵¹, B. Golob⁴⁴, V. M. Golovatyuk¹⁴, J. J. Gomez Y Cadenas⁷, G. Gopal³⁷, L. Gorn¹, M. Gorski¹⁴, V. Gracco¹¹, A. Grant⁷, F. Grand⁷, E. Graziani⁴¹, G. Grosdidier¹⁶, E. Gross⁷, P. Grosse Wiesmann¹, B. Grossclette²², J. Guay³⁷, U. Haedinger¹⁵, F. Hahn⁵², M. Hahn¹⁵, S. Haider³⁰, A. Habekuss²³, A. Hallgrun⁴⁸, K. Hamacher²², G. Hamel De Monchenault³⁹, W. Hao³⁰, F. J. Harris³⁴, V. Hedberg²³, T. Henkes⁴, J. J. Hernandez⁴⁹, P. Herquet², H. Herr⁷, T. L. Hessing²¹, I. Hietanen¹³, C. O. Higgins²¹, E. Higou⁴⁹, H. J. Hille⁷, S. D. Hodgson³⁴, T. Hofmohl⁵¹, S.-O. Holmgren⁴⁵, D. Holtzhausen³⁰, P. F. Honore¹, J. E. Hooper²⁸, M. Houlden⁷, J. Hrubec³⁰, K. Huet³, P. O. Hulth⁴⁸, K. Hultqvist⁴⁵, P. Ioannou³, P. S. Iwersen⁴, J. N. Jackson²¹, P. Jalocha¹⁶, G. Jarlskog²³, P. Jarry³⁹, B. Jean-Marie¹⁸, E. K. Johansson⁴⁵, D. Johnson², M. Jonker⁷, L. Jonsson²³, P. Juillot⁶, G. Kalkans³⁷, G. Kalinush³⁷, F. Kapusta²², M. Karlsen⁷, E. Karvelas⁹, S. Katsanavas³¹, R. Keranen⁷, J. Kesteman², B. A. Khomenko¹⁴, N. N. Khovanskii¹⁴, B. King¹, N. J. Kjaer⁷, H. Klein⁷, A. Klovning⁴, P. Kluit³⁰, A. Koch-Mehrin¹, J. H. Kochne¹⁵, B. Koene²⁰, P. Kokkinias⁹, M. Koratzinos²², A. V. Korytov¹⁴, V. Kostoukhine⁵¹, C. Kourkoumelis³², O. Kouznetsov¹⁴, P. H. Kramer⁵², C. Kreuter¹⁵, J. Krollikowski⁵¹, I. Kronkvist²³, U. Krueuer-Marquis⁵², W. Krupinski¹⁶, K. Kulka⁴⁸, K. Kurvinen¹³, C. Lacasta⁴⁹, C. Lambropoulos⁹, J. W. Lamza¹, L. Lauceri⁴⁷, V. Lapin⁴³, J.-P. Laugier³⁹, R. Lauhakangas¹³, G. Leder⁵⁰, F. Ledroit¹², R. Leitner²⁹, Y. Lemoigne³⁹, J. Lecomte², G. Lenzen⁵², V. Lepeltier¹⁶, T. Lesiak¹⁶, J. M. Levy⁸, E. Lieb³², D. Liko³⁰, J. Lindgren¹⁵, R. Lindner⁵², A. Lipniacka⁵¹, I. Lippi³⁵, B. Loverstad²³, M. Lokajicek¹⁰, J. G. Loken³⁴, A. Lopez-Fernandez⁷, M. A. Lopez-Aguera⁴², M. Los⁵⁰, D. Loukas¹, J. J. Lozano⁶, P. Lutz⁶, L. Lyons³⁴, G. Maehlum³², J. Maillard¹⁶, A. Maio⁴⁰, A. Maltezos⁹, F. Mandl⁵⁰, J. Marco⁴², M. Margoni³⁵, J.-C. Marin⁷, A. Markou⁷, T. Maron⁵², S. Marti⁴⁹, F. Martorel⁴², C. Matteuzzi²⁷, G. Matthiae³⁸, M. Mazzucato³⁵, M. Mc Cubbin³¹, R. Mc Kay¹, R. Mc Nulty²¹, G. Micola¹¹, C. Meroni²⁷, W. T. Meyer¹, M. Michelotto³⁵, I. Mikulec⁵⁰, L. Mirabito²⁴, W. A. Mitaroff⁵⁰, G. V. Mitselmakher¹⁴, U. Mjornmark²³, T. Moa⁴⁵, R. Moeller²⁸, K. Moenig⁷, M. R. Monge¹¹, P. Morettini¹¹, H. Mueller¹⁵, W. J. Murray⁴⁷, B. Muryn¹⁶, G. Myatt³⁴, F. L. Navarria⁵, P. Negr²⁷, R. Nicolaoudou¹⁶, B. S. Nielsen²⁸, B. Nijthar²¹, V. Nikolaenko⁴³, P. E. S. Nilsson⁴, P. Niss⁴⁵, A. Nomerotski³⁵, V. Obraztsov⁴³, A. G. Olshevskii¹⁴, R. Orava¹³, A. Ostankov⁴³, K. Osterberg⁵, A. Ouraou³⁹, M. Paganoni²⁷, R. Pain²⁸, H. Palka¹⁶, Th. D. Papadopoulos³¹, L. Pape¹⁷, F. Parodi¹¹, A. Petrolini¹, F. Pierre³⁹, M. Pimenta²⁰, O. Pingot², S. Piaszczyński¹⁶, O. Podobrin¹⁵, M. E. Pol¹⁷, G. Polok¹⁶, P. Poropat⁴⁷, V. Pozdniakov¹⁴, P. Privitera¹⁵, A. Pullia²⁷, D. Radajicac³⁴, S. Ragazzi²⁷, H. Rahaman³¹, P. N. Ratcoff⁴⁹, A. L. Read⁵², P. Rebecchi⁷, N. G. Redaelli³⁷, M. Regler⁵⁰, D. Reid⁷, P. B. Renton³⁴, L.-K. Resvanis³, F. Richard¹⁸, M. Richardson²¹, J. Ritzky¹⁰, G. Rinaudo⁴⁶, I. Roditi¹⁷, A. Romero⁴⁶, I. Roncagliolo¹¹, P. Roncace³⁵, C. Rounqvist¹⁵, E. I. Rosenberg¹, S. Rossi⁷, E. Rosso⁷, P. Roudreau¹⁸, T. Rovelli¹⁵, W. Ruckstuhl¹⁰, V. Ruhlmann-Kleider³⁹, A. Ruiz⁴², K. Rybicki¹⁶, H. Saarikko¹³, Y. Sacquin³⁹, G. Sajo⁴⁹, J. Sal⁴⁹, J. Sanchez²⁵, M. Sannino^{11,40}, S. Schael⁷, H. Schneider¹⁵, M. A. E. Schyns⁵², G. Sciolla⁴⁶, F. Scuri⁴⁷, A. M. Segar³⁴, A. Schitz¹⁵, R. Sekulin³⁷, M. Sessa⁴⁷, R. Seufert¹⁵, R. C. Shellard³⁶, I. Siccamo⁵⁰, P. Siegrist³⁹, S. Simonetti¹¹, F. Simonetti³⁵,

1 Introduction

The aim of this analysis is to measure the charged and neutral B-hadron lifetimes using the event topology, without explicit identification of the final states. The method is entirely dependent upon finding the production and decay vertices using the charged particle tracks, and therefore relies largely upon the vertex detector of DELPHI to identify which charged particles come from a secondary vertex, and hence to ensure that the B charge is well estimated.

According to the spectator model [1], the light constituents are expected to play a passive role in weak decays of hadrons composed of a heavy quark and light quarks. This model predicts that the lifetimes of all weak decays with a heavy quark are equal and are determined by the lifetime of the heavy quark. However, the lifetime differences between charmed particles clearly indicate corrections to the spectator model.

A brief description of the detector can be found in section 2. Section 3 details the event selection procedure and section 4 describes the fit technique. The B lifetime results are presented in section 5.

2 The Apparatus

The DELPHI detector has been described in detail elsewhere [2]. Only the properties relevant to this analysis are summarized here.

In the barrel region, charged particles are measured by a set of cylindrical tracking detectors whose z axes are common with the beam direction and with the axis of the solenoidal magnet which produces a 1.23 T field. The coordinate system is defined by the azimuthal angle ϕ and the radius R from the axis, and either the polar angle θ to the electron beam direction, or the z distance along that direction.

The Time Projection Chamber (TPC) is the main tracking device. Charged particles tracks are reconstructed in three dimensions for radii between 30 cm and 122 cm with up to 16 space points for polar angles between 39° and 141° , and four or more space points for polar angles between 21° and 39° and between 141° and 159° .

Additional measurements are provided by the Inner and Outer detectors. The Inner detector (ID) is a cylindrical drift chamber covering radii between 12 cm and 28 cm and θ between 29° and 151° . A central jet chamber giving up to 24 $R\phi$ coordinates is surrounded by five layers of proportional chambers providing both $R\phi$ and z coordinates. The Outer detector has five layers of drift cells at radii between 198 cm and 206 cm and θ between 42° and 138° .

The vertex detector (VD) [3] used in this analysis consisted of two independent half shells of silicon microstrip detectors inserted between the beam pipe and the ID. Each half shell had three concentric and overlapping layers of silicon microstrip detectors located at average radii 6.3 cm, 8.8 cm and 10.9 cm. The overlap between detectors in a layer was about 10%; the split between the two half-shells also had this overlap.

The vertex detector measured three $R\phi$ coordinates for particles with polar angle between 43° and 137° . The intrinsic precision of the microstrip detectors was measured to be $6 \mu\text{m}$ and the precision of a $R\phi$ measurement on a charged particle was $8 \mu\text{m}$. A three-dimensional survey of the sensitive elements (with a precision in $R\phi$ of 20 μm) provided the alignment prior to installation. The final alignment used Z^0 decays into muon pairs or hadronic final states. Particles passing through the overlapping VD layers were used as a cross-check on this alignment. Fibre optic and capacitive devices monitored

[†]The symbol B means charged or neutral B-hadron.

A.N.Sisakian¹⁴, G.Skjvelving³², G.Smadja^{39,24}, N.Smirnov⁴³, O.Smirnov¹⁴, G.R.Smith³⁷, R.Sosnowski⁵¹, D.Souza-Santos³⁶, T.S.Spasooff¹², E.Spiriti⁴¹, S.Squarcia¹¹, H.Staack⁵², C.Stanescu⁴¹, S.Stapnes³², G.Stavropoulos⁹, F.Stichelbaud², A.Stocchi¹⁶, J.Strauss⁵⁰, J.Straver⁷, R.Strub⁸, B.Stugu¹, M.Szczekowski¹⁷, M.Szeptycka³¹, P.Szymanski⁵¹, T.Tabarelli²⁷, O.Tchikilev⁴³, G.E.Theodosios⁹, A.Tiquini²⁶, J.Timmermans³⁰, V.G.Tinofeev¹⁴, L.G.Thakuche¹⁴, T.Todorov⁶, D.Z.Toet³⁰, O.Toker¹³, B.Tome²⁰, E.Torassa⁴⁶, L.Tortora¹, D.Treille⁷, W.Trischuk⁷, G.Tristram⁶, C.Troncon³⁷, A.Tsirou¹, E.N.Tsyganov¹⁴, M.Turata¹⁶, M.L.Turluc³⁹, T.Tuuva¹³, J.A.Tyapkin²², M.Tyndel³⁷, S.Tzamaras²¹, S.Ueberschaer⁵², O.Ullaland⁷, V.Uvarov⁴³, G.Valent¹, E.Vallazza⁴⁶, J.A.Valls Ferrer⁴⁶, C.Vander Veldde⁶, G.W.Van Apeldoorn¹⁰, P.Van Dam¹⁰, M.Van Der Heijden³⁰, W.K.Van Doninck², P.Vaz⁷, G.Vegni²⁷, L.Ventura³⁵, W.Venus³⁷, F.Verbeure², M.Verlaato³⁵, L.S.Vertogradov¹⁴, D.Vilanova³⁹, P.Vincent²⁴, L.Vitale¹³, E.Vlasov⁴³, A.S.Vodopyanov¹, M.Vollmer⁵², M.Voutilainen⁵, V.Vrba¹, H.Wahlén³², C.Walck⁴, F.Waldner⁴⁷, A.Wehr⁵², M.Weierstal⁵², P.Weillhammer⁷, J.Werner⁵², A.M.Weucher¹⁷, J.H.Wickens³, G.R.Wilkinson³⁴, W.S.C.Williams³⁴, M.Winter⁶, M.Witek¹⁶, G.Wormser¹⁸, K.Woschnagg⁴⁸, N.Yamaguchi⁴⁵, P.Yepes¹⁷, A.Zaitsev⁴³, A.Zalawski¹⁶, P.Zalawski¹⁶, D.Zavrtanik⁴⁵, E.Zevgoulatos⁹, G.Zhang⁵², N.I.Zimin¹⁴, M.Zito³⁹, R.Zuberi³⁴, R.Zukanovich Funchal¹⁶, G.Zumentis³⁵, J.Zumiga¹⁰

¹ Ames Laboratory and Department of Physics, Iowa State University, Ames IA 50011, USA

² Physics Department, Univ. Instelling Antwerpen, Universiteitsplein 1, B-2610 Wilrijk, Belgium

³ IHEP, ULB-VUB, Pleinlaan 2, B-1050 Brussels, Belgium

⁴ and Faculté des Sciences, Univ. de l'Etat Mons, Av. Maistriau 19, B-7000 Mons, Belgium

⁵ Physics Laboratory, University of Athens, Solonos Str. 104, GR-10680 Athens, Greece

⁶ Department of Physics, University of Bergen, Allégaten 55, N-5007 Bergen, Norway

⁷ Dipartimento di Fisica, Università di Bologna and INFN, Via Irnerio 46, I-40126 Bologna, Italy

⁸ Collège de France, Lab. de Physique Corpusculaire, IN2P3-CNRS, F-75231 Paris Cedex 05, France

⁹ CERN, CH-1211 Geneva 23, Switzerland

¹⁰ Centre de Recherche Nucléaire, IN2P3-CNRS/ULP, BP20, F-67037 Strasbourg Cedex, France

¹¹ Institute of Nuclear Physics, N.C.S.R. Demokritos, P.O. Box 60228, GR-15310 Athens, Greece

¹² FZU, Inst. of Physics of the C.A.S. High Energy Physics Division, Na Slovance 2, CS-180 40, Praha 8, Czechoslovakia

¹³ Dipartimento di Fisica, Università di Genova and INFN, Via Dodecaneso 33, I-16146 Genova, Italy

¹⁴ Institut des Sciences Nucléaires, IN2P3-CNRS, Université de Grenoble 1, F-38026 Grenoble, France

¹⁵ Research Institute for High Energy Physics, SEFT, Siltavuorenpolku 20 C, SF-00170 Helsinki, Finland

¹⁶ Joint Institute for Nuclear Research, Dubna, Head Post Office, P.O. Box 79, 101 000 Moscow, Russian Federation

¹⁷ Institut für Experimentelle Kernphysik, Universität Karlsruhe, Postfach 6980, D-7500 Karlsruhe 1, Germany

¹⁸ High Energy Physics Laboratory, Institute of Nuclear Physics, Ul. Kawary 26 a, PL-30055 Krakow 30, Poland

¹⁹ Centro Brasileiro de Pesquisas Físicas, rua Xavier Sigaud 150, RJ-22290 Rio de Janeiro, Brazil

²⁰ School of Physics and Materials, University of Lancaster, GB - Lancaster LA1 4YB, UK

²¹ LIP, IST, FCUL - Av. Elias Garcia, 14 - 1°, P-1000 Lisboa Codex, Portugal

²² Department of Physics, University of Liverpool, P.O. Box 147, GB - Liverpool L69 3BX, UK

²³ LPNHE, IN2P3-CNRS, Universités Paris VI et VII, Tour 33 (RdC), 4 place Jussieu, F-75252 Paris Cedex 05, France

²⁴ Université Claude Bernard de Lyon, IPNL, IN2P3-CNRS, F-69622 Villeurbanne Cedex, France

²⁵ Universidad Complutense, Avda. Complutense s/n, E-28040 Madrid, Spain

²⁶ Univ. d'Aix - Marseille II - CPP, IN2P3-CNRS, F-13288 Marseille Cedex 09, France

²⁷ Dipartimento di Fisica, Università di Milano and INFN, Via Celoria 16, I-20133 Milan, Italy

²⁸ Niels Bohr Institute, Blegdamsvej 17, DK-2100 Copenhagen 0, Denmark

²⁹ NC, Nuclear Centre of MFF, Charles University, Areal MFF, V Holešovičkách 2, CS-180 00, Praha 8, Czechoslovakia

³⁰ NIKHEF-H, Postbus 41882, NL-1009 DB Amsterdam, The Netherlands

³¹ National Technical University, Physics Department, Zografou Campus, GR-15773 Athens, Greece

³² Physics Department, University of Oslo, Blindern, Nj 1060 Oslo 3, Norway

³³ Depto. Fisica, Univ. Oviedo, C/P Jimenez Casas, S/N-33006 Oviedo, Spain

³⁴ Department of Physics, University of Oxford, Keble Road, Oxford OX1 3RH, UK

³⁵ Dipartimento di Fisica, Università di Padova and INFN, Via Marzolo 8, I-35131 Padua, Italy

³⁶ Depto. de Fisica, Pontificia Univ. Católica, C.P. 38071 RJ-22453 Rio de Janeiro, Brazil

³⁷ Rutherford Appleton Laboratory, Chilton, GB - Didcot OX11 0QX, UK

³⁸ Centre d'Etude de Saclay, DSM/DAPNIA, F-91191 Gif-sur-Yvette Cedex, France

³⁹ Dipartimento di Fisica - Università di Salerno, I-84100 Salerno, Italy

⁴⁰ Istituto Superiore di Sanità, Ist. Naz. di Fisica Nucl. (INFN), Viale Regina Elena 299, I-00161 Rome, Italy

⁴¹ C.E.A.F.M. - C.S.I.C. - Univ. Cantabria, Avda. los Castros, S/N-39006 Santander, Spain

⁴² Inst. for High Energy Physics, Serpukhov P.O. Box 35, Protvino, (Moscow Region), Russian Federation

⁴³ J. Stefan Institute and Department of Physics, University of Ljubljana, Jamova 39, SI-61000 Ljubljana, Slovenia

⁴⁴ Fysikum, Stockholm University, Box 6730, S-113 85 Stockholm, Sweden

⁴⁵ Dipartimento di Fisica Sperimentale, Università di Torino and INFN, Via F. Ciurina 1, I-10125 Turin, Italy

⁴⁶ Instituto di Fisica, Università di Trieste and INFN, Via A. Valerio 2, I-34127 Trieste, Italy

⁴⁷ Dipartimento di Fisica, Università di Udine, I-33100 Udine, Italy

⁴⁸ Department of Radiation Sciences, University of Uppsala, P.O. Box 535, S-751 21 Uppsala, Sweden

⁴⁹ IJPC, Valencia-CSIC, and D.F.A.M.N., U. de Valencia, Avda. Dr. Moliner 50, E-46100 Burjassot (Valencia), Spain

⁵⁰ Institut für Hochenergiephysik, Österr. Akad. d. Wissensch., Nikolsdorfergasse 18, A-1050 Vienna, Austria

⁵¹ Inst. Nuclear Studies and University of Warsaw, Ul. Hoza 69, PL-00681 Warsaw, Poland

⁵² Fachbereich Physik, University of Wuppertal, Postfach 100 127, D-5600 Wuppertal 1, Germany

the stability of the detector during the data-taking and showed the maximum movements of the detector to be less than $10 \mu\text{m}$.

To measure charged particle tracks accurately needed a combination of VD, ID, TPC and OD detectors. In particular the vertex detector precision alone was not sufficient to measure accurately the particle momenta, or even the charges. Tracks from one detector were thus associated to the next component, a procedure which in general started from the TPC tracks, and an overall track fit was applied to each particle.

The position and size of the LEP beam was found on a run by run basis, as described in reference [4]. The mean intersection point of charged particle trajectories with this beam spot was checked and showed negligible residual systematics.

3 Event Analysis

3.1 Hadronic Event Selection

Only charged particles measured in the tracking chambers and with a momentum p above $0.1 \text{ GeV}/c$, a measured track length over 50 cm and an angle to the beam axis exceeding 25° were used in this analysis.

The sum of the energies of these charged particles in each of the forward and backward hemispheres (with respect to the beams) was required to exceed 3 GeV , and the total energy had to be more than 15 GeV , assuming the pion mass for each particle. Furthermore, at least six charged particles were required with momenta over $0.2 \text{ GeV}/c$. These cuts selected 232 114 events as hadronic Z^0 decays.

After this hadronic event selection, the JADE jet clustering algorithm [5] was applied with a scaled invariant mass squared cut of 0.04 . The mean number of jets per event was 2.39.

3.2 Charged Particle Selection

The charged particles from light hadron decays or from secondary interactions can confuse an attempt to find a secondary vertex close to the beam spot. To reduce this problem all pairs of oppositely charged particles were combined to see if they were consistent with a K_s^0 decay or γ conversion. About $0.1 K_s^0$ and 0.25γ per event were identified and the charged particles tagged so that they were not considered further.

After the jet finding and pair rejection, only charged particles with momentum over $0.5 \text{ GeV}/c$ and lying within 40° of the jet axis were used in the subsequent analysis. Only jets with at least three such charged particles were accepted. All selected particles in the jet were required to have hits on at least two (of the three) different layers of the vertex detector, in order to be considered to be reliably measured. Only one jet in five met this requirement. Over half the loss of jets was due to purely geometric effects coming from the finite size of the Vertex Detector. The remaining loss was attributed to interactions in the material beyond the silicon, vertex detector inefficiencies and track fitting problems.

The effect of these two requirements on the data sample is listed in the first three rows of Table 1. Also shown are the results of a full Monte Carlo simulation, starting from Z^0 decays generated by the program JETSET 7.3 [6] and including particle interactions in materials and detector resolutions [7]. The fractions of the four dominant B species assumed in this simulation can be seen in Table 3 below; their lifetimes were all taken to be 1.2 ps except for the Λ_b^0 whose lifetimes was set at 1.3 ps .

Selection	Number of Jets		
	Data	Simulation	Ratio
Initial jet sample	554484	878285	0.63
≥ 3 charged particles per jet	499178	793053	0.63
Each particle with ≥ 2 VD hits	96659	187199	0.52
Not all from primary vertex	41941	72147	0.58
Clear secondary vertex	6528	11502	0.57

Table 1: Cumulative effect of each selection on the 232 114 data and 369 609 simulated selected hadronic events.

It can be seen in Table 1 that the requirement of 2 vertex detector hits on each charged particle was not well reproduced by the Monte Carlo simulation. This probably reflected the difficulty of reproducing particle reinteractions and track association. The probability of having two hits on any given particle track in the data was 96% to 99% of that in the simulation for momenta below $20 \text{ GeV}/c$; this fraction was lower for particles of higher momentum.

3.3 Calibration of Track Extrapolation Errors

The assignment of particles to the primary vertex or B-hadron used the extrapolated track positions in the plane perpendicular to the beam direction. An accurate knowledge of the uncertainty on this extrapolation was therefore essential. The z coordinate was much less precise than $R\phi$, therefore the vertex reconstruction used only the $R\phi$ projection of the charged particle tracks with the z coordinate used to resolve ambiguities.

There were two contributions to the extrapolation error: the intrinsic measurement resolution (σ_{meas}) and the multiple scattering (σ_{scat}). The track extrapolation error, $\sigma_{R\phi}$, was parameterized by:

$$\sigma_{R\phi} = \left[\sigma_{\text{meas}}^2 + \frac{\sigma_{\text{scat}}^2}{p^2 \sin^2 \theta} \right]^{\frac{1}{2}} \quad (1)$$

where p is the particle momentum in GeV/c and θ is its polar angle. The coefficients σ_{meas} and σ_{scat} were determined using the same charged particles as were used in the analysis. In all jets with at least four charged particles, the three particles of highest momentum and the three particles of lowest momentum were each taken to form a vertex, and the χ^2 probability, $P(\chi^2)$, that all three come from a common point was found. This χ^2 probability was required to be greater than 0.2. The coefficients (σ_{meas}) and (σ_{scat}) were varied until a flat distribution was obtained for both the high and low momentum triplets. The high momentum distribution was more sensitive to the asymptotic uncertainty, and the low momentum distribution to the multiple scattering. The values obtained, $\sigma_{\text{meas}} = 30 \pm 3 \mu\text{m}$ and $\sigma_{\text{scat}} = 70 \pm 4 \mu\text{m}$, represent an average over different classes of track, and are slightly larger than those in reference [3], for which hits in all three silicon layers were required on each charged particle.

3.4 Secondary Vertex Identification

Particles had to be assigned to the correct vertex in order to determine the charge of the B-hadron. Each jet was examined independently. If produced by a b quark it will in

general contain several vertices: the primary interaction, b decay, c decay and perhaps s decay. However, in order to simplify the analysis, the jet was assumed to contain only the primary vertex and a single decay vertex. The flight distance of secondary charmed hadrons from B decay was thus ignored.

A vertex was formed from all selected particles in the jet constrained to pass through the measured beam spot, which was assumed to have a size of $150 \mu\text{m}$ by $10 \mu\text{m}$. If there was a resolvable secondary vertex, then the χ^2 probability that all charged particle tracks come from a single vertex consistent with the beam spot was very small. Therefore, if the jet vertex had a χ^2 probability greater than 1% it was not considered further.

Next all the particles within the same jet were divided into two groups, with all possible permutations being tried. One group was used to make a vertex which was constrained by the beam spot, while a secondary vertex was formed using the particles in the other group with no such constraint. At least two particles were required in the secondary vertex. The combined χ^2 probability, for which the number of degrees of freedom is the number of particles minus two, was required to exceed 1%. If there was one and only one combination which satisfied this requirement, a satisfactory secondary vertex was considered to have been found. Jets with more possible combinations were regarded as ambiguous, and rejected.

3.5 Secondary Vertex Selection

After these requirements (see Table 1), the invariant mass at the secondary vertex, M_{vis}^* , was calculated, assuming that all charged particles were pions. Figure 1 shows the mass distribution for data and Monte Carlo simulation, after all other selections have been applied, and with the simulated events subdivided into different quark flavours. A K_S^0 peak can be seen, because the criteria for their prior removal were very tight. The observed mass was less than the true mass because of the unused neutral particles and missing charged particles. On the basis of the observed distribution of the different quark flavours in the simulated sample, B decays were selected by requiring that M_{vis}^* be greater than $2.2 \text{ GeV}/c^2$. The absence of events above the kinematic limit at about the B^0 mass is consistent with the expectation of a correct assignment of particles to the vertices.

Table 2 shows this and the other selections explained below. It has two columns for the simulation in which generated B particles lifetimes were 1.2 ps except for the Λ_b^0 which was 1.3 ps. The first column, labelled unweighted, counts vertices in a straightforward manner, while in the second they are weighted to simulate a B-hadron lifetime of 1.5 ps. This weight is $W = \frac{\tau}{\tau_g} \exp(t/\tau_g - t/\tau)$, where τ_g is the generated lifetime, τ is the required lifetime and t is the proper time of the B decay. This procedure demonstrates the consistency of the selections if the mean B lifetime is around 1.5 ps.

The transverse distance between the two vertices, $l_{R\phi}$, was calculated, and its uncertainty, σ_l , was derived from the vertex errors. The vertices were used only if this uncertainty was less than $600 \mu\text{m}$, to remove configurations with nearly parallel charged particle tracks. This rejected few B candidates, as their typical uncertainty was $190 \mu\text{m}$.

Next, the vector sum of the momenta of all the particles assigned to the secondary vertex was found, and its azimuthal angle, ϕ_{mom} , obtained. Taking the difference $\delta\phi = \phi_{\text{geom}}$, of the vector joining the primary and secondary vertices, the difference $\delta\phi = \phi_{\text{mom}} - \phi_{\text{geom}}$ was computed. This was expected to be near zero for B candidates because the momentum will point in the same direction as the line of flight. However, ϕ_{mom} did not coincide with the B momentum, mostly due to the momentum carried by neutral particles. Furthermore, the measurement of the primary and secondary vertices produced an error

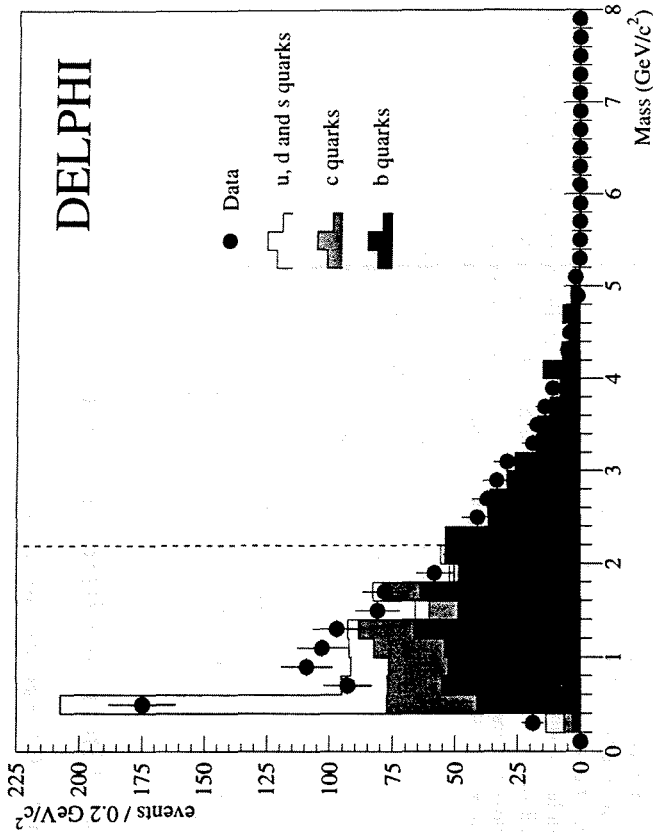


Figure 1: The reconstructed mass, M_{vis}^* , for Data and Monte Carlo simulation, with the cut at $2.2 \text{ GeV}/c^2$ indicated by the dashed line. The simulation has been weighted to correspond to a B lifetime of 1.5 ps and normalized to the same number of selected vertices as the Data. All selections have been made except for the missing charged particle search and the mass cut. A residual peak of K_S^0 can be seen, because the rejection criteria were conservative.

on $\delta\phi$ which decreases with increasing decay length. The error, $\sigma_{\delta\phi}$, was parameterized from the Monte Carlo simulation as $\sqrt{0.033^2 + (1.40 \mu\text{m}/l_{R\phi})^2}$. Only vertices with $\delta\phi/\sigma_{\delta\phi}$ less than three were accepted.

A comparison of these quantities and their errors in real and simulated data indicates that they are well modelled by the Monte Carlo simulation, as might be inferred from Table 2. The following additional criteria were applied :

- The number of jets in the event was required to be three or less, which reduced the chance of assigning the charged particles from a B decay to more than one jet. Note that if this happened the particle would have been ignored, and the charge would almost certainly be wrong. This rejected 1% of the events.
- The decay length, $l_{R\phi}$, was required to be less than 4 cm, well inside the beam pipe. This rejected 3% of events.
- The minimum acceptable decay length (see section 4.2.1) was more than $5 \sigma_l$.
- The χ^2 probability of the accepted vertex combination was required to be greater than 10%, while preserving the previous criterion that no other combination should

Selection	Data	Number of Vertices		
		Unweighted	Ratio	Weighted
Initial vertex sample	6528	11502	0.57	11881
Mass > 2.2 GeV/c ²	544	744	0.73	935
$\sigma_I < 600 \mu\text{m}$	514	706	0.73	898
$\delta\phi/\sigma_{\delta\phi} < 3$	455	612	0.74	804
Number of jets ≤ 3	451	601	0.75	791
$l_{R\phi} < 4 \text{ cm}$	436	568	0.77	758
$l_{R\phi}^{\text{min}} > 5\sigma_I$	428	566	0.76	756
$P(\chi^2) > 0.10$	265	360	0.74	496
No missing charged particle	253	341	0.74	473

Table 2: Cumulated effect of each selection applied to the vertices. See section 3.5 for a discussion of the weighting procedure.

have a probability over 1%. A flat probability distribution is not expected for the correct assignment in B events, because of the decay length of the charmed hadrons. By requiring this large difference in probability, the chance of associating the wrong particles to the secondary vertex has been minimized.

The decay length distribution for the vertices finally selected is shown in Figure 2. The mean charged multiplicity of the accepted secondary vertices was 3.75 ± 0.08 for the data and 3.60 ± 0.07 for the Monte Carlo simulation. This showed agreement between simulation and data, but is not the mean charged particle multiplicity in B decay, which was 5.1 in the simulation. The difference is due to bias in the selections, not to losing 1.5 tracks per jet.

3.6 Missing Charged Particle Search

The analysis requires a good estimate of the charge of the decaying B-hadron, and so the loss of charged particles must be minimized. Hits in the vertex detector compatible with being produced by a particle coming from the B decay, but not associated to any particle track reconstructed by the main tracking chambers, are an indication of inefficiencies in the tracking system or interactions before the TPC. To avoid introducing an error in the measured charge, jets which contained such hits were removed as follows.

The vertex detector was searched for unassociated hits in all three layers which form a circle consistent with coming from the B decay point. The errors on the individual silicon points were considerably larger than the $8 \mu\text{m}$ previously stated since the z of the hypothetical particle was unknown, and the detector elements were not perfectly parallel to the z axis. This led to an extrapolation precision, based on the vertex detector alone, of around $400 \mu\text{m}$. A candidate particle formed in this way was therefore regarded as compatible with the B decay point if its distance of closest approach to that point was less than 1 mm. To be accepted it had to be within 40° in ϕ of the jet direction with a momentum to the beam direction, p_T , of more than $0.5 \text{ GeV}/c$.

The accuracy with which such a particle track was measured was not sufficient for it to be used in the analysis, and so if any were found the jet was discarded. This procedure rejected 5% of the jets, as can be seen in Table 2.

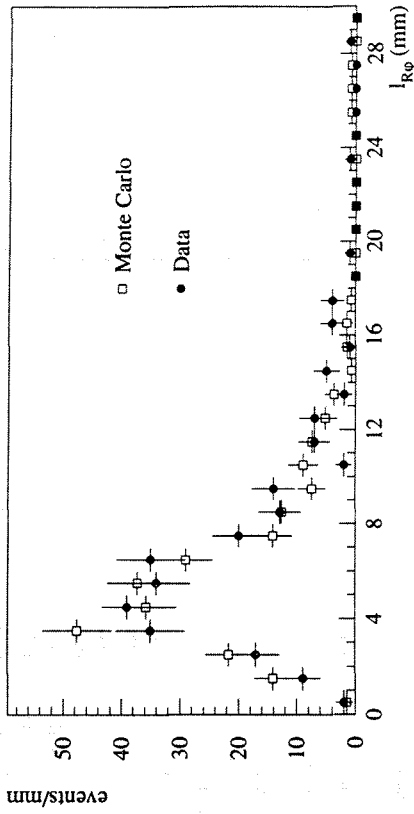


Figure 2: The $R\phi$ decay lengths of the accepted events in Monte Carlo simulation and data.

3.7 Selected Sample Composition

The composition of the simulated events passing all the selections is listed in Table 3. The fraction of B jets is estimated to be 98%. There is evidence of an enhancement in the selection of B^+ with respect to B^0 mesons. This could come from a variety of different effects, such as the longer D^+ lifetime as discussed later and the variation of efficiency with charged multiplicity, which peaks at a multiplicity of three and could favour charged B-hadrons. There must be a small enhancement in Λ_b^0 selection efficiency in the simulation arising from its longer lifetime, but this has been neglected throughout.

Type	Fraction of selected vertices	Initial fraction of B-hadrons
B^+	$53 \pm 4\%$	40.1%
B^0	$30 \pm 3\%$	40.1%
B_s^0	$9 \pm 2\%$	11.9%
Λ_b^0	$6 \pm 2\%$	7.9%
Background	$2 \pm 1\%$	—

Table 3: The composition of the selected event sample in the Monte Carlo simulation, where all the B-hadron lifetimes are 1.2 ps except the Λ_b^0 , which is 1.3 ps.

4 Lifetime Fitting Procedure

4.1 Charge Estimation

In order to extract the charged and neutral B lifetimes, it is important to estimate the charge at the detected secondary vertex as accurately as possible. A correction was made

for undetected charged particles from B decays using the fraction of doubly and triply charged secondary vertices found. The procedure assumes the quark model prediction that there are no multiply-charged B-hadrons. The probability of getting the charge of the decaying particle wrong was fitted as :

$$P(q \rightarrow Q) = \mathcal{P}^{|q-Q|} \cdot \frac{1-\mathcal{P}}{1+\mathcal{P}} \quad (2)$$

where q is the true charge, Q is the observed charge and \mathcal{P} is a free parameter, which for small \mathcal{P} is the probability of measuring a charge difference of one in either direction. This can be seen to be a reasonable description, as shown in Figure 3 a). The charge was measured correctly in $71 \pm 3\%$ of the simulated events, and the numbers of multiply-charged vertices, shown in Figure 3 b), were used to estimate the parameter \mathcal{P} in the data (see Table 4 below).

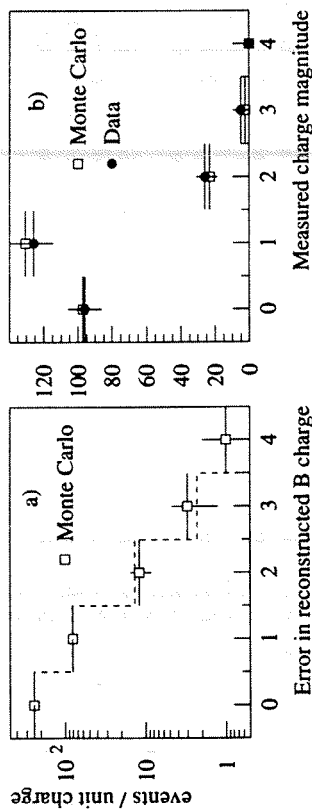


Figure 3: a) The modulus of the difference between the true charge and the reconstructed charge in Monte Carlo simulation, fitted using equation (2). b) The measured charge magnitude distribution including charged B-hadrons.

4.2 Proper Time Estimation

The B lifetime is fitted from the proper time distribution of the reconstructed decays. This requires a knowledge of the decay length and the B-hadron velocity. The former was found from the positions of the primary and secondary vertices; the latter was calculated from the measured momentum and invariant mass.

4.2.1 Decay Length Measurement

The measured decay length, $l_{R\phi}$, is a convolution of the decay length of the B-hadron with that due to the subsequent decays of B decay products, particularly D mesons.

One of the selection criteria was that all particles assigned to the B should be compatible with coming from a single vertex and this requirement acted as a bias against the longer lived D hadrons, particularly the D^+ . The results of the simulation imply that the mean shift of the reconstructed vertex away from the real B decay point was $220 \pm 30 \mu\text{m}$ and $320 \pm 60 \mu\text{m}$ for D^0 and D^+ mesons, respectively. This should be contrasted with a factor 2.5 difference in the D lifetimes.

In fact, in order to extract the lifetime, the excess decay length, $l_{R\phi}^{\text{excess}}$, beyond the minimum required to identify the vertex, $l_{R\phi}^{\text{min}}$, was used rather than the full decay length, $l_{R\phi}$. The charged particle tracks identified as coming from the decay were moved back towards the primary interaction vertex without changing their relative positions. The point at which the decay vertex could just be distinguished with the procedure described above was found individually for each decay. The next best vertex combination has a probability of exactly 1% at this point. The distance to the primary vertex was then the minimum acceptable decay length, and the time distribution of the decaying particles beyond this point was just given by their lifetime.

While the change in the calculated proper time due to the finite decay time of the secondary D hadrons is not completely removed for individual events, in this method it is significantly reduced. More important is that the influence of the D lifetime is not only to increase the apparent proper time of the events which would have been accepted in any case, but also to allow some events to be seen which would otherwise not have been accepted.

The minimum acceptable decay length of each event, as defined above, was required to be greater than 5 standard deviations σ_l . This selection ensures that an excess decay time distribution where resolution effects can be neglected and where the acceptance is constant is obtained. The excess decay time distribution can then be described by an exponential with a slope given by the B lifetime to a very good approximation †.

The excess three dimensional decay length, l^{excess} , was found from this excess length in the $R\phi$ plane, $l_{R\phi}^{\text{excess}}$, as

$$l^{\text{excess}} = \frac{l_{R\phi}^{\text{excess}}}{\sin \theta} \quad (3)$$

where θ is the polar angle of the vector sum of the momenta of the charged particles assigned to the decay vertex.

4.2.2 Boost Estimation

The momentum of the parent B was found using the method of reference [8], which uses the fact that for sufficiently large boost, the velocity of the B is the same as that of the observed component :

$$\left(\frac{1}{P_B}\right)^{\text{est}} = \alpha \frac{M_{\text{vis}}^{\pi} 1}{M_B P_{\text{vis}}} \quad (4)$$

where $\left(\frac{1}{P_B}\right)^{\text{est}}$ is the estimate of the inverse of the B momentum, M_{vis}^{π} is the effective visible mass, assuming that all the particles are pions, P_{vis} is the sum of the momenta of the particles at the secondary vertex and α is a correction factor of order one. Substituting this into the equation for the excess proper time gives :

$$l^{\text{excess}} = M_B l^{\text{excess}} \left(\frac{1}{P_B}\right)^{\text{est}} = \alpha \frac{M_{\text{vis}}^{\pi} l^{\text{excess}}}{P_{\text{vis}}} \quad (5)$$

The value of α used was $1.25 - 0.061 M_{\text{vis}}^{\pi} (\text{GeV}/c^2)$ for both charged and neutral B-hadrons. It deviated from one because of the exclusion of charged particles of momentum less than $0.5 \text{ GeV}/c$, the fact that M_{vis}^{π} was calculated on the assumption that all the particles were pions when it was very likely that at least one was a kaon, and the missing transverse momentum which biased the estimator for low momentum. The coefficients of α were

†The convolution of an infinite exponential with an unknown (but finite) distribution is an exponential with the slope of the original.

derived from Monte Carlo simulation, and depended upon the B decay scheme assumed there. However, the dependence was rather weak.

The estimate of the proper time has statistical accuracy of 25% in the Monte Carlo simulation, and this increased the spread of the proper time distribution by a factor of $\sqrt{1 + 0.25^2} = 1.03$. The value of α had some dependence on the species, and was 3% smaller for B^0 and 1% larger for B-baryons in the simulation used. No correction was made for this effect.

The mean momentum of the accepted events, using equation (4) and assuming that the mass of each B-hadron is $5.27 \text{ GeV}/c^2$, was found to be $33.4 \pm 0.5 \text{ GeV}/c$ for the data and $32.6 \pm 0.5 \text{ GeV}/c$ for the Monte Carlo simulation. Thus there is no apparent inconsistency when using an expression for α derived from simulated events.

4.3 The Fit Method

An unbinned maximum likelihood fit was made to the distribution of excess proper times. This included an estimation of the probability of reconstructing the charge wrongly, using the number of doubly and triply charged secondary vertices observed. The likelihood of event i to have observed charge Q_i and excess proper time t_i^{excess} was taken to be:

$$\mathcal{L}_i = \sum_{\nu} P(q_{\nu} \rightarrow Q_i) C_{\nu} e^{-t_i^{\text{excess}}/\tau_{\nu}} \quad (6)$$

where the sum runs over the B-hadron species considered in the fit and over the background. The three fits considered later allow the species to be the average B, the charged and neutral B-hadrons, and the four most common species (B^+ , B^0 , B_s^0 , Λ_b^0) at LEP, respectively. $P(q_{\nu} \rightarrow Q_i)$ is the probability that a B-hadron of charge q_{ν} will be reconstructed as having charge Q_i , C_{ν} is the normalization constant for species ν , and τ_{ν} is the mean lifetime of the B-hadrons from species ν .

$P(q_{\nu} \rightarrow Q_i)$ was given in equation (2). It depended on the parameter \mathcal{P} , which was allowed to vary in the fit and was constrained by the observed number of multiply-charged events. The background fraction, seen to be 2% in Table 3, was taken to have the charge distribution expected by combining four or five charged particles of random charge.

The normalization constants C_{ν} are given as:

$$C_{\nu} = \frac{F_{\nu}}{\tau_{\nu} [1 - e^{-t^{\text{max}}/\tau_{\nu}}]} \quad (7)$$

where the F_{ν} are the relative fractions of the various B species (and the background) in the selected sample, and t^{max} is the maximum allowed excess proper time of the events used in the fit and was set to 8 ps. The fractions of the selected sample, F_{ν} , are related to the fractions f_{ν} which would have been observed if the lifetimes had been equal:

$$F_{\nu} = \frac{1}{N} \times \sum_i \frac{f_{\nu} e^{-t_i^{\text{min}}/\tau_{\nu}}}{\sum_{\mu} f_{\mu} e^{-t_i^{\text{min}}/\tau_{\mu}}} \quad (8)$$

where N is the number of selected events and t_i^{min} is the proper time of the minimum decay distance at which event i would have been observed. The fractions f_{ν} are not the same as the production rates of the various B species because of the different selection efficiencies for the different decay topologies, but are as given in Table 3.

5 B Lifetime Results

5.1 Fit to Mean B Lifetime

In a first fit the charge information was ignored and all the data were fitted to give an average B lifetime. This average is not the usual mixture of species seen at LEP, but includes relatively more of the longer lived varieties. A background fraction of 2% with an apparent lifetime of 3.0 ps, which is simply a parameterization of the background seen in Monte Carlo simulation, was allowed in this fit. The result is:

$$\langle \tau_B \rangle = 1.49 \pm 0.11 \text{ (stat) ps} \quad (9)$$

Applying the same treatment to simulated events gave $\langle \tau_B \rangle = 1.17 \pm 0.09$, while the mean B lifetime in the simulation was 1.21 ps. Fitting the reweighted events also gave good agreement, but the fluctuations in such fits were found to be bigger than the reported statistical errors, and so the results are not used.

Variation of the exact values of the cuts used did not give changes in the results larger than would have been expected statistically, and thus show no evidence for systematic effects. The major systematic error was therefore estimated as the same fractional size of effect as could be present without being seen in the simulated sample, 0.11 ps. A 3% systematic uncertainty in the momentum estimation was also allowed for, coming from the difference between the value of α applicable for different B species. This gave a contribution to the systematic error of 0.05 ps. Finally, varying the background in the fit from zero to 4% changed the result by 0.02 ps. These have been combined to give:

$$\langle \tau_B \rangle = 1.49 \pm 0.11 \text{ (stat)} \pm 0.12 \text{ (sys) ps} \quad (10)$$

5.2 Fit to Charged and Neutral B-hadron Lifetimes

The excess proper time distributions of the charged and neutral events are shown in Figure 4. The fit to the average charged and neutral B lifetimes, as described below, is superimposed. In this fit it was assumed that all charged B species have one lifetime and all neutral ones have another. The relative normalization of the two species was left free to reduce the dependence upon the Monte Carlo simulation. The results of this fit are shown in Table 4.

Parameter	Data	Simulation	
		Fit result	Correct value
$\langle \tau_{\text{charged}} \rangle$ (ps)	1.56 ± 0.19	1.13 ± 0.11	1.20
$\langle \tau_{\text{neutral}} \rangle$ (ps)	1.44 ± 0.21	1.34 ± 0.16	1.21
f_+	0.52 ± 0.08	0.63 ± 0.06	0.53
\mathcal{P}	0.18 ± 0.03	0.14 ± 0.02	0.16
$\langle \tau_{\text{charged}} \rangle / \langle \tau_{\text{neutral}} \rangle$	$1.09^{+0.28}_{-0.23}$	$0.84^{+0.17}_{-0.14}$	0.99

Table 4: Fit to average charged and neutral lifetimes, with the statistical errors shown. \mathcal{P} is defined in section 4.1, and f_+ is the fraction of charged B-hadrons which would have been selected if the lifetimes had been equal. The lifetime ratio is not an independent parameter, but the errors have been calculated separately. The parameter \mathcal{P} in the data corresponds to a 30% chance of getting the charge wrong. The B lifetime was 1.2 ps in the simulation, for all states except the Λ_b^0 for which it was 1.3 ps.

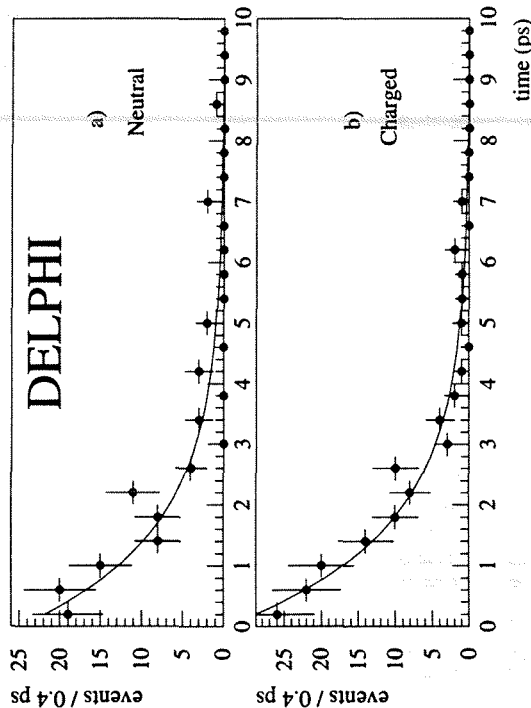


Figure 4: The excess proper time distributions of the charged and neutral events

Table 5 shows the systematic uncertainties estimated in the analysis. The background fraction was varied from zero to double, and the changes interpreted as a systematic error. In the simulation the weighting technique was used to introduce different charged and neutral lifetimes. Then the ability of the fit program to recover those lifetimes was tested and a charge unfolding systematic error derived. This error is compatible with the Monte Carlo statistics, but such an effect cannot be excluded.

Systematic	$< \tau_{\text{charged}} >$ (ps)	$< \tau_{\text{neutral}} >$ (ps)	$< \tau_{\text{charged}} > / < \tau_{\text{neutral}} >$
Background fraction	± 0.01	± 0.01	± 0.01
Charge unfolding	± 0.03	± 0.05	± 0.06
Momentum estimation	± 0.06	± 0.06	± 0.05
Possible analysis bias	± 0.11	± 0.11	± 0.07
Total systematic	± 0.13	± 0.14	± 0.11

Table 5: Systematic uncertainties in the fit to the average charged and neutral B lifetimes.

The momentum estimation includes not only the 0.05 ps coming from variation of α referred to in section 5.1, but also an allowance for a small bias in the value of α of events where a low momentum particle has been missed. Furthermore, variation of the parameter α in equation (5) for different neutral B-hadrons leads to a systematic uncertainty on their lifetimes. The maximum variation of the α parameter between B species is 3%, and so this is the systematic uncertainty which is used.

The systematic assigned for any bias in the analysis was discussed in section 5.1 above; the systematic error on the ratio comes from the hypothesis that such a bias occurs for only one of the B species.

Variation of the exact values of the cuts used produced changes in the results compatible with the statistical fluctuations expected. These have therefore not been quoted as systematic errors. The results for the mean charged and neutral lifetimes are :

$$\begin{aligned}
 < \tau_{\text{charged}} > &= 1.56 \pm 0.19 \text{ (stat)} \pm 0.13 \text{ (sys)} \text{ ps} \\
 < \tau_{\text{neutral}} > &= 1.44 \pm 0.21 \text{ (stat)} \pm 0.14 \text{ (sys)} \text{ ps} \\
 < \tau_{\text{charged}} > / < \tau_{\text{neutral}} > &= 1.09^{+0.28}_{-0.23} \text{ (stat)} \pm 0.11 \text{ (sys)}
 \end{aligned}
 \quad (11)$$

5.3 Fit to B^0 and B^+ Lifetimes

The data were also interpreted in terms of the lifetimes of the B^0 and B^+ mesons, by assuming a composition for the neutral B-hadrons and also by using the lifetimes for the B_s^0 and Λ_b^0 as measured in independent analyses of LEP data. The B^0 lifetime extracted in such a manner depended critically upon these assumptions, but the B^+ was relatively insensitive to them. The B_s^0 and Λ_b^0 lifetimes were set to the average of ALEPH and DELPHI results : 1.05 ± 0.33 ps [9] and 0.98 ± 0.23 ps [10], respectively. The neutral species were divided in the same proportions as in Table 3, and the relative amount of B^+ was fitted. No other B-hadrons were allowed for. The results are shown in Table 6.

Parameter	Data value	Simulation
τ_{B^+} (ps)	1.56 ± 0.19	1.13 ± 0.11
τ_{B^0} (ps)	1.55 ± 0.25	1.41 ± 0.22
f_{B^+}	0.51 ± 0.08	0.63 ± 0.06
\mathcal{P}	0.18 ± 0.03	0.14 ± 0.02
τ_{B^+} / τ_{B^0}	$1.01^{+0.29}_{-0.22}$	$0.80^{+0.22}_{-0.15}$

Table 6: Results for the B^+ and B^0 lifetimes; only statistical errors are quoted. The B lifetimes were set to 1.2 ps in the simulation for all states except the Λ_b^0 which was assigned a lifetime of 1.3 ps.

The systematic uncertainties have been taken from Table 5, but rescaled appropriately. The systematic error on the composition of the sample, due to varying the B_s^0 and Λ_b^0 lifetimes by one standard deviation and to changing their fractions by a factor of two, has been added. The final values for the B^+ and B^0 meson lifetimes are :

$$\begin{aligned}
 \tau_{B^+} &= 1.56 \pm 0.19 \text{ (stat)} \pm 0.13 \text{ (sys)} \pm 0.00 \text{ (composition)} \text{ ps} \\
 \tau_{B^0} &= 1.55 \pm 0.25 \text{ (stat)} \pm 0.17 \text{ (sys)}^{+0.07}_{-0.06} \text{ (composition)} \text{ ps} \\
 \tau_{B^+} / \tau_{B^0} &= 1.01^{+0.29}_{-0.22} \text{ (stat)} \pm 0.11 \text{ (sys)}^{+0.04}_{-0.05} \text{ (composition)}
 \end{aligned}
 \quad (12)$$

Note that, if the four B lifetimes from this fit are combined to form a weighted LEP average, using the production fractions as given by the simulation, the result is $< \tau_B > = 1.44$ ps, 0.05 ps lower than that deduced in section 5.1 because that sample was enriched in longer lived species.

6 Summary

From 232 114 hadronic Z^0 decays collected at the LEP collider with the DELPHI detector, a sample of 253 B-hadron candidates with an estimated purity of 98% has been extracted and the mean B lifetime has been measured to be :

$$< \tau_B > = 1.49 \pm 0.11 \text{ (stat)} \pm 0.12 \text{ (sys)} \text{ ps}$$

This result has somewhat larger errors than the $\langle \tau_B \rangle$ previously presented by DELPHI of 1.41 ± 0.07 ps [11], but is an independent number with different systematics. The mean presented here is over a mixture of events which contains more than the LEP average of the longest lived species, and is increased by about 0.05 ps as compared with that derived with some assumptions about the B_s^0 and Λ_b^0 .

The results for the mean charged and neutral lifetimes are :

$$\begin{aligned} \langle \tau_{\text{charged}} \rangle &= 1.56 \pm 0.19 \text{ (stat)} \pm 0.13 \text{ (sys)} \text{ ps} \\ \langle \tau_{\text{neutral}} \rangle &= 1.44 \pm 0.21 \text{ (stat)} \pm 0.14 \text{ (sys)} \text{ ps} \\ \langle \tau_{\text{neutral}} \rangle &= 1.09^{+0.28}_{-0.23} \text{ (stat)} \pm 0.11 \text{ (sys)} \\ \langle \tau_{\text{charged}} \rangle / \langle \tau_{\text{neutral}} \rangle &= 1.01^{+0.29}_{-0.22} \text{ (stat)} \pm 0.12 \text{ (sys)} \end{aligned}$$

The assumptions stated in the previous section allow the B^+ and B^0 lifetimes to be measured. Combining the systematic uncertainties, these are as follows :

$$\begin{aligned} \tau_{B^+} &= 1.56 \pm 0.19 \text{ (stat)} \pm 0.13 \text{ (sys)} \text{ ps} \\ \tau_{B^0} &= 1.55 \pm 0.25 \text{ (stat)} \pm 0.18 \text{ (sys)} \text{ ps} \\ \tau_{B^+}/\tau_{B^0} &= 1.01^{+0.29}_{-0.22} \text{ (stat)} \pm 0.12 \text{ (sys)} \end{aligned}$$

A composition systematic uncertainty is taken into account for the B^0 . The B^+ is assumed to completely dominate the charged state, so there is little composition uncertainty associated with its lifetime.

Previous measurements at CLEO and ARGUS [12] of the semi-leptonic branching ratios of the B^0 and B^+ mesons can be used to infer lifetimes which are equal to within about 25% if the semi-leptonic decay widths are assumed to be identical. DELPHI has previously measured the B^0 and B^+ lifetimes in an analysis based on $D\ell^-$ and $D^*\ell^-$ events [13]. This gave $\tau_{B^0} = 1.17^{+0.29}_{-0.23} \pm 0.15 \pm 0.05$ ps, $\tau_{B^+} = 1.30^{+0.33}_{-0.29} \pm 0.15 \pm 0.05$ ps, $\tau_{B^+}/\tau_{B^0} = 1.11^{+0.51}_{-0.39} \pm 0.15 \pm 0.10$, in good agreement with other LEP measurements [14].

Acknowledgements

We are greatly indebted to our technical collaborators and to the funding agencies for their support in building and operating the DELPHI detector, and to the members of the CERN-SL Division for the excellent performance of the LEP collider.

References

- [1] "Z Physics at LEP 1", ed. G. Altarelli, R. Kleiss and Z. Verzhnassi, CERN 89-08, Geneva (1989), Vol. 1, p. 311-320.
- [2] DELPHI coll., P. Aarnio et al.: "The DELPHI Detector at LEP", Nucl. Inst. and Meth. **A303** (1991) 233.
- [3] N. Bingsfors et al.: "The DELPHI Microvertex Detector", preprint CERN-PPE/92-173 (1992), Nuc. Inst. and Meth., to be published.
- [4] D. Johnson, D. Reid and W. Trischuk: "A Beamsplit Database for Lifetime Measurements", DELPHI 92-36 PHYS 168, Geneva, 18 March 1992.
- [5] JADE coll., W. Bartel et al.: "Experimental Studies on Multijet Production in e^+e^- Annihilation at Petra Energies", Zeit. Phys. **C 33** (1986) 23.
- [6] T. Sjöstrand: Comp. Phys. Comm. **39** (1986) 347; T. Sjöstrand and M Bengtsson: Comp. Phys. Comm. **43** (1987) 367.
- [7] DELSIM Reference Manual, DELPHI 87-98 PROG 100, Geneva, July 1989.
- [8] B. Franek: Rutherford Appleton Laboratory, RAL-85-026 (1985).
- [9] DELPHI coll., P. Abreu et al.: "Evidence for B_s^0 Meson Production in Z^0 Decays", Phys. Lett. **B 289** (1992) 199; ALEPH coll., "A Measurement of the B_s^0 Lifetime", Proc. 7th Meeting of the American Physical Society, Division of Particle and Fields (DPF92), Fermi National Accelerator Laboratory, U.S.A, November 10-14, 1992.
- [10] DELPHI coll.: "Measurement of Λ_b^0 Production and Lifetime in Z^0 Hadronic Decays", DELPHI 92-81 PHYS 192, Proc. 7th Meeting of the American Physical Society, Division of Particle and Fields (DPF92), Fermi National Accelerator Laboratory, U.S.A, November 10-14, 1992; ALEPH coll., D. Buskulic et al.: "A Measurement of the b Baryon Lifetime", Phys. Lett. **B 297** (1992) 449.
- [11] DELPHI coll., P. Abreu et al.: "Inclusive measurement of the average lifetime of B-hadrons produced at the Z peak", DELPHI 92-108, submitted to the XXVI International Conference on High Energy Physics, August 6-12, 1992 Dallas, Texas, U.S.A.
- [12] S. Stone : "Semileptonic B Decays : Experimental", HEPHY-4-91 (October 1991). To be published in 'B decays', ed. by S. Stone, World Scientific.
- [13] DELPHI coll., P. Abreu et al.: "A Measurement of B Meson Production and Lifetime Using $D\ell^-$ Events in Z^0 Decays", Zeit. Phys. **C 57** (1993) 181.
- [14] OPAL coll., P.D. Acton et al.: "Measurement of the B^0 and B^- lifetimes", preprint CERN-PPE/93-33 (1993), Phys. Lett. **B**, to be published; ALEPH coll., D. Buskulic et al.: "Measurement of the B^0 and B^- meson lifetimes", preprint CERN-PPE/93-42 (1993), Phys. Lett. **B**, to be published.